Humid Post-Combustion CO_2 capture By Vacuum Swing Adsorption Using CALF-20

by

Tran Thanh Tai Nguyen

A thesis submitted in partial fulfillment of the requirements for the degree of

Doctor of Philosophy

in

CHEMICAL ENGINEERING

Department of Chemical and Materials Engineering

University of Alberta

Abstract

Carbon capture utilization and storage (CCUS) play a crucial contribution in reducing CO_2 emissions and obtaining net-zero emission by 2050. Adsorbent-based technology offers an opportunity to separate CO_2 under mild regeneration conditions. However, low CO_2 concentration and water vapour in the flue gas make it challenging to separate CO_2. In this thesis, CALF-20, a water-stable metal-organic framework (MOF), was characterized and demonstrated for humid post-combustion CO_2 capture. Single-component CO_2 and N_2 isotherms were measured at various pressures and temperatures using volumetric and gravimetric methods. The dual-site Langmuir model was used to describe the CO_2 and N_2 isotherms. The adsorption equilibrium of water was measured from 0%-100% relative humidity (RH) at various temperatures using thermogravimetry analysis and volumetric methods. A hysteresis loop was observed from 8%-22% RH. The Quadratic-Langmuir model was used to describe water isotherms. The competitive loadings of CO_2 and N_2 were quantified by performing both adsorption and desorption dynamic column breakthrough (DCB) experiments. The CO_2 loading barely changed under the competition of N_2. The adsorption and desorption DCB of water were also performed. Multiple transitions corresponding to the shape of the isotherm were observed in the water DCB curves. A one-dimensional column model, including all dispersion, convection, heat transfer and pressure drop, was used to describe the adsorption dynamic in the column. The competitive loadings of CO_2 and H_2O were collected using both thermogravimetry analysis and dynamic column breakthrough techniques. At RH<40%, the competitive CO_2 loadings barely changed. Water still exhibited a type V isotherm, but the inflection point shifted to higher RH, at ≈65% RH. The modified Langmuir isotherm model was used to describe the competitive CO_2 loading. The framework of CALF-20 showed an extension under the presence of CO_2. Basic four-step vacuum swing adsorption (VSA) and four-step VSA with light-product pressurization (LPP) cycles were used to evaluate the performance of CALF-20 under dry and wet conditions. Multi-objective optimizations were used to optimize process performances. Five points on the Pareto curves were chosen randomly to validate the model predictions. The adsorption of CO_2 was not affected by water at RH<45%. Similar purity, recovery and productivity compared to the dry case were obtained. The CO_2 separation at high RH (70%) was also demonstrated in this study. The results of this thesis showed that CALF-20 was capable of separating CO_2 under both wet and dry conditions.

Preface

This thesis focuses on the characterization of CALF-20 for humid post-combustion CO_2 capture. Part of the thesis is the result of the collaboration between the University of Alberta and the University of Calgary. The research conducted in this thesis was funded by the Canada Foundation for Innovation, Carbon Capture Initiative, Natural Sciences and Engineering Research Council (NSERC), and Alberta Innovates.

The material used in this study was synthesized and provided by Jian-Bin Lin and Nicholas Fylstra from the Shimizu Group, University of Calgary. Alberta Innovates provided resources for conducting the vacuum swing adsorption experiments. This thesis is written in a paper-based format; thus, several minor parts might be overlapped between chapters. A. Rajendran and G. Shimizu were the supervisory authors, and they were involved in concept formation, analysis and manuscript composition.

Chapter 2 of this thesis will be submitted for publication as T. T. T. Nguyen, J. B. Lin, A. Rajendran and G. Shimizu, "Adsorption equilibrium and dynamic column breakthrough studies of CO_2 and N_2 on CALF-20". In this paper, Tran Thanh Tai Nguyen was responsible for data collection and analysis. The manuscript was also composed by Tran Thanh Tai Nguyen.

Chapter 3 of this thesis will be submitted for publication as T. T. T. Nguyen, J. B. Lin, N. Fylstra, R. Huynh, G. Shimizu and A. Rajendran, "Adsorption equilibrium and breakthrough studies for water on CALF-20". In this paper, Tran Thanh Tai Nguyen was responsible for data collection and analysis. He was also responsible for the design of breakthrough experiments. R. Huynh and N. Fylstra assisted in measuring the adsorption and desorption water isotherm on CALF-20 at 22°C. Tran Thanh Tai Nguyen was responsible for the manuscript composition.

Chapter 4 and chapter 5 will be submitted for publication as T. T. T. Nguyen, B. Balasubramaniam, J. B. Lin, N. Fylstra, G. Shimizu and A. Rajendran, "Characterization of the CO_2/H_2O competitive adsorption on CALF-20". Tran Thanh Tai Nguyen was responsible for data collection and analysis. He was also responsible for the design of experiments and the manuscript composition. N. Fylstra assisted in measuring the powder X-ray diffraction of CALF-20. B. Balasubramaniam supported collecting the total loading of CO_2 and H_2O by the thermogravimetric analyzer.

Chapter 6 will be submitted as T. T. T. Nguyen, G. Shimizu and A. Rajendran, "Post-combustion CO_2 capture by vacuum swing adsorption using CALF-20: Multi-objective optimizations and experimental validations". In this paper, Tran Thanh Tai Nguyen was responsible for data collection and analysis. He was also responsible for the design of experiments and the manuscript composition.

Chapter 7 will be submitted as T. T. T. Nguyen, G. Shimizu and A. Rajendran, "Experimental demonstrations of humid post-combustion CO_2 capture by vacuum swing adsorption using CALF-20". In this paper, Tran Thanh Tai Nguyen was responsible for data collection and analysis. He was also responsible for the design of experiments and the manuscript composition.

Owing to the format of the thesis, some level of repetition of topics is unavoidable.

To my family

For their support and their love

“We do not need to be afraid of questions and doubts because they are the beginning of a path of knowledge”

Pope Francis

Weekly General Audience

November 23rd, 2016

Acknowledgements

I would like to express my gratitude to my supervisors, Dr. Arvind Rajendran, for giving me the opportunity to pursue doctoral studies at the University of Alberta. His passion and dedication to chemical engineering have inspired me. I learnt to look at a problem with different perspectives, thanks to Arvind, his insightful discussions and inspirations. I would also like to thank my supervisory committee, Dr. George Shimizu and Dr. Natalia Semagina. Their guidance and support encouraged me to overcome countless challenges and difficulties during my PhD. It would have been more challenging to complete this dissertation without the support of my supervisors.

I would like to thank Alberta Innovates for access to their facilities during my PhD. I would like to thank Dr. Partha Sarkar, Mr. Frank Tosto, Mr. Juan Segura and Ms. Twyla Malcolm for their support while working at Alberta Innovates.

I acknowledge the funding from Canada Foundation for Innovation, Carbon Capture Initiative, Natural Sciences and Engineering Research Council (NSERC), and Alberta Innovates.

Thank you to my former and current colleagues and friends, Bhubesh, Brad, Gokul, Gwyneth, Jim, Libardo, Nagesh, Nick W., Rafael, Vishal, Yogashree. I enjoyed every story, every intellectual discussion we shared during lunch breaks. I would never forget the joy and journey we had playing boardgames. Thank you to all the friends I have met at the University of Calgary, Ben, Garima, Jian-Bin, Jinfeng, Kamila, Martin, Nedal, Nick F., Patrick, Rachael.

I would like to thank St. Joseph College at the University of Alberta. Thank you to the Alpha team, the University of Alberta Catholic Student Association (UofA CSA), the 4:30 choir, the 6:30 Praise and Worship. This is my second home, where I always feel peace and welcome.

I am sincerely grateful to my family for their love and support. My dad teaches me how to be persistent in pursuing my passions. My mom always shows her unconditional love and empathy whenever I need her. Thanks to my brothers and sisters for updating news and stories back in Vietnam, thanks for patiently talking to me every weekend. My oldest sister, thank you for giving endless support and travelling half of the world to visit me.

Contents

List of Figures

List of Tables

1 Introduction

1.1. Global warming and climate change

Climate change is evident, and it is accelerating because of human-induced warming [1, 2]. Relative to the pre-industrial period (1850-1900), the average global temperature has increased by approximately 1°C (Fig. 1.1a) [1, 2]. Many regions are experiencing higher warming than the global average, which result in profound natural conditions, such as droughts [3], floods [4, 5], extreme weather [6], ocean acidification [7], sea-level rise [8, 9], loss of biodiversity [10, 11]. People from low and middle-income countries have been suffering from food shortages [12]. Severe impacts put numerous ecosystems at risk, tropical reefs and the Arctic ecosystems, in particular [7, 13].

In December 2015, the United Nations Framework Convention on Climate Change (UNFCCC) urged Parties to limit the rise of global temperature at 1.5°C by cutting greenhouse gas emissions. The Paris Agreement was adopted by 195 nations at the 21st Conference of the Parties (COP21) to reinforce the global response to climate change threats. The Intergovernmental Panel on Climate Change (IPCC) issued special reports on the impacts of global warming of 1.5°C and emissions pathways to a 1.5°C warmer world [2].

The IPCC reported several mitigation pathways to limit global warming to 1.5°C. To meet the 1.5°C target, many factors have been considered, such as the role of CO_2 and non-CO_2 emissions, technology developments, economic growth, energy and land transformation, global collaboration. With high confidence, this report showed that net-zero CO_2 emissions would need to be obtained in less than 15 years to achieve 1.5°C above pre-industrial levels. This requirement translates to a reduction of 45% anthropogenic CO_2 emissions from 2010 levels by 2030, and net-zero emissions by 2050 [2]. These mitigation pathways are measured by a decrease in energy demands, the use of clean and renewable energy sources, reducing emissions from agriculture activities, the role of carbon capture and storage (CCS) and carbon dioxide removal (CDR). Both CCS and CDR contribute to a finite extent to mitigate the CO_2 emissions in most analyzed pathways (Fig. 1.1b).

Note that renewable energy (wind, solar, bioenergy, hydrogen) can only share about 60% of energy demand by 2050 [2]. The remaining demands still rely on the use of fossil fuels with the support of CCS technology.

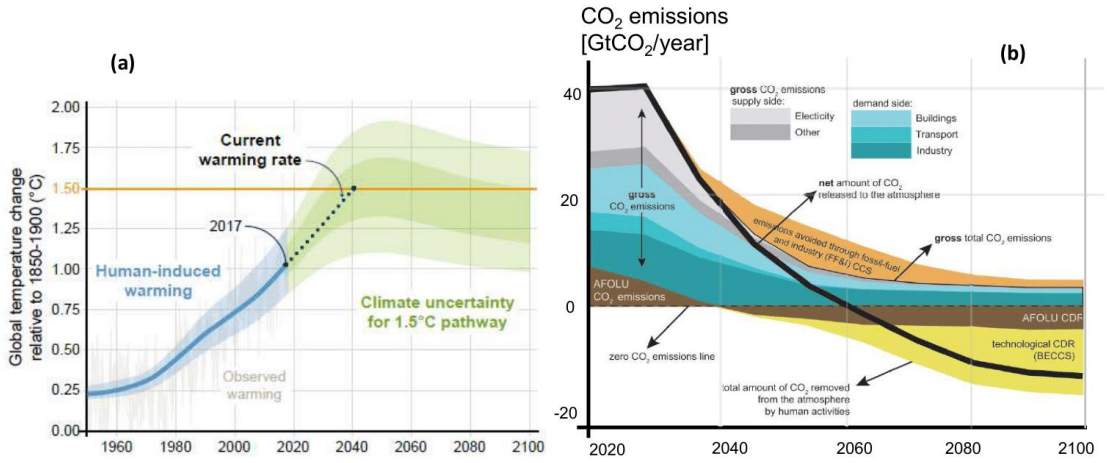

Figure 1.1: Global temperature change over year and a pathway to net-zero emission; Data modified from [2]. (a) The global temperature change over year relative to the pre-industrial period (1850-1900); (b) An example of a pathway to reach zero emission by 2060 which involves the reduction of emissions in the use of fossil fuels and industry (orange pattern), buildings, transport and industry (cyan pattern), the agriculture, forestry and land uses (AFOLU - brown pattern), and the bioenergy with carbon capture and storage (light green pattern).

In the energy sector, the largest end-user sector belongs to the industry in terms of energy demands and total greenhouse gases (GHG) emissions. An increase of 3.4% per year in the CO_2 emissions was observed in the period of 2000 – 2014 in this sector [14]. Typical industrial end-users are the petrochemical industry, chemical production, cement production, material industry, and pulp and paper industry. To meet the 1.5°C target, the analyzed mitigation pathways suggested key objectives to achieve by 2050: an increase of 42% in energy efficiency, a growth of 37% in innovations and CCS technologies, a 13% development in low-carbon investments [2].

The transformation of the energy system keeps a key contribution to 1.5°C pathways. Key characteristics are the decarbonization of energy supply by upscaling renewable and sustainable energies and the rapid implementation of CCS, the reduction in energy demands, the transition of fossil fuels to electricity, and the switch to low carbon energy investments. By 2050, it is suggested

that renewable energies (bioenergy, hydrogen, wind, solar and geothermal) will share 40% - 60% of the energy supply and power generations with CCS will contribute 40% [2]. The use of fossil fuels without CCS technology will be unfavourable. Therefore, CCS plays a crucial role in the CO_2 decarbonization to limit the global temperature at 1.5°C by 2050.

1.2. Carbon capture and storage technology

Zero-emission pathways require a significant contribution from CCS and CDR. While CCS technology allows using fossil fuels with net zero-emission, CDR deployment, also known as negative emission technology, will provide the means to mitigate the CO_2 emissions deeply [15, 16]. Numerous approaches to remove carbon dioxide from the atmosphere have been studied in the literature. Soil carbon enhancement and reforestation are actively studied to improve terrestrial carbon capture [15-17]. Another approach is the use of CO_2 reduction by bio-mitigation methods, such as microalgae [18] and Chlorella Vulgaris [19, 20]. Direct air capture (DAC) using chemical solvents and solid sorbents draw an extent of interest [21, 22]. The use of fossil fuels and bioenergy combining with CCS is also expected to play a vital role [23].

Carbon capture and storage technology include three main phases: capture, transport and storage. CO_2 is usually captured from the flue gas containing 5% - 20% of CO_2 at large facilities such as coal power plants, natural gas power plants, refineries, steel and cement plants. CO_2 can also be separated directly from the air (DAC), which only contains ≈400 ppm of CO_2. Afterwards, the captured CO_2 is compressed to ≈150 bars (dense phase) for transporting to geological storage. Depleted oil and gas fields and deep saline formations located over one-kilometre underground are used to sequester CO_2 [24].

1.2.1. Carbon capture and storage applications

Natural gas

The demand for natural gas in the global energy market has been accelerating since 2010, with a growth of 1.6% per year [25]. Compared to the coal power generation plants, natural gas produces half of the CO_2 emissions, at 350 kg CO_2/MWh [26]. However, it still releases about 700 Mtpa of CO_2, which is equal to the total amount of CO_2 emission in Germany in 2016 [27]. CCS technology, coupled with natural gas power generation, provides a feasible approach to reach a net-zero emission by the mid of this century. It is also one of the lowest cost CCS applications, at approximately USD$25/tonne CO_2 [28].

Several large-scale facilities have proved the feasibility of capturing CO_2 from natural gas power plants. About 0.7 Mtpa of CO_2 has been captured from the Snøhvit LNG plant in Norway and stored in the depleted natural gas field since 2008 [26]. The Gorgon CCS project in Australia separated CO_2 and stored at facilities on Barrow Island with a capacity of 3.4 – 4.0 Mtpa, reducing 40% of the total facilities' emissions [29]. Up to date, about 25 Mtpa of CO_2 have been captured at natural gas plants from ten large-scale CCS facilities [27].

Within the next five years, numerous natural gas power plants combined CCS are to be launched worldwide. The Abu Dhabi CCS Phase 2 aims to capture 1.9 to 2.3 Mtpa of CO_2 from its natural gas processing plant for enhanced oil recovery (EOR) in 2025 [26]. The Caledonia Clean Energy in Central Scotland set a target to capture 3 Mtpa of CO_2 and store it in the depleted gas field in 2024 [26]. Cal Capture, located in California, plans to retrofit a CCS facility to the natural gas combined cycle plant to capture 1.4 Mtpa of CO_2 in 2024 [29]. Natural gas power generation with CCS is a growing market with high demands. It offers plenty of opportunities to apply CCS technology to meet the low CO_2 emission pathway.

Hydrogen production

Hydrogen production with CCS regained the attention as a clean fuel with net-zero CO_2 emissions. In 2019, the European Union and 18 national governments placed significant incentives in using hydrogen in many industrial processes (chemical plants, steel mills, refineries), transport, domestic heating and power generation [26]. In fact, 98% of hydrogen production comes from fossil fuels and releases about 830 Mtpa of CO_2 during the production, which is equal to the total CO_2 emission of the UK in 2018 [29, 30]. To meet the 1.5°C emission pathway, it is crucial to integrate CCS into hydrogen production.

There are three main approaches to produce hydrogen with CCS: steam methane reforming, coal gasification, and electrolysis powered by renewables. Gas reforming and coal gasification have an advantage in technology maturity, which is ready to use in large-scale operational plants. Steam methane reforming with CCS from Quest Carbon Capture located in Alberta, Canada, has been in operation since 2015 with a capture capacity of 1 Mtpa of CO_2 [31]. The Air Products Steam Methane Reformer in Texas, USA, has been running since 2013 with a capture capacity of 1 Mtpa [29]. An amount of 2.5 – 3.0 Mtpa of CO_2 is captured in the gasification from the Great Plains Synfuel Plant in North Dakota, USA [32]. To make a significant contribution to the global CO_2

mitigation, hydrogen production will have to gain a notable amount to replace fossil fuel demand. Immediate actions and supports in capital grants and incentive policies from governments are required to scale up hydrogen production with CCS.

Power generation

The CO_2 emissions from power generation plants contribute half of the total anthropogenic CO_2 emissions, where coal-fired power plants are responsible for a third of the total energy-related emissions [2]. From the CCS perspective, it is more cost-effective to capture CO_2 from these large sources due to a high concentration of CO_2 in the flue gas. For the next few decades, power generation from coal is still required to meet the high energy demands, specifically in developing countries. To enable the continued use of coal, there is a need to retrofit CCS technologies into the current power generation facilities to maintain a low carbon emission pathway.

Post-combustion CO_2 capture can be retrofitted directly to any currently coal-fired power plants. In the post-combustion process, fuel is mixed and burned with air to generate power. The exhaust gas contains mostly N_2 (80%-85%), CO_2 (5%-15%), SO_x, NO_x and water vapour. The resulting flue gas is transferred to remove SO_x and NO_x before separating CO_2 from the mixture of CO_2/N_2. The diluted concentration of CO_2 in the flue gas and the low pressure at which the gas is emitted are the main challenges for CO_2 separation.

Currently, there are only two large scale coal-fired power plants with CCS in operation. The Boundary Dam 3 (BD3) located in Saskatchewan, Canada, was the first large scale CCS facility that was launched in 2014 [33]. Its capacity is 1 Mtpa of CO_2, and a part of captured CO_2 is used for EOR. Petra Nova Carbon Capture, located in Texas, USA, was operated in 2017. This is the largest post-combustion CO_2 capture in the world, with a capacity of 1.4 Mtpa [29]. However, NRG energy, the co-owner of Petra Nova project, announced to suspend the carbon capture operations at Petra Nova on August 26, 2020 [34], leaving BD3 as the leader. These large-scale CCS facilities have proven the feasibility of capturing CO_2 from industrial levels. However, there is a need for CCS technology development to reduce the cost of CO_2 capture.

Bioenergy with carbon capture and storage

Bioenergy with carbon capture and storage (BECCS) provides an opportunity to achieve negative emissions. Sustainable biomass is a source of renewable energy throughout the bioenergy production by combustion or fermentation with CCS [26]. Bioethanol is typical bioenergy that is

used to generate electricity by biomass combustion. IPCC placed BECCS as a feature technology in numerous scenario pathways to achieve the 1.5°C target [2].

Currently, BECCS technology is still in the developmental stage. Drax power station based in the UK is the first BECCS pilot plant, which was initiated in 2019 with a capture capacity of one tonne of CO_2 per day [29]. The success of BECCS is expected to open the door to building negative power generation plants. However, large-scale BECCS deployments may compete with food production and forest restoration. Also, a vast amount of water and fertilizers are required for biomass productions. Ecosystems will be changed under the impacts of these activities [35].

Direct air capture

The concept of direct air capture (DAC) is to separate CO_2 directly from the atmosphere. Extremely diluted CO_2 concentration in the air (0.04%) makes it challenged to capture CO_2 and restraints the efficiency. The use of chemicals is necessary to form a strong bond with CO_2 in this case. There are two potential approaches to proceed with DAC technology. CO_2 can be extracted by using a hydroxide solution and regenerated at high temperatures (≈ 900°C). Calcium looping is a typical example to illustrate this approach. The use of amine materials embedded in porous solid support is another solution, which requires less energy for regeneration (85°C - 120°C) [26].

At present, DAC is still in the design and development phase. Carbon Engineering Ltd, based in the USA, initiated a pilot testing site in Squamish, Canada. This facility is building a DAC plant with a target of 1 Mtpa of CO_2. Potassium hydroxide solution is used to strip the CO_2 from the air to form potassium carbonate. The CO_2 will be released in the calciner during the regeneration at elevated temperature (≈900°C) [36]. The cost of DAC makes it less appealing to the large-scale deployment without an improvement in CCS technology. Climeworks, a Swiss company that uses an adsorption-based technology, estimated the cost of DAC is ≈US$500-700 per tonnes of CO_2 captured [37].

1.2.2. CO_2 Capture technology and innovations

Using liquid solvents for CO_2 absorption is one of the mature techniques for CO_2 separation. Absorption can be a physical or chemical phenomenon where atoms, molecules and ions are absorbed in the bulk phase by physical or chemical bonding. Aqueous amines are the most common solvents for a CO_2 capture based absorption process [38, 39].

Liquid solvents have shown progress in CO_2 capture. The Boundary Dam coal power plant located in Saskatchewan is one of the large scale CO_2 capture plants using an aqueous amine [33]. The Shell Quest project using amine-based CO_2 capture has been running since 2015, which is located at Scotford Upgrader is capable of capturing a million tonne of CO_2 per year [40]. Petra Nova is another post-combustion CO_2 capture facility using liquid amines located in Texas, USA, with a capacity of 1.4 Mtpa [29]. Many issues still exist, such as solvent degradation and high regeneration energy, and the capture cost is still expensive (Fig. 1.2) that hinder the growth of this technology.

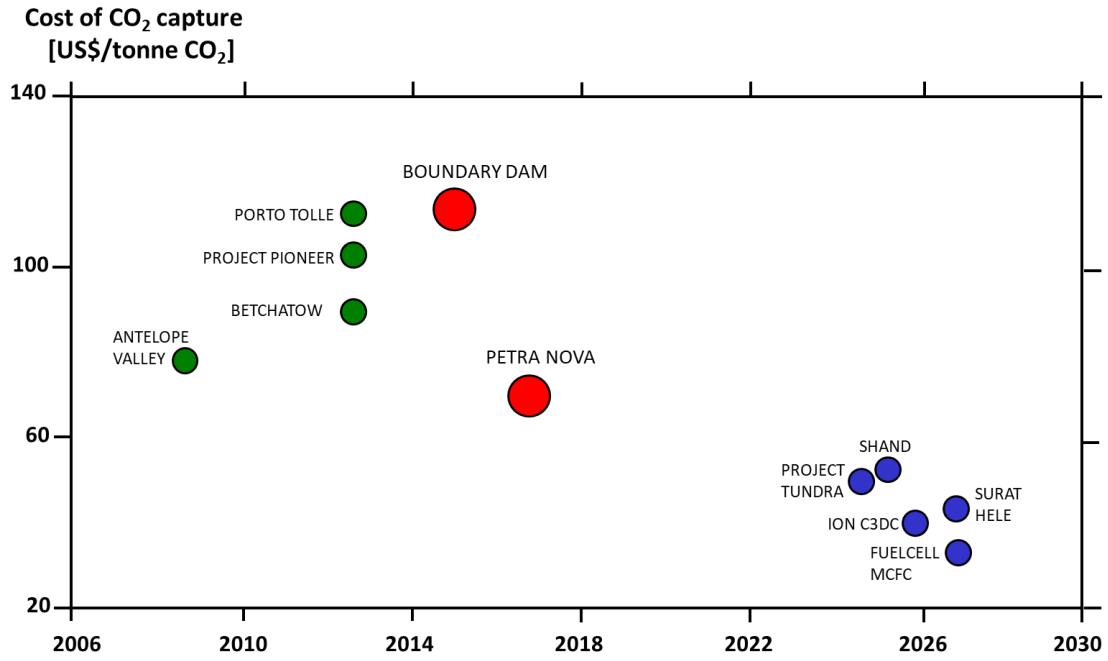

Figure 1.2: Estimated cost of CO_2 capture for large scale post-combustion capture facilities; Data replotted from [26]; Green markers are the previous studies, red markers represent the current operating facilities, and blue markers are the future facilities

Next-generation CO_2 capture technologies require novel materials with unique characteristics or process developments to diminish the capital and operating costs. Several CO_2 capture techniques are currently being developed. Table 1 provides an overview of the advantages/disadvantages and status of some key technologies.

Table 1.1: A summary of post-combustion CO_2 capture techniques

	Advantage	Drawback	Current status
Absorption	High capture rate Mature process	High regeneration energy Solvent degradation Corrosive solvents Heat stable salts build-up	Large-scale performance, 100 MW coal plant in Boundary Dam, Shell Quest [33]
Adsorption	Less regeneration energy Less toxic Stable adsorbents	Adsorbents are sensitive to humidity The high cost of materials High capital and operating cost	Pilot scale, 0.7 Mtpa at Svante Lafarge Holcim [29]
Membrane	No regeneration energy No waste streams	Membrane wetting Impurities plug membrane Difficult to scale up	Pilot-scale, e.g. Tiller plant in Norway [41]
Chemical looping (CLC)	Harmless exhaust gas stream from the air reactor Less energy penalty No gas separation needed	Under developing stage No large-scale experience	Pilot-scale, DAC at Carbon Engineering [36]

1.3. Adsorption processes

1.3.1. An overview of adsorption

Adsorption processes using solid sorbents have been attracting attention as a highly potential technology for CO_2 capture. This technique was first introduced in the 18th century and was implemented in industrial processes in the 19th century [42]. At first, adsorption was mostly applied to remove moisture from gas or liquid streams [42]. Later, it was adopted for purification processes such as the purification and separation of pigments, the removal of coloured impurities from sugar, and the removal of H_2S from natural gas [42]. Gas separation is a major application of adsorption processes. Some examples are removing CO_2 from syngas, enriching O_2 from the air or separating CO_2 from the flue gas.

Adsorption processes depend on the ability of solid sorbents to separate two or more components in a gas mixture [43, 44]. Each component may exhibit different affinities depending on the surface properties of the sorbent, which result in physisorption (physical bonding) or chemisorption (chemical bonding). There are two main adsorption mechanisms: equilibrium separation and kinetic separation. By exploiting the differences in the affinity, an equilibrium separation mechanism can be established. The kinetic separation exploits the differences in the diffusive properties of each component in the solid sorbent.

An adsorption isotherm carries important information for designing an adsorption process. It represents the relationship between the concentration in the gas phase and the solid phase (Fig. 1.3a). Adsorption is an exothermic process; when the temperature increases, the adsorbed phase concentration (also known as the solid loading q^*) decreases at a given pressure. The effect of temperature and pressure on the solid loading forms the basis of the adsorption process design.

To separate a gas mixture, the adsorbents are packed in a column, and the feed is introduced at the inlet end (Fig. 1.3b). The feed contains a strongly adsorbed component A (heavy component) and a weakly adsorbed component B (light component). Since the solid sorbent has different affinities to the gases, A and B travel through the column at different velocities. The light component (B) breaks through the column earlier, and it is collected at the other end of the column (raffinate product). The process is continued until the heavy component (A) nearly breaks through the column. Afterwards, the column is regenerated to reuse the solid sorbents. The regeneration process is performed either by increasing the temperature (TSA - Temperature swing adsorption) or reducing the pressure (PSA - Pressure swing adsorption). When the low pressure is below one atmosphere, it is called vacuum swing adsorption (VSA).

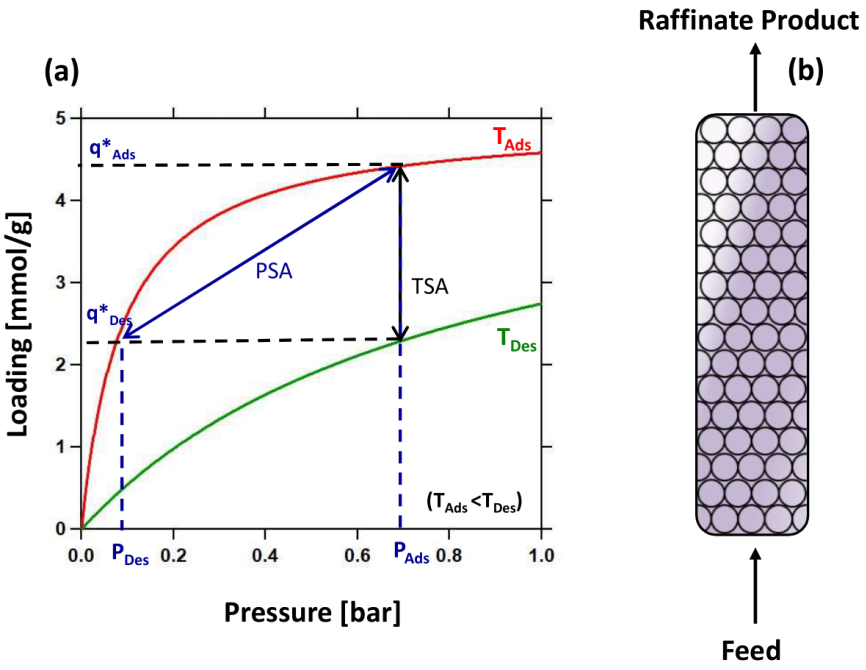

Figure 1.3: An isotherm illustration and pathways to design of adsorption processes; (a) An isotherm example at two different temperatures; (b) a packed bed column. PSA - Pressure swing adsorption process where the pressure is changed from high pressure (P_{Ads}) to low pressure (P_{Des}) at a given temperature; TSA - Temperature swing adsorption process where the temperature swings from low temperature (T_{Ads}) to high temperature (T_{Des}) at a given pressure; q^* is the equilibrium loading of the solid phase.

1.3.2. Solid sorbents for CO_2 capture

The adsorbents keep a key contribution to any adsorption processes. Activated carbon, activated alumina, zeolite and metal-organic frameworks (MOFs) are typical solid sorbents.

Activated carbon

Activated carbon is formed by the thermal decomposition of carbonaceous materials such as charcoal, coconut shells, nutshells or wood. It is then activated at the temperature of 700°C-1100°C, resulting in creating a very high porous material with a large surface area (500-1500 m^2/g) [43]. The pore size distribution of activated carbon varies from macropore to micropore, which could be favourable for removing contaminants, purifying substances, gas separation, etc.

Activated carbon was considered as a potential candidate for CO_2 capture. Activated carbon exhibits a larger capacity at higher pressure; it is also easy to regenerate, stable in the presence of moisture and low material cost [45]. Drage *et al*. examined nine different activated carbons for pre-combustion processes. The results showed that the maximum CO_2 capacity was recorded at 58 wt.% (13 mmol/g) at 3 MPa, while the H_2 uptake was at 0.3 wt.% [45].

Activated carbons demonstrated their potential in pre-combustion CO_2 capture. Their hydrophobic property makes them stable in humid conditions, and regeneration requires less energy than zeolite 13X, and the cost of material is reasonable. The heat of adsorption is 20 kJ/mol, i.e., half of zeolite 13X [46]. Commercial activated carbons were also examined for post-combustion CO_2 capture using VSA, TSA, VTSA. The highest purity and recovery were 43% and 97%, respectively, and the productivity was 1.9 mol/kg.h for the VTSA process [46]. However, owing to lower selectivity, achieving a high CO_2 purity product is a challenge.

Zeolites

Zeolites are a class of microporous materials, known as porous crystalline aluminosilicates, which are built based on SiO_4 and AlO_4 frameworks. Zeolites exist in both natural and synthetic forms. Various zeolites have been studied to evaluate their potential in CO_2 capture. Liu *et al*. simulated the performance of zeolite 5A for a VPSA process [47]. A mixture of CO_2/N_2 (15/85 mol%) was simulated with different cycle configurations containing two to four columns. The simulation results indicated that a single VPSA unit could not reach a purity of CO_2 higher than 77%. A two-stage VPSA configuration showed a possibility to obtain 96% of purity and 91.05% of the recovery. The productivity for this configuration was 0.0146 kg CO_2/ kg_{ads}.h, and the energy consumption was 180 kWh/tonne CO_2 [47].

Cation-exchanged zeolite 13X samples were examined for post-combustion CO_2 capture by Chen *et al*. [48]. These cations exchanged zeolites were found to enhance the intensity of diffraction peaks, which means to be able to improve the activity of zeolite 13X. Among these cation exchanged zeolites, the highest CO_2/N_2 selectivity was observed for LiPdAgX, and the CO_2/N_2 separation factor was as twice as zeolite 13X. The regeneration energy for LiPdAgX was 667 kWh_e/tonne CO_2, lower than zeolite 13X and MEA (approximately 1000 kWh_e/tonne CO_2) [48].

Activated carbons and zeolites have been contributing to many industrial applications, such as: removing moisture, removing impurities, purification and separation of polar species [49].

Numerous studies on activated carbons and zeolites have been reported on pre and post-combustion CO_2 capture [50-52]. However, the low purity and selectivity of activated carbons make them less attractive. On the other hand, the performance of zeolites was diminished dramatically under the presence of water vapour.

1.4. Metal-organic frameworks

The term "coordination polymers" was introduced in the early 1960s, in which structures were formed by metal nodes and organic linkers by coordination bonding [53]. Porous coordination polymers (PCPs) were developed based on the coordination polymer foundation. PCPs formed porous compounds with completely regular, high porosity, and highly designable frameworks [54]. In the 1990s, Yaghi's group introduced a new class of solid porous materials called metal-organic frameworks (MOFs). They have crystalline structures that can be predicted and are tunable [55]. Furthermore, large surface areas [56] make them favourable in many applications, such as gas storage [57], gas separation [58], and catalysis [59, 60].

The structure of a MOF is constructed with primary building units (PBUs) and secondary building units (SBUs). A PBU can be a metal ion (i.e. zinc, iron, nickel, zirconium, etc.) or an organic linker (i.e. benzene1,4-dicarboxylic acid, benzene-1,3,5-tricarboxylic acid, propanedioic acid). Two or more PBUs are combined to form an SBU [61]. MOF-5 (Fig. 1.4), which was reported in 1999 by Yaghi's group, was formed from $Zn(NO_3)_2$ salt as a metal center and BDC linker to create a cubic form [62].

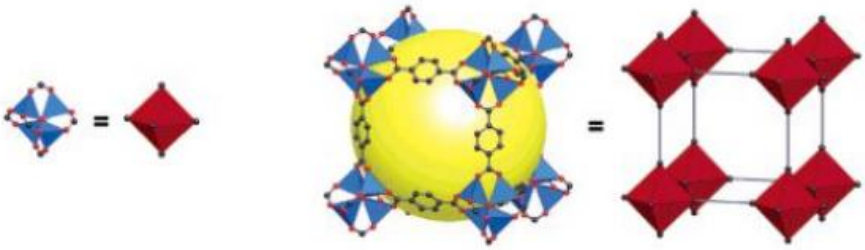

Figure 1.4: Structure of MOF-5 [62]

1.4.1. The development of MOFs for CO_2 capture

It was found that MOFs have great potential in CO_2 capture due to their unique structure and high surface area. Numerous studies of MOFs on enhancing CO_2 capacity have been performed [63].

In general, several methods to improve CO_2 uptake have been proposed, such as: increasing the surface area, adding functional groups and modifying metal ions.

Huang *et al*. reported a simulation and experimental study on enhancing CO_2 adsorption of Zr(IV) based MOFs [64]. In this work, the organic linkers were modified by different functional groups (-NO_2, -NH_2, -SO_3H). Both simulation and experiment results showed an improvement of CO_2 capacity. The equilibrium capacity at 298K and 1 bar was three times higher than the original MOF's capacity (200 cm^3 CO_2/cm^3 adsorbent vs 60 cm^3 CO_2/cm^3 adsorbent). Among these functional groups, -SO_3H displayed the highest CO_2 capacity, followed by –NH_2 and –NO_2. Also, the highest CO_2/N_2 selectivity was observed on -SO_3H (122.6), which was 7 times higher than the original Zr-MOF (16.2) [64].

A computational study on MIL-53(Al) with various functional groups (-OH, -COOH, -NH_2, -CH_3) was performed by Torrisi *et al*. [65]. Grand Canonical Monte Carlo (GCMC) and density functional theory (DFT) were employed. The result showed that there was a significant impact of functional groups at low pressure (0.01 – 0.5 bar) and room temperature. The CO_2 uptake at low pressure was strongly enhanced, especially by adding -OH and –COOH [65].

To improve the performance of adsorbents for post-combustion CO_2 capture, various exchanged cations (Li^+, K^+, Na^+) were examined on Zr-UiO-66 by Zhigang Hu *et al*. [66]. Dynamic column breakthrough was employed to evaluate the CO_2 separation from a mixture of CO_2/N_2 (15:85). The results suggested that there was a positive effect by introducing ions into the MOFs network. An increase of the selectivity was observed for each cation exchanged Zr-UiO-66. The highest selectivity was recorded in the case of Na^+ exchanged Zr-UiO-66, at 99.6 [66].

Babarao and Jiang studied the cation exchanged MOFs for CO_2 capture [67]. Li^+ exchanged MOFs were examined to separate CO_2 from the mixture of CO_2/H_2 and CO_2/N_2. Li^+ cation was observed to occupy the position near the carboxylic O-donor of the metal cluster. For a gaseous mixture of CO_2/H_2, the electrostatic interactions for CO_2 were stronger under the presence of the ionic framework due to a higher quadrupole moment than H_2. A similar phenomenon was also observed in the case of CO_2/N_2. The adsorption of CO_2 is much stronger than H_2 and N_2. The selectivity values of CO_2 over H_2 and N_2 were 550 and 60, respectively [67].

Using hetero ligands is another approach to enhance CO_2 adsorption. Hu *et al*. reported N(UiO(BPYDC)), S (Zr-BTDC)and O (Zr-BFDC) heterocyclic ligands on UiO-67 for post-combustion CO_2 capture. At low pressure up to 1 bar, Zr-BFDC, an O heterocyclic ligand MOF, showed the highest CO_2 adsorption capacity, at 95.14 cm^3/cm^3, which is four times higher than its parent UiO-67. Due to this steep isotherm, Zr-BFDC was claimed to have a great potential for post-combustion CO_2 capture. The heat of adsorption of Zr-BFDC is 32.23 kJ/mol, which is higher than UiO-67 (21.90 kJ/mol) [68].

1.4.2. Water stable MOFs for CO_2 capture

The stability of MOFs in a humid condition is one of the major concerns for post-combustion CO_2 capture. Yang *et al*. reported UiO-66-Zr as water-stable MOFs for CO_2 capture [69]. It is noted that Zr ions enhance water resistance. To evaluate the water stability, UiO-66-Zr was dispersed in water for 16 h at 373K. The adsorption isotherm confirmed the same uptake. The working capacity from 0.1 bar to 1.0 bar was 42 cm^3/cm^3, which is slightly higher than zeolite 13X (34 cm^3/cm^3). The CO_2 adsorption enthalpy at 303K was 34.8 kJ/mol [69].

LeVan's group reported the CO_2/H_2O adsorption equilibrium of HKUST-1 and Ni-DOBDC. The volumetric system was used to measure pure isotherms and CO_2/H_2O binary isotherm adsorption. The CO_2 uptake of HKUST-1 and Ni-DOBDC at 25ºC and 0.1 atm were 0.55 and 3.28 mmol/g, respectively. It was observed that H_2O had less effect on these two MOFs compared to zeolite 5A and NaX [70].

Chanut *et al*. proposed a simple thermal gravimetric analysis (TGA) for screening the effect of water vapour on CO_2 adsorption [71]. This protocol is composed of five main steps to evaluate the water effect. 45 MOFs were chosen to study this method. A majority of these MOFs indicated less than 25% loss in CO_2 capacity. ZIF-8, ZIF-93, MIL-121s, MIL-140A, MIL-69(Al) showed a negligible loss in CO_2 uptake under the presence of water. Conversely, MIL-91(Ti) and Mg(H_2gal) experienced a significant decrease in CO_2 uptake, more than 75% [71].

Interestingly, several MOFs displayed an increase of CO_2 uptake under the presence of a certain amount of water. The CO_2 adsorption of HKUST-1 was slightly enhanced (about 5%) in the condition of 2-4% relative humidity (RH). The UiO-66 series indicated a maximum CO_2 uptake before starting to fall. It can be explained there was a dehydroxylation of the sample resulting in a loss of CO_2 attractive sites [71].

1.4.3. Progress of MOFs for CO_2 capture

Numerous numerical studies on CO_2 capture and separation by MOFs have been reported in terms of pressure (PSA) and temperature swing adsorption (TSA). Most of these researches were conducted on Mg-MOF-74 as a potential candidate for CO_2 capture thanks to its high CO_2 capacity. Qasem and Ben-Mansour reported a VPSA and TSA process to separate CO_2 from a mixture of CO_2/N_2 by Mg-MOF-74 [72, 73]. In the VPSA process, a five-steps (pressurization, feed, rinse, blowdown and purge) VPSA was examined by CFD simulation. Both two (2D) and three-dimensional (3D) CFD models were considered and compared to one dimensional (1D) model. The result suggested that both 2D and 3D models showed a better agreement with the experiments than the 1D model. This process obtained a 95.3% purity and 94.8% recovery, with a total energy consumption of 68.7 kWh_e/tonne CO_2 captured and a productivity of 2.875 mole $CO_2/m^3/s$. In the case of the TSA process, higher energy consumption and lower productivity was observed, at 663.8 kWh_e/tonne and 1.604 mole $CO_2/m^3/s$, respectively [72].

Several works have been done to compare the performance of Mg-MOF-74 and zeolite 13X under certain conditions. Zhao *et al*. reported a four-step (Pressurization, adsorption, heating, cooling) TSA process for CO_2 capture in the dry condition (15% CO_2: 85% N_2) [74]. Several performance categories were included to examine their performances, i.e. purity, recovery, energy consumption and productivity. In this process, zeolite 13X displayed slightly higher in recovery and purity than Mg-MOF-74. Both zeolite 13X and Mg-MOF-74 showed a high value of recovery (>99.9%). However, they suffered a low purity, which is approximately 44%. In terms of energy consumption and productivity, Mg-MOF-74 indicated better performance. The productivity of 0.1583 $mol/m^3/s$ and energy consumption of 594 kWh/tonne CO_2 captured were recorded for Mg-MOF-74 [74]. In contrast, zeolite 13X showed half of the productivity and twice times higher in energy consumption in this case.

Rajagopalan and co-workers applied a four-step PSA cycle with light product pressurization (LPP) to compare the performance of zeolite 13X and Mg-MOF-74 under the dry condition [50]. Purity, recovery, energy consumption and productivity were also employed as process indicators. In this configuration, zeolite 13X showed a higher purity and recovery than Mg-MOF-74. With a constraint of 90% purity-recovery, zeolite 13X also indicated a better performance than Mg-MOF-

74 in terms of energy consumption and productivity. To produce 0.4 mole $CO_2/m^3/s$, using zeolite 13X required 141 kWh_e/tonne, while it was 220 kWh_e/tonne by using Mg-MOF-74 [50].

Besides Mg-MOF-74, a few potential MOFs were also reported for post-combustion CO_2 capture in the literature. Leperi *et al*. studied HKUST-1 and Ni-MOF-74 to capture CO_2 by a two-stage four-step PVSA cycle [75] at 1 atm and 313 K. However, none of these MOFs could achieve a target of 90% purity-recovery. 27% of purity and 99% of recovery were observed for HKUST-1, and 65% of purity and 98% of recovery were recorded for Ni-MOF-74.

Pai and co-workers studied five diamine-appended MOFs with an S-shape isotherm for post-combustion CO_2 capture [51]. These MOFs shared the same organic linkers, but the metal sites were varied, i.e. Mn, Fe, Co, Zn and Mg. A four-step VSA with an LPP cycle with a constraint of 95% purity and 90% recovery was applied to study their performance. The results showed that the MOFs with Mg and Mn metal sites showed better performance than others. The productivity of 0.45 mole $CO_2/m^3/s$ with a 142 kWh_e/tonne CO_2 captured was observed for Mn-MOFs. In the case of Mg-MOF, lower productivity and higher energy consumption were observed at 0.40 mole $CO_2/m^3/s$ and 152 kWh_e/tonne [51].

Another promising MOFs, UTSA-16, has been considered as a high potential candidate for CO_2 capture. Rajagopalan *et al*. examined the performance of UTSA-16 for post-combustion CO_2 capture by a four-step PSA with LPP [50]. The results displayed a better performance than zeolite 13X with a constraint of 90% purity-recovery. Productivity of 0.7 mole $CO_2/m^3/s$ with an energy consumption of 120 kWh_e/tonne could be obtained by UTSA-16. In another work, Khurana and Farooq studied a six-step VSA configuration to further improve the performance of UTSA-16. This work also indicated the important role of low pressure on energy consumption and productivity. Higher productivity (~4.5 $mol/m^3/s$) could be achieved with similar energy consumption (~125 kWh_e/tonne) by controlling the low pressure using UTSA-16 [50].

Very few studies on post-combustion CO_2 capture under the moist condition using MOFs were reported. Bahamon *et al*. examined the ability of Mg-MOF-74, CuBTC and zeolite 13X to capture CO_2 from the wet flue gas [76]. The hybrid VTSA process was chosen to evaluate the performance of these materials. A feed containing 1.00% water was considered in this VTSA process using CuBTC. The proposed desorption condition was at 0.15 bar and 343 K. A working capacity of 0.38 kmol/m3 and energy consumption of 333.3 kWh_e/tonne CO_2 were obtained with 81% purity

and 92% recovery. For Mg-MOF-74, a feed containing 0.5% water was considered at the desorption condition of 0.2 bar, and 423 K. Higher working capacity (3.5 kmol/m^3) and lower energy consumption (100 kWh_e/tonne) were achieved with 98% purity and 86% recovery. In the case of zeolite 13X, only 0.02% water in the feed flue gas was studied at the desorption of 0.6 bar and 413 K [76]. Working capacity of 2.5 kmol/m^3 and energy consumption of 127.78 kWh_e/tonne was recorded with a 92% purity and 82% recovery. In conclusion, at a higher percentage of moisture, CuBTC could be a good candidate.

A few experimental studies on CO_2 capture using MOFs were reported in the literature. Majchrzak-Kuceba and co-workers presented a four-step two-column VPSA cycle to capture CO_2 using MIL-53(Al) [77]. The adsorbent was pelletized without a binder to form 2.00 – 5.00 mm particles prior to use. A total of 69.3 g adsorbent was applied with the feed flowrate at 150 ccm, and 30 °C. The adsorption was set at 1.25 bar, and the desorption pressure was at 0.2 bar. A 40% purity and 55% recovery were obtained under this condition. If the desorption pressure was at 0.1 bar, higher purity and recovery were achieved, at 60% and 80%, respectively [77].

Table 1.2: A survey of CO_2 capture studies using MOFs

Note: Pu – Purity [%]; Re – Recovery [%]; En – Energy [kWh_e/tonne CO_2]; Pr – Productivity [mol $CO_2/m^3/s$]; Sim. – Simulation; Exp. - Experiment

Material	Process type	Process conditions	Type of study	Scope	Feed	Results	Ref.
Mg-MOF-74	TSA	Ads: 300s, 101.3 kPa Des: 200s, 393K Cooling: 100 s, air Qin = 90 sccm	Sim.	Post-combustion	20% CO_2 80% N_2	Pu: 75 Re: 80 En: 569 Pr: 5.75	[78]
MIL-53(Al)	VPSA	Ads: 1.25 bar Des: 0.1 bar Qin = 150 ccm 2 columns VPSA	Exp.	Post-combustion	16% CO_2 3.5% O_2 80.5% N_2	Des: 0.1 Pu: 60 Re: 80	[77]
Diamine-appended MOFs	VSA	Ads: 50s, 1 bar BD: 50s, 0.12 bar Evac: 50s, 0.03 bar LPP V_{feed} = 1 m/s	Sim.	Post-combustion	15% CO_2 85% N_2	Pu: 95 Re: 90 En: 152 Pr: 0.45	[51]
Mg-MOF-74	TSA	Ads: 313K Des: 443K	Sim.	Post-combustion	15% CO_2 84.9% N_2 0.1% H_2O	Pu: 98 Re: 86 En: 315	[76]

Cu-BTC	TSA	Ads: 313K Des: 443K	Sim.	Post-combustion	15% CO_2 84.9% N_2 0.1% H_2O	En: 153	[76]
Mg-MOF-74	VPSA	Press: 1.3 bar Ads: 1.3 bar, 323K Rinse: pure CO_2 BD: 0.02 bar Purge: pure N_2	Sim.	Post-combustion	15% CO_2 85% N_2	Pu: 95.3 Re: 94.8	[72]
Mg-MOF-74	TSA	Ads: 323K Rinse: pure CO_2, 300K Des: 393K Cooling: 300K	Sim.	Post-Combustion	15% CO_2 85% N_2	Pu: 96.2 Re: 86.5 En: 663.8 Pr: 1.6	[73]
13X and Mg-MOF-74	PVSA	Two-stage 6-step with PE Evac: 0.1 bar	Sim.	Post-Combustion	15% CO_2 85% N_2	Pu: 97.4 Re: 92.5 En: 200	[79]
13X and Mg-MOF-74	TSA	Press: 1 bar Ads: 1 bar 303K Heating: 373K Cooling	Sim.	Post-Combustion	15% CO_2 85% N_2	Pu: 44 Re: 99.6 En: 594 Pr: 0.16	[74]
UTSA-16	VSA	4-step LPP	Sim.	Post-Combustion	15% CO_2 85% N_2	Pu: 90 Re: 90 En: 120 Pr: 0.7	[80]
Mg-MOF-74	VSA	4-step LPP	Sim.	Post-Combustion	15% CO_2 85% N_2	Pu: 90 Re: 90 En: 220 Pr: 0.4	[80]
USO-2-Ni	PSA	6-step with PE Ads: 34 bar, 308K Purge: 1 bar	Sim.	Pre-Combustion	40% CO_2 60% H_2	Pu: 95 Re: 95 Pr: 6.64	[81]
UiO-67	PSA	6-step with PE Ads: 34 bar, 308K Purge: 1 bar	Sim.	Pre-Combustion	40% CO_2 60% H_2	Pu: 93 Re: 90 Pr: 5.9	[81]
MIL-101-Cr	TVSA	Ads: 1 atm Evac: 373K Press: 1 atm, 373K Des: 1 atm, 373K Cool: 348K	Sim.	DAC	400 ppm CO_2 25% RH	-	[82]
Mmen-Mg2-(dobpdc)	TVSA	Ads: 1 atm Evac: 373K Press: 1 atm, 373K Des: 1 atm, 373K Cool: 348K	Sim.	DAC	400 ppm CO_2 25% RH	-	[82]

HKUST-1	PVSA	Two-stage 4-step LPP	Sim.	Post-combustion	14% CO_2 80% N_2 6% H_2O	Pu: 27 Re: 99	[83]
Ni-MOF-74	PVSA	Two-stage 4-step LPP	Sim.	Post-combustion	14% CO_2 80% N_2 6% H_2O	Pu: 65 Re: 98	[83]
UTSA-16	VSA	6-step with heavy and light reflux	Sim.	Post-combustion	15% CO_2 85% N_2	Pu: 95 Re: 90 En: 125 Pr: 4.5	[84]

1.5. Knowledge gaps and challenges

Flue gas from a coal power plant typically contents 5%-15% CO_2, 80%-85% N_2 and water vapour. The current benchmark adsorbent for CO_2 capture is known as zeolite 13X. It has a large CO_2 capacity at low pressure and high selectivity over N_2. However, under the presence of water vapour, zeolite 13X will lose its capacity dramatically due to its higher affinity to water. In addition, the high energy penalty is one of the most important concerns in capturing CO_2. In fact, CO_2 capture is responsible for 70% of the total cost for a CCS project. A proper sorbent for CO_2 separation is still in need and requires further investigations. Designing processes to minimize energy and maximize productivity is also considered a crucial challenge.

Process studies are essential to bringing new material into practice. In the early stage, a new adsorbent is usually synthesized and characterized in a small amount, i.e. milligrams to grams. It is important to understand the interaction between the surface and different gases at this stage. Key characteristics are single-component isotherms, surface area, pore size distribution, the stability of the structure, thermal stability, solvent stability. Little or no information about the diffusion properties of the solids is examined at this stage. Often, the performance of a new adsorbent is compared based on classical metrics, i.e. selectivity, working capacity [85]. However, Rajagopalan *et al*. demonstrated that it is inclusive to evaluate the process performance of different adsorbents based on a single metric alone (i.e. selectivity, saturated loadings, or working capacity) [50]. UTSA-16 showed higher productivity and lower energy consumption than Mg-MOF-74 and zeolite 13X, even though its CO_2 equilibrium loading is much smaller, only a third of Mg-MOF-74 at 0.15 bar and 25°C [50]. A detailed process study is required to understand and to evaluate the performance of each material at a process level. In the process stage, a larger amount of adsorbent is required (i.e. 100s of grams) to study competitive adsorption, diffusion properties,

cycling stability. Based on these preliminary data, a process is designed and demonstrated in a lab-scale environment. Typical process indicators, such as purity, recovery, energy consumption and productivity, are collected from this study. Initial results collected from process studies allow to scale up the size of an adsorption process with less time and resources. Although this process framework is by no means exhaustive, it demonstrates the complexities involved in developing a process for new material. These process studies also cope with many challenges, such as competitive adsorption, water adsorption measurement, and process demonstrations.

Competitive adsorption measurement

One of the main challenges is to measure the competitive adsorption isotherms for components that have significant differences in affinity. While it is straightforward to measure the total amount adsorbed, it is complicated to quantify the specific adsorbed amount for each component. In the flue gas containing $H_2O/CO_2/N_2$, it is important to understand the competitive nature of CO_2 and N_2, and the competition of water adsorption on CO_2 and N_2 and its effect on column dynamics.

Dynamic column breakthrough of water

Performing a water vapour breakthrough experiment is one of the key challenges. The feed needs to be maintained at a constant relative humidity during the experiment. An oscillating relative humidity feed will result in a false breakthrough profile. Furthermore, water condensation happens at the saturation condition, which will lead to a false reading. Removing condensed water from the packed bed is also difficult.

Hysteresis

The water isotherm on many adsorbents shows a hysteresis loop with an inflection point. The hysteresis loop is typically located within a narrow range of relative humidity, which makes it a significant challenged to quantify. This information is of importance to simulate the water adsorption and desorption breakthrough. Modelling the isotherm with an inflection point is complicated since the isotherm contains several transitions. A more complex isotherm model is required to capture these transitions. Hefti *et al*. [86] and Kasturi *et al*. [51] used the weighting function to describe the isotherms of several diamine MOFs with an inflection point. This model required more than ten isotherm parameters to describe the isotherms.

CO_2 and H_2O competitive adsorption

Only a few studies attempted to quantify the competitive amount adsorbed of CO_2 and H_2O [87, 88]. In the CO_2/H_2O binary mixture, water is strongly adsorbed with a rectangular type I isotherm, even at very low relative humidity. Moreover, the CO_2/H_2O binary breakthrough experiments take a long time for both components to completely breakthrough. Performing the adsorption experiment alone is not adequate to measure the amount adsorbed of two components. Further approaches need to be developed to collect competitive CO_2/H_2O isotherm.

CALF-20 showed a unique competition between CO_2 and H_2O in this study. Often, the effect of CO_2 on the adsorption of H_2O is negligible since the affinity of water on the solid surface is significantly higher. For CALF-20, depending on the relative humidity and the temperature, the solid surface prefers to adsorb either CO_2 or H_2O. In this case, CO_2 has a strong impact on the adsorption of water, which makes it more complicated to model competitive isotherm.

Adsorption process demonstration under a humid environment

To the best of our knowledge, there is no experimental study on adsorption processes under a moist environment for MOFs. Only a few studies with a numerical approach were reported in the literature [76]. It is very challenging to calculate the mass water balance for each cycle since it is hard to measure the relative humidity. During the VSA process, the pressure of the column rapidly changes from high to low pressure. The relative humidity depends on both temperature and pressure, and the water condensation occurs at the saturation condition. Also, the humid VSA process takes an extremely long time to reach the cyclic steady state. A modification in the experimental apparatus is necessary to control a stable humid stream and to ignore the water condensation during the whole experiment.

The durability of the adsorbent

The durability of the adsorbents is barely discussed in existing studies. The adsorbents are expected to maintain their performances under working conditions over a long period of time. In fact, the adsorbents slowly degrade during the operation. The adsorbents are required to be replaced when they can no longer meet specifications. From the design perspective, it is necessary to study the durability of the adsorbents, i.e., cyclic stability.

1.6. Objectives and structure of the thesis

The aim of this thesis is to study the viability of humid post-combustion CO_2 capture using novel metal-organic frameworks (CALF-20). To obtain this target, the following studies have been carried out:

- Characterized the adsorption equilibrium of CO_2 and N_2 and their competition
- Studied the adsorption of water on CALF-20 and its column dynamics
- Characterized the competitive adsorption of CO_2 and H_2O on CALF-20
- Simulated the CO_2/H_2O dynamic column breakthrough
- Modelled the VSA configurations under dry and wet conditions
- Demonstrated VSA processes for both dry and wet conditions
- Tested cyclic stability of CALF-20

Structure of the thesis:

CHAPTER 2 discusses the CO_2 and N_2 adsorption equilibrium on CALF-20. Single component isotherms were measured in a wide range of temperature and pressure using volumetric and gravimetric methods. The CO_2/N_2 binary adsorption loadings were collected by performing several sets of adsorption and desorption dynamic column breakthrough experiments with various CO_2 and N_2 compositions. The extended dual-site Langmuir model with different schemes (PP, PN, EES) was used to describe the competitive isotherm.

CHAPTER 3 presents the study on the H_2O adsorption equilibrium and column dynamics. The water adsorption isotherms were measured by the thermalgravimetric analysis at different temperatures. The hysteresis of the water isotherm was studied at 22°C using volumetric and TGA. The water adsorption and desorption dynamic column breakthrough were performed at different relative humidity values to capture the complexity in the water isotherm. To model the isotherm with an inflection point, the Quadratic-Langmuir model was developed based on the concept of the Quadratic model and Langmuir isotherm model.

CHAPTER 4 is devoted to studying the competition between CO_2 and H_2O on CALF-20. The competitive loadings of each component were measured by dynamic column breakthrough experiments and TGA measurements at various relative humidity. A humidifier was installed to the existing DCB apparatus to perform the CO_2/H_2O binary breakthrough experiments. The competitive CO_2 isotherm was described by the modified dual-site Langmuir, while the

competitive water isotherm was described by the Quadratic-Langmuir model. The competitive CO_2 loadings did not change at RH<40%. Beyond 70% RH, the CO_2 loading was dropped significantly. The water isotherm still showed an inflection point, which shifted to higher relative humidity. This result indicated that CO_2 strongly affected the adsorption of water. CO_2/H_2O competitive adsorption breakthrough curves at different relative humidity values were successfully simulated, and it was in a good agreement with the experimental breakthrough profile.

CHAPTER 5 investigated an anomaly behaviour of CALF-20 in the CO_2/H_2O competitive adsorption. The adsorbent was saturated with different gases, CO_2, H_2O or a combination of CO_2 and H_2O. Under the presence of CO_2, the framework of CALF-20 showed an extension resulting in a higher total loading of CO_2 and H_2O. This phenomenon was reversible once CO_2 was removed. If the pores were fully filled with water first, CO_2 could not access the pores due to the capillary condensation. It means CALF-20 only adsorbs water at high RH if water enters and fills the pores first. In contrast, the framework was extended, and a small amount of CO_2 was still adsorbed at high RH if CO_2 entered the pores first. Note that the framework remained the same once water fully filled the pores due to the capillary condensation. To reverse back to its original shape, all water needed to be evacuated.

CHAPTER 6 studied the rigorous optimization approach to optimize adsorption processes under dry conditions. Based on the competitive adsorption model built in the previous studies, the performance of CALF-20 was predicted using basic four-step VSA and four-step VSA with light product pressurization (LPP) configurations. The key process performance indicators, i.e. CO_2 purity and recovery, were optimized using the full detailed model with a genetic algorithm (GA). The process parameters corresponding to selected points on the Pareto curve were demonstrated in the lab using a two-column VSA apparatus. The experimental performance indicators, i.e. the column temperature, the outlet flow rate and the composition profile in every step, purity and recovery, showed a good agreement with the model prediction.

CHAPTER 7 studied the effect of the water vapour on the performance of CALF-20. The four-step VSA with the LPP cycle was chosen to evaluate. A humidifier was retrofitted into the existing VSA apparatus to create a constant humid feed. Different values of relative humidity were selected to understand how the process performances changed under the presence of water vapour. Two case studies were conducted at two different feed velocity and recovery values. At low to

intermediate relative humidity (<45%), purity, recovery, and productivity showed similar evolution with the dry case. Beyond 70%, water condensation occurred, which made it challenging to perform the evacuation step. The results from the first 100 cycles still showed a good performance between wet and dry cycles.

CHAPTER 8 provides a summary of the main results of this thesis. Several future research directions are also proposed.

2 Adsorption Equilibrium and Dynamic Column Breakthrough Studies of CO_2 and N_2 on CALF-20

2.1. Introduction

Anthropogenic CO_2 emissions are increasing rapidly worldwide because of human activities [1, 2]. To achieve net-zero emissions and negative emissions by 2050, a combination of various measures needs to be considered, including carbon capture and storage (CCS) [2]. CO_2 can be captured directly from the air or from large-scale emission sources, i.e. coal-fired power plants [89]. Because of the high demand for energy, the use of coal is still favourable due to its low cost and abundant sources. Thus, CCS technology is necessary to keep coal-fired power plants operating while adapting to the low CO_2 emission economy. The flue gas coming from a coal-fired power plant usually contains CO_2, N_2 and water vapour. Dilute CO_2 concentration in the flue gas requires to be separated from a mixture of ≈85% N_2, 10% - 15% CO_2 and water vapour. Absorption using liquid solvents is the current technology for CO_2 capture [26, 36]. However, it still faces high energy consumption, solvent degradation and toxicity [90]. Adsorption using porous sorbents is an alternative approach to capture CO_2 from the flue gas [91].

Solid adsorbents play a crucial role in designing an adsorption process. An adsorbent with high CO_2 capacity, low N_2 affinity and relatively low heat of adsorption is preferred to reduce the energy consumption while maintaining high purity, recovery and productivity [50]. Zeolite 13X is a typical adsorbent with high CO_2 saturation loadings at low pressure [92]. But it also exhibits a strong affinity to water, which makes it lose the performance in moist conditions [87, 88]. Metal-organic frameworks, a new class of porous materials, offer a vast number of adsorbents for CO_2 capture due to their rigid, completely regular, predictable, porous and tunable frameworks. By adjusting functional groups, organic linkers, or metal nodes, new MOFs with desired properties could be obtained [93-96]. MOF-74, Cu-BTC, HKUST-1, MOF-177, MIL-53 are typical examples metal-organic frameworks for CO_2 capture [97, 98]. Among those adsorbents, Mg-MOF-74 exhibits the highest CO_2 capacity and high CO_2/N_2 selectivity [99].

Thousands of new MOFs have been reported every year [100]. Dealing with new adsorbents, many studies often reported the pure CO_2 isotherm only. From the process perspective, it is not recommended to evaluate the performance of an adsorbent based on its pure CO_2 isotherm alone [50, 100]. It is critical to know both single and binary isotherms of CO_2 and N_2 to evaluate their performance. Rajagopalan *et al*. indicated that UTSA-16 showed a better performance than Mg-MOF-74, even though the CO_2 equilibrium loading of UTSA-16 is lower than Mg-MOF-74, ≈2.0 and 6.0 mmol/g at 25°C and 0.15 bar, respectively [50]. They also concluded that nitrogen is another key contribution to enhancing CO_2 separation efficiency. A low nitrogen capacity with relatively high CO_2 loading is preferred. Thus, understanding the competitive adsorption is a prerequisite condition to evaluate the process performance [101].

Surprisingly, very few studies reported the competitive CO_2/N_2 isotherms. Most process modelling research estimated the competitive adsorption based on the pure component isotherms using the ideal adsorbed solution theory (IAST) or an extended form of the single component model [102, 103]. Wilkins and Rajendran indicated that an extension form of the single component isotherm model is inadequate to evaluate the process performance. Using different combinations of low and high energy sites in the dual-site Langmuir model led to different competitive isotherms, which returned to various process performance indicators, i.e. purity, recovery, energy and productivity [92, 104]. There is a need to measure the competitive adsorption isotherm experimentally to validate the binary isotherm model.

It is very challenging to quantify the amount adsorbed of each component in a binary mixture. The amount adsorbed of the strong component could be determined by performing binary adsorption dynamic column breakthrough experiments [105]. However, it is uncertain to determine the amount adsorbed of the light component based on the adsorption DCB experiments [92]. Several studies proposed an approach to determine competitive adsorption isotherms. Hefti *et al*. measured the competitive CO_2/N_2 adsorption isotherm of zeolite 13X using a magnetic suspension balance [52]. Wilkins *et al*. confirmed the competitive CO_2/N_2 adsorption isotherm of zeolite 13X by performing a series of adsorption and desorption DCB experiments [92].

In this study, CALF-20, a potential adsorbent for CO_2 capture, is examined. The volumetric and gravimetric methods were used to measure the single-component isotherms of CO_2 and N_2 at various temperatures. The pure component CO_2 and N_2 isotherms were fitted using dual-site and

single-site Langmuir, respectively. The extension dual-site Langmuir model with a different combination of energy sites was used to model the competitive CO_2/N_2 isotherms. A series of adsorption and desorption dynamic column breakthrough experiments were performed to estimate the competitive CO_2/N_2 adsorption isotherms and to validate the model predictions. Both single and binary DCB experiments were performed to fully understand the column dynamics and the adsorption kinetics of CO_2 and N_2 on CALF-20.

2.2. Synthesis of CALF-20

CALF-20 was synthesized and characterized by our colleagues from the University of Calgary (Shimizu group) following a previously reported procedure (Patent number: US 9,782,745 B2). 185 mg of zinc oxalate and 337 mg of 1,2,4-triazole were dissolved in 4 mL of water in a 23 mL Teflon™ liner. Afterwards, 6 mL of methanol was added, and the resulting mixture was stirred for an hour. Then, it was placed in an oven at 180 °C for 48 hours. The obtained precipitates were washed with 200 mL of water and 75 mL of methanol. The powder form of CALF-20 was collected after applying a vacuum filter and drying for 30 minutes (Fig. 2.1).

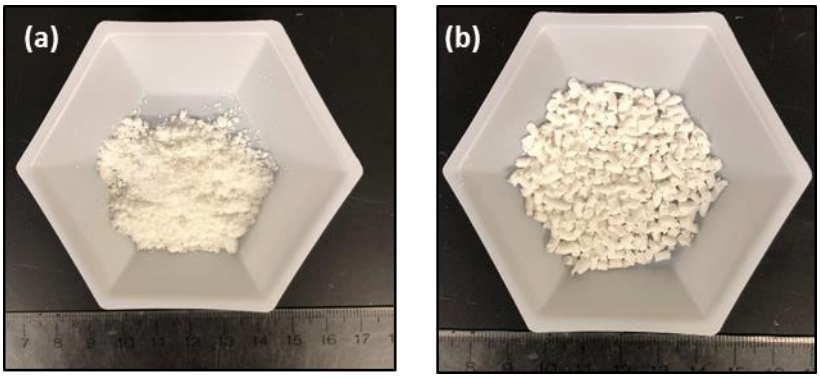

Figure 2.1: The appearance of CALF-20. (a) Powder CALF-20 as-synthesized; (b) Structured CALF-20 with cylindrical shape (1.0 mm in diameter and 1.0 – 3.0 mm in length)

For further experimental purposes, powdered CALF-20 was structured using a phase inversion method. 0.75 g of polysulfone was added to a beaker containing 6.26 g of N-methyl-2-pyrrolidone and 0.25 g of pluronic F127. The mixture was stirred at room temperature overnight to dissolve polysulfone completely. Then, 9 g of powder CALF-20 was added and stirred for 3 hours. The resulting mixture was extruded into a water tank to form a structured CALF-20 by solvent/water

exchange. The particle density of the structured CALF-20 sample was estimated at 570 kg/m^3, and the particle size was from 1.0-3.0 mm using polysulfone as a binder.

2.3. Experimental methods

CO_2 and N_2 single component isotherms were measured by volumetric and gravimetric methods. Column dynamics, single and multi-component adsorption equilibrium were studied by dynamic column breakthrough (DCB) experiments. Both adsorption and desorption experiments were performed at low pressure conditions (<1.2 bar) and room temperature (≈22°C). Under these conditions, the measured quantity can be considered as the absolute amount adsorbed, because the adsorbed phase density is significantly higher than the fluid phase density [106, 107]. Hence, all adsorption equilibrium data were reported in absolute values. Helium (99.998%), nitrogen (99.998%) and CO_2 (99.998%) were purchased from Praxair Canada Inc.

2.3.1. Static isotherm measurements

Volumetric measurements

Micromeritics ASAP 2020 (Norcross, GA, USA) was used to measure CO_2 and N_2 volumetric isotherms from 1 mbar to 1200 mbar at various temperatures (22°C to 100°C). Initially, the sample cell filled with a certain amount of adsorbents (≈ 200 mg) is evacuated. Afterward, a known amount of gas is dosed into the sample cell from a calibrated dosing volume. The adsorbed amount is determined by measuring the pressure change (ΔP) [108]. Prior to each measurement, the adsorbent was activated overnight, at 150°C and under vacuum. The accuracy of measuring the pressure and the corresponding loadings were 1.3 x10^{-7} mbar and 0.15%, respectively.

Gravimetric measurements

Rubotherm Type E10 (Bochum, Germany) magnetic suspension balance (MSB) was used to measure the CO_2 and N_2 isotherms. High pressure adsorption measurement (up to 50 bar) can be performed by the MSB. In this method, 2 g of the adsorbent was placed in the basket and the mass change was measured as a function of pressure. Prior to each isotherm measurement, the adsorbent was activated under vacuum, at 150°C for 12 hours. The skeletal volume of the adsorbent was quantified by performing He measurement [106] since the adsorption of He was negligible.

2.3.2. Dynamic column breakthrough study

A lab-scale dynamic column breakthrough (DCB) apparatus (Fig. 2.2) was built to perform DCB experiments. The aims of the DCB experiments were multifold: i. To confirm the single component loadings measured from volumetric and gravimetric; ii. To obtain transport properties; iii. To measure CO_2/N_2 competitive isotherm data.

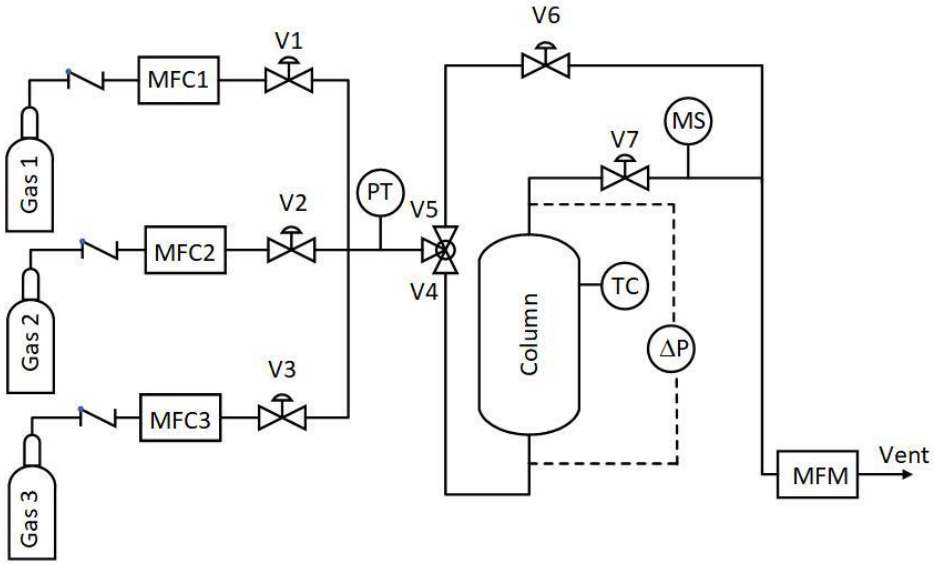

Figure 2.2: The dynamic column breakthrough apparatus schematic. MFC – Mass flow controller; PT – Pressure transducer; RHM – Relative humidity meter; TC – thermal couple; MS – Mass spectrometer; MFM – Mass flow meter; V1 to V7 – Valves 1 to 7

In the DCB apparatus, the mass flow controllers (MFCs) 1 and 2 (Alicat Scientific, Tucson, AZ, USA) controlled the feed gas to 1.0 SLPM. The MFC 3 (Alicat Scientific, Tucson, AZ, USA) controlled the flow to 0.5 SLPM. The heart of the system is a 40 mL stainless steel column (Swagelok 304L-HDF2-40, length 7.86 cm; inner diameter 2.82 cm) packed with the structured CALF-20 sample (16.7 g). Prior to each experiment, the column was activated at 150 °C overnight, using Helium as a purge gas. To record the thermal history, a thermocouple (Omega Engineering, Laval, QC, Canada) was placed 1.82 cm from the column outlet. A pressure transducer and a differential pressure gauge (GE Druck, Billerica, MA, USA) were used to measure the inlet pressure and pressure drop across the column, respectively. The outlet gas composition was measured by a mass spectrometer (MS, Pfeiffer Vacuum OmniStar GSD 320, Asslar, Germany).

A mass flow meter (Alicat Scientific, Tucson, AZ, USA) was used to measure the outlet flowrate to 2.0 SLPM. All DCB experiments were conducted at ≈22 °C and ≈0.97 bar total pressure.

To perform an adsorption experiment, the bed was initially saturated with Helium (V3, V4 and V7 were opened). At t = 0, a step signal of test gas was introduced to the column (V1/V2, V4 and V7 were opened). The column temperature, the pressure history, the inlet and outlet flow, and the outlet concentration were recorded by a built-in data acquisition system (Labview). The adsorption experiment was considered to be completed when the outlet concentration was equal to the inlet concentration and the thermal breakthrough was completed.

Prior to a desorption experiment, the bed was equilibrated with a test gas (V1/V2, V4 and V7 were opened). At t = 0, an inert gas (He) was sent to the column (V3, V4 and V7 were opened). The desorption experiment was finished when the concentration of the test gas was significantly lower than the initial equilibrium concentration, and the temperature reached the initial temperature.

All mass flow controllers were calibrated using a universal gas flow meter (Agilent Technologies, Santa Clara, CA, USA). A known concentration of the test gas (pure or mixture of CO_2, N_2 and He) was used to calibrate the MS signal. The effluent mass flow meter was similarly calibrated with various concentrations of CO_2, N_2 and He at different total flowrates. Thus, the real effluent flow was built as a function of the effluent concentration and the total flowrate.

Blank response correction

All the measured breakthrough curves included the system dead volume and the delay from the detector (MS). To obtain a true breakthrough profile, the overall response was corrected from the dead volume and the detector (MS) response. To study the detector response, the MS was placed directly downstream of the mass flow controller (MFC). Step changes were sent to the MS by switching pure He to pure CO_2, pure N_2 or mixtures of CO_2/N_2 and vice versa. Different total flowrates of the test gas were also examined. The detector response was defined as the time for the MS to receive the signal (step changes). This MS response was within a second; hence it was negligible compared to the duration of the DCB experiments.

To evaluate the dead volume of the system (V_d), the adsorption column (Fig. 2.2) was replaced by a small tube whose volume was negligible. Other parts of the system were kept the same. Similarly, switching from pure He to mixtures of CO_2/N_2 and recording the time to detect the signal gained

the dead volume time. This was defined as the time for the gas to travel from the MFC to the detector, excluding the column. The result also showed a quick response of ≈3 seconds. Hence, the dead volume was negligible compared to the duration of the experiments.

2.4. Adsorption modelling and optimization

2.4.1. Simulation of adsorption column dynamics

To describe the adsorption dynamic in the column, a one-dimensional mathematic model was developed. A set of coupled non-linear partial differential equations and boundary conditions were solved. All dispersion, convection, adsorption, heat transfer and pressure drop were included in this model. Several assumptions were made to model an adsorption process:

i. The gas phase behaves according to the ideal gas law. This is justifiable for operation at low pressure (≈0.97 bar)
ii. The column is one dimensional, without radial gradients for composition and temperature
iii. The gas flow through the fixed bed is described by the axial dispersed plug flow model
iv. The ambient temperature is stable. This was verified by monitoring the lab temperature. A maximum discrepancy of 0.5 °C was recorded during an experiment
v. The pressure drop is adequately described by Darcy's law since all experiments were conducted at low flowrates (< 100 ccm) and the pressure drop in the column is considerably small (<0.03 bar)
vi. The solid and gas phases reach thermal equilibrium instantaneously
vii. The particle size and the bed voidage are uniform across the column
viii. The mass transfer rate of the solid phase is adequately described by the linear driving force (LDF) model
ix. Thermal properties such as specific heat capacity and thermal conductivity are constant

With respect to the assumptions, the mass balance of the component i in the fluid phase is defined:

$$\frac{\partial c_i}{\partial t} = \frac{\partial}{\partial z}\left(cD_L \frac{\partial y_i}{\partial z} + c_i v\right) - \frac{1-\varepsilon}{\varepsilon}\frac{\partial q_i}{\partial t} \tag{2.1}$$

In this equation, z and t denote the axial length and the time, c_i and y_i are the concentration and the mole fraction in the gas phase of component *i*, v is the interstitial velocity, ε is the bed voidage, q_i is the solid loading of component *i*, and D_L is the axial dispersion coefficient.

Assuming ideal gas behavior, the total gas phase concentration will be expressed as $c = \frac{P}{RT}$, and $c_i = \frac{Py_i}{RT}$, where P and T are the pressure and the temperature, R is the universal gas constant. Thus, Eqn. (2.1) becomes:

$$\frac{\partial y_i}{\partial t} + \frac{y_i}{P}\frac{\partial P}{\partial t} - \frac{y_i}{T}\frac{\partial T}{\partial t} = D_L \frac{T}{P}\frac{\partial}{\partial z}\left(\frac{P}{T}\frac{\partial y_i}{\partial z}\right) - \frac{T}{P}\frac{\partial}{\partial z}\left(\frac{Py_i}{T}v\right) - \frac{RT}{P}\frac{1-\varepsilon}{\varepsilon}\frac{\partial q_i}{\partial t} \tag{2.2}$$

Similarly, the total mass balance is given:

$$\frac{1}{P}\frac{\partial P}{\partial t} - \frac{1}{T}\frac{\partial T}{\partial t} = -\frac{T}{P}\frac{\partial}{\partial z}\left(\frac{P}{T}v\right) - \frac{RT}{P}\frac{1-\varepsilon}{\varepsilon}\sum_{i=1}^{n_{comp}}\frac{\partial q_i}{\partial t} \tag{2.3}$$

The linear driving force (LDF) model is applied to describe the mass transfer in the solid phase:

$$\frac{\partial q_i}{\partial t} = k_i(q_i^* - q_i) \tag{2.4}$$

where q_i^* is the equilibrium loading of component *i* on the solid phase, k_i is the lumped mass transfer coefficient of component *i*, which is described as [49]:

$$k_i = \frac{15\epsilon_p D_p}{r_p^2}\frac{c_i}{q_i^*} \tag{2.5}$$

where r_p and ϵ_p, are the particle radius and particle porosity, respectively, D_p is the macropore diffusivity. The axial dispersion D_L can be determined:

$$D_L = 0.7D_m + vr_p \tag{2.6}$$

where D_m is the molecular diffusion coefficient. The pressure drop across the column is described by Darcy's law:

$$-\frac{\partial P}{\partial z} = \frac{150}{4}\frac{1}{r_p^2}\left(\frac{1-\varepsilon}{\varepsilon}\right)^2 \mu v \tag{2.7}$$

where μ is the fluid viscosity, which is assumed to be constant. The column energy balance, including conduction through the column wall, convection and dispersion along the packed bed and heat transfer between the column wall and the bed, is described as:

$$\left[\frac{1-\varepsilon}{\varepsilon}\left(\rho_s C_{p,s} + C_{p,a}\sum_{i=1}^{n_{comp}} q_i\right)\right]\frac{\partial T}{\partial t} = \frac{K_z}{\varepsilon}\frac{\partial^2 t}{\partial z^2} - \frac{C_{p,g}}{R}\frac{\partial}{\partial z}(vP) - \frac{C_{p,g}}{R}\frac{\partial P}{\partial t} - \frac{1-\varepsilon}{\varepsilon}C_{p,a}T\sum_{i=1}^{n_{comp}}\frac{\partial q_i}{\partial t} + \frac{1-\varepsilon}{\varepsilon}\sum_{i=1}^{n_{comp}}\left((-\Delta H_i)\frac{\partial q_i}{\partial t}\right) - \frac{2h_{in}}{\varepsilon r_{in}}(T - T_w) \quad (2.8)$$

where ρ_s is the particle density of the adsorbent, $C_{p,s}$ and $C_{p,g}$ are the heat capacity of the adsorbent and the fluid phase, $C_{p,a}$ is the heat capacity of the adsorbed phase, K_z is the gas thermal conductivity, ΔH_i is the heat of adsorption of component i, h_{in} is the overall internal heat transfer coefficient, r_{in} is the inner radius of the column and T_w is the column wall temperature. T_w can be found from the wall energy balance:

$$\rho_w C_{p,w}\frac{\partial T_w}{\partial t} = K_w\frac{\partial^2 T_w}{\partial z^2} + \frac{2r_{in}h_{in}}{r_{out}^2 - r_{in}^2}(T - T_w) - \frac{2r_{out}h_{out}}{r_{out}^2 - r_{in}^2}(T_w - T_{amb}) \quad (2.9)$$

ρ_w, $C_{p,w}$ and K_w are the density, the heat capacity and the thermal conductivity of the column wall, respectively, r_{out} is the outer radius of the column, h_{out} is the heat transfer coefficient between the column wall and the ambient air, T_{amb} is the ambient temperature.

All the equations were discretized in space using the finite volume method with a total variation diminishing (TVD) scheme [109]. The column was divided into 30 cells, and the obtained set of ordinary differential equations (ODE) were solved by *ode23s*, provided in MATLAB ODE solver. The details of the solution methodology can be found in the previous study [109].

2.4.2. Mass balance calculations

The equilibrium loading of the solid phase is calculated by performing a mass balance around the packed bed for each DCB experiment [105]. It can be expressed in a molar balance since there was no reaction in the column:

$$n_{in} - n_{out} = n_{acc} \quad (2.10)$$

The difference between the moles entering (n_{in}) and leaving (n_{out}) the column provides the accumulation (n_{acc}). The accumulation is the sum of moles in the solid phase, the gas phase and the dead volume. Using the ideal gas law, the above equation can be expanded:

$$\int_0^\infty \left(\frac{Q_{in}P_{avg}y_{i,in}}{RT_{in}}\right)dt - \int_0^\infty \left(\frac{Q_{out}P_{avg}y_{i,out}}{RT_{out}}\right)dt = q_i^* m_{ads} + \frac{P_{avg}y_{i,in}}{RT_{in}}V_{col}\varepsilon + \frac{P_{avg}y_{i,in}}{RT_{in}}V_d \tag{2.11}$$

y_i is the mole fraction of component i, P, Q and T represent the total pressure, the flow rate and the temperature respectively, R is the universal gas constant, ε is the bed voidage, m_{ads} is the total mass of the adsorbent, V_{col} is the volume of the column and V_d is the dead volume of the system. The solid equilibrium loading, q_i^*, is obtained by solving the Eqn. (2.11). The average column pressure, $P_{avg} = \frac{P_{in}+P_{out}}{2}$, was used in this expression since the pressure drop was negligible (<0.03 bar) [110]. In a binary gas mixture, this mass balance expression is also applied to measure the solid loading for each component (q_i^*) corresponding to its partial pressure ($P_{ave}y_{i,in}$). It is important to perform a complete breakthrough experiment when both composition and thermal fronts have been broken through.

In binary breakthrough experiments, the goal is to measure the competitive loading of both the components in systems where one component adsorbs much stronger than the other. It would be possible to measure the competitive loading of heavy-component using an adsorption breakthrough experiment. However, it could be challenging to measure the loading of the lighter component from the adsorption breakthrough profiles [92]. A desorption experiment is required to precisely estimate the lighter component loading. In this case, the mass balance is described as:

$$n_{out} = n_{acc} \tag{2.12}$$

$$q_i^* m_{ads} = \int_0^{t_{des}} \left(\frac{Q_{out}P_{avg}y_{i,out}}{RT_{out}}\right)dt \tag{2.13}$$

In the above expression, all the quantities on the right-hand side are measured from the experiments and accordingly, the competitive loading q_i^* can be evaluated.

2.5. Single-component measurements

2.5.1. Batch experiments

The experimental equilibrium data of CO_2 and N_2 measured using volumetric and gravimetric methods at various temperatures are shown in Fig. 2.3.

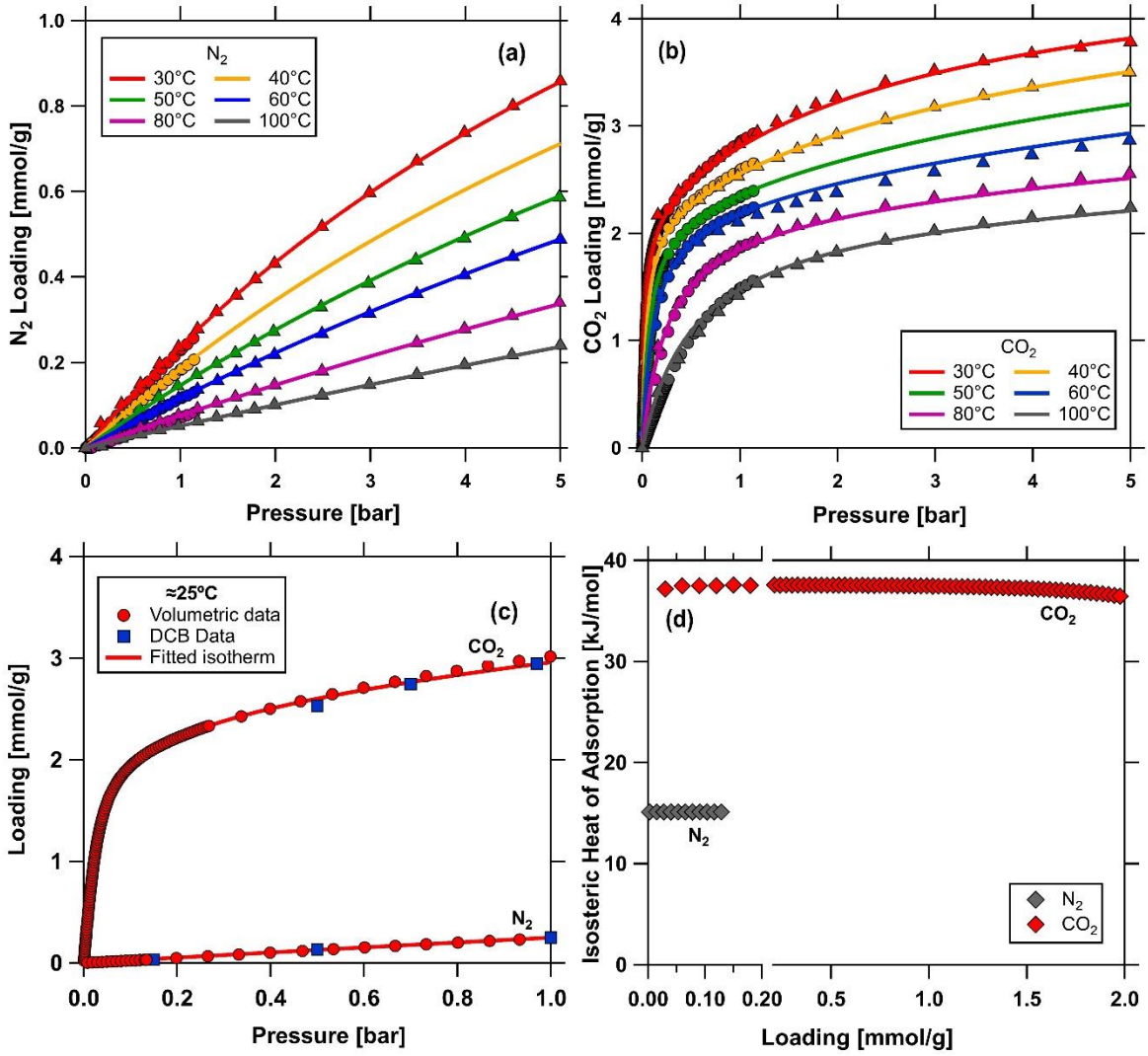

Figure 2.3: Single component adsorption isotherms of CALF-20 at various temperatures. (a) N_2 adsorption isotherms from 0 to 5 bar; (b) CO_2 adsorption isotherms from 0 to 5 bar; (c) Single adsorption isotherms of CO_2 and N_2 at ≈25°C; (d) Isosteric heat of adsorption of CO_2 and N_2. Circle markers represent volumetric data, triangle markers are gravimetric data, and square markers are dynamic column breakthrough data. Markers represent the experimental data; solid lines are the fitted isotherms.

Both CO_2 and N_2 exhibited favourable isotherms, in which CO_2 displayed a stronger affinity on CALF-20. CO_2 isotherms showed a nonlinear form. In contrast, N_2 showed a fairly linear isotherm form with significantly lower loadings than CO_2 at the same conditions. The N_2 isotherms showed slight non-linearity at higher pressures. The volumetric and gravimetric data for both CO_2 and N_2 isotherms were consistent with one another.

The CO_2 and N_2 isosteric heat of adsorption (ΔH_{iso}) were calculated from the Clausius-Clapeyron equation [111] using the experimental isotherm data:

$$\left(\frac{\partial ln p_i}{\partial (1/T)}\right)_{q_i} = -\frac{\Delta H_{\mathrm{iso}}}{R} \tag{2.14}$$

The isosteric heat of adsorption as a function of loading is shown in Fig. 2.3d. The experimental dataset contained a sufficient number of points, and hence using a linear interpolation between two adjacent points was considered reasonable. It is nearly constant within the range of N_2 loading, which implied that CALF-20 is energetically homogeneous with respect to N_2. In the case of CO_2, the isosteric heat of adsorption maintains constant up to 1.5 mmol/g. Then, it decreases slightly. This suggests the possibility of a mild energetically heterogeneous at higher CO_2 loadings.

2.5.2. Description of single adsorption isotherms

The adsorption isotherm is perhaps the most important information that is required for process design and analysis. The key desired features are: i. The isotherm function is based on the physical model; ii. It is available in an explicit form; iii. It also provides a simple extension to describe competitive data. From these perspectives, two forms, the single-site Langmuir (SSL) and dual-site Langmuir (DSL), are suitable for Type I isotherm. The SSL isotherm takes the form:

$$q_i^* = \frac{q_{sb,i} b_i c_i}{(1 + b_i c_i)} \tag{2.15}$$

$$b_i = b_{0,i} e^{-\Delta U_{b,i}/(RT)} \tag{2.16}$$

The DSL isotherm takes the form:

$$q_i^* = \frac{q_{sb,i} b_i c_i}{(1 + b_i c_i)} + \frac{q_{sd,i} d_i c_i}{(1 + d_i c_i)} \tag{2.17}$$

$$d_i = d_{0,i} e^{-\Delta U_{d,i}/(RT)} \tag{2.18}$$

where q_i^* is the equilibrium loading on the solid phase of component i, c_i is the concentration of the fluid phase, $q_{sb,i}$ and $q_{sd,i}$ represent the saturation capacity of site b and d, $\Delta U_{b,i}$ and $\Delta U_{d,i}$ are the internal energy of site b and d, respectively.

Here the adsorbent is considered to be comprised of two distinct sites: "*b*" and "*d*" sites. The two forms were fitted to the batch adsorption data (volumetric data). For the fitting process, the MATLAB *fmincon* tool was used in order to minimize the objective function *J*:

$$J = \sum_{i=T_1}^{T_n} \sum_{j=P_1}^{P_m} \left(q^*_{measured}(T_i, P_{i,j}) - q^*_{fitted}(T_i, P_{i,j}) \right)^2 \tag{2.19}$$

where the pressure varied from 0 bar to 1.2 bar and the temperatures were from 25°C to 100°C. The fitted isotherms are shown in Fig. 2.3, and the fitted parameters are provided in Table 2.1.

Figure 2.4 shows a comparison of single-site isotherm and dual-site isotherm fitted to the CO_2 experimental isotherm data. As can be seen, the SSL formalism does not provide a good description over the entire pressure range. This isotherm model merely describes the CO_2 loading at low pressure range (<0.1 bar), and it fails to describe the CO_2 loading at higher pressures. The DSL fit, however, provides a good description for the entire pressure range and temperatures. It is worth noting that while CO_2 requires the use of two sites, N_2 equilibrium data can be adequately described by an SSL isotherm (Fig. 2.3).

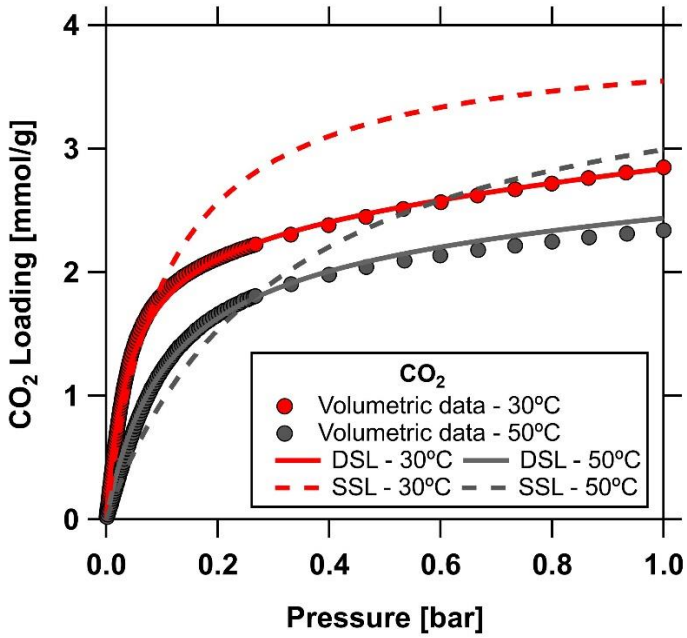

Figure 2.4: A comparison of single-site and dual-site Langmuir isotherm of CO_2 at 30°C and 50°C from 0 bar to 1.0 bar. Markers are the experimental data, broken lines are the SSL isotherm, and solid lines are the DSL isotherm.

Table 2.1: Fitted Langmuir isotherm parameters for CO_2 and N_2 on CALF-20

Parameter		CO_2 - SSL	CO_2 - DSL	N_2 - SSL
q_{sb}	mmol/g	3.927	2.387	5.658
b_0	m^3/mol	1.889 x 10^{-8}	5.519 x 10^{-7}	8.143 x 10^{-7}
ΔU_b	kJ/mol	-41.19	-35.06	-17.96
q_{sd}	mmol/g	-	3.2711	-
d_0	m^3/mol	-	5.187 x 10^{-8}	-
ΔU_d	kJ/mol	-	-28.95	-

2.5.3. Single dynamic column breakthrough experiments

All single component CO_2 and single component N_2 breakthrough experiments were conducted at ≈22°C and 0.97 bar total pressure. Helium was used as the carrier gas for those experiments, and the column was saturated with He initially. Detail conditions for every experiment were

summarized in the Appendix (Table A2.1). All breakthrough profiles were reported in dimensionless time $\left(\bar{t} = \frac{tv}{L}\right)$.

The single N_2 breakthrough experiments at 15%, 50% and 100% mole fraction (balance helium) are shown in Fig. 2.5. In the breakthrough profiles, the 100% N_2 case exited the column slightly earlier than 50% and 15% N_2, at $\bar{t} \approx 2$ and $\bar{t} \approx 4$, respectively. Furthermore, a front was observed in the case of 100% N_2. When reducing N_2 mole fraction by adding He (considered as a non-adsorbed gas or a lighter component), the effect of dispersion is noticeable. This is an indication of a nonlinear isotherm [112, 113]. The N_2 equilibrium loading of each experiment was calculated using the mass balance calculation described earlier. The results are comparable with the volumetric data and the simulations (Fig. 2.3c).

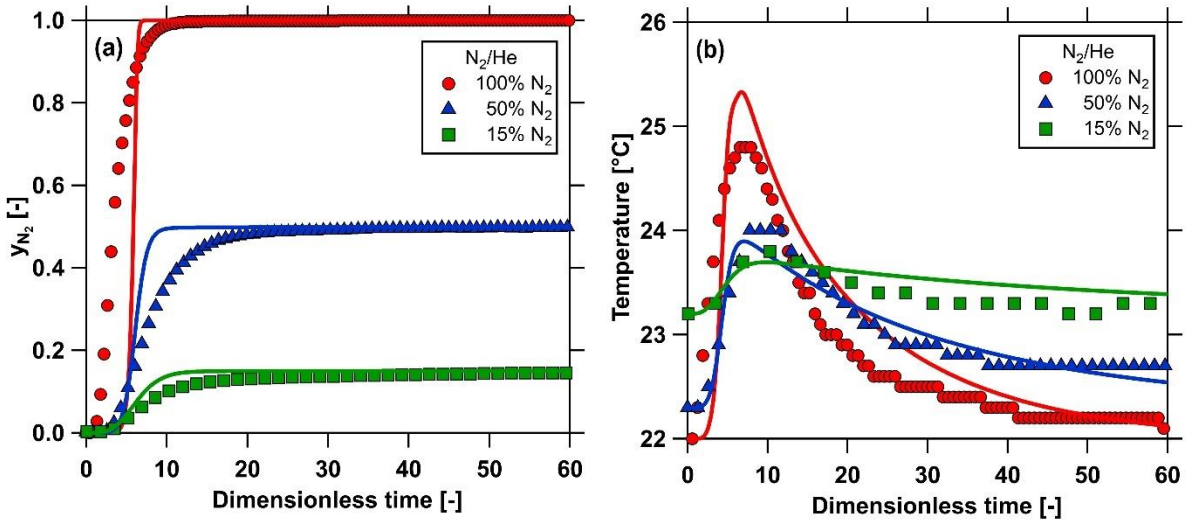

Figure 2.5: Single component N_2 breakthrough experiments at different mole fractions. (a) N_2 breakthrough curves; (b) N_2 temperature history. Markers represent the experimental data and the simulations are shown as solid lines.

Figure 2.5b shows the temperature histories of the single component N_2 breakthrough experiments. Overall, only a slight increase in temperature was observed. The biggest change in the temperature was recorded for the 100% N_2 experiment, at ≈3°C difference.

The single-component CO_2 breakthrough experiments at the composition of 50%, 70% and 100% mole fraction (balance helium) were displayed in Fig. 2.6. In the CO_2 breakthrough curves, a sharp

front was observed in all three CO_2 mole fraction experiments. This typical self-sharpening effect is usually seen in a non-linear isotherm (Langmuir type isotherm) [112, 114]. The breakthrough curves corresponding to higher feed compositions broke through earlier compared to those at lower feed compositions. The CO_2 at 100%, 70% and 50% mole fraction exited the column at $\bar{t} \approx 50$, $\bar{t} \approx 62$, and $\bar{t} \approx 87$, respectively. This trend is characteristic of favourable isotherms where breakthrough curves of lower compositions elute later compared to those of higher compositions.

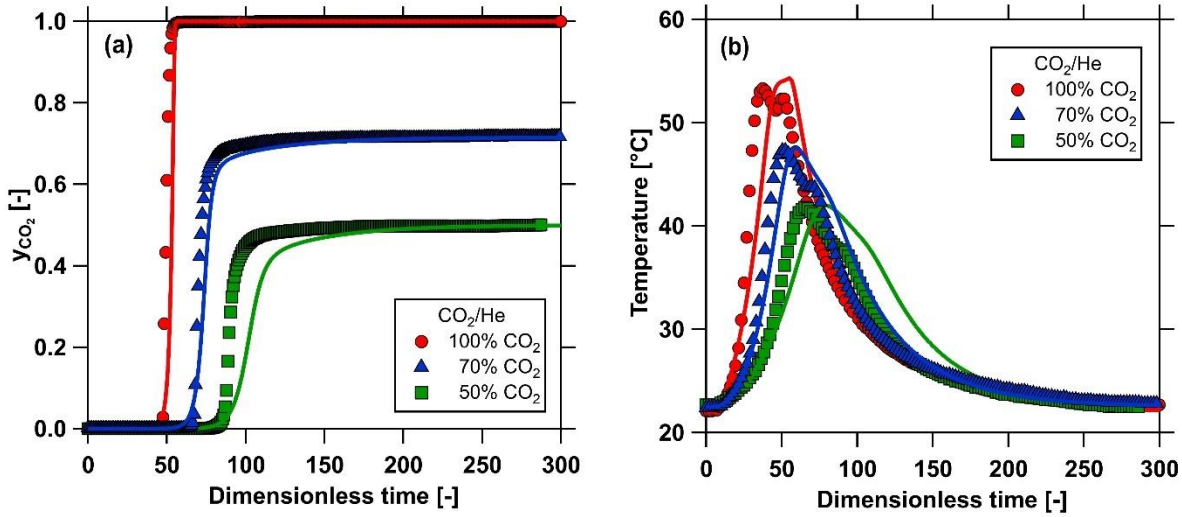

Figure 2.6: Single component CO_2 breakthrough experiments at different mole fractions. (a) CO_2 breakthrough curves; (b) CO_2 temperature curves; Markers represent the experimental data and the simulations are shown as solid lines.

Figure 2.6b shows the CO_2 temperature histories at different mole fractions. A significant increase in the temperature was observed, up to ≈30°C depending on the CO_2 mole fractions. This result confirmed the high heat of adsorption for CO_2, compared to N_2, on CALF-20.

2.5.4. Dynamic column breakthrough simulations

All parameters for the experiments and simulations are given in Table 2.2. To measure the adsorbent bulk density (ρ_{bulk}), the structured CALF-20 was packed well in a graduated cylinder, then the total volume and mass of the adsorbent were recorded. The bed voidage (ε) was estimated by running a breakthrough experiment using two non-adsorbed gases (He and Ar) [110]. The particle void fraction (ϵ_p), the tortuosity (τ), the column wall density (ρ_w), the specific heat capacity of column wall ($C_{p,w}$), and the thermal conductivity of column wall (K_w) were assumed

to be similar to the Haghpanah *et al.*, which had a similar stainless steel column [109]. The specific heat capacity of the gas ($C_{p,g}$), was obtained from NIST database for different gases [115]. The specific heat capacity of the adsorbent ($C_{p,a}$) was assumed to be equal to the specific heat capacity of the gas. The molecular diffusion coefficient (D_m) was estimated from Chapman-Enskog equation [116]. To determine the specific heat capacity of the adsorbent ($C_{p,s}$), the effective gas thermal conductivity (K_z), the internal and external heat transfer coefficients (h_{in}, h_{out}), the experimental breakthrough profiles of single component CO_2 were used to run an optimization. By minimizing the difference in the thermal profiles of the simulations and the experiments, these values were found and validated by various CO_2/N_2 gas mixtures.

By solving the column dynamics model described earlier, the breakthrough curves and temperature histories were simulated and compared with the experimental data. Fig. 2.5 shows the single component N_2 breakthrough profiles. In this case, the simulations and experiments showed a good agreement in both breakthrough curves and temperature histories. However, the experimental breakthrough curves exhibited slightly more diffused profiles. The simulations well predicted both the temperature peak and the temperature decay after the adsorptive heat front passed.

The single-component CO_2 breakthrough profiles are indicated in Fig. 2.6. A good agreement between the simulations and the experiments was also achieved. The breakthrough curves were captured well for 100% and 70% of CO_2. The experimental breakthrough curve of 50% of CO_2, however, showed a sharper front compared to the simulation. In the temperature histories, the simulations captured the CO_2 adsorptive heat front well. The temperature decay after the CO_2 adsorptive heat front passed was slightly slower than the experiments.

Table 2.2: Dynamic column breakthrough simulation parameters for CALF-20

Parameter	Symbol			Value	Source
		Column properties			
Column length	L	m		0.0786	measured
Inner column diameter	d_{in}	m		0.0282	measured
Outer column diameter	d_{out}	m		0.0318	measured
Bed voidage	ε	-		0.4	measured
Particle void fraction	ϵ_p	-		0.35	assumed
Tortuosity	τ	-		3.0	assumed
Adsorbent mass	m_{ads}	g		16.7	measured
		Properties and constants			
Universal gas constant	R	m^3 bar mol^{-1} K^{-1}		8.314x10^{-5}	standard
Adsorbent particle density	ρ_p	kg m^{-3}		570	measured
Column wall density	ρ_w	kg m^{-3}		7800	standard
Specific heat capacity	$C_{p,g}$	J kg^{-1} K^{-1}	(He)	5200	NIST database
			(CO_2)	841	NIST database
			(N_2)	1040	NIST database
Specific heat capacity of adsorbed phase	$C_{p,a}$	J kg^{-1} K^{-1}		$C_{p,g}$	assumed
Specific heat capacity of adsorbent	$C_{p,s}$	J kg^{-1} K^{-1}		1371	fitted
Specific heat capacity of column wall	$C_{p,w}$	J kg^{-1} K^{-1}		502	standard
Fluid viscosity	μ	kg m^{-1} s^{-1}		1.812x10^{-5}	standard
Molecular diffusion	D_m	m s^{-2}		1.496x10^{-5}	standard
Effective gas thermal conductivity	K_z	W m^{-1} K^{-1}		0.4	fitted
Thermal conductivity of column wall	K_w	W m^{-1} K^{-1}		16	standard
Internal heat transfer coefficient	h_{in}	W m^{-2} K^{-1}		6.963	fitted
External heat transfer coefficient	h_{out}	W m^{-2} K^{-1}		14	fitted

2.6. Binary-component measurements

2.6.1. Competitive CO_2/N_2 adsorption dynamic column breakthrough experiments

Various CO_2/N_2 mixtures were examined at ≈22°C and 0.97 bar. The detailed experimental conditions are provided in the Appendix (Table A2.1). Prior to each experiment, the column was saturated with Helium, and the desired composition was fed to the column. Fig. 2.7 shows the competitive CO_2/N_2 adsorption breakthrough results at 5/95, 15/85 and 30/70 CO_2/N_2 mixture, respectively. In the N_2 concentration profiles, a sharp front which indicated a complete breakthrough of N_2 was observed at $\bar{t} \approx 4$ in all three cases. The "roll-up" effect of N_2 was well captured in each experiment when CO_2 broke through. This effect is well-known as evidence of the competitive nature of adsorption.

The CO_2 concentration profiles show different breakthrough times for various CO_2/N_2 compositions (Fig. 2.7c). The higher the CO_2 composition in the feed, the shorter the breakthrough time. A shock front of CO_2 was observed for 30% and 15% of CO_2 mole fraction. The dynamics of the CO_2 front was changed in the case of 5/95 CO_2/N_2. The shock front showed noticeable dispersions when the feed gas was diluted with the lighter component (N_2).

Figure 2.7b shows the temperature history of the column at $z = 0.75L$. Two distinct temperature peaks were seen in each case. A slight increase of ≈5°C at $\bar{t} \approx 4$ corresponded to the heat generated by the adsorption of N_2, while a prominent temperature increase was from the CO_2 adsorption. All experiments were kept running until the temperature front completely broke through the column and reached the surrounding temperature. Since the temperature decreases, the adsorption capacity will be enhanced. Thus, the mass balance calculation and the competitive loading estimation would be affected.

From the adsorption breakthrough curves, the CO_2 and N_2 competitive loadings were calculated using Eqn. (2.11). The CO_2 and N_2 competitive isotherms were indicated in Fig. 2.9, and all competitive data were reported in the Appendix (Table A2.1 & A2.2). It is straightforward to measure the competitive loadings of CO_2. Graphically, the CO_2 capacity is the area before the CO_2 breakthrough curve. For the light component (N_2 in particular), the competitive loading is the difference between the area before the breakthrough curve and the area where the outlet concentration is greater than the inlet concentration [87, 105]. It is challenging to measure the lighter component capacity in some cases where the difference between these two areas is too

small to measure. This usually happens in a system where the heavy component is dominant. An unrealistic negative value might be obtained due to the limitation of the experimental measurement [92, 117].

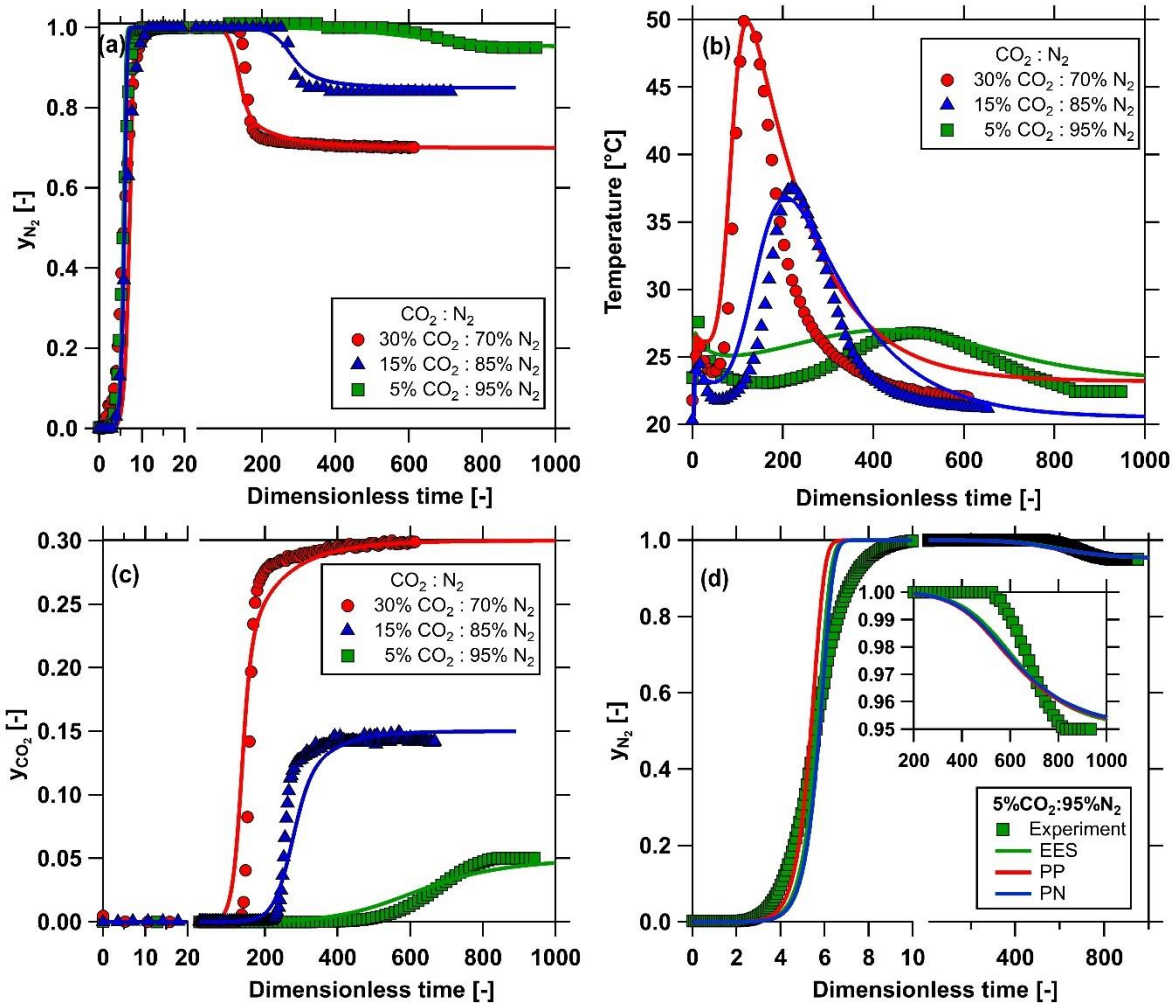

Figure 2.7: Competitive CO_2/N_2 adsorption breakthrough curves at different compositions on CALF-20. (a) N_2 concentration profiles; (b) Column temperature histories measured at $z = 0.75L$; (c) CO_2 concentration profiles; (d) N_2 concentration profile at 5% CO_2:95% N_2 using equal energy site (EES), perfect positive (PP) and perfect negative (PN) fitting schemes. Markers represent experimental data, and solid lines are the simulations.

2.6.2. Competitive CO_2/N_2 desorption breakthrough experiments

To measure the N_2 competitive loadings, a series of CO_2/N_2 desorption experiments were performed. In these experiments, the column was first fully saturated with a certain composition

of CO_2/N_2. At $\bar{t} \approx 0$, Helium was introduced to the column and maintained at a certain flowrate. The desorption curve is now measured at the column outlet. Often, the competitive loading of the light component is relatively small, so the desorption is completed quickly. To quantify the N_2 loadings, a low helium flowrate is preferred to let the desorption experiment run long enough. A flow rate of 0.025 LPM of Helium was used for all these desorption experiments.

Figure 2.8 shows the CO_2 and N_2 desorption curves at five different initial CO_2/N_2 compositions. A simple wave was observed in all experiments. As can be seen, it took approximately $\bar{t} \approx 200$ to desorb most of CO_2 in the solid. In contrast, N_2 was desorbed faster, at $\bar{t} \approx 10$, and the area under the desorption curves were used to estimate the competitive loadings. By using Eqn. (2.13), the N_2 competitive loadings were calculated and shown in Fig. 2.9. The specific competitive loadings are summarized in the Appendix (Table A2.2). Meaningful competitive N_2 capacities were obtained from the desorption experiments.

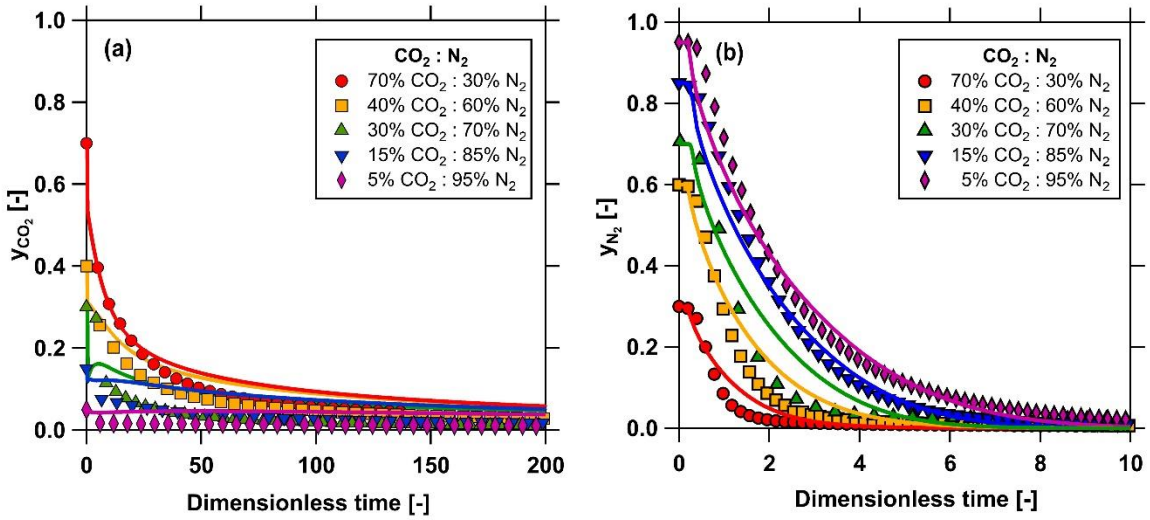

Figure 2.8: Competitive CO_2/N_2 desorption breakthrough curves at different compositions. (a) CO_2 desorption curves; (b) N_2 desorption curves. Markers represent the experimental data and solid lines show the simulation results.

2.6.3. Description of binary adsorption isotherms

It is essential to describe the isotherms precisely since all simulating and modelling predictions are based on isotherm information. In this work, three different schemes were examined to describe the competitive CO_2 and N_2 loadings [92, 118], namely: perfect positive (PP), perfect negative

(PN) and equal energy site (EES). In all these cases, the CO_2 isotherms are fitted first by dual-site Langmuir using the experimental data from 0 to 1.2 bar. Then, an extended dual-site Langmuir is employed to describe the competitive CO_2/N_2 loadings.

$$q_i^* = \frac{q_{sb,i} b_i c_i}{(1 + \sum_{i=1}^{n} b_i c_i)} + \frac{q_{sd,i} d_i c_i}{(1 + \sum_{i=1}^{n} d_i c_i)} \tag{20}$$

where i denotes the component 1 or 2, n is the total number of components; other descriptions are similar to Eqn. (2.17). If there is only one component in the system, the extended dual-site Langmuir model Eqn. (2.20), will become the dual-site Langmuir isotherm model Eqn. (2.17).

Perfect positive scheme: In this approach, the N_2 isotherms are fitted using a single-site Langmuir model (b site only). There is one constraint that the N_2 saturation capacity equals to the total CO_2 saturation loadings of b site and d site, i.e. $q_{sb,N_2} = q_{sb,CO_2} + q_{sd,CO_2}$.

Perfect negative scheme: Similar to PP approach, the PN scheme describes the N_2 isotherm by single-site Langmuir model, but using d site in this case with the constraint: $q_{sd,N_2} = q_{sb,CO_2} + q_{sd,CO_2}$. Depending on pairing N_2 isotherms on b site or d site, different competitive loadings could be obtained.

Equal energy site scheme: The EES approach considers the N_2 isotherm description is split into two equal energy sites, denoted b site and d site [92]. The N_2 saturation capacity of each site is equal to the corresponding CO_2 saturation capacity site, as followed:

$$q_{sb,N_2} = q_{sb,CO_2}$$

$$q_{sd,N_2} = q_{sd,CO_2}$$

$$b_{0,N_2} = d_{0,N_2}$$

$$\Delta U_{b,N_2} = \Delta U_{d,N_2}$$

All isotherm parameters of PP, PN and EES scheme are shown in Table 2.3.

Table 2.3: Extended dual-site Langmuir parameters on CALF-20

Parameter		CO_2 - DSL	N_2 - PP	N_2 - PN	N_2 - EES
q_{sb}	mmol/g	2.387	5.658	-	2.387
b_0	m^3/mol	5.519 x 10^{-7}	8.143 x 10^{-7}	-	8.139 x 10^{-7}
ΔU_b	kJ/mol	-35.06	-17.96	-	-17.96
q_{sd}	mmol/g	3.271	-	5.658	3.271
d_0	m^3/mol	5.187 x 10^{-8}	-	8.143 x 10^{-7}	8.139 x 10^{-7}
ΔU_d	kJ/mol	-28.95	-	-17.96	-17.96

The calculated competitive CO_2/N_2 equilibrium loadings are shown in Fig. 2.9. All the data were examined at 22°C and 0.97 bar total pressure.

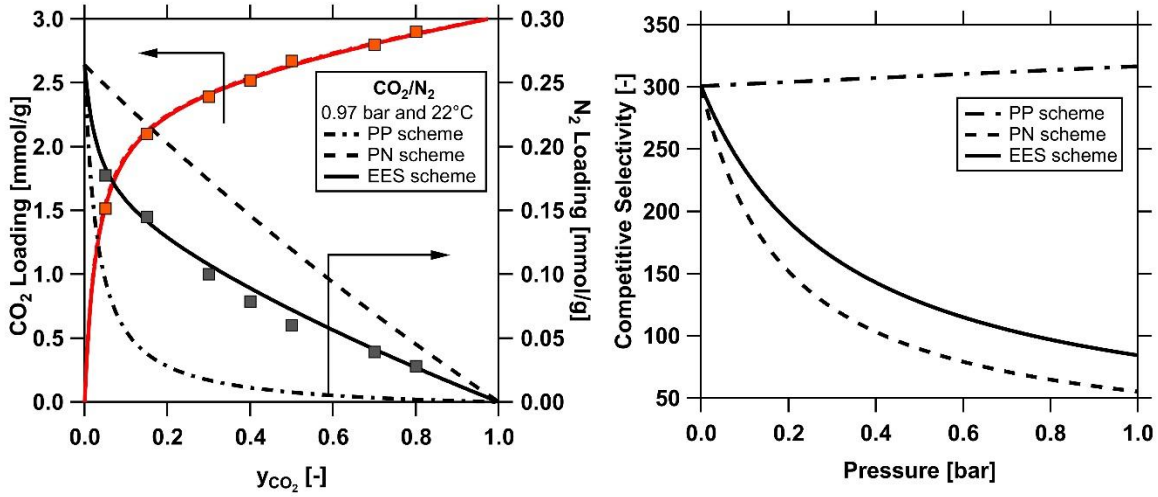

Figure 2.9: (a) Competitive loadings of CO_2/N_2 on CALF-20; (b) The equilibrium selectivity of 15/85 CO_2/N_2 at different total pressures. Markers represent experimental data, solid lines and broken lines represent the simulations; CO_2 is plotted in red and N_2 is plotted in black

In Fig. 2.9a, the PP, PN and EES schemes showed very similar CO_2 loadings. In contrast, a distinct difference in the N_2 competitive capacities was observed depending on CO_2/N_2 competitive model combinations. In all three schemes, the N_2 capacity was dropped significantly when the CO_2 mole fraction increased. The lowest N_2 capacity was indicated in the PP scheme, where N_2 competed with the favourable site of CO_2. The highest N_2 capacity was predicted by the PN scheme where N_2 competed with the less favourable site of CO_2. The N_2 loading prediction from the EES scheme

fell into the middle of PP and PN schemes. In the EES, N_2 was considered to compete with both CO_2 sites. Fig. 2.9a shows that the EES scheme showed a good agreement with the competitive N_2 loadings obtained from the binary DCB experiments. These observations are similar to those seen for CO_2/N_2 adsorption on zeolite 13X [92]. For further modelling purposes, the EES scheme was used.

The equilibrium selectivity of a binary mixture can be defined as [85]:

$$\alpha_{CO_2/N_2} = \frac{q^*_{CO_2}}{q^*_{N_2}} . \frac{y_{N_2}}{y_{CO_2}} \tag{2.21}$$

where α_{CO_2/N_2} is the selectivity of CO_2/N_2, y_{N_2} and y_{CO_2} are the mole fractions of the two components in the fluid phase, $q^*_{N_2}$ and $q^*_{CO_2}$ are the equilibrium loadings of N_2 and CO_2 in the solid phase, respectively.

Figure 2.9b shows the CO_2/N_2 selectivity as a function of total pressure calculated from the three formulations. The mole fraction of CO_2 and N_2 in the fluid phase was fixed at 15/85, which is a typical composition of CO_2 and N_2 in the flue gas from a coal power plant. An expected tendency was seen in the PN and EES scheme, where a significant decrease in the selectivity was observed while increasing the total pressure. In contrast, a slight increase in the selectivity was indicated in the PP scheme. In this PP fitting, N_2 competes with CO_2 at high energy sites, which are filled at low pressure ranges. At higher pressures, the low energy sites (*d* sites) become significant. There is no N_2 competition on those sites resulting in an increase of selectivity. This is unrealistic, emphasizing the need for finding suitable competitive isotherm expression.

2.6.4. Modelling binary dynamic column breakthrough

Based on the single component breakthrough profiles, all simulation parameters were found and used to predict the competitive CO_2/N_2 breakthrough experiments (Table 2.2). Three different schemes of the competitive isotherm, i.e. PP, PN and EES, were used to predict the competitive CO_2/N_2 breakthrough at 5/95 CO_2/N_2 (Fig 2.7d). The PP scheme tended to break through slightly earlier and the PN scheme broke through slightly later than the EES scheme (Fig. 2.7d). Fig. 2.9a indicated that competitive loadings from the EES scheme were comparable with the experimental DCB data. Hence, the EES scheme was used to simulate the competitive CO_2/N_2 DCB.

Figure 2.7 shows a comparison of the simulations and experiments from three different CO_2/N_2 compositions. The model captured both the competitive N_2 breakthrough fronts and the roll-up effect very well in all three experiments. In the competitive CO_2 breakthrough curves, the model provided a good prediction. However, the experimental profiles showed sharper CO_2 fronts compared to the simulations. In the temperature histories, the model captured well both the N_2 adsorptive heat fronts and the CO_2 adsorptive heat fronts. After the adsorptive heat front passed, the temperature decay from the simulations was slower than the experimental temperature curves, which led to a higher temperature in the simulation. However, the peaks from N_2 adsorption and CO_2 adsorption were well captured in all experiments.

The desorption curve simulations of CO_2 and N_2 at various compositions using the EES scheme are shown in Fig. 2.8. In general, the CO_2 desorption simulations are in good agreement with the experiments. A sudden drop in the CO_2 mole fraction following by a slow decay was observed in the CO_2 desorption curves. The simulation was able to capture the sudden drop, but the tails from the simulation are slightly higher than the experiments, which means the simulation took a slightly longer desorption time than the experiments. N_2 desorbed much faster than CO_2, i.e. 20 times faster ($\bar{t} \approx 10$). The simulation was well captured the N_2 desorption curves at different compositions (Fig. 2.8b). There was only a slight difference at 30/70 and 40/60 CO_2/N_2 compositions. The extended DSL isotherm with the EES scheme was able to predict the competitive CO_2/N_2 dynamic column breakthrough well.

2.7. Conclusions

Single component CO_2 and N_2 isotherms on CALF-20 were measured by volumetric and gravimetric from 0 bar to 5 bar at 30, 40, 50, 60, 80 and 100°C. Dual-site Langmuir isotherm model was used to fit the CO_2, and N_2 equilibrium isotherms were described by single-site Langmuir. Single CO_2 and N_2 dynamic column breakthrough experiments were performed at ≈22°C and 0.97 bar total pressure using Helium as the inert gas. More diluted concentration in the feed showed a longer breakthrough time. The equilibrium loadings collected from the single DCB experiments were comparable with the data collected from volumetric and gravimetric methods.

Binary CO_2/N_2 dynamic column breakthrough experiments were performed at various compositions. The breakthrough curves showed a “roll-up” effect, which was the evidence for the competitive adsorption. The temperature histories indicated both temperature peaks of N_2

adsorption and CO_2 adsorption. The equilibrium loadings of CO_2 were calculated from the adsorption DCB experiments. It is inadequate to estimate the competitive N_2 loadings based on the adsorption DCB. The N_2 loadings required data from the desorption DCB experiments. The extended dual-site Langmuir was used to describe the competitive adsorption of CO_2 and N_2. Three different isotherm schemes were considered to predict the N_2 competitive loadings: perfect positive (PP), perfect negative (PN) and equal energy site (EES). A better prediction was obtained from the EES scheme, while the PP and PN schemes showed an under and over prediction. For further studies, the EES scheme was chosen to describe the competitive adsorption.

One dimensional mathematical model was used to simulate the column dynamics, including all dispersion, convection, heat transfer, and pressure drop of the column. The breakthrough curves showed a good agreement between the experiments and simulations. The temperature history of the column was also captured. The position of the temperature peaks and the magnitude of the temperature were well described. However, the model showed a slight difference in the temperature decay after the heat wave passed the column. The extended DSL model with the EES scheme is adequate to describe the CO_2/N_2 competitive adsorption.

3 Adsorption Equilibrium And Breakthrough Studies For Water On CALF-20

3.1. Introduction

Flue gas from coal-fired power plants is usually saturated with water vapour together with CO_2 and N_2. Water has a strong affinity to most solid adsorbents [87, 102, 119], which makes it more difficult to separate CO_2 in the flue gas. Zeolite 13X, a benchmark adsorbent, is considered as a potential candidate for CO_2 capture due to its high CO_2 saturation loading and high CO_2/N_2 selectivity [50]. This adsorbent could meet 95% purity and 90% recovery with high productivity and relatively low energy consumption on a dry basis [50]. However, the CO_2 capacity of zeolite 13X significantly decreases under the presence of a small amount of water (≈1% relative humidity) [87, 88]. Metal-organic frameworks (MOFs), a new class of hybrid porous materials, has been growing rapidly in the last decades [120, 121]. The structure of MOFs are porous, predictable, tunable, regular and highly crystalline [62]. Their structures can be designed and modified to use in a specific application. MOFs for CO_2 capture, especially water-stable MOFs, are desirable to use for capturing CO_2 in moist conditions without losing their performance [122].

A water-stable MOF should preserve its structure after exposure to water. To meet this expectation, MOFs should be constructed from highly coordinated metal-nodes with strong metal-linker bonds to protect the coordination sites [122-124]. Several computational and experimental studies were reported to develop new MOFs for CO_2 capture with high water stability [123, 125]. Liu *et al*. studied the water adsorption isotherm and the water stability of HKUST-1, also called Cu-BTC, using a volumetric system [126]. HKUST-1 showed a similar CO_2 isotherm after exposure to water several times. The water saturation capacity of HKUST-1 was ≈25 mmol/g [126]. Llewelllyn's group also reported the water isotherm of HKUST-1, UiO-66 and MIL-100 [127]. The water isotherm of UiO-66 showed an S-shape isotherm with two inflection points, and the saturation capacity was ≈ 20 mmol/g [127]. HKUST-1 showed a Langmuir type isotherm with the saturation capacity of water at ≈27 mmol/g [127]. The water isotherm of MIL-100 exhibited a type V

isotherm with the saturation loading at ≈35 mmol/g [127]. Qasem and Ben-Mansour reported the water isotherm of Mg-MOF74, which exhibited a rectangular type I isotherm with a saturation capacity of ≈35 mmol/g [128]. Chanut *et al*. studied the water stability of 45 MOFs using thermogravimetry analysis (TGA) [122]. The adsorbents were saturated with water initially. Then, the purge gas, i.e. N_2 or CO_2, was introduced to desorb the water. Multiple cycles were performed by switching the feed gas from N_2 to CO_2 and vice versa. The results suggested that five out of 45 MOFs had the potential for CO_2 capture [122].

Studying the adsorption equilibrium of water is necessary to understand its behaviour on solid sorbents. Depending on the surface properties, the adsorbent could exhibit a rectangular type I isotherm, which shows a very strong affinity with water, and it reaches the saturated capacity at very small relative humidity [87]. High temperatures and low vacuum are required to desorb water, which makes it challenge [87]. Type V isotherm is another common water isotherm, which is usually observed on hydrophobic surfaces, e.g., activated carbons [129]. Activated carbons show unfavourable water adsorption at low relative humidity and become a favourable isotherm at high relative humidity [129]. However, the adsorbent is not suitable for CO_2 capture owning to its low CO_2/N_2 selectivity. Often, water isotherms show a hysteresis loop with inflection points [130]. The water loading in the desorption curve is higher than the adsorption one at the same relative humidity, which is usually caused by capillary condensation [130, 131]. Owning to complexity of the isotherm, it is difficult to describe the water isotherm, the hysteresis loop, in particular. A more complicated model is required to describe the isotherm [51, 129, 132].

Unlike non-condensable gasses, measuring the water equilibrium loading is quite different because of its condensation phenomenon. Key challenges are the reliability of detectors, i.e., relative humidity meters, stable water vapour generation, and vapour condensation [129]. The water isotherm database on solid porous materials is insufficient for CO_2 capture applications. Water is usually ignored or removed in many CO_2 capture studies [50, 103, 133]. Furthermore, water breakthrough studies are also required to have better insights into the column dynamics. Both adsorption and desorption breakthrough experiments are necessary, especially when the isotherm contains a hysteresis loop as they are different because of the complicated shape of the isotherm [129, 132]. Only a few studies on water breakthrough have been reported. Hefti and co-workers studied the adsorption and desorption breakthrough of water vapour on activated carbon at 45°C

with different feed velocities [129]. Both adsorption and desorption breakthrough curves showed many transitions due to an inflection point in the isotherm [129]. Wilkins *et al*. reported the adsorption breakthrough of water on zeolite 13X at different relative humidities [87]. A sharp water front was observed in all breakthrough curves due to the rectangular type I isotherm [87].

In this study, the water isotherm on CALF-20 was measured from 22°C to 100°C at various relative humidity values using volumetric and thermogravimetric techniques. The Quadratic-Langmuir isotherm model was used to describe the water adsorption and desorption isotherms. Both adsorption and desorption dynamic column breakthrough (DCB) experiments were performed at 22°C and various relative humidity values. A column model was developed to simulate the adsorption and desorption DCB experiments.

3.2. Materials and methods

3.2.1. Materials

CALF-20 was synthesized and characterized by our colleagues at the University of Calgary. The powder CALF-20 was structured by the phase inversion method mentioned in the previous study. The obtained particles had a cylindrical shape with a diameter of 1 mm and a length of 1-3 mm. The particle density of the structured CALF-20 was estimated at 570 kg/m^3. The instrument air was used as a carrier gas to create a humid stream for all dynamic column breakthrough studies.

3.2.2. Static measurements

The determination of the adsorption behaviour of water on the adsorbent is critical for process design. Most practical applications of CO_2 capture involve flue gas that is fully (or partially) saturated with water. A scan of the literature reveals that very few studies consider the adsorption of water. Part of this observation can be attributed to the challenges associated with performing experiments using water vapour [129]. Extreme care has to be taken to ensure that water does not condense anywhere on the experimental setup. Further, the measurement of relative humidity is important. These aspects were carefully considered in this study. Single component water isotherms were measured by volumetric and thermogravimetric analysis (TGA).

Volumetric measurements

H_2O isotherms at 22°C were measured by the Micromeritics ASAP 2020 (Norcross, GA, USA) available at the University of Calgary. The ASAP 2020 equipped with enhanced water vapour

generation allows measuring the H_2O adsorption equilibrium at very low relative humidity (RH) values. Both adsorption and desorption of H_2O isotherms were measured at 22°C from 0% RH to almost 100% RH. A mass of ≈200 mg structured CALF-20 was used for these measurements. At first, the sample cell containing the adsorbent was evacuated. Prior to the measurement, the adsorbents were activated at 150°C for 12 hours. The volumetric equilibrium data was collected by dosing a known amount of gas into the sample cell. By monitoring the pressure change and solving the mass balance, the adsorbed amount can be calculated. The reading loading accuracy of this Micromeritics system is 0.15%, and the pressure accuracy is $1.3x10^{-7}$ mbar.

Thermogravimetric analysis

A TA Q500 (TA Instruments, DE, USA), thermogravimetric analyzer (TGA), was used to measure single component H_2O isotherms at ≈0.97 bar total pressure and various temperatures. A custom-made bubbler humidifier was used to generate a stable humid stream at the desired RH level (Fig. 3.1). This humidifier contains a tank filled with deionized water and two mass flow controllers, MFC-1 and MFC-2 (Alicat Scientific, Tucson, AZ, USA). To humidify gas, dry instrument air was divided into two separate streams. The first stream passed the MFC-2 and travelled to the bottom of the tank. After bubbling through the tank, this stream, saturated with water, was mixed with the second dry stream (passed through the MFC-1). The relative humidity of this mixed stream was measured to ensure that the desired RH value was reached. Note that the RH can be controlled by suitably adjusting the flow rates in MFC-1 and MFC-2. This humid stream was then introduced to the TGA chamber containing ≈65 mg of the structured CALF-20 at the desired temperature. The total mass of the sample was measured and recorded over time. The equilibrium is reached when the mass change of the sample is less than 0.01%. The difference between the initial and final mass of the sample is the amount of H_2O adsorbed. The equilibrium H_2O loadings were measured at various RH values and various temperatures (22°C, 30°C, 40°C, 50°C, 60°C, 80°C and 100°C). Prior to the experiments, the adsorbent was activated at 150°C for 12 hours. For these measurements, dry instrument air was used as a carrier gas. The constituents of the instrument air (N_2, O_2 and Ar) were assumed to have negligible affinity in the presence of water. The weighing precision of this TGA is ±0.01%, and the sensitivity is 0.1μg.

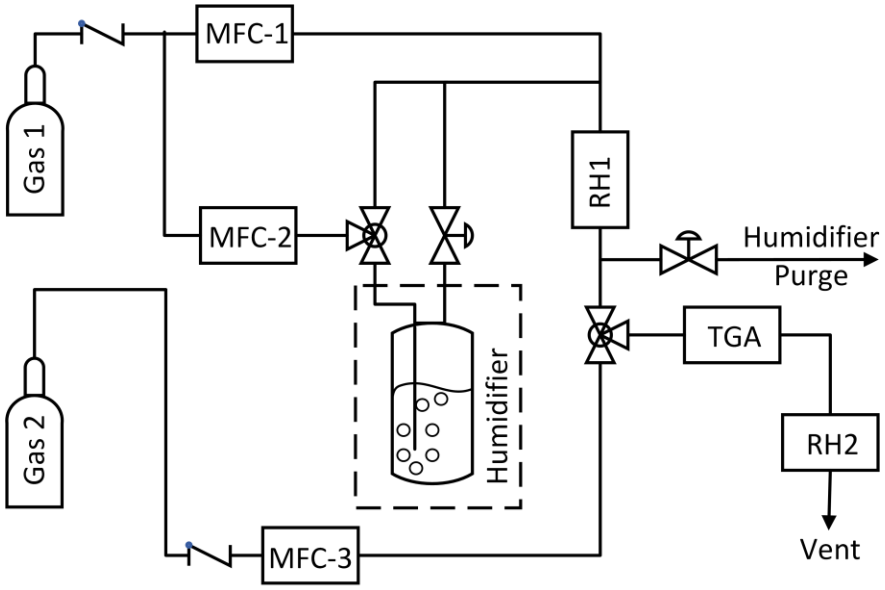

Figure 3.1: The schematic of the modified thermogravimetric analysis for measuring water isotherms; MFC – Mass flow controller, RH - Relative humidity meter; TGA – Thermogravimetric analyzer

3.2.3. Dynamic column breakthrough studies

The dynamic column breakthrough (DCB) apparatus that was reported in our previous study, was used to perform water DCB experiments. To create a humid stream, a bubbler humidifier was added to this current DCB set-up (Fig. 3.2). A SensorPush RH meter (Brooklynn, NY, USA) was used to measure the relative humidity at both the inlet and outlet of the column. The temperature accuracy of this SensorPush is ±0.3°C, and the humidity accuracy is ±3%. The inlet pressure and pressure drop across the column were measured by a pressure transducer and a differential pressure gauge (GE Druck, Billerica, MA, USA). The column thermal history was measured by a thermocouple (Omega Engineering, Laval, QC, Canada) placed 1.82 cm from the outlet. Prior to the start of any experiment, sufficient time was provided to create the humid stream.

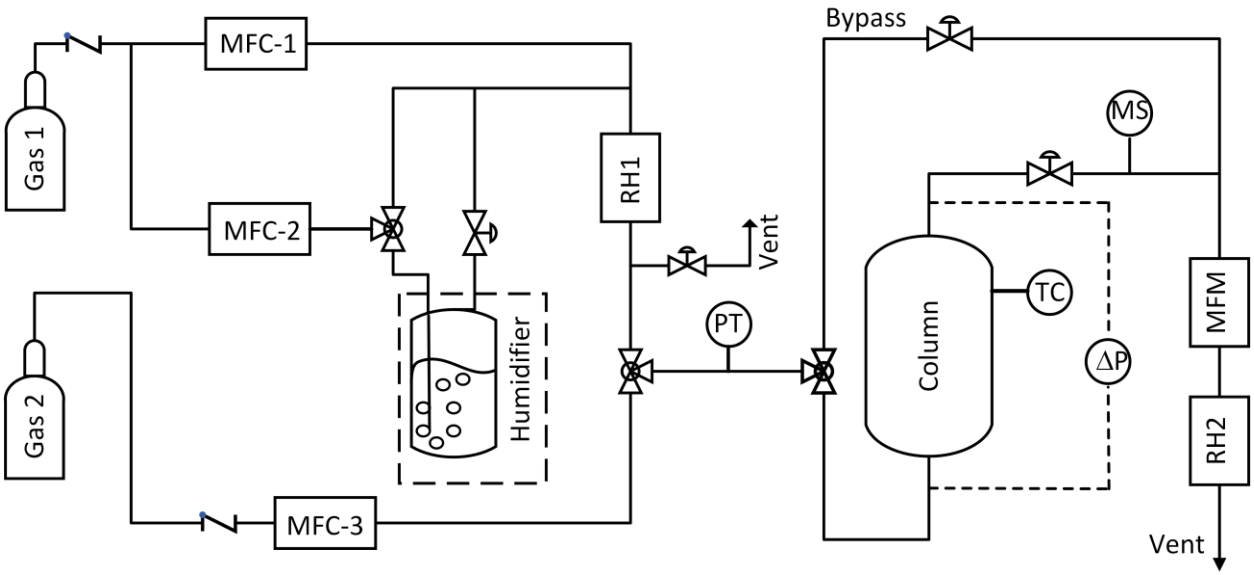

Figure 3.2: The dynamic column breakthrough apparatus with the humidifier. MFC - Mass flow controller; RH - Relative humidity meter; PT - Pressure transducer; TC - Thermo couple; MS - Mass spectrometer; MFM - Mass flow meter

In adsorption experiments, the column was first saturated with an inert gas (Helium). At $t = 0$, a step signal of the humid stream was fed to the column. The column temperature history and the outlet relative humidity were recorded over time. The inlet and outlet flow and the pressure history were also recorded by a data acquisition system. The adsorption experiment is completed when the outlet relative humidity and the outlet temperature equal to the inlet feed. Three sets of H_2O adsorption experiments were performed: 8%, 22% and 45% RH. All breakthrough experiments were run at ≈22°C and 0.97 bar total pressure. Prior to each experiment, the column was regenerated at 150°C for 12 hours. The humidifier was set to run until a stable desired RH value was obtained before the experiment.

In desorption experiments, the bed was equilibrated at a certain RH level initially (8%, 22% or 45% RH). At $t = 0$, dry instrument air was introduced to the column. The column temperature and the outlet RH were measured. The desorption experiment is finished when the outlet relative humidity is nearly 0%, and the temperature is equal to the surrounding environment.

Prior to the experiments, all mass flow controllers and mass flow meter were calibrated by a universal gas flow meter (Agilent Technologies, Santa Clara, CA, USA). The blank response was

also performed, and it was negligible. This is reasonable since the blank response was less than 5 seconds and the entire adsorption/desorption experiments took longer than two days.

Difficulties in performing water breakthrough experiments

Before performing a humid breakthrough experiment, many uncertainties need to be addressed. First, water condensation in the system might happen at the saturation condition [129]. Once this phenomenon occurs, it is difficult to completely remove condensed water from the column. To avoid the condensation of water, the humid breakthrough experiments were kept far from the dew point. Furthermore, to create a stable humid stream, the bubbler humidifier is required to run at a constant flow rate for a long time (≈6 hours). Note that the volume of water in the tank was ≈250 mL and the flow rate was ≈200 ccm. This ensures the steady-state is reached, and a constant relative humidity feed was generated and maintained [87]. Measuring the relative humidity was also very challenging since it depended on both temperature and pressure. A small fluctuation in the lab temperature (±1°C) is usually observed, which might affect the RH reading and the experimental reproducibility. The water breakthrough experiment at 22% RH was repeated to confirm the reproducibility.

3.3. Adsorption modelling

3.3.1. Column model development

A one-dimensional column model was used to simulate the water breakthrough experiments. All partial differential equations were discretized in space by the finite difference method with 60 grid points. The resulting set of ordinary differential equations was solved using the ode15s, a built-in MATLAB ODE solver. This model assumes:

- The gas phase is ideal since the breakthrough experiments are performed at relatively low pressure (≈0.97 bar)
- The system operates under an isothermal condition
- The linear driving force model adequately describes the mass transfer in the solid phase
- Axial dispersion is considered
- Frictional pressure drop is negligible

The mass balance of component *i* in the fluid phase can be written:

$$\frac{\partial c_i}{\partial t} = D_L \frac{\partial^2 c_i}{\partial z^2} - \frac{\partial (v c_i)}{\partial z} - \frac{1-\varepsilon}{\varepsilon} \frac{\partial q_i}{\partial t} \tag{3.1}$$

And the overall mass balance around the packed bed is given by [134]:

$$\frac{\partial v}{\partial z} = -\frac{1}{P}\frac{dP}{dt} - \frac{RT}{P}\frac{1-\varepsilon}{\varepsilon}\sum_{i=1}^{2}\frac{\partial q_i}{\partial t} \tag{3.2}$$

where *i* denotes the component, either 1 for H_2O or 2 for the inert gas; *c* represents the concentration in the fluid phase, *t* and *z* are the time and the axial length, v denotes the interstitial velocity, ε is the bed voidage, *q* is the water loadings in the solid phase, *R* and *T* are the universal gas constant and temperature, and *P* is the total pressure.

When the pressure drop is negligible and the second component (inert gas) does not adsorb $\left(\frac{\partial q_2}{\partial t} = 0\right)$, the Eqn. (3.2) becomes:

$$\frac{\partial v}{\partial z} = -\frac{RT}{P}\frac{1-\varepsilon}{\varepsilon}\frac{\partial q_1}{\partial t} \tag{3.3}$$

To describe the mass transfer rate, the linear driving force (LDF) is defined:

$$\frac{\partial q_i}{\partial t} = k_i (q_i^* - q_i) \tag{3.4}$$

where q^* is the solid phase loading at equilibrium, and *q* is the solid loading at time *t*, *k* represents the mass transfer coefficient. The value of the solid loading at equilibrium with the local fluid phase concentration (q^*) is calculated from a proper water isotherm model.

3.3.2. Mass balance calculations

To calculate the H_2O loading in the solid phase at the equilibrium, a mass balance around the column is written for every adsorption dynamic column breakthrough experiment. Since no reaction occurs, the mass balance can be defined in a molar balance:

$$n_{in} - n_{out} = n_{acc} \tag{3.5}$$

where n_{in} and n_{out} are the total number of moles at the inlet and outlet respectively, n_{acc} is the accumulation. Most of the accumulation is in the adsorbent, and the remaining quantity stays in the gas phase. When the ideal gas law is assumed, this mass balance equation is expressed:

$$\int_0^\infty \left(\frac{Q_{in}P_{avg}y_{i,in}}{RT_{in}}\right)dt - \int_0^\infty \left(\frac{Q_{out}P_{avg}y_{i,out}}{RT_{out}}\right)dt = q_i^* m_{ads} + \frac{P_{avg}y_{i,in}}{RT_{in}}V_b\varepsilon + \frac{P_{avg}y_{i,in}}{RT_{in}}V_d \quad (3.6)$$

where Q_{in} and Q_{out} are the inlet and outlet flow rates, respectively, y_i is the composition of component *i* in the fluid phase, *P* and *T* denote the total pressure and the temperature, m_{ads} is the total weight of the adsorbent, V_b and V_d are the column volume and the total dead volume of the system, respectively. Solving the Eqn. (3.6) will provide the solid equilibrium loading of component *i*. Assuming there is no pressure drop, the average pressure of the column $\left(P_{avg} = \frac{P_{in}+P_{out}}{2}\right)$ can be used in this equation [110]. To obtain a precise solid loading, a complete adsorption breakthrough is required where both the concentration front and the thermal wave have been broken through the column.

3.4. Batch experiment results

3.4.1. Single component water isotherms

Pure water isotherms were measured at various temperatures (22, 30, 40, 50, 60, 80 and 100°C), from 0 bar to 0.027 bar partial pressure by TA Q500 thermogravimetric analyzer. All H_2O equilibrium data are shown in Fig. 3.3. An S-shape isotherm with an inflection point (Type V) was observed in the H_2O isotherms [135, 136], which was clearly seen at lower temperatures (22°C and 30°C). Interestingly, the H_2O loadings on CALF-20 strongly depend on the temperature. At high temperatures, CALF-20 behaves like a hydrophobic material. Only a very small amount of H_2O (< 0.5 mmol/g) was adsorbed at a temperature over 80°C within the experimental pressure range. Furthermore, at a low partial pressure of H_2O (<10% RH, at 22°C), CALF-20 also showed little to no adsorbed amount of H_2O.

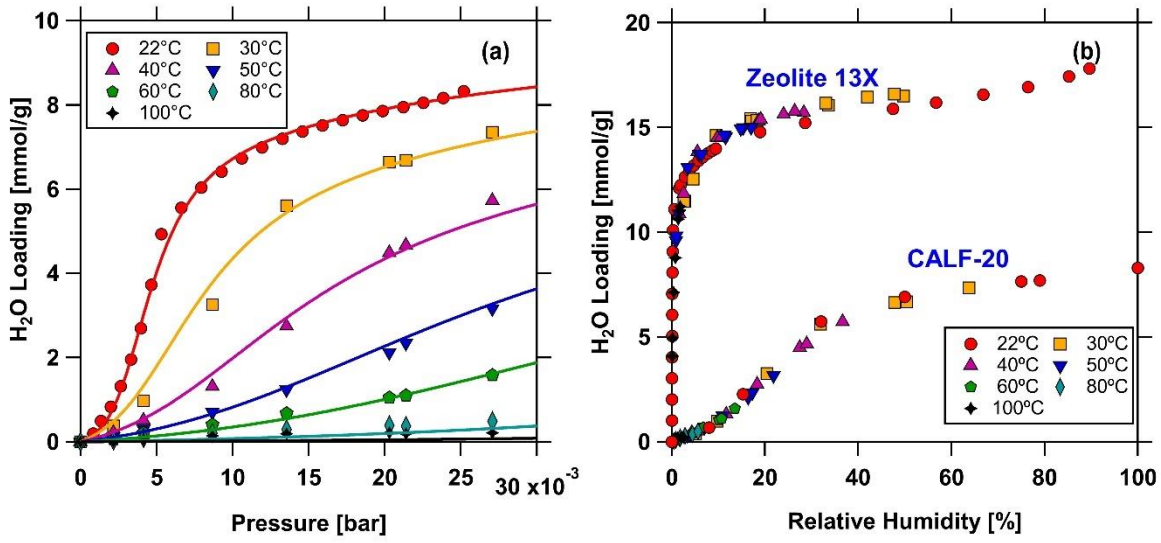

Figure 3.3: H_2O adsorption isotherms of CALF-20. (a) Water isotherms of CALF-20 as a function of pressure at various temperatures. (b) A comparison of H_2O isotherms on CALF-20 and zeolite 13X as a function of relative humidity. Markers represent the experimental data, and solid lines are the fitted isotherms. Zeolite 13X data were obtained from [87].

Figure 3.3b shows the same data as in Fig. 3.3a but is now plotted as a function of RH. Similar to many materials, when the loadings are plotted as a function of RH, all curves collapse on to one another. The corresponding water loading on the current benchmark CO_2 capture material (zeolite 13X) is plotted alongside [87]. A few important observations can be made. First, the saturation capacity of water on CALF-20 is much lower compared to zeolite 13X. Second, while the water isotherm on zeolite 13X is a type I system, that on CALF-20 follows a type V. Finally, it is also noticeable that the water loading of CALF-20 up to ≈ 10% RH is very small. Under corresponding conditions, H_2O loading on zeolite 13X is almost close to saturation. These observations indicate that CALF-20 has superior water tolerance properties compared to zeolite 13X, making it attractive for practical applications.

The isosteric heat of adsorption for water on CALF-20 shown in Fig. 3.4 was calculated by the Clausius-Clapeyron equation using the isotherm data at different temperatures [111]:

$$\left(\frac{\partial \ln p_i}{\partial (1/T)}\right)_{q_i} = -\frac{\Delta H_{iso}}{R} \tag{3.7}$$

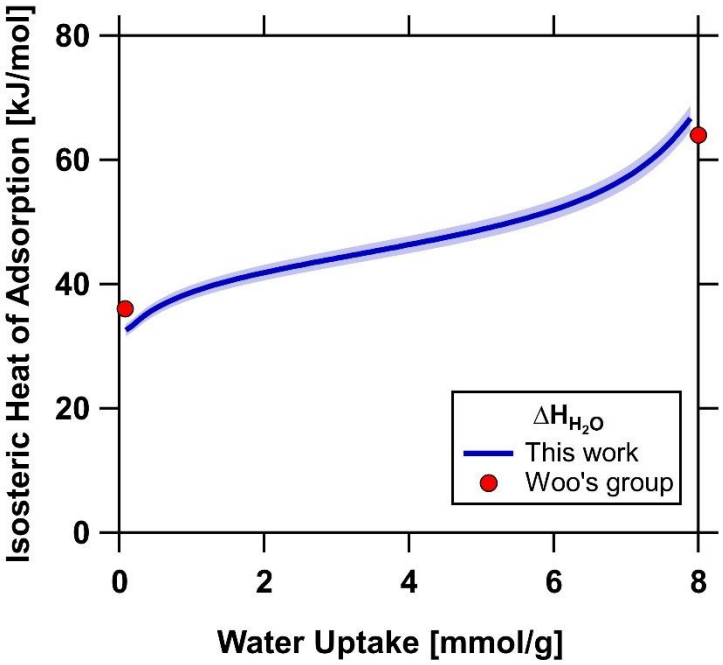

Figure 3.4: Isosteric heat of adsorption for H_2O on CALF-20 calculated from three different temperatures (22°C, 30°C and 40°C) using the Clausius-Clapeyron equation. The solid line is the isosteric heat of adsorption for H_2O on CALF-20 calculated from fitted isotherms in this work. The shading area indicates 3% of uncertainty in the fitting data. The circle markers are the data collected from molecular simulation from Woo's group [137].

Figure 3.4 shows the variation of isosteric heat of adsorption of CALF-20 water solid loading. It is calculated from the fitted isotherm data at 22°C, 30°C and 40°C using the Quadratic-Langmuir model. At lower H_2O loadings, the H_2O heat of adsorption is ≈35 kJ/mol, which implies a low affinity of H_2O onto the adsorbents. When the H_2O loading increases, the isosteric heat of adsorption of H_2O also increases. A linear relationship between the H_2O uptake and heat of adsorption is observed up to 6 mmol/g, and the heat of adsorption at ≈8 mmol/g is ≈65 kJ/mol. A slight discrepancy between the fitted isotherms and the experimental data was observed during the fitting procedure. Thus, a 3% uncertainty was estimated based on the calculation of the isosteric heat of adsorption from two, three and four different temperatures (Fig. 3.4). The magnitude of the isosteric heat of adsorption for water on CALF-20 is comparable with the molecular simulation done by our colleagues at the University of Ottawa (Woo's group) [137]. The isosteric heat of

adsorption on CALF-20 at 1% RH and 100% RH were predicted to be 36 kJ/mol and 64 kJ/mol, respectively [137].

3.4.2. Hysteresis in H_2O isotherms

To study the hysteresis phenomenon, the H_2O adsorption and desorption isotherms of CALF-20 were measured at 22°C, from nearly 0% RH to almost 100% RH using the Micromeritic ASAP 2020 available at the University of Calgary (Shimizu's group). This volumetric system can measure the water loadings at very low relative humidity values. The collected data is compared with the TGA data and showed in Fig. 3.5.

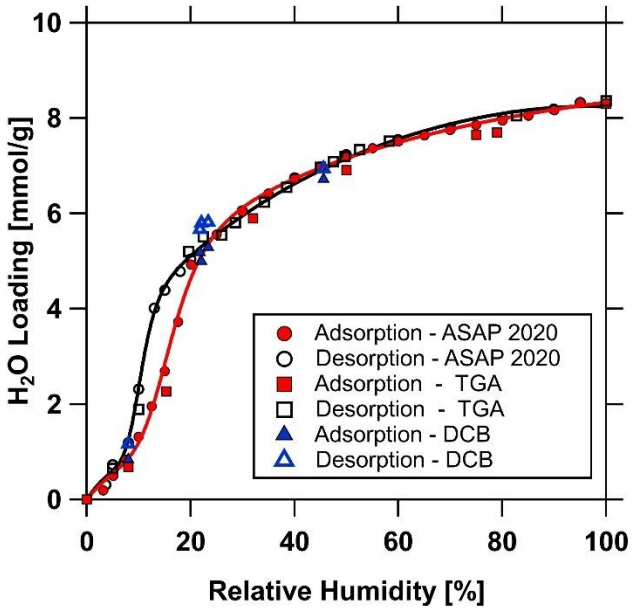

Figure 3.5: H_2O Adsorption and desorption isotherm of CALF-20 at 22°C. Markers represent the experimental data; Squares are the adsorption and desorption data from the TGA measurements; Circles represent the adsorption and desorption data collected from the ASAP 2020; Triangles are the data collected from dynamic column breakthrough experiments. Filled markers are the adsorption data; Hollow markers are the desorption data; Solid lines show the fitted isotherms, the adsorption is red, and the desorption is black

Figure 3.5 shows that the H_2O adsorption and desorption data at 22°C from the TGA and the ASAP 2020 were in good agreement. At low RH (<10% RH), the H_2O adsorption isotherm exhibited an anti-Langmuir type isotherm. An inflection point at ≈15% RH was seen, and the isotherm becomes

favourable beyond that. The desorption isotherm showed a hysteresis loop from 8% RH to 22% RH where the inflection point is located. This phenomenon can be explained because of capillary condensation. In a finite volume system (i.e. porous solids), capillary condensation usually occurs to form a liquid-like dense state. Adsorption hysteresis is usually observed in the water adsorption when there is a delay in the vapour-liquid transition [130, 131, 138].

3.4.3. Descriptions of water adsorption isotherms

Often, the Langmuir isotherm model is used to describe a nonlinear single component isotherm. To describe an isotherm with inflection points, a more complex isotherm model is required [51, 129, 139, 140]. An inflection point on the isotherm can be caused by different reasons such as multi-layer adsorption, phase transitions, capillary condensation phenomenon, change in the sorbent structure [131, 138]. Based on an early work on the lattice statistics by Hill [141], and using a mth order Padé approximant [142], a general form to describe an adsorption phenomenon can be defined:

$$q_i^*(C_i) = q_{sat,i} C_i \frac{\left[\frac{dv_i(C_i)}{dC_i}\right]}{v_i(C_i)} \tag{3.8}$$

$$v_i(C_i) = 1 + \sum_j^m b_{i,j}(C_i)^j \tag{3.9}$$

where q_i^* and $q_{sat,i}$ denote the equilibrium loading and saturation loading of component *i*, *C* is the concentration, *b* is the adsorption equilibrium constant. When m is equal to three, a third-order approximation can be obtained:

$$v_i(C_i) = 1 + b_{i,1}C_i + b_{i,2}(C_i)^2 + b_{i,3}(C_i)^3 \tag{3.10}$$

Replacing the Eqn. (3.10) into the Eqn. (3.8), a well-known Quadratic isotherm model can be written [49]:

$$q_i^*(C_i) = q_{sat,i} \frac{[b_{i,1}C_i + 2b_{i,2}(C_i)^2 + 3b_{i,3}(C_i)^3]}{[1 + b_{i,1}C_i + b_{i,2}(C_i)^2 + b_{i,3}(C_i)^3]} \tag{3.11}$$

To describe the H_2O isotherms on CALF-20, it is assumed there are two main adsorption sites. The first site is described by a third-order Padé approximation, and the second site is written by a first-order Padé approximation. The resulting model is the so-called Quadratic-Langmuir model [132]:

$$q^*_{H_2O}(C_{H_2O}) = q_{sb}\frac{[b_1 C_{H_2O} + 2b_2(C_{H_2O})^2 + 3b_3(C_{H_2O})^3]}{[1 + b_1 C_{H_2O} + b_2(C_{H_2O})^2 + b_3(C_{H_2O})^3]} + q_{sd}\frac{dC_{H_2O}}{1 + dC_{H_2O}} \quad (3.12)$$

where q_{sb} and q_{sd} represent the saturated loadings of *b* site and *d* site, b_1, b_2 and b_3 are the adsorption equilibrium constants of *b* site, and *d* is the adsorption equilibrium constant of *d* site. To describe the temperature dependence, the Van't Hoff type equation is applied to express the adsorption equilibrium constants following:

$$b_1 = b_{0,1}e^{-\Delta U_1/(RT)} \quad (3.13)$$

$$b_2 = b_{0,2}e^{-\Delta U_1/(RT)} \quad (3.14)$$

$$b_3 = b_{0,3}e^{-\Delta U_1/(RT)} \quad (3.15)$$

$$d = d_0 e^{-\Delta U_2/(RT)} \quad (3.16)$$

where ΔU_1 and ΔU_2 are the internal energy of site b and d, respectively. Using the H_2O equilibrium experimental isotherms at various temperatures and from 0 bar to 0.027 bar partial pressure, these parameters (q_{sb}, q_{sd}, $b_{0,1}$, $b_{0,2}$, , $b_{0,3}$, d_0, ΔU_1 and ΔU_2) can be found. A curve fitting tool in MATLAB (*fmincon*) was used to match these experimental isotherm data by minimizing the objective function *J*:

$$J = \sum_{i=T_1}^{T_n}\sum_{j=P_1}^{P_m}\left(q^*_{\text{measured}}(T_i, P_{i,j}) - q^*_{\text{fitted}}(T_i, P_{i,j})\right)^2 \quad (3.17)$$

where the pressure changed from 0 to 0.027 bar, and the temperature varied from 22°C to 100°C. All fitted parameters from the Quadratic-Langmuir model are given in Table 3.1. Fig. 3.3a shows a good agreement between the fitted isotherms and the experimental isotherms at various temperatures. The inflection points on the isotherm at different temperatures were also well captured by this model.

Table 3.1: The Fitted Quadratic-Langmuir isotherm parameters for H_2O on CALF-20

Parameter		H_2O Adsorption	H_2O Desorption
q_{sb}	mmol/g	1.629	0.731
$b_{0,1}$	m^3/mol	-2.685 x 10^{-17}	-5.405 x 10^{-17}
$b_{0,2}$	$(m^3/mol)^2$	1.158 x 10^{-16}	1.825 x 10^{-16}
$b_{0,3}$	$(m^3/mol)^3$	5.374 x 10^{-17}	7.311 x 10^{-16}
ΔU_1	kJ/mol	-97.99	-97.99
q_{sd}	mmol/g	5.781	8.940
d_0	m^3/mol	8.773 x 10^{-12}	7.879 x 10^{-12}
ΔU_2	kJ/mol	-64.72	-64.72

3.4.4. Descriptions of water desorption isotherms with a hysteresis loop

The H_2O adsorption isotherm at 22°C shows a hysteresis loop from 8% RH to 22% RH (Fig. 3.5). Because of the delay in the vapour-liquid transition, the desorption loadings are higher than the adsorption loadings at the same partial pressure within the hysteresis loop. To capture this phenomenon, the desorption isotherm needs to be treated differently. An additional term might be required to add to the adsorption isotherm model to take into account the exceeding loading amounts in the hysteresis loop [129]. To avoid an isotherm model that is too complicated, the desorption isotherm is fitted separately using the same Quadratic-Langmuir isotherm model. In other words, the desorption isotherm is considered as another isotherm.

Since the experimental desorption isotherm was only measured at 22°C, the internal energy ΔU_1 and ΔU_2 were assumed to be the same as the adsorption. The total number of fitted parameters for the desorption isotherm is six parameters: q_{sb}, q_{sd}, $b_{0,1}$, $b_{0,2}$, , $b_{0,3}$, d_0, excluded ΔU_1 and ΔU_2. Using *fmincon* curve fitting tool in MATLAB (Eqn. 3.17), these parameters were determined and shown in Table 3.1. A good agreement between the fitted isotherm and the measured isotherm as indicated in Fig. 3.5.

3.5. Dynamic column breakthrough results

3.5.1 Water adsorption breakthrough experiments

The water adsorption breakthrough experiments were performed at ≈22°C and 0.97 bar total pressure. At 22°C, the H_2O isotherm starts with an anti-Langmuir behaviour following by a Langmuir type isotherm. To characterize the complexity in the shape of the isotherm, three distinct positions on the H_2O adsorption isotherm were chosen, namely 8%, 22% and 45%. These values corresponded to a point below the inflection point (8% RH), a point around the inflection point (22% RH) and one point close to the H_2O saturation loading (45% RH). The detailed experimental parameters are provided in Table 3.2. The breakthrough curves are described in the dimensionless time $\left(\bar{t} = \frac{tv}{L}\right)$.

Table 3.2: List of H_2O breakthrough experiments on CALF-20

Test gas	Q_{in} [ccm]	T [°C]	P [bar]	RH [%]	$q^*_{H_2O-Ads}$ [mmol/g]	$q^*_{H_2O-Des}$ [mmol/g]
H_2O/Air	195	22.2	0.97	8.0	0.839	1.158
H_2O/Air	200	24.2	0.97	22.1	4.997	5.798
H_2O/Air	197	22.7	0.97	21.8	5.179	5.663
H_2O/Air	200	24.1	0.97	23.4	5.287	5.811
H_2O/Air	200	24.3	0.98	45.6	6.716	6.937

A variety of breakthrough shapes were observed as shown in Fig. 3.6a. A simple breakthrough wave was seen at 8% RH which was below the inflection point (≈15% RH). At this RH, the isotherm has a shape of an anti-Langmuir type, which results in a simple wave transition for an adsorption breakthrough experiment [132]. At 22% RH, a simple wave was also seen, which shares similar behaviour to the 8% RH. Afterwards, a shock was observed in the H_2O breakthrough profile, which indicated a transition in the shape of the isotherm. Unlike 8% and 22% RH experiments, a very different H_2O breakthrough profile was observed in the case of 45% RH. It started with a simple wave following by a significant shock until the final state was reached.

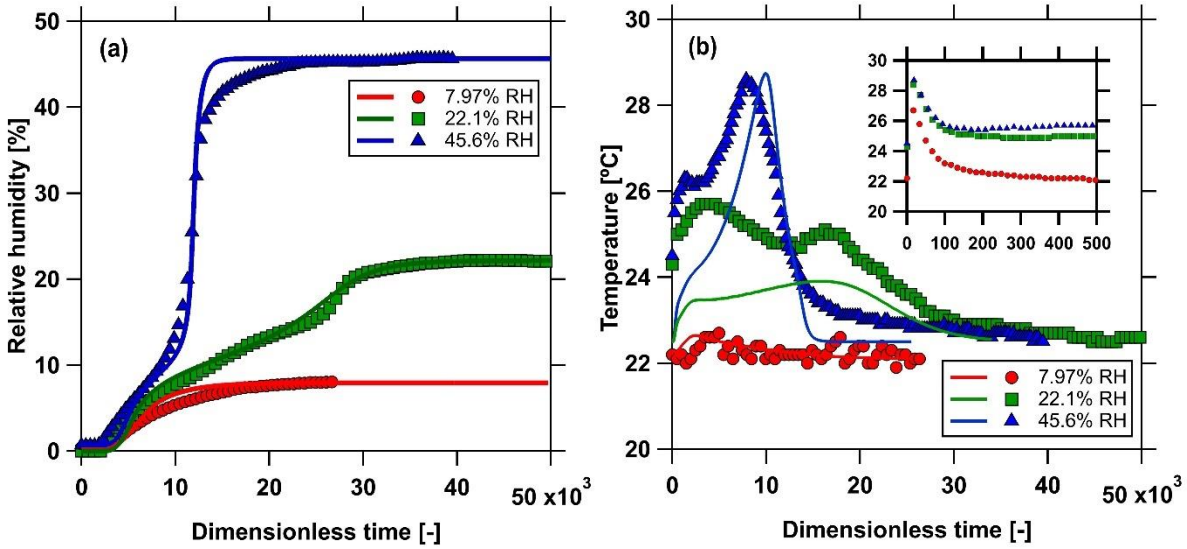

Figure 3.6: H_2O adsorption breakthrough curves of CALF-20 at 22°C and 0.97 bar. (a) Relative humidity curves at different RH values; (b) Temperature histories placed at 1.82 cm from the column outlet; Markers represent experimental data; Solid lines indicate simulation results. The inlay in (b) is the initial thermal breakthrough.

Figure 3.7 explains the relationship between the isotherm shape and the breakthrough curve on CALF-20. The unique behaviours observed in the dynamic column breakthrough curves could be explained based on the shape of the isotherm [132]. Multiple transitions in the DCB curves can be seen depending on the number of inflection points on the isotherms. The inflection points indicate a shift from one particular behaviour between gas molecules and the solid surface to another. The 8% RH is located well below the inflection point (Fig. 3.6a), and the isotherm at this condition exhibited an anti-Langmuir isotherm. Thus, only a simple wave was seen in the breakthrough curve at ≈8% RH. Another scenario was seen in the case of 22% RH, where we observed a transition in the isotherm. The inflection point is located at ≈15% RH, and the isotherm shifts from an anti-Langmuir to a Langmuir isotherm. The transitions of the breakthrough curves can be predicted by drawing characteristics on the isotherm (Fig. 3.7a). The first line is from 0% to ≈8% RH, the unfavourable isotherm, and the second line is from 8% to the final value of the breakthrough experiment, i.e. 22% RH. This is translated into a simple wave and a shock front in the breakthrough curve. The 45% RH position in the isotherm is well above the inflection point, and it almost reaches the saturation loading. Using the same explanation, the first line can be drawn

from 0% to 8% RH, and the second one is from 8% to 45% RH, translated in a wave and a shock front in the breakthrough curve (Fig. 3.6a). These observations were also seen in the water breakthrough experiments on activated carbon, which has a type V isotherm with an inflection point [129].

The 45% RH experiment shows a faster breakthrough than the 22% RH experiment (Fig. 3.6a). This could be explained from the H_2O adsorption isotherm at 22°C in Fig. 3.7a. Typically, the retention time in the adsorption breakthrough profile depends on the initial concentration and the final concentration [132]. The slope connecting two points on the isotherm translates to the retention time. A steeper slope results in a longer retention time [132]. The 22% RH and 45% RH travelled through the same anti-Langmuir region from 0% to 8% RH (Fig3.7a, first line), then they showed different retention time because of the Langmuir region (Fig. 3.7a, second line). A steeper slope can be seen in the 22% RH, which leads to a longer retention time in the breakthrough profile ($\bar{t} \approx 35000$). The 45% RH breakthrough experiment has a smaller slope which results in a shorter retention time ($\bar{t} \approx 25000$).

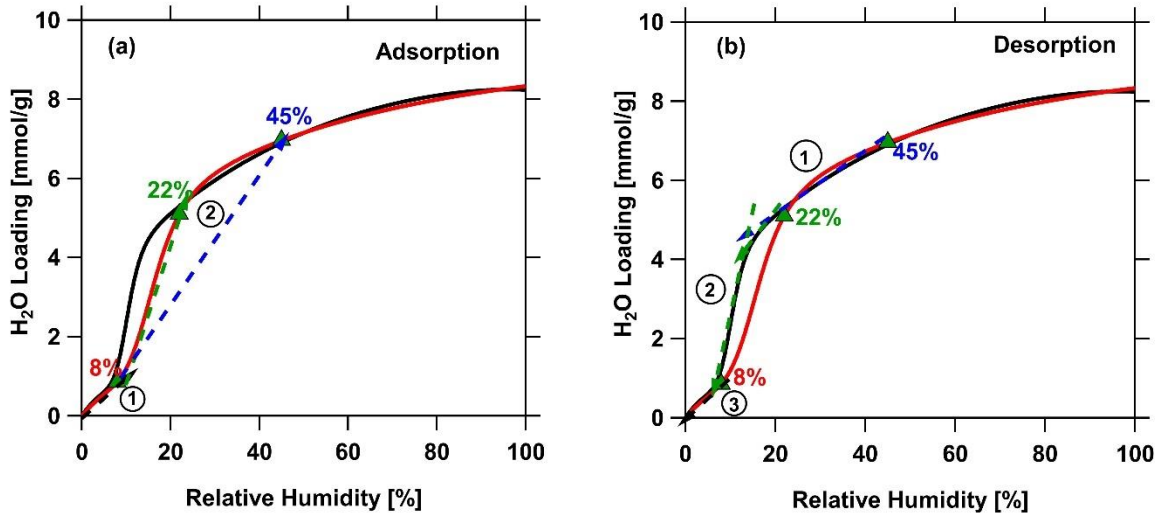

Figure 3.7: The H_2O adsorption (red line) and desorption (black line) isotherm on CALF-20 at 22°C. (a) The transition in the adsorption breakthrough; (b) The transition in the desorption curve

Figure 3.6b shows the adsorption temperature histories of the column. Overall, no significant heat wave was recorded. At 8% RH, the temperature fluctuated around 22.2°C, which means only a little amount of H_2O was adsorbed. In the 22% and 45% RH experiment, two separate temperature

peaks were recorded. The first peak corresponded to the simple wave in the breakthrough profiles. The second peak, which was significant in case of 45% RH (up to ≈28.5°C), indicated the transition to a favorable isotherm behavior in the breakthrough profiles. Note that the time of these temperature peaks match well with the transition in the water breakthrough profiles, which reflects two different behaviour mechanisms of the isotherm. If we look at the very beginning of each experiment, an increase of ≈4°C was seen in the temperature histories (the inlay in Fig. 3.6). This can be attributed to the adsorption of nitrogen and oxygen present in the air, i.e., when they are not competing with water.

3.5.2. Water desorption breakthrough experiments

To perform the H_2O desorption experiments, the column was fully saturated with water at a certain RH value initially. Three desorption experiments at 8%, 22% and 45% RH were examined at ≈22°C and ≈0.97 bar total pressure. Dry air was used as the purge gas in these desorption experiments. The detailed experiment parameters are provided in Table 3.2. The desorption curves and the column temperature histories are shown in Fig. 3.8.

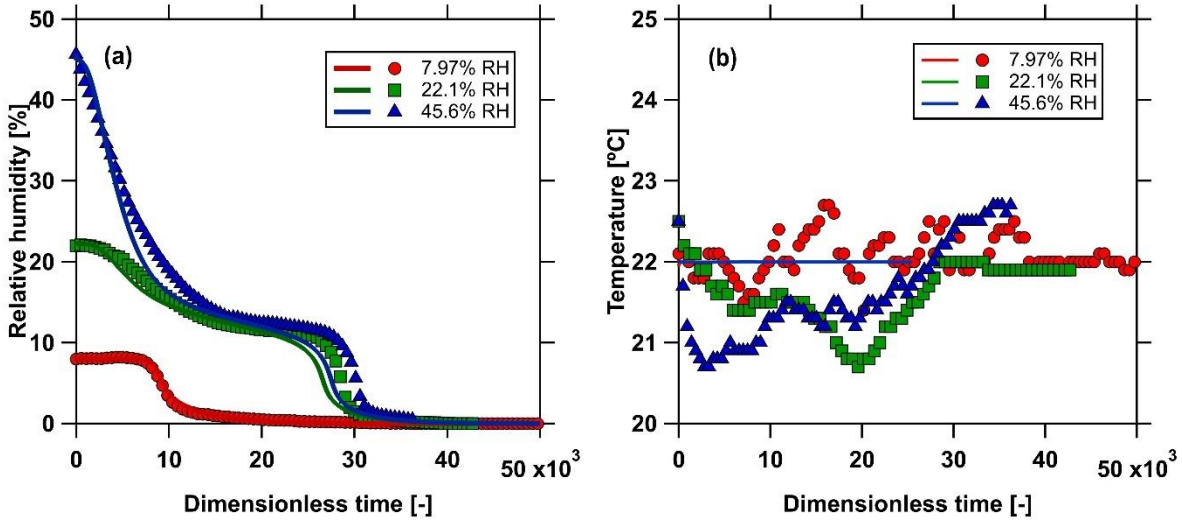

Figure 3.8: H_2O desorption breakthrough curves of CALF-20 at 22°C. (a) Relative humidity curves at the outlet; (b) Temperature histories at 1.82 cm from the column outlet; Markers are the experimental data; Solid lines indicate the simulation data

From the H_2O desorption breakthrough curves, a shock transition was observed in the 8% RH experiment. Multiple transitions are seen for 22% and 45% RH experiments. For both the 22% and 45% curves, the feed eluted for a while and transition is seen until an intermediate state, characterized by a plateau, is reached. Then, a shock transition, similar to the one observed for the 8% RH, is seen. Beyond $\bar{t} \approx 15000$, the curves for 22% and 45% RH nearly overlap. It is worth noting that a $\bar{t} \approx 50000$ corresponds to multiple days of the experiment, making it challenging to exactly reproduce the results. The time required for the completion of the adsorption and desorption experiments is nearly identical. This is a completely different scenario compared to the curve of type I isotherm, where the desorption experiment takes a much longer time compared to the adsorption experiment.

The transitions in the desorption curves can be explained based on the shape of the isotherm. In contrast with the adsorption, the desorption curve is characterized by travelling backward and moving along the tangents of the isotherm (Fig. 3.7b). The 8% RH experiment is well below the inflection point, and it exhibits an unfavourable isotherm. A shock front in the desorption curve represents this type of isotherm [132], which can be seen in Fig. 3.7b. There is no further transition in this case. For the 22% and 45% RH, multiple transitions are observed because of the inflection point at ≈15% RH. Since there is an inflection point, the isotherm could be divided into three small parts corresponding to various transitions in the desorption curves. The first part is from the initial saturation point, either 22% or 45% RH, to ≈15% RH where the inflection point is located. This part is translated into the first wave in the desorption curves (Fig. 3.8a). The second part of the isotherm shows a steep change (Fig. 3.7b), which translates into a shock front in the adsorption curve. In contrast, this transition is translated into a plateau in the desorption curve, which takes the longest time in the entire desorption experiment. Finally, it moves to the third part, where a shock is seen. This transition is very similar to the 8% RH, which represents an anti-Langmuir isotherm. Note that both 22% and 45% RH experiments travel a same path from 15% to 8%, and from 8% to 0% (Fig. 3.7b). Thus, the desorption curves of 22% and 45% RH beyond $\bar{t} \approx 15000$ are nearly overlapped (Fig. 3.8a).

The column temperature histories from the desorption experiments are also indicated in Fig. 3.8b. No significant change in the temperature was seen in the desorption curves. In the 8% RH desorption experiment, the temperature fluctuated around 22°C. A decrease of ≈1.5°C was

observed in the 22% and 45% RH desorption experiments. It is worth noting that the entire experiment took between a couple of days to a week. A slight temperature change in the lab, approximately ±1.0°C, was observed, and the accuracy of the thermocouples is ±1.0°C.

3.5.3. Estimation of water loadings from dynamic column breakthrough experiments

All experiments were performed at ≈22°C and ≈0.97 bar total pressure. The equilibrium water loading at a specific relative humidity can be calculated for each dynamic column breakthrough experiment. The flow rate and the relative humidity at the inlet and outlet of the column were recorded for the entire experiment. The equilibrium H_2O loading for each experiment was calculated using the mass balance calculation described earlier (Eqn. 3.6).

A comparable loading was obtained from the adsorption dynamic column breakthrough experiments. Table 3.2 provides all calculated solid loadings from the DCB experiments. Fig. 3.5 also shows a comparison of water loadings between the volumetric, thermogravimetric analysis and the dynamic column breakthrough experiments at ≈22°C. A slight difference, approximately 3%, was seen between these measurements.

Similarly, the water loadings from the desorption experiments were also calculated by performing the mass balance around the column (Eqn. 3.6). The water capacity estimated from the desorption DCB experiments showed a higher loading compared to the adsorption DCB experiment at the same relative humidity (Table 3.2). This result confirmed the existence of the hysteresis loop from 8% to 22% RH, where a higher loading in the desorption was observed. However, the 45% RH desorption experiment also showed a higher loading than the adsorption DCB, approximately 3%. This slight difference can be caused by the experimental uncertainties since the experiment was run for a couple of days. In general, the water loadings are comparable with the volumetric and thermogravimetric analysis measurements.

3.5.4. Reproducibility of dynamic column breakthrough experiments

The ability to reproduce experimental results is an important aspect to diminish any errors and to obtain high precision results. Since the relative humidity depends on the temperature and pressure, it is challenging to maintain a constant RH value over a long period of time. To confirm the reproducibility of the H_2O DCB experiments, the breakthrough experiment at ≈22% RH was repeated three times and shown in Fig. 3.9.

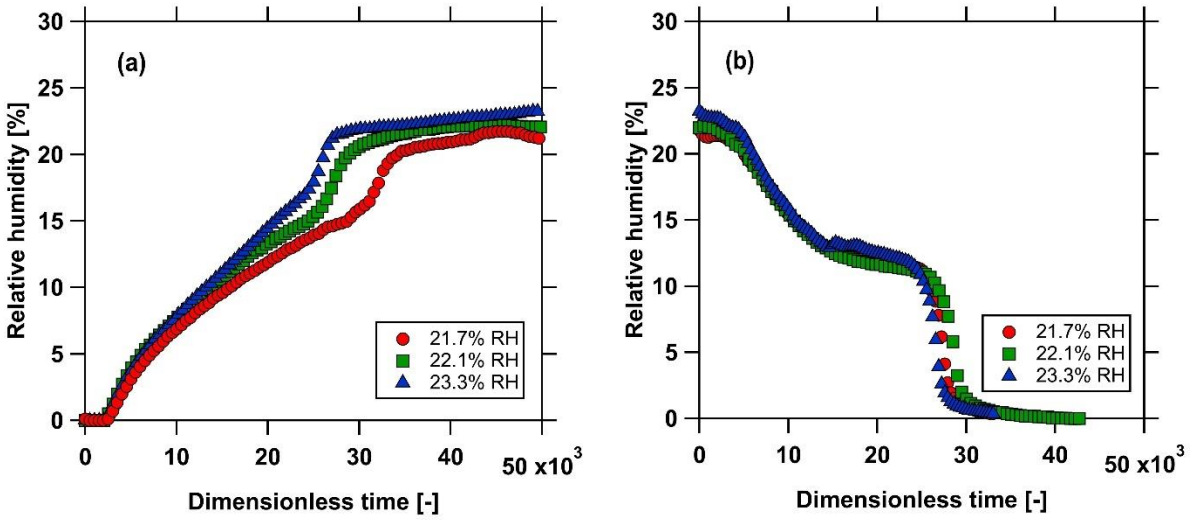

Figure 3.9: Reproducibility of the H_2O DCB experiment at 22% RH. (a) H_2O adsorption breakthrough curves from three experiments; (b) H_2O desorption breakthrough curves from three different experiments

Overall, a similar shape and transition profile was observed in these three experiments. The adsorption breakthrough profiles at ≈22% RH indicated a small deviation since there was a slight difference in the RH of the feed. Note that at 22% RH the final state is very close to the inflection point where the isotherm shifts from an unfavourable isotherm to a favourable one. A small change in the relative humidity could result in a significant difference in the equilibrium solid loading. A very similar observation can be made for the desorption experiments. The transition from a shock and a wave overlapped, indicating high reproducibility of these experiments. The results from the adsorption and desorption DCB experiments at ≈22% RH confirmed the reproducibility of the DCB apparatus and the unique stability of the material.

3.5.5. Water stability of CALF-20

To study the water stability of CALF-20, the water adsorption at 100% RH was performed for more than 30 cycles using a thermogravimetric analyzer. A small amount of CALF-20 (≈70 mg) was used. Each cycle includes a regeneration step at 150°C and an adsorption step at 22°C and 100% RH. Each step was run until the equilibrium was reached.

Figure 3.10 shows the loading of water over time for 30 cycles. The difference between the mass after the adsorption step and the mass after the regeneration step yields the water loading of each

cycle. As can be seen, the water loading is very comparable between cycles, at ≈ 8.0 mmol/g. This value is also in good agreement with the data collected from the volumetric and gravimetric reported earlier (Fig. 3.5). The result suggests that the framework of CALF-20 does not change after exposure to water multiple times.

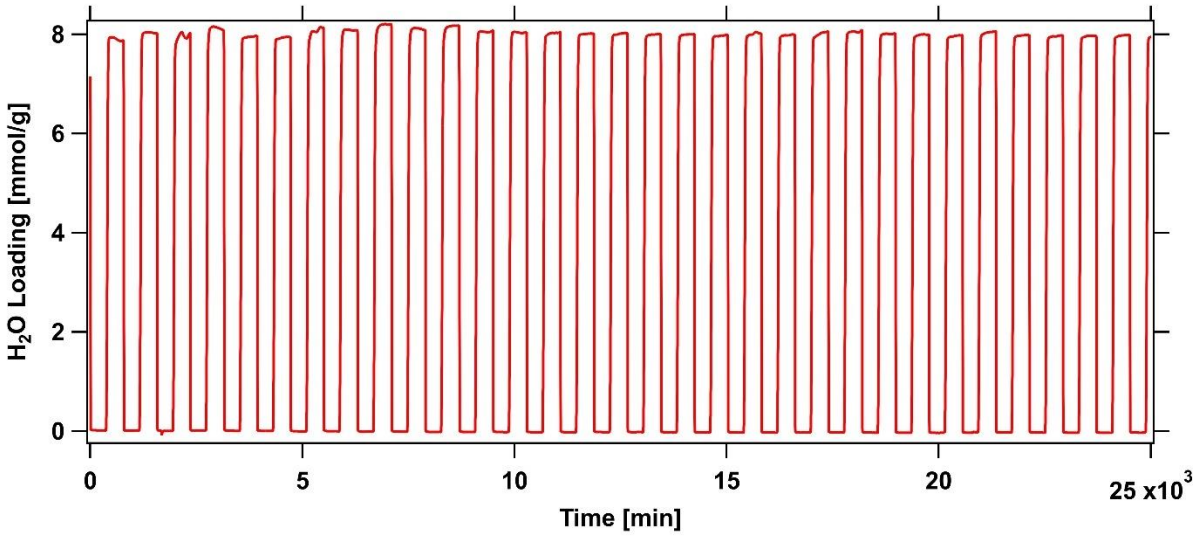

Figure 3.10: The adsorption of water at 100% RH and 22°C over 30 cycles.

3.6. Modelling water dynamic column breakthrough

3.6.1. Column parameter estimation

Since the same column was used to run H_2O dynamic column breakthrough (DCB) experiments, most of the column parameters could be found in the previous study. The adsorbent particle density, the bed voidage, the column diameter, the bed length and the mass of the adsorbents are shown in Table 3.3 To estimate the dispersion coefficient (D_L) and the mass transfer coefficient (k) of H_2O, the adsorption breakthrough experiment data at 22% RH and 22°C were used as a reference to simulate the adsorption breakthrough experiment. This is because at this relative humidity, the DCB profile contains most of the important information from the isotherm. Using the column model discussed earlier, the H_2O adsorption DCB could be predicted. There are two variables: the dispersion coefficient (D_L) and the mass transfer coefficient (k) of H_2O. The objective function (J) is to minimize the difference between the experimental breakthrough profile and the simulating profile.

$$J = \sum_{i=1}^{t_\infty} (C_i^{exp} - C_i^{simul})^2 \quad (3.18)$$

where t_∞ is the total time of the adsorption DCB experiment, C_i^{exp} and C_i^{simul} denote the H_2O concentration in the fluid phase at the column outlet at time *t* from the experiment and the simulation profile data, respectively. The dispersion coefficient (D_L) and the mass transfer coefficient (k) of H_2O were found and are shown in Table 3.3. These values were used to simulate both the adsorption and the desorption dynamic column breakthrough experiments at 8%, 22% and 45% RH.

Table 3.3: H_2O dynamic column breakthrough simulation parameters

Parameter	**Symbol**		**Value**	**Source**
Column length	L	m	0.0786	measured
Inner column diameter	d_{in}	m	0.0282	measured
Outer column diameter	d_{out}	m	0.0318	measured
Bed voidage	ε	-	0.4	measured
Particle void fraction	ϵ_p	-	0.35	assumed
Adsorbent mass	m_{ads}	g	16.7	measured
Universal gas constant	R	m^3 bar mol^{-1} K^{-1}	$8.314x10^{-5}$	standard
Adsorbent particle density	ρ_p	kg m^3	570	measured
H_2O dispersion coefficient	D_L	m^2 s^{-1}	$9.364x10^{-5}$	fitted
H_2O mass transfer coefficient	k	s^{-1}	0.005	fitted

3.6.2. Estimation of the mass transfer coefficient of water

The mass transfer coefficient of water (k) can be fitted using the objective function (Eqn. 3.18) described earlier. This parameter can also be estimated experimentally using the linear driving force (LDF) description:

$$\frac{\partial q_{H_2O}}{\partial t} = k(q^*_{H_2O} - q_{H_2O}) \quad (3.4)$$

The solution of Eqn. (3.4) yields:

$$\bar{q} = q^*_{H_2O}(1 - e^{-kt}) \tag{3.19}$$

To validate the prediction of the LDF model, the adsorption of water was performed at 100% RH and 22°C. The thermogravimetric analysis (TGA) was used to measure the change in solid loading ($\bar{q}$) by time (t). The adsorbent was activated at 150°C for 12 hours using dry air. Instrument air was used as the carrier gas to create a humid feed. The change in weight over time was recorded.

Figure 3.11 shows the average loadings of water over time at 100% RH from the TGA measurement in comparison with the LDF prediction. A steep increase in the water loading was observed in the experiment, then it reached the saturation loading after ≈2000 seconds. The linear driving force (LDF) model was used to predict the evolution of the water loading by time. The Eqn. (3.19) expression was used to predict the water loading, and the mass transfer coefficient of water was obtained from the DCB experiments described ealier (k = *0.005* s^{-1}). A good agreement between the experiment and the model prediction was observed. Thus, the LDF model is sufficient to describe the mass transfer rate of water in the solid.

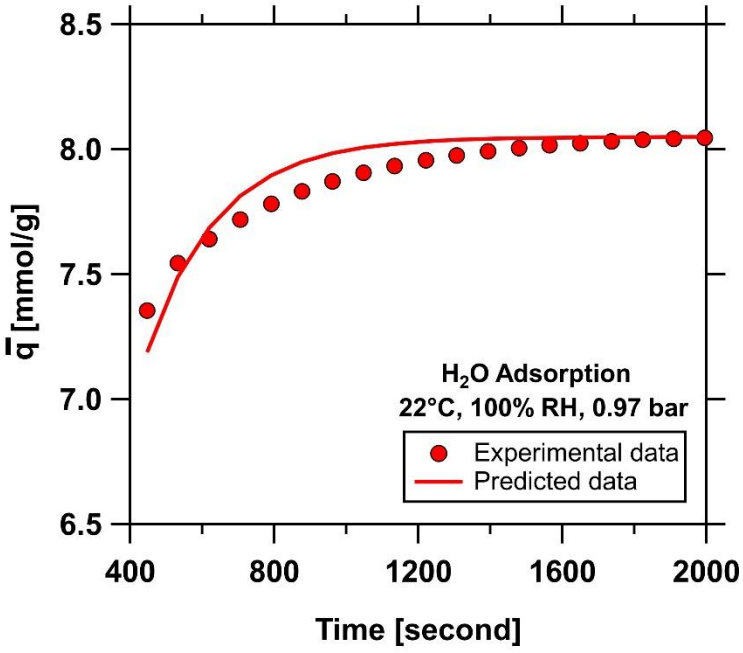

Figure 3.11: A comparison of the water loadings from the experiment and the LDF prediction at 22°C and 100% RH. Markers are the experimental data, and the solid line is the prediction from the LDF model using the fitted mass transfer coefficient from the DCB experiments (k=0.005 s^{-1})

3.6.3. Simulating dynamic column breakthrough using the Quadratic-Langmuir model

The adsorption and the desorption H_2O breakthrough curves were simulated by solving the column model described earlier. The accumulation in the solid phase is defined by the LDF in the Eqn. (3.4). In this case, the equilibrium solid loadings q^* is calculated from the corresponding adsorption/desorption Quadratic-Langmuir isotherm model. Three different relative humidity values were simulated and compared with the experimental curves. Both H_2O dispersion coefficient and mass transfer coefficient are the same for the adsorption and desorption DCB simulations. The results were indicated in Fig. 3.6 and Fig. 3.8.

In the adsorption breakthrough curves (Fig. 3.6), a good agreement between the simulations and the experiments was observed. The model captured most of the main transitions in the H_2O breakthrough profile well. The simple wave in the 8% RH experiment indicated the unfavorable part of the isotherm was well predicted. Similarly, the wave and the small shock in the 22% RH were also captured by this column model. In the 45% RH experiment, there was a small offset in the shock front. The simulation was unable to capture a slight dispersion in the shock front. This could be a limitation of the LDF model since all the resistances in the micropore and macropore were lumped as a single mass transfer coefficient k.

The H_2O concentration desorption curves were also simulated and are shown in Fig. 3.8. In this case, the corresponding desorption isotherm was used to calculate the solid loading. The shock transition in the desorption experiment at 8% RH was predicted well. In the 22% RH and 45% RH, the H_2O desorption curves show a complicated shape with many transitions, including a semi shock followed by a medium transition and a shock. The model well captured the shapes and the transitions in the desorption profiles. However, the simulation was underpredicted for the second shock in the 22% and 45% RH experiments. This can be caused by inadequate information on the hysteresis loop. It is worth noting that the hysteresis loop is located in a very narrow range of relative humidity. Within this range, a slight change in the RH, i.e. a couple of percentages, could lead to a significant solid loading. For instance, the water loadings at 13.7% and 12.0% RH are 4.15 and 3.52 mmol/g, respectively. Finer isotherm data within this range is required to have a better description. In addition, the Quadratic-Langmuir model provides a relatively good isotherm description. But there is still a slight discrepancy between the fitted data and the experimental data. This could attribute to the underpredicted of the desorption of DCB.

The temperature histories of the column from the adsorption and desorption DCB experiments were also predicted. Fig. 3.6b and Fig. 3.8b show the predictions of the temperature curves. In the adsorption experiments, the model could capture the position of the first and second temperatures peak well. It also shows a comparable temperature magnitude. However, a difference of ≈2°C was observed in the first temperature peak. The model tends to underpredict the temperature in this case. It is worth noting that, the temperature of the entire experiments changed a couple of degrees only, approximately 3°C - 5°C, even at 45% RH. It takes days to a week to perform an experiment, and the temperature of the lab slightly changed (±1°C) during the experiment. In the desorption experiments, the temperature barely changed in all experiments, and they almost overlapped. A fluctuation of ±1.5°C was observed in these experiments. The model, on the other hand, shows a nearly constant temperature history for the desorption curves.

3.6.4. Simulating dynamic column breakthrough using discrete equilibrium data

Traditionally, the solid concentration in equilibrium with the fluid concentration is described by fitting the experimental equilibrium data using a continuous function (Fig. 3.12a), i.e. an isotherm model [143]. The function can be simple and straightforward if the solid surface is energetically homogeneous and uniform. However, if the adsorbent surface is energetically heterogeneous, a complex function is required to describe the relationship between the fluid phase and the adsorbed phase. Often, the relationship between a sorbent-sorbate system is unknown. The equilibrium data collected from static measurements can be fitted using any isotherm model (i.e. Langmuir, Sips, Freundlich isotherm models), which returns the best fits. In some cases, the equilibrium isotherms are very complex, which contains various transitions and inflection points. It is challenging to describe the isotherm precisely, and a complicated isotherm model is required to describe the equilibrium data. It is worth noting that different functional forms may yield similar breakthrough curves; the equilibrium data may not be guaranteed to be captured [92, 143].

To avoid complexity in the isotherm model, the discrete equilibrium data concept was presented [143, 144]. Unlike the conventional approach, the equilibrium data can be fitted using any arbitrary functional form, which returns the best fits. The isotherms can also be divided into small parts and fitted separately. This is very helpful, especially when there are many transitions in the isotherms. Afterwards, a set of discrete data points can be generated, which represents the entire isotherm.

These discrete data points can be used for simulation purposes using the interpolation technique without a need of any mathematical function.

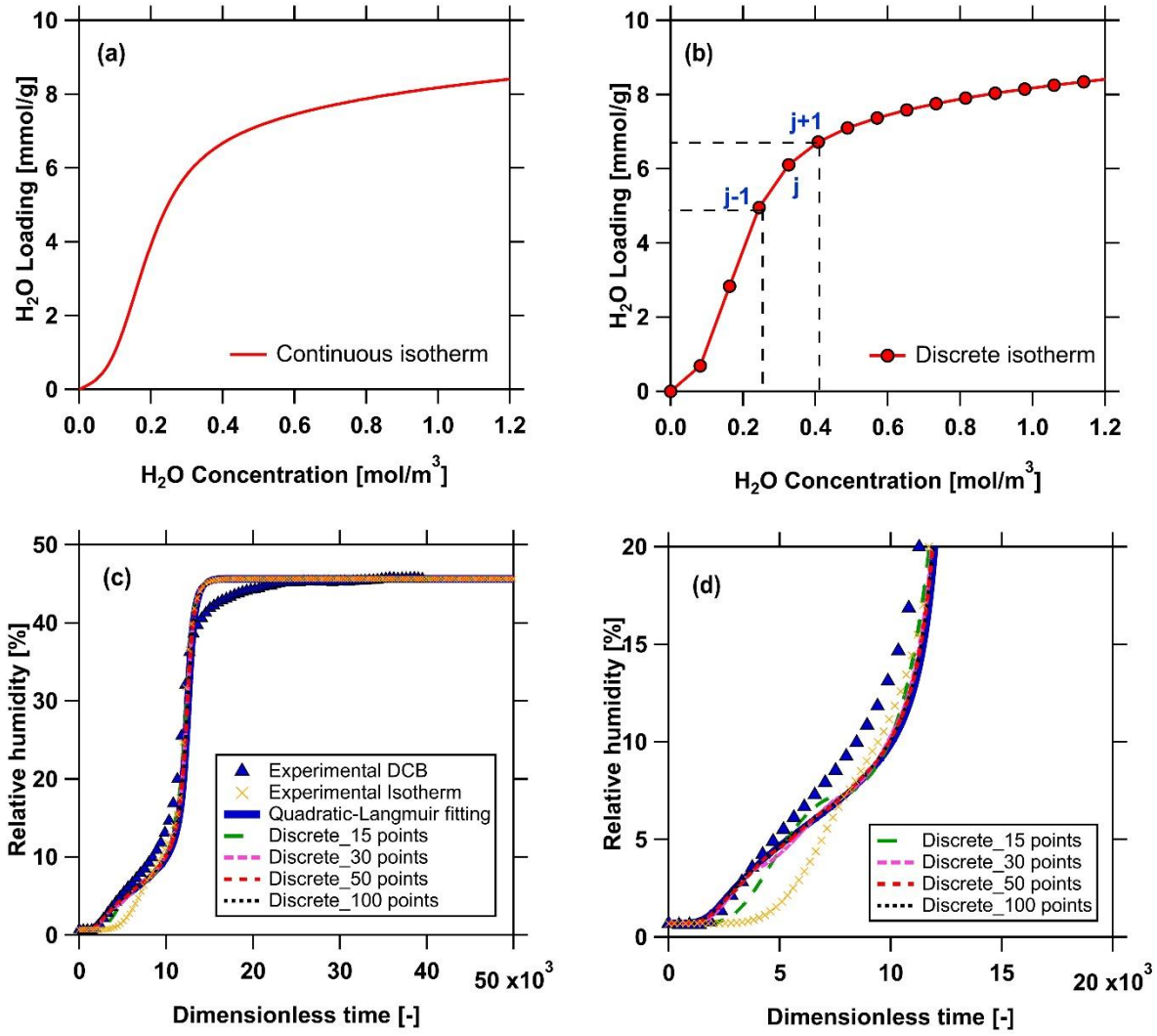

Figure 3.12: The H_2O adsorption breakthrough curves at 45% RH and 22°C using discrete equilibrium data. (a) Continuous water isotherm; (b) Discrete equilibrium isotherm (15 points); (c, d) The adsorption breakthrough curves using different isotherm forms. The triangle markers are the experimental DCB. The cross markers (x) are the DCB curve using the experimental isotherm data. The solid line is the DCB curve using the Quadratic-Langmuir isotherm. The dash lines represent the DCB curve using different discrete data points.

In the discrete equilibrium data approach, the equilibrium relationship between the solid phase concentration and the fluid phase concentration is not limited by an isotherm function.

Alternatively, the isotherm is presented by a set of discrete data points (Fig. 3.12b). At any fluid phase concentration c_j, the corresponding solid loading q_j^* can be estimated by applying linear interpolation from two adjacent discrete points (Fig. 3.10b).

$$q_j^* = \frac{(c_j - c_{j-1})}{(c_{j+1} - c_{j-1})}(q_{j+1}^* - q_{j-1}^*) + q_{j-1}^* \tag{3.20}$$

where $c_{j-1} < c_j < c_{j+1}$ and $q_{j-1}^* < q_j^* < q_{j+1}^*$

To confirm the feasibility of the discrete equilibrium data, the H_2O adsorption breakthrough at 45% RH was simulated using the experimental isotherm, the Quadratic-Langmuir isotherm model and the discrete equilibrium data. The simulated results were compared with the experimental adsorption breakthrough data (Fig. 3.12c). To evaluate the minimum number of discrete points, the breakthrough curve was predicted using 15 to 100 discrete equilibrium points. The Quadratic-Langmuir isotherm model was employed to generate these discrete equilibrium data points. Bearing in mind that the discrete equilibrium data could be obtained from any function forms.

Figure 3.12c shows the water adsorption breakthrough curves at 45% RH and 22°C using different isotherm forms. The adsorption breakthrough curve predicted by the experimental isotherm shows a discrepancy at low relative humidity. A longer breakthrough time was seen using the experimental isotherm data directly. It was not able to capture the anti-Langmuir region due to an extrapolation within this region. Both the Quadratic-Langmuir isotherm model and the discrete equilibrium data returned a similar profile, which is very similar to the experimental breakthrough curve. However, there was an oscillation in the adsorption profile in 15 and 30 discrete points at low relative humidity range (Fig. 3.12d). This is because fewer discrete points lead to less accurate estimations in the equilibrium solid loading. When the number of discrete data increased to 50 and 100 points, the oscillation was negligible, and the predicted profile overlapped with the Quadratic-Langmuir simulation. A minimum of 50 discrete points is required to simulate the H_2O adsorption breakthrough in this case. Briefly, the discrete equilibrium data is capable of simulating the dynamic column breakthrough curve without using any functional isotherm model.

3.7. Conclusions

The H_2O equilibrium data were measured by thermogravimetric analyzer from 0 bar to 0.027 bar partial pressure at 22, 30, 40, 50, 60, 80 and 100°C. The micromeritics ASAP 2020 volumetric system was also applied to measure the H_2O isotherm from 0 bar to 0.027 bar partial pressure at 22°C. The H_2O isotherms showed an inflection point indicating a transition in the shape of the isotherm. At low relative humidity values, the adsorbed amount of H_2O is very small (<0.5 mmol/g), which means CALF-20 exhibits an unfavourable isotherm under these conditions. A hysteresis loop was observed from 8% RH to 22% RH at 22°C indicating a delay in the vapour-liquid transition. The Quadratic-Langmuir model was applied to describe the equilibrium relationship between the solid phase concentration and the fluid phase concentration.

CALF-20 exhibits a type V isotherm with an inflection point. Water barely adsorbs on CALF-20 at low relative humidity (<10% RH). In contrast, zeolite 13X shows a rectangular type I isotherm, where water almost reaches its saturation loading at very low RH (≈1% RH). Furthermore, the saturation loading of water on CALF-20 is relatively small at ≈8.0 mmol/g and 100% RH. By exploiting this unique behaviour, CALF-20 is a potential candidate for humid post-combustion CO_2 capture, where the water does not affect the overall process performance.

Both the adsorption and the desorption breakthrough experiments were performed at 22°C and 0.97 bar total pressure. Three different relative humidity values were chosen: 8%, 22% and 45%, which translates to a point under the inflection point, around the inflection point, and beyond that. The breakthrough curves show many transitions and shapes depending on the feed relative humidity. These unique breakthrough curves reflect complexity in the shape of the isotherm. Depending on the relative humidity of the feed, various breakthrough curves can be observed. The equilibrium loadings of water collected from DCB experiments showed comparable loadings with the volumetric and thermogravimetric measurements. A difference of ≈3% between these measurements was observed. The water breakthrough experiments are also repeatable, which was shown in the case of 22% RH. These results confirmed the accuracy of dynamic column breakthrough measurement, although it took a couple of days to a week to perform.

A column model was developed to simulate the dynamic column breakthrough curves. The H_2O isotherm was described by the Quadratic-Langmuir model and the discrete equilibrium data

concept. The experimental isotherm was also used directly to predict the breakthrough curve at 45% RH. The result shows that using the experimental isotherm returns a good fit, but it could not capture the breakthrough curve at low RH due to the extrapolation. Both the Quadratic-Langmuir model and the discrete equilibrium data show similar breakthrough curves. They are also comparable with the experimental breakthrough curve. However, a small oscillation was observed using 15 to 30 discrete points only. A minimum of 50 discrete points is required to have a better prediction in this case. The result indicated that the discrete equilibrium data approach is adequate to predict a breakthrough curve. This observation is valuable when the isotherm is very complex with many transitions and inflection points. Using a discrete data approach can avoid a complicated isotherm functional form without losing the accuracy in the breakthrough simulation.

4 Characterization Of The CO_2/H_2O Competitive Adsorption On CALF-20

4.1. Introduction

The special report from the Intergovernmental Panel on Climate Change (IPCC) on Global warming of 1.5°C highlighted the importance of carbon capture and storage (CCS) technology to meet the net-zero emission [2]. In CCS technology, the cost of CO_2 separation is responsible for ≈70% of the total cost [145, 146]. Adsorption-based processes offer an opportunity to reduce the CO_2 capture cost due to its low regeneration energy [147, 148]. However, the presence of water in the flue gas makes it very challenging to separate CO_2 since most solid porous materials exhibit a high affinity to water [52, 102, 128]. It is crucial to exploit both material and process perspectives to design a suitable adsorption process to separate CO_2 from a humid environment.

A suitable adsorbent for CO_2 capture is still in need, where water does not have a significant effect on the adsorption of CO_2. The benchmark adsorbent, zeolite 13X, shows a poor performance in the presence of water [87]. A decrease of ≈90% in the competitive CO_2 loading is seen in zeolite 13X at 5% relative humidity (RH) [87]. Furthermore, it is extremely difficult to remove water from zeolite 13X since it exhibits a rectangular type I isotherm with high saturation capacity, at ≈17 mmol/g [52, 87]. Mg-MOF-74 is a potential candidate for CO_2 capture due to its high CO_2 capacity, up to 7.0 mmol/g at 0.15 bar partial pressure [76, 128, 149]. However, the water isotherm on Mg-MOF-74 also exhibits a type I isotherm with a saturation capacity of ≈35 mmol/g [128]. Thus, a significant decrease in CO_2 loading was also observed under wet conditions [122, 150].

Understanding the competition between CO_2 and H_2O is crucial to design an adsorption process for CO_2 capture. Several studies on the effect of water on CO_2 were reported. Levan's group examined the reduction of CO_2 loading on HKUST-1 under different RH values using a volumetric system coupled with gas chromatography (GC). HKUST-1 showed a type II isotherm with two inflection points, and the saturation capacity of water was ≈40 mmol/g [70]. The competitive water loading on HKUST-1 was not affected by the adsorption of CO_2. However, the CO_2 capacity dropped in the presence of water, and it was nearly 0 mmol/g at the relative humidity of 67% RH

[70]. The decrease of CO_2 loading in wet conditions on HKUST-1 and MIL-101(Cr) was also confirmed by Pirngruber *et al*. [151]. The effect of water on CO_2 loading was also studied on MIL-101(Cr) using the dynamic column breakthrough technique. The column was saturated with water vapour initially, then CO_2 was introduced into the column. A zero loading of CO_2 was observed from this study, indicating that water was strongly adsorbed [151].

In this chapter, the competitive adsorption of CO_2 and H_2O on CALF-20 is studied. To quantify the equilibrium loading of each component, both thermogravimetric analyzer (TGA) and binary dynamic column breakthrough (DCB) experiments were performed at various relative humidity values. The total loading of CO_2 and H_2O was obtained from the TGA measurements, while the CO_2+H_2O adsorption DCB experiments gave the competitive water loadings. Then, the competitive CO_2 loading could be calculated by the difference of these two measurements. A bubbler humidifier was used to generate the humid feed at certain RH values. Prior to each experiment, the adsorbent was activated at 150°C. A one-dimensional column model including heat transfer, mass transfer, dispersion and pressure drop was used to simulate the CO_2+H_2O DCB experiments at various RH values. The competitive CO_2 isotherm was described by a modified Langmuir isotherm, while the competitive water isotherm was described by the discrete data points. All breakthrough curves, temperature histories from the experiments and simulations were reported.

4.2. Materials and methods

4.2.1 Materials

Structured CALF-20 was prepared in the Shimizu lab (University of Calgary) by a phase inversion method mentioned in the previous study. The adsorbents have a cylindrical shape with ≈ 1 mm in diameter and ≈ 2 mm in length. The particle density of the adsorbent is estimated at ≈570 kg/m^3. CO_2 was used to perform dynamic column breakthrough experiments. Pure Helium (99.998%) and pure CO_2 (99.998%) was purchased from Praxair Canada Inc.

4.2.2. CO_2/H_2O competitive isotherm measurements

The total loadings of CO_2 and H_2O at various relative humidity (RH) values were measured by thermogravimetric analyzer (TGA). The H_2O competitive loadings at similar relative humidity were calculated from CO_2+H_2O competitive dynamic column breakthrough (DCB) experiments. Since H_2O and CO_2 under certain conditions exhibit strong competition, it was difficult to measure

CO_2 competitive isotherms from DCB experiments. Thus, they were calculated by combining data from the TGA and DCB experiments.

Thermogravimetric analysis

The total CO_2 and H_2O competitive loadings were measured by the Thermogravimetric analyzer TA Q500 (TA Instruments, DE, USA) from 10% RH to 90% RH at ≈22°C and 0.97 bar. A bubbler humidifier described in the previous chapter was used to create different RH streams. This bubbler comprises of a tank filled with deionized water to saturate the feed with water vapour (Fig. 4.1). A specific RH value can be obtained by controlling the ratio between the dry gas and the humid gas, i.e. by suitably controlling the set points of two mass flow controllers (Alicat Scientific, Tuscon, AZ, USA) MFC-1 and MFC-2. By monitoring the relative humidity meter (RH1, SensorPush, Brooklyn, NY, USA) located at the outlet of the humidifier, a stable RH stream can be generated. It is worth noting that in the design available in our laboratory, it took approximately 5-6 hours for the RH value to stabilize. The resulting feed is introduced to the TGA chamber holding ≈70 mg of structured CALF-20. Since the TGA works on the principle of gravimetry, only the total mass of the sample and the adsorbates can be measured. Hence, when CO_2 is used as the carrier gas, only the total amount of CO_2 and H_2O can be measured. The equilibrium is considered to be reached when the change in mass for a period of 120 mins was less than 0.01%. Prior to each experiment, the sample was activated at 150°C for 12 hours. This TGA has a weighing precision of ±0.01% and a sensitivity of 0.1µg.

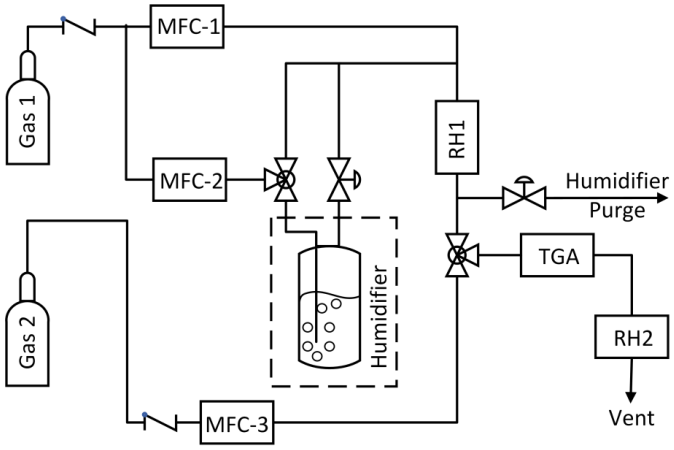

Figure 4.1: The schematic of the thermogravimetric analyzer coupled with the bubbler humidifier. MFC: Mass flow controller; RH: Relative humidity meter; TGA: Thermogravimetric analyzer

Dynamic column breakthrough experiments

The H_2O loadings from the CO_2/H_2O competitive adsorption were measured by performing adsorption dynamic column breakthrough experiments at different RH values. The dynamic column breakthrough (DCB) apparatus, shown in Fig. 4.2, was used. The bubbler humidifier was added to the DCB apparatus to generate a humid stream. A 40 mL stainless steel column (Swagelok 304L-HDF2-40, length 7.86 cm; inner diameter 2.82 cm) packed with 16.7 g structured CALF-20 was used. Two relative humidity meters (SensorPush, Brooklyn, NY, USA) were placed at the inlet and outlet of the column. The pressure at the inlet and the pressure drop of the column were measured by a pressure transducer and a differential pressure gauge (GE Druck, Billerica, MA, USA). A thermocouple (Omega Engineering, Laval, QC, Canada) was placed 1.82 cm from the column outlet to record the column temperature history. A mass spectrometer (Pfeiffer Vacuum OmniStar GSD 320, Asslar, Germany) was placed at the outlet to record the composition of the effluent gas. All data were recorded every second automatically by a Labview data acquisition system. The column was activated at 150°C for 12 hours using helium as a purge gas prior to each experiment.

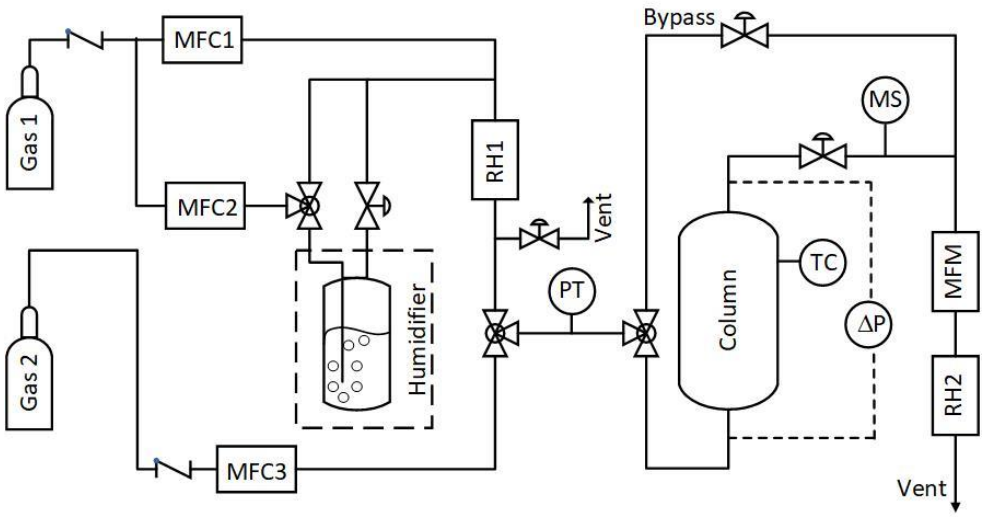

Figure 4.2: The CO_2+H_2O dynamic column breakthrough apparatus. MFC: Mass flow controller; RH: Relative humidity meter; MS: Mass spectrometer; PT: Pressure transducer; TC: Thermocouple; MFM: Mass flow meter

A stable humid stream was prepared prior to starting a DCB experiment. CO_2 was used as a carrier gas to produce a humid gas containing a specific composition of CO_2 and H_2O. Initially, the

column was saturated with Helium. Once the humidifier produced a stable stream of moist gas, the stream was introduced into the column, and the adsorption experiment was initiated at *t=0*. The experiment was kept running until an equilibrium between the solid and the fluid phase was established. A range of RH values, i.e., 13%, 18%, 23%, 32%, 45%, 70% and 88% RH, were chosen for individual DCB experiments. The relative humidity of the feed was measured at the exit of the humidifier (RH1), at ≈22°C. All breakthrough experiments were performed at ≈22°C and 0.97 bar total pressure.

To calibrate the mass flow controllers and mass flow meters, an universal gas flow meter (Agilent Technologies, Santa Clara, CA, USA) was used. A calibration was performed prior to the start of each experiment. The blank response was negligible since the entire adsorption DCB experiment took approximately three days, and the blank response was less than 5 seconds.

4.2.3. Challenges in performing humid dynamic column breakthrough experiment

Water condensation phenomenon, relative humidity measurements and stable humid stream preparations are some typical difficulties addressed in the previous study. Under the presence of CO_2, there are more challenges that need to be mentioned. CO_2 can dissolve in water, so it required a longer time to generate a constant humid stream. The signal of many relative humidity sensors is influenced by the presence of CO_2 [87, 152]. To examine the effect of CO_2 on the RH signal, a humid gas was generated at a fixed ratio of dry and wet flowrates using two different carrier gases. In the first experiment, instrument air was used as a carrier gas, and in the following experiment, the carrier gas was replaced with CO_2. A similar relative humidity signal should be obtained in these two experiments since the pressure and temperature of the system were kept identical and the equipment was operated at low pressures. However, a lower relative humidity value was observed under the presence of CO_2. To correct the RH signal in the CO_2 environment, a calibration curve was built based on performing a set of similar experiments using instrument air and pure CO_2 as carrier gases. The calibration was performed at 22°C and 0.97 bar total pressure provided the following relationship:

$$RH_{CO_2}^{\text{corrected}} = 1.2583 RH_{CO_2}^{\text{measured}} - 2.4031 \quad (4.1)$$

The detailed calibration data is provided in the appendix (Table A4.1). This RH calibration curve is only valid within the scope of the experimental conditions in this study. A suitable RH calibration would need to be constructed if experiments were performed at different conditions.

4.3. Column modelling and simulations

4.3.1. Single-component adsorption isotherm models

The single-component CO_2 and H_2O isotherm models were reported in chapter 2 and chapter 3. The dual-site Langmuir model was applied to describe the single component CO_2 isotherms at different temperatures and pressures.

$$q_i^* = \frac{q_{sb,i} b_i c_i}{(1 + b_i c_i)} + \frac{q_{sd,i} d_i c_i}{(1 + d_i c_i)} \tag{4.2}$$

$$b_i = b_{0,i} e^{-\Delta U_{b,i}/(RT)} \tag{4.3}$$

$$d_i = d_{0,i} e^{-\Delta U_{d,i}/(RT)} \tag{4.4}$$

where *i* denotes CO_2, q_i^* is the solid phase equilibrium loading, c_i is the concentration of CO_2 in the fluid phase, $q_{sb,i}$ and $q_{sd,i}$ are the saturation loadings of site *b* and *d*, $\Delta U_{b,i}$ and $\Delta U_{d,i}$ are the internal energy of site *b* and *d*, respectively. The Quadratic-Langmuir model was used to describe the single component H_2O isotherms at different temperatures, from 0 bar to 0.027 bar partial pressure.

$$q_{H_2O}^*(C_{H_2O}) = q_{sb} \frac{[b_1 C_{H_2O} + 2b_2 (C_{H_2O})^2 + 3b_3 (C_{H_2O})^3]}{[1 + b_1 C_{H_2O} + b_2 (C_{H_2O})^2 + b_3 (C_{H_2O})^3]} + q_{sd} \frac{d C_{H_2O}}{1 + d C_{H_2O}} \tag{4.5}$$

$$b_1 = b_{0,1} e^{-\Delta U_1/(RT)} \tag{4.6}$$

$$b_2 = b_{0,2} e^{-\Delta U_1/(RT)} \tag{4.7}$$

$$b_3 = b_{0,3} e^{-\Delta U_1/(RT)} \tag{4.8}$$

$$d = d_0 e^{-\Delta U_2/(RT)} \tag{4.9}$$

where b_1, b_2 and b_3 are the adsorption equilibrium constants of *b* site, and *d* is the adsorption equilibrium constant of *d* site. All fitted parameters for the CO_2 and H_2O isotherms are shown in the Appendix (Table A4.2 and A4.3).

4.3.2. Ideal adsorbed solution theory

The description of competitive adsorption between two gases on an adsorbent is challenging both for experimental and theoretical perspectives. Myers and Prausnitz proposed the ideal adsorbed solution theory (IAST) to describe competitive adsorption using pure component equilibrium data at a fixed temperature [153]. The IAST assumes:

- The surface of the adsorbent is homogeneous
- The adsorbent is thermodynamically inert
- The available surface area is identical for every solute. It means all adsorbates have the same saturation capacity
- The adsorbed phase is ideal

At equilibrium, the chemical potential in the adsorbed phase equals the chemical potential in the fluid phase. In the case of an ideal adsorbed phase, the analogy with Raoult's law for vapour-liquid equilibria can be applied, resulting:

$$Py_i = P_i^{\circ}(\pi)x_i \tag{4.10}$$

where P is the total pressure, y_i is the composition of the component i in the fluid phase. P_i° is the pressure where the pure component is at the same spreading pressure as the pressure of the mixture, π_i is the spreading pressure and x_i is the mole fraction of the component i in the solid phase.

The mole fraction of the component i onto the solid phase, x_i^*, is defined:

$$x_i^* = \frac{q_i^*}{\sum_{i=1}^{n} q_i^*} \tag{4.11}$$

where n is the total number of components, q_i^* is the equilibrium solid loading of the component i. Note that $\sum_{i=1}^{n} x_i = 1$.

The spreading pressure can be defined as:

$$\frac{\pi_i A}{RT} = \int_0^{P_i^{\circ}} \frac{q_i^{*,0}}{P} dP \tag{4.12}$$

where A is the total surface area of the adsorbent, R is the gas constant, $q_i^{*,0}$ is the equilibrium loading of the pure component. Note that thermodynamic equilibrium requires:

$$\pi_1 = \pi_2 = \cdots = \pi_n = \pi \tag{4.13}$$

The total amount adsorbed, q_{total}, is:

$$\frac{1}{q_{\text{total}}} = \sum_{i=1}^{n} \frac{x_i}{q_i^{*,0}} \tag{4.14}$$

At a known total pressure P and a specific composition in the fluid phase y_i, the competitive equilibrium can be predicted by solving Eqn. (4.10) to Eqn. (4.14) simultaneously. In most cases, it is difficult to solve them analytically, and numerical approaches are preferred.

4.3.3. Detailed column model for dynamic column breakthrough simulations

A one dimensional mathematical model including dispersion, convection, heat transfer and pressure drop in the column was applied to simulate the column dynamics. The following assumptions were made in this model:

- The gas phase is ideal
- There is no composition and temperature gradient in the radial direction, i.e. the column is one dimensional.
- Axial dispersion is included
- Darcy's law is applied to describe the pressure drop
- The ambient temperature is stable
- Local thermal equilibrium between the gas and the solid phase is achieved instantaneously
- The adsorbent's properties are uniform along the column
- The linear driving force (LDF) is adequate to describe the mass transfer in the solid phase

A set of partial differential equations (PDE) and boundary conditions were discretized by using the finite volume method. The column was split into 30 cells, and the obtaining set of ordinary differential equations (ODE) was solved by a MATLAB ODE solver (*ode23s*). All equations in this model were summarized and showed in Table 4.1.

Table 4.1: A summary of equations for the detailed column model

Component mass balance	$\frac{\partial y_i}{\partial t} + \frac{y_i}{P}\frac{\partial P}{\partial t} - \frac{y_i}{T}\frac{\partial T}{\partial t} = D_L \frac{T}{P}\frac{\partial}{\partial z}\left(\frac{P}{T}\frac{\partial y_i}{\partial z}\right) - \frac{T}{P}\frac{\partial}{\partial z}\left(\frac{P y_i}{T} v\right) - \frac{RT}{P}\frac{1-\varepsilon}{\varepsilon}\frac{\partial q_i}{\partial t}$
Total mass balance	$\frac{1}{P}\frac{\partial P}{\partial t} - \frac{1}{T}\frac{\partial T}{\partial t} = -\frac{T}{P}\frac{\partial}{\partial z}\left(\frac{P}{T} v\right) - \frac{RT}{P}\frac{1-\varepsilon}{\varepsilon}\sum_{i=1}^{n_{comp}}\frac{\partial q_i}{\partial t}$
Solid phase mass balance	$\frac{\partial q_i}{\partial t} = k_i(q_i^* - q_i)$
Pressure drop	$-\frac{\partial P}{\partial z} = \frac{150}{4}\frac{1}{r_p^2}\left(\frac{1-\varepsilon}{\varepsilon}\right)^2 \mu v$

Column energy balance	$\left[\frac{1-\varepsilon}{\varepsilon}\left(\rho_s C_{p,s} + C_{p,a}\sum_{i=1}^{n_{comp}} q_i\right)\right]\frac{\partial T}{\partial t} = \frac{K_z}{\varepsilon}\frac{\partial^2 t}{\partial z^2} - \frac{C_{p,g}}{R}\frac{\partial}{\partial z}(vP) - \frac{C_{p,g}}{R}\frac{\partial P}{\partial t} - \frac{1-\varepsilon}{\varepsilon}C_{p,a}T\sum_{i=1}^{n_{comp}}\frac{\partial q_i}{\partial t} + \frac{1-\varepsilon}{\varepsilon}\sum_{i=1}^{n_{comp}}\left((-\Delta H_i)\frac{\partial q_i}{\partial t}\right) - \frac{2h_{in}}{\varepsilon r_{in}}(T - T_w)$
Wall energy balance	$\rho_w C_{p,w}\frac{\partial T_w}{\partial t} = K_w\frac{\partial^2 T_w}{\partial z^2} + \frac{2r_{in}h_{in}}{r_{out}^2 - r_{in}^2}(T - T_w) - \frac{2r_{out}h_{out}}{r_{out}^2 - r_{in}^2}(T_w - T_{amb})$

4.3.4. Mass balance calculations

The competitive H_2O loading in the solid phase at equilibrium is calculated by performing a mass balance around the column. In each dynamic column breakthrough experiment, the H_2O mass balance can be written as:

$$n_{i,in} - n_{i,out} = n_{i,acc} \tag{4.15}$$

where *i* denotes the component, n_{in} and n_{out} are the total number of moles of H_2O at the inlet and outlet, n_{acc} is the accumulation of H_2O in the system. The adsorbents contain most of the accumulation, and the remaining is in the fluid phase. Using the ideal gas law, this equation can be expanded as:

$$\int_0^{t_{ads}}\left(\frac{Q_{in}P_{avg}y_{i,in}}{RT}\right)dt - \int_0^{t_{ads}}\left(\frac{Q_{out}P_{avg}y_{i,out}}{RT}\right)dt = q_i^* m_{ads} + \frac{P_{avg}y_{i,in}}{RT}V_b\varepsilon + \frac{P_{avg}y_{i,in}}{RT}V_d \tag{4.16}$$

where Q, P and T indicate the flowrate, pressure and temperature, respectively, y_{in} and y_{out} are the inlet and outlet compositions in the fluid phase, V_b and V_d represent the bed volume and the dead volume of the system, t_{ads} and m_{ads} are the total adsorption time and the total weight of the adsorbents. The competitive H_2O loading at equilibrium q_i^* can be obtained by solving this equation. When the pressure drop is negligible, the average pressure $\left(P_{avg} = \frac{P_{in}+P_{out}}{2}\right)$ can be

applied. A complete breakthrough experiment is expected to be performed to obtain an accurate loading in the solid phase.

To estimate the competitive CO_2 loadings, the Eqn. (4.16) can be used. Another expression can be written to reflect the competitive CO_2 loading [110]:

$$\int_0^{t_{ads}} \left[1 - \frac{Q_{out} y_{i,out}}{Q_{in} y_{i,in}}\right] dt = \frac{RT}{Q_{in} P_{avg} y_{i,in}} \left[q_i^* m_{ads} + C_{avg} V_b \varepsilon + C_{avg} V_d\right] \tag{4.17}$$

$$C_{avg} = \frac{P_{avg} y_{i,in}}{RT} \tag{4.18}$$

The left-hand side of Eqn. (4.17) is the difference between the area under the CO_2 adsorption curve and the area of the roll-up curve, which yields the accumulation of CO_2 [92]. Note that in the system where one component is much strongly adsorbed than the other, the expression on the left-hand side of the Eqn. (4.17) might result in a negative value, if the accuracies of the composition and flow measurements are not high. This is naturally unrealistic. In the literature, desorption experiments starting from a column saturated with a mixture has been proposed [92]. In this study, a different approach that employs two independent techniques, namely TGA and DCB, is proposed to estimate the competitive loading of CO_2.

4.4. Experimental results and discussions

The following approach consists of two steps, i.) A TGA experiment with the mixture to measure the total loading of CO_2 + H_2O; and ii) A competitive adsorption breakthrough experiment to measure the competitive H_2O loading. The competitive CO_2 loading is then calculated from the difference between the two experiments.

4.4.1. Total equilibrium capacity of CO_2 and H_2O

The total equilibrium loadings of CO_2 and H_2O at different relative humidity values were measured by the thermogravimetric analyzer (TGA) at ≈0.97 bar total pressure and ≈22°C and shown in Fig. 4.3. Both total loadings of the adsorption and the desorption were collected. In the adsorption experiments, the relative humidity was increased from ≈10% to 90% RH. Pure CO_2 was used as the carrier gas (CO_2+H_2O) to create a specific relative humidity. In the desorption experiments, the adsorbents were saturated with the humid CO_2 (CO_2+H_2O) at 100% RH initially.

Then the RH was reduced stepwise to ≈10% RH. The total weight ws recorded after each step, which was the total loading of CO_2 and H_2O at a certain RH. A mass of ≈70 mg structured CALF-20 was used in these measurements. In each experiment, after around 6 hours, the change in the mass was negligible; the equilibrium was reached ($\Delta m < 0.01\%$).

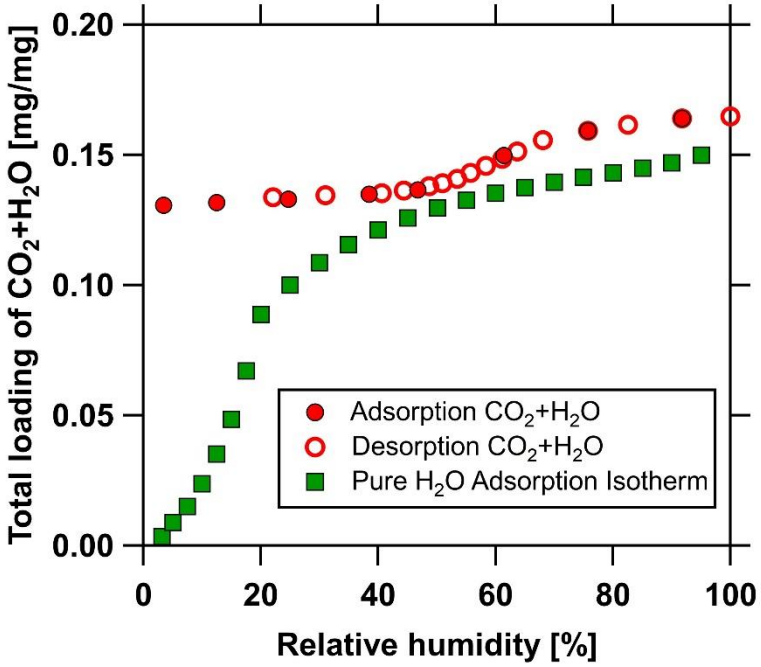

Figure 4.3: Total equilibrium loadings of CO_2 and H_2O at different RH values at 22°C and 0.97 bar total pressure. Filled markers indicate the adsorption data; Hollow markers represent the desorption data; Square markers are the pure H_2O adsorption isotherms for a comparison

Figure 4.3 shows the total equilibrium capacity of CO_2 and H_2O at 22°C and 0.97 total pressure, from 0% to 100% RH. It can be seen that the total loadings of the adsorption and the desorption are similar. This observation confirms the repeatability of the measurement, and there is no hysteresis in the competitive CO_2+H_2O adsorption. At the RH < 40%, the total loadings of CO_2 and H_2O are higher compared with the pure water isotherm (Fig. 4.3), since there is competitive adsorption between CO_2 and H_2O. This noticeable difference in the total loading suggests a large amount of CO_2 is adsorbed, leading to a huge increase in the total weight at low RH. Furthermore, the total loadings are nearly constant, and they are comparable with the pure CO_2 adsorption loading at the same condition ($q^*_{CO_2}$= 0.132 mg/mg at 22°C and 0.97 bar). This result confirms that

CO_2 is strongly adsorbed, and it is a dominant component at the relative humidity smaller than 40% RH.

An interesting behaviour is observed in the total loadings at the RH > 40%. Higher total loading of CO_2 and H_2O is indicated (Fig. 4.3), which was confirmed by both adsorption and desorption measurements. The experiments at 65% and 75% RH were run for more than 48 hours to confirm the equilibrium was established, and there was no artifact in the measurement. The detailed TGA measurement data are provided in the Appendix. There are several possibilities to explain this observation. CO_2 might strongly compete with H_2O even at high RH, and a relatively large amount of CO_2 is adsorbed. On the other hand, if we assume the loading of water is similar to the pure water loading, the remaining increase in the total loading should be attributed to CO_2 adsorption. Note that at high RH, water likely fills the entire pores, which leaves no available site for CO_2 to be adsorbed, unless there is an increase in the pore volume. This explanation needs to be justified by examining the mechanism of H_2O and CO_2 adsorption on CALF-20. The CO_2+H_2O dynamic column breakthrough experiments will provide a better insight after the competitive H_2O loading is estimated. Further discussions on this interesting behaviour is also exploited in the next chapter of this thesis.

4.4.2. Competitive CO_2+H_2O dynamic column breakthrough results

The competitive CO_2+H_2O DCB studies were performed from 13% RH to 90% RH at 22°C and 0.97 bar total pressure. A humidifier was used to create a stable humid stream using CO_2 as the carrier gas. Note that it takes ≈5-6 hours to create a constant humid feed. The adsorbent was activated at 150°C for 12 hours prior to each experiment. It is worth noting that each adsorption breakthrough needs to be run for two to three days to obtain full breakthrough curves of both H_2O and CO_2. An incomplete breakthrough will result in a false competitive loading. Since the experiments take a long time to perform, it is important to pay more attention to every detail and not to disturb the system during the entire experiment, especially the relative humidity of the feed gas. The CO_2 concentration profile and the RH of the effluent were measured by the MS and the RH meter placed at the outlet of the column. The column temperature was also recorded at 1.82 cm from the column outlet. A summary of all the CO_2+H_2O competitive DCB experiments is given in Table 4.2. All results are reported in dimensionless time $\left(\bar{t} = \frac{tv}{L}\right)$.

Table 4.2: List of CO_2+H_2O competitive adsorption DCB experiments

Test gas	Q_{in} [ccm]	T [°C]	P [bar]	RH [%]	$q^*_{H_2O}$ [mmol/g]	$q^*_{CO_2}$ [mmol/g]
CO_2/H_2O	200	22.2	0.97	13	0.137	2.95
CO_2/H_2O	200	22.5	0.97	18	0.22	2.93
CO_2/H_2O	200	24.2	0.97	23	0.45	2.90
CO_2/H_2O	200	22.7	0.97	32	1.07	2.51
CO_2/H_2O	206	23.1	0.97	47	2.08	2.00
CO_2/H_2O	200	23.1	0.97	72	7.85	0.26
CO_2/H_2O	201	22.5	0.97	87	9.01	0.03

In the competitive CO_2 breakthrough profiles (Fig. 4.4), the CO_2 front breaks through at $\bar{t} \approx 47$, in all experiments, and they are overlapped. The breakthrough time is also comparable with pure CO_2 adsorption breakthrough since the feed gas is rich in CO_2. Thus, the entire column is quickly filled with CO_2 in the mixture. This observation is expected since the H_2O front moves slowly through the column. Only a small mole fraction of water exists in the feed, even at 100% RH, i.e. ≈3% at 22°C. Thus, the CO_2 travels in a water-free column, which behaves similarly to the pure CO_2 breakthrough.

A new transition is observed in the CO_2 breakthrough curves when the H_2O front starts to break through the column, at $\bar{t} \approx 400$. The CO_2 "roll-up" effect is seen, and the concentration starts to decrease. This transition is a signature of the competitive adsorption. The CO_2 breakthrough curves from 13% to 47% RH show a gradual decrease in the CO_2 concentration and reach its initial concentration. However, when the relative humidity is higher than 70%, another transition is also observed in the CO_2 breakthrough curves, i.e. 73% and 87% RH. The CO_2 concentration tends to reduce faster in this second transition. This observation could be related to the complexity of the water isotherm, where an inflection point exists.

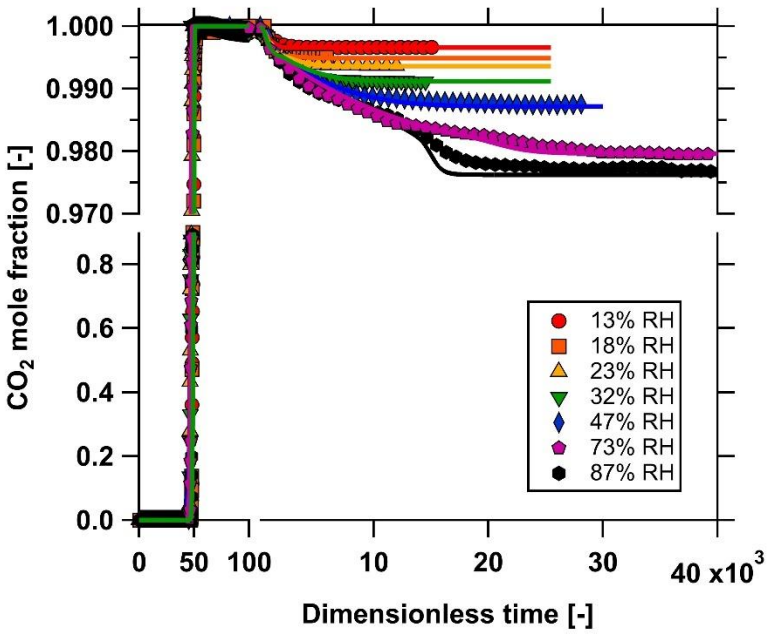

Figure 4.4: The competitive CO_2 breakthrough curves at various RH values at 22°C and 0.97 bar total pressure. Markers represent the experimental data. Solid lines are the simulations using the column model.

Figure 4.5 shows the competitive H_2O breakthrough curves at various RH values and the corresponding temperature histories of the CO_2+H_2O breakthrough experiments. The first impression in the competitive H_2O breakthrough curves is that H_2O broke through very early in all experiments, at $\bar{t} \approx 400$. A simple wave is observed in the breakthrough curves from 13% to 47% RH experiments. Furthermore, a transition in the H_2O breakthrough curves is also seen at 73% and 87% RH. This observation suggests that the competitive H_2O isotherm also contains an inflection point, which results in different behaviours of the breakthrough curves depending on the relative humidity. This transition in the H_2O breakthrough curves also strengthens the second change in the CO_2 breakthrough curves we observed (Fig. 4.4).

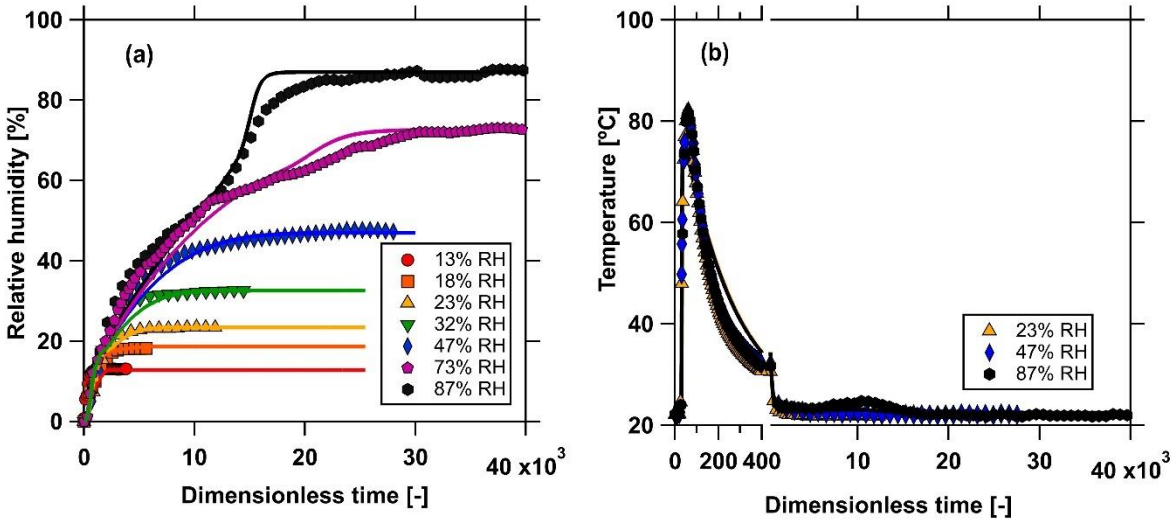

Figure 4.5: Competitive H_2O dynamic column breakthrough curves at various RH values, at 22°C and 0.97 bar total pressure. Markers represent the experimental data; Solid lines are the simulations; (a) Water adsorption breakthrough curves at different RH values; (b) Column temperature history at 1.82 cm from the column outlet

The temperature histories show a peak at $\bar{t} \approx 40$, which corresponds to the heat generated by the CO_2 adsorption. The temperature quickly increases and reaches ≈80°C (Fig. 4.5b). All competitive breakthrough experiments show similar evolutions in the temperature curves (Fig. 4.5b). After reaching the maximum value, the temperature starts to decay, and there is not any significant change later, except a small bump at $\bar{t} \approx 10000$ at 87% RH. This small change in the temperature is caused by the H_2O adsorption at high relative humidity, where the transition in the H_2O breakthrough curves occurs. This observation suggests that a non-negligible amount of water is adsorbed, resulting in a higher temperature.

Figure 4.6 shows an interesting comparison of the single and competitive H_2O breakthrough curves at 13% and 47% RH. The square markers represent the single-component H_2O breakthrough experiments using instrument air as the carrier gas. The circle markers indicate the competitive H_2O breakthrough profiles using CO_2 as the carrier gas. At 13% RH, the H_2O broke through very early in the binary CO_2+H_2O breakthrough experiment, at $\bar{t} \approx 300$. In contrast, it took $\bar{t} \approx 5000$ for water to break through in the single H_2O breakthrough experiment at the same RH. Similarly, at 47% RH, the competitive H_2O experiment broke through earlier than the single H_2O experiment. This observation suggests that the water adsorption is strongly affected by the adsorption of CO_2

at low to intermediate RH. The area behind the breakthrough curves is considered as the accumulated water loading. It is clearly seen that the area behind the competitive water breakthrough curve is significantly reduced compared to the pure water breakthrough curve (Fig. 4.6). Thus, much lower water loading would be expected in the presence of CO_2.

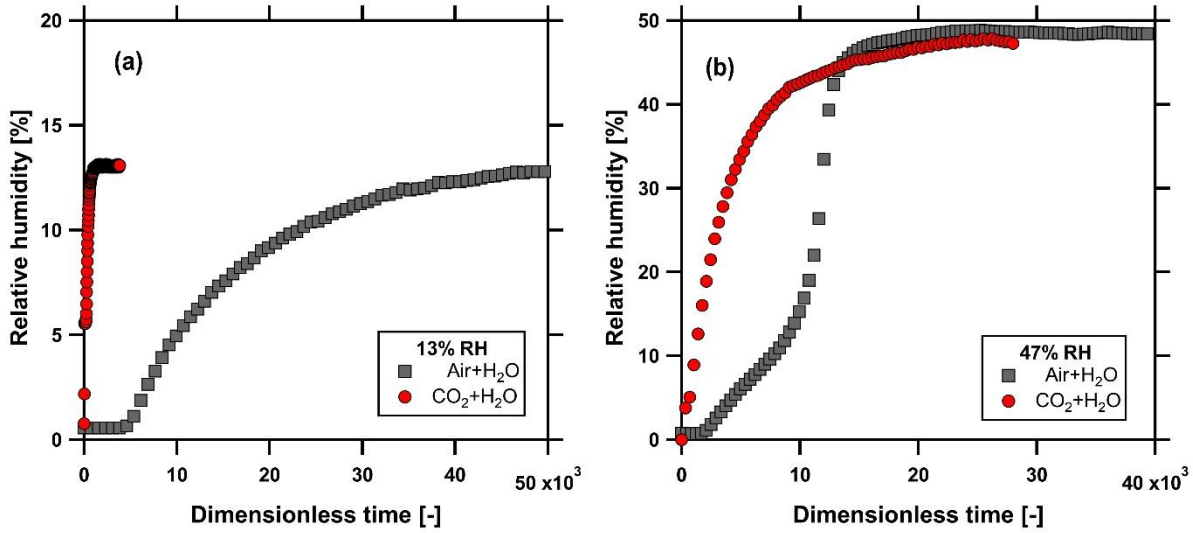

Figure 4.6: A comparison of single and competitive H_2O breakthrough curves. (a) 13% RH and (b) 47% RH. Squares indicate the single H_2O breakthrough curves using air as the carrier gas; Circles show the competitive H_2O breakthrough curves using CO_2 as the carrier gas. The experiments were performed at ≈22°C and 0.97 bar total pressure.

Furthermore, a simple wave is observed in the binary CO_2+H_2O breakthrough curve at 47% RH, instead of a wave followed by a shock front in the single-compoent H_2O breakthrough experiment (Fig. 4.6b). Note that the pure water isotherm contains an inflection point at ≈15% RH (Fig. 4.3). Hence, a transition in the pure water breakthrough curve is seen beyond 15% RH, and it nearly reaches the saturation loading at 47% RH. The competitive CO_2+H_2O breakthrough at 47% RH, on the other hand, shows a completely different behaviour. The water breakthrough curve in this case only shows a simple wave, and the breakthrough time is much shorter (Fig. 4.6b). It is worth noting that an unfavourable isotherm results in a wave in the breakthrough curve. This observation implies there is strong competitive adsorption between CO_2 and H_2O. Under the presence of CO_2, the H_2O tends to break through significantly earlier, which suggests a dramatic reduction of the H_2O loadings. In the case of zeolite 13X, there is no difference in the single and binary water breakthrough profiles, and the H_2O loadings are similar with/without the presence of CO_2 [87].

This behaviour is unique, and it supports the fact that CO_2 is still strongly adsorbed on CALF-20 at low to intermediate relative humidity (RH<47%).

At high relative humidity (RH>70%), the competitive H_2O breakthrough curves show a transition in their breakthrough curves (Fig. 4.5a). This means an inflection point still exists in the competitive H_2O isotherm, and it changes from an unfavourable to a favourable type of isotherm. Beyond the inflection point, the adsorption of H_2O becomes significant, and it hinders the CO_2 adsorption. The result from the pure H_2O breakthrough study showed the transition in the water breakthrough curve at 22% RH. In the competitive CO_2+H_2O breakthrough, this transition is not observed until the relative humidity is higher than 70% RH. Thus, the inflection point in the competitive H_2O isotherm must be shifted to higher relative humidity. By exploiting this unique behaviour, a better CO_2 adsorption process can be designed where water only has little effect on the adsorption of CO_2 under wet conditions.

4.4.2. Estimation of the competitive CO_2+H_2O isotherm

To estimate the competitive loading of H_2O, a series of CO_2+H_2O competitive dynamic column breakthrough experiments were performed at various relative humidity at 22°C and 0.97 bar total pressure. The competitive water loadings were calculated by performing a mass balance around the column using the Eqn. (4.16). The total loadings of CO_2 and H_2O at similar relative humidity were also measured by thermogravimetry analysis. The competitive CO_2 loadings were obtained by the difference of the total loading and the competitive water loading at various relative humidity. The CO_2 capacity can also be estimated directly from the DCB experiments using the Eqn. (4.17), but it is challenging in a binary system where the heavy component is strongly adsorbed, and the uncertainties built-up in a long experiment, i.e. up to three days.

Figure 4.7 shows the competitive isotherms of CO_2 and H_2O at 22°C and 0.97 total pressure. An interesting observation is seen in the competitive CO_2 loading. At low relative humidity (RH<20%), the CO_2 capacity barely changes while there is only a small amount of H_2O adsorbed. This observation is consistent with the previous competitive breakthrough curves. The binary water breakthrough curve at 13% (Fig. 4.6a) also confirmed a significant loss of H_2O capacity under the presence of CO_2. These results strengthen that water does not affect the adsorption of CO_2 when the relative humidity is smaller than 20%. From 20% to 40% RH, the CO_2 capacity slightly decreases. This is the region where there is a competition between CO_2 and H_2O. It is

worth noting that the competitive CO_2 loading on CALF-20 is still relatively high (>2.00 mol/g) at low to intermediate relative humidity (RH<40%). In contrast, a significant loss of CO_2 capacity was observed in Zeolite 13X, even at 1% RH [87]. From 50% to 70% RH, the CO_2 capacity drops faster. This is the region where the adsorption of water becomes stronger, and it has a great impact on the adsorption of CO_2. When the RH is beyond 70%, the competitive CO_2 loading is very small. This result is in agreement with the competitive breakthrough curves where a transition in the water breakthrough curves was observed. Beyond 70% RH, water is strongly adsorbed, resulting in a significant drop in CO_2 loadings.

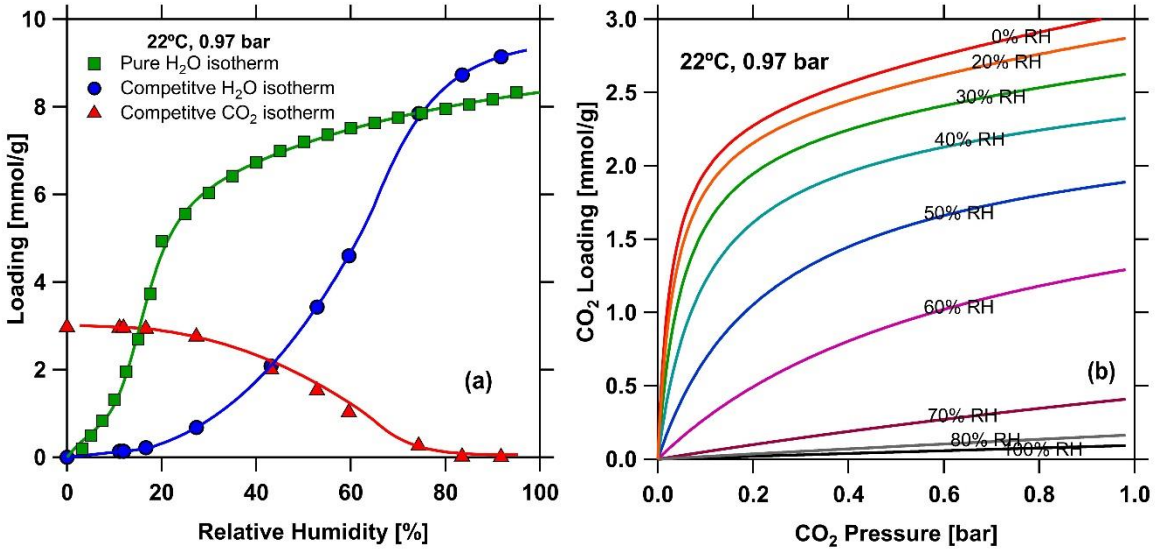

Figure 4.7: Competitive CO_2+H_2O equilibrium loadings on CALF-20 at 22°C and 0.97 bar collected from TGA and DCB experiments. (a) The competitive loading of CO_2 and H_2O at various relative humidity. Markers are the experimental data from binary dynamic column breakthrough experiments and thermogravimetry analysis. Solid lines are the fitted competitive isotherms. Triangle markers are the competitive CO_2 loadings, and circles markers are the competitive H_2O loading. The pure water isotherm at 22°C is shown for comparison. (b) The effect of water on the CO_2 capacity from the modified dual-site Langmuir isotherm simulations at various RH values.

A type V isotherm with an inflection point is still observed in the competitive H_2O isotherm. In the pure H_2O isotherm, at 22°C and 0.97 bar, the inflection point locates at ≈15% RH, then it quickly reaches the saturation loading (Fig. 4.7a). In the binary CO_2+H_2O isotherm, the inflection point shifts further to the high relative humidity at ≈65% RH. The isotherm changes from an anti-

Langmuir to a Langmuir type isotherm at this inflection point. This unique transition is clearly seen in the breakthrough curves. The binary CO_2+H_2O breakthrough at 47% RH (Fig. 4.6b) only shows a wave instead of a wave and a shock front in the pure H_2O breakthrough. This result reinforces that water has not passed the inflection point yet, and it still exhibits an unfavourable isotherm resulting in a simple wave in the breakthrough curve. At high RH, a wave and a shock front were observed in the binary CO_2+H_2O breakthrough, i.e. at 73% RH and 87% RH (Fig. 4.5a). At this point, water has travelled through the inflection point, and it exhibits a favourable isotherm, where water is strongly adsorbed. As a result, competitive H_2O loading is quickly increased (Fig. 4.7a).

Figure 4.7a also indicates another interesting observation. A higher water loading is seen in the competitive water capacity compared to the pure H_2O isotherm at RH>70%. The TGA experiments have shown that the total loading of CO_2 and H_2O is higher than the pure H_2O isotherm at high RH (Fig. 4.3). However, it is inadequate to decide whether the extra loading is contributed by H_2O or CO_2 based on the TGA data only. The competitive DCB experiments confirmed that CALF-20 mostly adsorbed H_2O beyond 70% RH, since only a small amount of CO_2 was recorded. This is interesting since the H_2O loadings are increased in comparison with the pure H_2O, i.e. ≈10%. If CALF-20 only adsorbed H_2O at high relative humidity, the H_2O capacity would be similar to the pure H_2O isotherm eventually. Unless the structure of CALF-20 is changed, how they accommodate more water molecules in their channels, which resulting in higher loadings. This question will be answered in the next chapter.

4.5. Modelling the competition of CO_2 and H_2O

4.5.1. Description of the competitive CO_2/H_2O isotherm

The ideal adsorbed solution theory (IAST) was applied to predict the competitive CO_2+H_2O capacity by solving Eqn. (4.10) to (4.14) numerically. In this model, it is assumed that the adsorbed phase is ideal, and all gases have equal saturation loadings. The single-component isotherms of CO_2 and H_2O were used to describe the binary adsorption capacity. Fig. 4.8 shows the prediction of competitive CO_2/H_2O equilibrium loadings from the IAST model. At the RH < 40%, the IAST model predicts the competitive CO_2 loadings well. However, an over prediction of the CO_2 capacity is seen when the relative humidity is higher than 40%. The IAST model is unable to

predict the competitive H_2O loadings. An over-prediction in the H_2O loadings is indicated at RH <55%, and it is under predicted the water loadings when the RH is higher than 55% (Fig. 4.8).

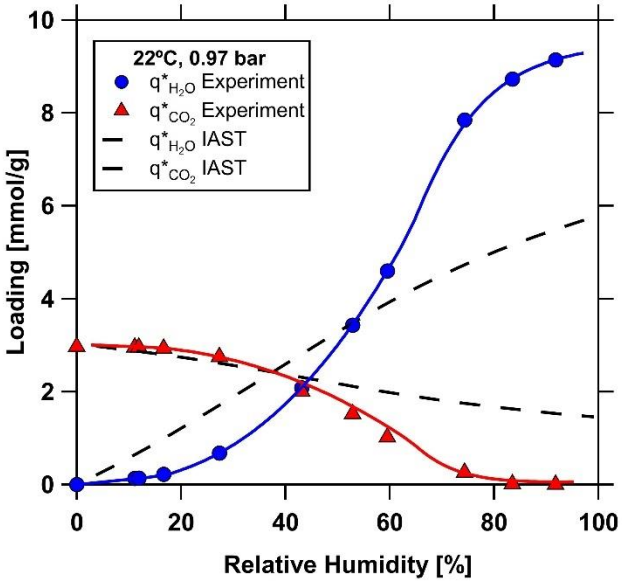

Figure 4.8: Description of the competitive CO_2/H_2O isotherm at 22°C and 0.97 bar. Markers are the experimental data. Solid lines are the fitting isotherms from the modified dual-site Langmuir. Dashed lines are the ideal adsorbed solution theory (IAST) predictions.

Due to a complex, competitive adsorption behaviour, an empirical model was developed to describe the binary CO_2+H_2O adsorption. Hefti and Mazzotti introduced a modified Sips model to describe the competition of CO_2 and H_2O on zeolite 13X [88]. Wilkins *et al*. proposed a modification to the Langmuir model to account for the impact of water on the CO_2 loadings on zeolite 13X [87]. A similar approach was used in this study to express the competitive CO_2 loadings on CALF-20. The pure CO_2 isotherm expression was adjusted to reflect the impact of water. Two more parameters, called λ_1 and λ_2, were added to describe a reduction of the CO_2 loadings when the water loadings increase. The resulting model is known as the modified dual-site Langmuir:

$$q^*_{CO_2} = \frac{1}{1+\lambda_1 q^*_{H_2O}}\left[\frac{q_{sb,CO_2} b_{CO_2} C_{CO_2}}{(1+b_{CO_2} C_{CO_2})} + \frac{q_{sd,CO_2} d_{CO_2} C_{CO_2}}{(1+d_{CO_2} C_{CO_2})}\right] \quad (4.19)$$

$$b_{CO_2} = b_{0,CO_2} e^{-\frac{\Delta U_b}{RT} - \lambda_2 q^*_{H_2O}} \tag{4.20}$$

$$d_{CO_2} = d_{0,CO_2} e^{-\frac{\Delta U_d}{RT} - \lambda_2 q^*_{H_2O}} \tag{4.21}$$

In this modified isotherm, the CO_2 loading is described as a function of the water loading, temperature and the concentration of CO_2. The saturation loadings q_{sb,CO_2} and q_{sd,CO_2} of CO_2 are diminished by a factor of $(1 + \lambda_1 q^*_{H_2O})$, where $q^*_{H_2O}$ is the competitive H_2O capacity at a specific relative humidity. The adsorption equilibrium constants b_{CO_2} and d_{CO_2} are also adjusted by another factor of $e^{-\lambda_2 q^*_{H_2O}}$. When the water loading increases, the CO_2 isotherms turn into a linear isotherm (Fig. 4.7b) because of the latter factor. If the water is not present ($q^*_{H_2O} = 0$), the Eqn. (4.19) becomes the pure CO_2 isotherm model. In comparison with the conventional competitive dual-site Langmuir model, the term $b_{H_2O} c_{H_2O}$ in the denominator is removed. λ_1 and λ_2 were fitted using the obtained CO_2 competitive loadings from the binary DCB and TGA experiments. The competitive CO_2 isotherm parameters are given in the Table 4.3.

Table 4.3: The modified Langmuir isotherm parameters to describe the competitive CO_2 loading on CALF-20 at 22°C and 0.97 bar total pressure

Parameter		**CO_2**
q_{sb}	[mmol/g]	2.387
b_0	[m^3/mol]	5.519 x 10^{-7}
ΔU_b	[kJ/mol]	-35.06
q_{sd}	[mmol/g]	3.271
d_0	[m^3/mol]	5.187 x 10^{-8}
ΔU_d	[kJ/mol]	-28.95
λ_1	[g/mmol]	0.027
λ_2	[g/mmol]	0.703

The competitive H_2O isotherm at 22°C was described using the Quadratic-Langmuir model mentioned in the previous study. All isotherm parameters were fitted again to match the

competitive H_2O loadings. Since we collected the binary CO_2+H_2O data at 22°C (T = 295.15K), these parameters only presented the competitive H_2O loadings at this temperature.

$$q^*_{H_2O} = q_{sb,H_2O}\frac{[b_1(C_{H_2O})^1 + 2b_2(C_{H_2O})^2 + 3b_3(C_{H_2O})^3]}{[1 + b_1(C_{H_2O})^1 + b_2(C_{H_2O})^2 + b_3(C_{H_2O})^3]} + q_{sd,H_2O}\frac{dC_{H_2O}}{1 + dC_{H_2O}} \quad (4.22)$$

$$b_i = b_{0,i}e^{-\Delta U_1/(RT)} \quad (4.23)$$

$$d = d_0 e^{-\Delta U_2/(RT)} \quad (4.24)$$

Table 4.4: The Quadratic-Langmuir adsorption isotherm parameters for H_2O on CALF-20

Parameter		Pure H_2O	Competitive H_2O
q_{sb}	[mmol/g]	1.629	1.795
$b_{0,1}$	[m^3/mol]	-2.685 x 10^{-17}	-5.937 x 10^{-15}
$b_{0,2}$	[(m^3/mol)^2]	1.158 x 10^{-16}	1.013 x 10^{-15}
$b_{0,3}$	[(m^3/mol)^3]	5.374 x 10^{-17}	6.197 x 10^{-15}
ΔU_1	[kJ/mol]	-97.99	-81.67
q_{sd}	[mmol/g]	5.7811	8.056
d_0	[m^3/mol]	8.773 x 10^{-12}	5.448 x 10^{-11}
ΔU_2	[kJ/mol]	-64.72	-54.41

Figure 4.8 shows a comparison of the fitted CO_2 and H_2O isotherm and the experimental competitive isotherms. Both competitive CO_2 and H_2O isotherm are well described using the modified Langmuir isotherm and the Quadratic isotherm model, respectively. The inflection point in the CO_2 and H_2O isotherm is also well captured. Using the modified Langmuir isotherm model, the competitive CO_2 loading as a function of relative humidity can be calculated (Fig. 4.7b). A small decrease in the CO_2 loading is seen in the model predictions, where it drop quickly beyond 50% RH. At 100% RH, the CO_2 loading is very small (Fig. 4.7b). The results from the modified Langmuir isotherm agrees with the competitive CO_2 data collected from TGA and DCB experiments.

4.5.2. Binary CO_2/H_2O dynamic column breakthrough simulations

The competitive CO_2+H_2O breakthrough curves at various relative humidity can be predicted by solving the detailed model described earlier. The bed is split into 30 cells, and the finite volume

method with a total variation diminishing (TVD) scheme is used to discretize all equations [109]. The resulting ordinary differential equations (ODE) are solved by *ode23s* using MATLAB ODE solver. The specific solution methodology can be found in the previous study [109]. The simulated results are compared with the experimental breakthrough curves and shown in Fig. 4.4 and Fig. 4.5. Both breakthrough curves and the temperature history of the column are reported.

The competitive CO_2 concentration curves (Fig. 4.4) show a good agreement between the simulations and the experiments. The model captures the CO_2 breakthrough time well, and it is also able to predict the "roll-up" effect when H_2O breaks through the column. The second transition in the CO_2 breakthrough curves at 73% and 87% RH is also predicted well. Note that the competitive CO_2 loadings need to be predicted properly with and without water. Initially, the CO_2 travels through the column without the presence of H_2O since the feed gas is rich in CO_2 and H_2O slowly moves across the column. In this case, the CO_2 loadings are similar to the pure CO_2 isotherms. Afterwards, the water starts to build up in the adsorbents, and there is competitive adsorption between CO_2 and H_2O. As a result, the CO_2 loading reduces in accordance with the relative humidity. Another important note is that the adsorption of CO_2 releases a significant amount of heat in the column. At higher temperatures, the CO_2 loadings will be lower. Without considering the effect of temperature, the CO_2 breakthrough time will be overpredicted. The modified Langmuir model takes into account both the effect of water loading and the temperature on the CO_2 adsorption. Thus, a good agreement between the simulation and the experiments is seen in all experiments, from 13% to 87% RH.

The model also predicts the competitive H_2O breakthrough curves at different relative humidity decently (Fig. 4.5a). A simple wave is indicated in the dynamic column breakthrough simulations at the RH < 47%. The transition in the competitive H_2O breakthrough curves is captured as well, at 73% and 87%. Both the wave and the shock front in the water curves are predicted, indicating the inflection point in the isotherm. To avoid the complexity in the model, the competitive H_2O loading is estimated using the discrete equilibrium data mentioned in the previous chapter. The Quadratic-Langmuir model is used to fit the binary H_2O isotherm. Then, a set of discrete data points is generated to estimate the competitive H_2O loadings by interpolation. This approach shows a good prediction in the competitive H_2O breakthrough curves. Only a small discrepancy is observed at high RH, i.e. 73% and 87% RH.

Figure 4.5b shows the temperature history of the column at 1.82 cm from the column outlet. A temperature peak at $\bar{t} \approx 40$ is recorded with a maximum value of ≈80°C. The model is able to predict both the position and the magnitude of the temperature in all experiments. The decay in the temperature after reaching its peak is also well captured. Afterward, the temperature fluctuates in a small range of temperatures, approximately ≈22°C. Briefly, the column model is adequate to simulate the competitive CO_2+H_2O breakthrough on CALF-20 in a wide range of relative humidity. Both the breakthrough curves and temperature history are predicted. The modified Langmuir isotherm model is suitable to describe the competitive CO_2 loading as a function of water loading and temperature. The discrete equilibrium data is also sufficient to describe the competitive water loading in all CO_2+H_2O breakthrough experiments.

4.6. Conclusions

This study shows that the competitive CO_2 and H_2O loadings can be estimated by combining the thermogravimetric analysis (TGA) and the binary dynamic column breakthrough (DCB) measurement. The competitive CO_2+H_2O loadings on CALF-20 at 22°C and 0.97 bar total pressure were measured at various relative humidity. The TGA measurements provided the total loading of CO_2 and H_2O at a certain RH. In the meantime, the competitive H_2O loading can be achieved by performing the CO_2+H_2O breakthrough experiment at the same RH. The difference between the total loading of CO_2 + H_2O and the competitive H_2O loading yields the competitive CO_2 loading.

CALF-20 shows unique competitive adsorption between CO_2 and H_2O. At the RH < 20%, the competitive CO_2 loadings are comparable with the pure CO_2 loading. This result indicates that water does not have a strong effect on CO_2. From 20% to 50% RH, there is a slight reduction in the CO_2 loadings; meanwhile, the competitive H_2O loadings increase. A significant decrease in the CO_2 capacity is observed at the RH > 70%. This observation implies H_2O is strongly adsorbed, and it dominates the competitive adsorption at high RH. It is worth noting that the competitive H_2O isotherm still exhibits a type V isotherm with an inflection point. However, it is shifted to higher relative humidity, at ≈ 65% RH, due to the competition of CO_2. This result suggests that CO_2 has a strong impact on the H_2O adsorption. Furthermore, the total loadings of CO_2 and H_2O at high RH (>70%) is higher than the pure water loading at the same RH. The competitive CO_2+H_2O DCB confirmed that the total loading is contributed mostly by the adsorption of H_2O at

high RH. If the structure of CALF-20 does not change, the total loading should be comparable with the pure H_2O loading. This interesting observation is explained in the next chapter by studying different CO_2 and H_2O adsorption mechanisms on CALF-20.

The modified dual-site Langmuir isotherm was used to describe the competitive CO_2 isotherm at various relative humidity. Two additional parameters, called λ_1 and λ_2, were added to take into account the effect of H_2O on the CO_2 loadings. The effect of temperature on the adsorption of CO_2 was also included. The binary H_2O loadings were fitted using the Quadratic-Langmuir model. A set of discrete equilibrium data points was generated from this model to estimate the competitive H_2O loading at a certain relative humidity. The binary CO_2+H_2O dynamic column breakthrough at various RH was simulated using a detailed column model reported in the previous study. The CO_2 and H_2O concentration curves were captured well, and the model was also able to predict the thermal history of the column.

5 Anomalous Behaviour Of CALF-20 Under Competitive CO_2 And H_2O Adsorption

5.1. Introduction

Metal-organic frameworks have been heavily studied for CO_2 capture in the last decades [68, 120-122, 154]. The structure of MOFs is porous, regular, repeatable, tunable and predictable [62, 155-157]. MOF design draws on principles from supramolecular and coordination chemistry, among others [55, 62]. Thousand of MOFs for CO_2 capture have been reported in the literature from both molecular simulation (hypothesis MOFs) and experiments [120, 158, 159]. Various approaches were studied to increase the CO_2 capacity of MOFs [64, 69, 71, 93]. Increasing the length of the organic linkers is an example. The ligands of DUT-48, DUT-46, DUT-49, DUT-50 and DUT-51 were extended by adding one, two, three or more benzene groups [160]. Extending linkers has a macroscopic effect on the material characteristics; higher surface areas could also be obtained by using this approach [160, 161]. Also, larger linkers can sometimes lead to interpenetrated networks, which might have significant effects on adsorption selectivity/capacity [162]. MOFs with the same topology but different linkers are usually called "isoreticular structures" [163]. Adding different functional groups is also another option to modify the properties of MOFs, i.e. NH_2, NO_2 [164]. The synthesis of UiO-66 is a typical example for this approach where different functional groups, e.g. NH_2, Br or NO_2, were added to its structure resulting in the difference of the surface area [165].

Several MOFs have shown flexibility in their frameworks. Depending on the guest molecules, the pressure, and the temperature, the framework of MOFs might change [166-168]. MIL-53 shows a breathing framework with temperatures and guest molecules [166, 167]. The window to the pore of MIL-53(Cr) becomes narrower under the presence of water. The hydrated form and anhydrous structure of MIL-53 are different (≈5Å), and this transition is fully reversible after removing the water molecules [166]. The shrinkage effect is also observed in MIL-53(Al) at room temperature after adsorbing water. The carboxylate groups form hydrogen bonds with guest water molecules

in the tunnels. At high temperature, ≈300°C, the water molecules are removed, and MIL-53(Al) becomes an open-framework [167]. The CO_2 capacity of HKUST-1 slightly increases at low RH, indicating a change in the framework [126]. The opening gate pressure of RPM3-Zn depends on the guest molecules due to either polarizability or size of the molecules [169].

The TGA measurements reported in the previous chapter revealed some anomalous behaviour of CALF-20 in the presence of CO_2 and H_2O. Although this behaviour was observed at high relative humidity values, i.e., in a region that might not be of interest from a process perspective, we report it in this chapter as it can contribute to the fundamental understanding of the behaviours of MOFs in the presence of gases and vapours. Three case studies were performed to understand the mechanism of CO_2+H_2O adsorption. In the first case study, wet air (Air+H_2O) was introduced to the adsorbent first, followed by a mixture of CO_2+H_2O at various relative humidities. In the second case study, both CO_2 and H_2O were introduced at the same time. The third case study is opposite to the first one, where the CO_2+H_2O mixture was introduced first, followed by the wet air.

5.2. Materials and methods

5.2.1. Materials

CALF-20 was synthesized by our colleagues at the University of Calgary. To structure CALF-20, polysulfone was added as a binder to form a cylindrical shape with a diameter of 1 mm and a length of 1-3 mm. The particle density of the structured CALF-20 sample was approximately 570 kg/m^3. Instrument air was used as the carrier gas for Air/H2O experiments. Pure CO_2 (99.998%) was purchased from Praxair Canada Inc.

5.2.2. Thermogravimetric analysis

A TA Q500 (TA Instruments, DE, USA) thermogravimetric analyzer (TGA) was used to measure the total loading of CO_2 and H_2O at ≈22°C and 0.97 bar total pressure at various relative humidity (RH) values. A bubbler humidifier was built to create humid streams placed upstream of the TGA chamber. This humidifier consists of a tank filled with deionized water and two mass flow controllers (MFCs). By adjusting the flow rates of the MFC-1 and MFC-2, the desired RH can be established (Fig. 5.1). The instrument air or pure CO_2 was used as a carrier gas depending on each experiment. Pure CO_2 (99.999%) was purchased from Praxair Canada Inc. Two relative humidity meters, RH1 and RH2 (SensorPush, Brooklyn, NY, USA), were placed upstream and downstream of the TGA chamber to control the relative humidity entering and leaving the TGA. A sample of

≈70 mg of structured CALF-20 was used for these experiments. The adsorbent was activated at 150°C for 12 hours prior to each experiment. The weighing precision of this TGA is ±0.01%, and the sensitivity is 0.1 μg.

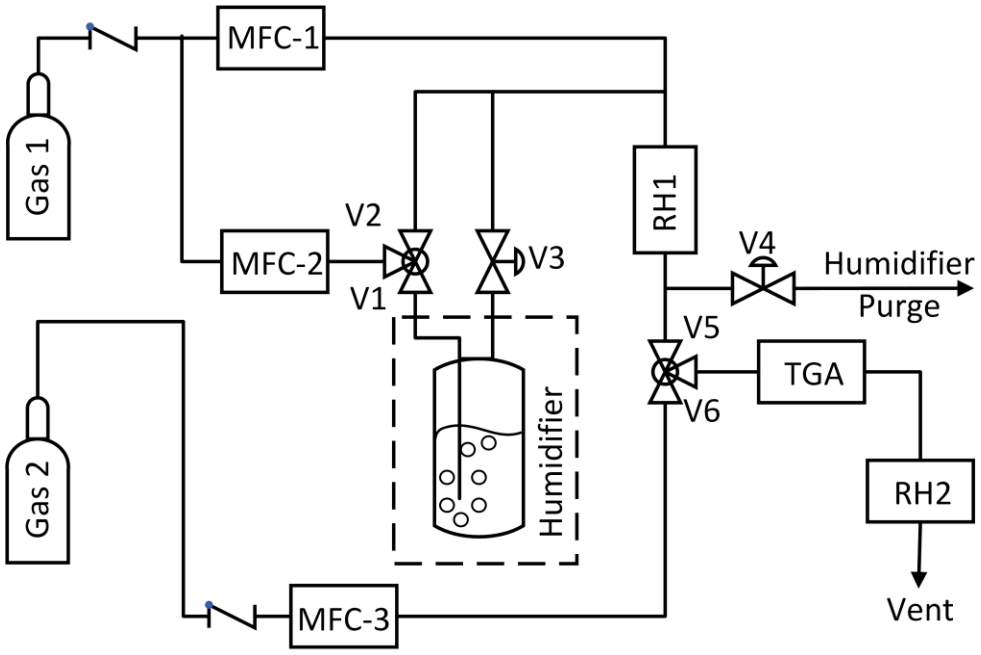

Figure 5.1 The schematic of thermogravimetric analysis coupled with a humidifier. MFC – Mass flow controller; RH – Relative humidity meter; TGA – thermogravimetric analyzer. V1 to V6 – Valve 1 to valve 6

5.3. Experimental procedure

All adsorption measurements were performed using the thermogravimetric analyzer at ≈22°C and 0.97 bar total pressure. The transitions of the total weight by time and temperature were recorded, and the data was interpreted in total amount adsorbed in weight fraction (mg/mg) of the dry adsorbent. The humidifier was used to create the humid feed at a desired relative humidity. Two mass flow controllers and two relative humidity meters were used to monitor the humidity during the experiment (Fig. 5.1).

5.3.1. Case study 1

This case study comprised of two steps. In the first step, the adsorbent was saturated with humid air (Air+H_2O) at a desired RH. To create a humid feed, Gas 1 was connected with instrument air, MFC-1 and MFC-2 were set at a certain value to obtain the desired RH. The total flow rate was

kept at 0.2 LPM. The feed gas traveled through the humidifier and entered the TGA chamber by opening V1, V3 and V5 (Fig. 5.1). This step was maintained until the equilibrium was reached. The equilibrium was considered to be established when the change in weight did not change for an hour ($\Delta m<0.01mg$).

In the second step, the adsorbent was in contact with CO_2+H_2O at the same RH. Gas 1 was replaced by pure CO_2, and the CO_2+H_2O feed at the same RH was obtained by controlling MFC-1 and MFC-2. The total flow rate was similar, at 0.2 LPM. V1, V3 and V5 were opened, and this step was also run long enough to reach the equilibrium ($\Delta m<0.01mg$). At the final equilibrium state, the adsorbent was in equilibrium with CO_2+H_2O at the desired RH.

A set of experiments at various RH values was performed following this procedure. Each step took approximately 6 hours. The final equilibrium state was CO_2+H_2O at a specific RH. The relative humidity was varied from 10% to 90%. The adsorbent was activated at 150°C before changing to the next relative humidity value. Gas 2 was connected with dry air, and V6 was opened to regenerate the adsorbent prior to each experiment.

5.3.2. Case study 2

Case study 2 only had one step which was similar to the second step of the case study 1. The adsorbent was saturated with CO_2+H_2O at various RH values. Gas 1 was connected with pure CO_2, MFC-1 and MFC-2 were set at a specific value to generate a desired RH value. V1, V3 and V5 were opened to perform the experiment (Fig. 5.1). When the change in the total weight was smaller than 0.01 mg for at least an hour, the equilibrium was considered to be reached.

In this case study, the RH increased from 10% to 100% RH, and the total flow rate was set at 0.2 LPM. The humid feed was run until the equilibrium was established, approximately 6 hours. At the final state, the adsorbent was in equilibrium with CO_2+H_2O at the desired RH. The adsorbent was activated at 150°C prior to starting a new experiment.

5.3.3. Case study 3

The third case study included two steps. In contrast with case study 1, the adsorbent was in equilibrium with CO_2+H_2O first; afterwards, it was saturated with Air+H_2O at the same RH and similar total flow rate. In the fisrt step, Gas 1 was connected with pure CO_2, MFC-1 and MFC-2 were set at a specific flow rate to obtain a desired RH. V1, V3 and V5 were openrd to let the test

gas travel to the humidifier and enter the TGA chamber. The equilibrium was reached when the change in the mass was less than 0.01 mg for an hour.

In the second step, Gas 1 was replaced by instrument air, and the humid stream (Air+H_2O) was generated by passing the instrument air to the tank, V1, V3 and V5 were opened. The RH was kept the same by adjuting MFC-1 anf MFC-2, and the total flow rate was 0.2 LPM. The new equilibrium was established when the difference in the weight was less than 0.01 mg dung one hour ($\Delta m<0.01mg$). At the final equilibrium state, the adsorbent was in equilibrium with Air+H_2O at the desired RH.

Five different RH values were performed: 25%, 45%, 55%, 66% and 81%. Prior to each experiment, the adsorbent was activated at 150°C. The total weight histories were recorded, and the total weight after each step was also calculated.

5.4. Results and discussions

The main purpose of these case studies is to understand the behaviour of CALF-20 under the presence of different gases and gas mixtures. We learned from the previous chapter that beyond 70% RH, CALF-20 mostly adsorbs H_2O, but the total loading of CO_2 and H_2O was noticeably higher than the pure H_2O loading. We try to explore this unique mechanism by introducing various sequences of H_2O and CO_2. In the first case study, the adsorbent "sees" water in the air first, then CO_2 is introduced. In the second case study, both CO_2 and water were introduced at the same time. Note that the feed was rich in CO_2 since the pure CO_2 was used as the carrier gas. In the third case study, both CO_2 and water were introduced to the adsorbent, and then the feed was replaced by the humid air (without the presence of CO_2).

5.4.1. Case study 1: Air+H_2O followed by CO_2+H_2O

In case study 1, the adsorbent was in equilibrium with Air+H_2O first and CO_2+H_2O later. The total loading (mg/mg) was recorded after each step and is shown in Fig. 5.2.

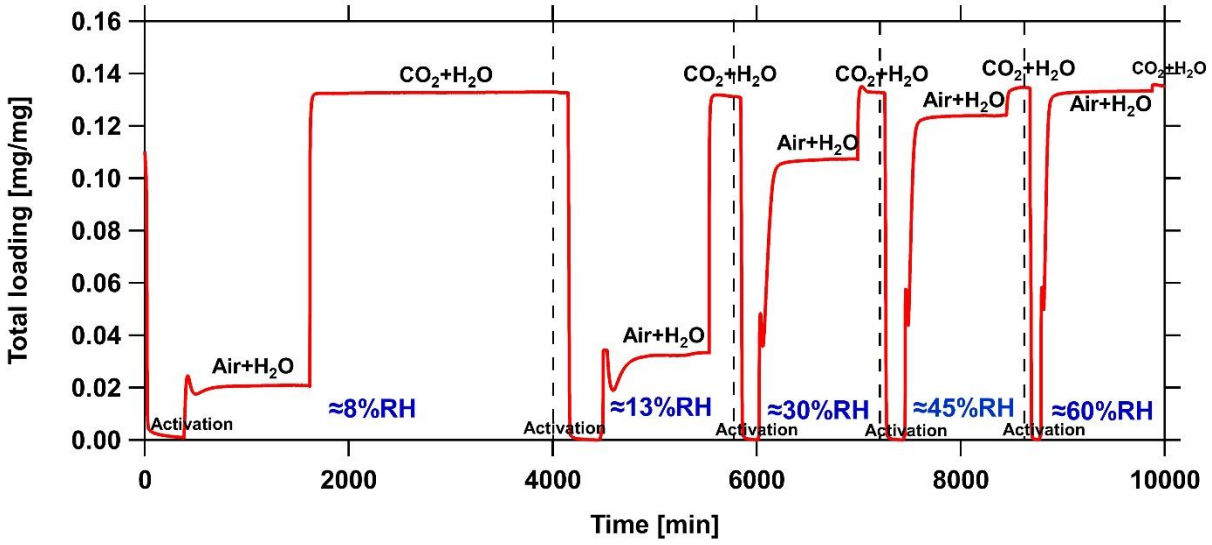

Figure 5.2: The transition of the total loading by time in case study 1 (Air+H_2O followed by CO_2+H_2O) at various relative humidity values. Solid lines represent the total amount adsorbed recorded by time.

As can be seen in Fig. 5.2, each experiment starts with the activation step using dry air, followed by the Air/H_2O and CO_2/H_2O adsorption with the same total flow rate. Five different RH values are indicated: 8%, 13%, 30%, 45% and 60% RH. In the first step, a noise signal was seen while changing from dry air to wet air. A disturbance is introduced to the system led to an oscillating signal for a short time. Afterwards, the signal was steady, and the increase in the total weight represent the adsorbed amount of H_2O. Fig. 5.3a shows that the total amount adsorbed after the Air+H_2O step overlapped with the pure H_2O adsorption isotherm for all experiments. This result confirmed that CALF-20 only adsorbs water after the first step.

In the second step, the feed was switched from wet air (Air+H_2O) to CO_2+H_2O. An increase in the total loading was observed in all experiments after the second step (Fig. 5.2). At this point, CO_2 is introduced into the system, and the competition between CO_2 and H_2O occurs. Depending on the relative humidity, either CO_2 or H_2O has a stronger affinity onto the surface. When the RH is smaller than 40%, a noticeable change in the total weight was observed (Fig. 5.2). The total amount adsorbed after the second step was also much higher than the pure water loadings at the same relative humidity (Fig. 5.3a). This observation suggests that a large amount of CO_2 was adsorbed at RH<40%.

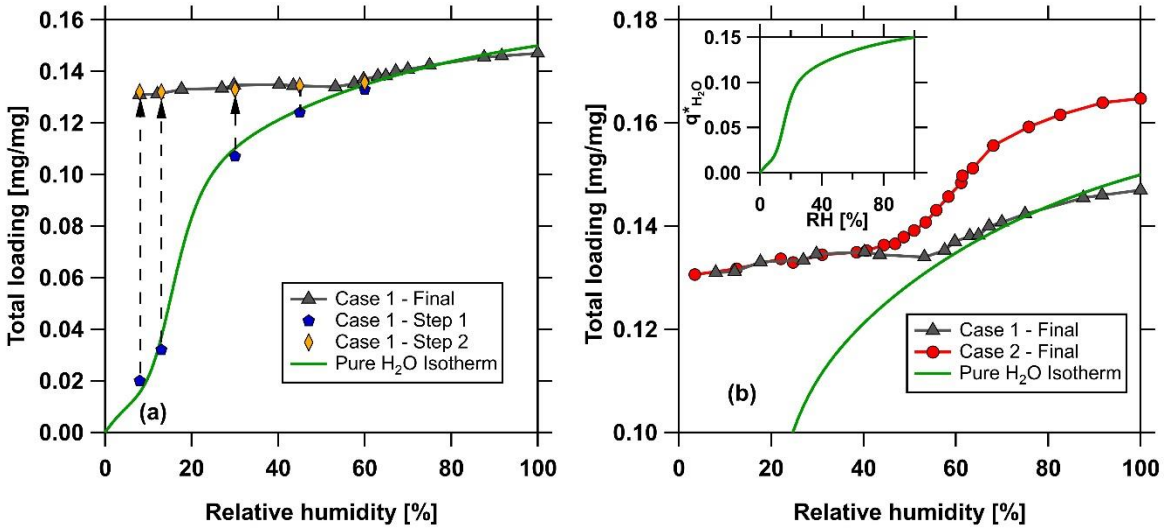

Figure 5.3: Total amount adsorbed as a function of relative humidity. (a) Case study 1. The solid green line is the pure H_2O adsorption isotherm at 22°C. Blue pentagon markers are the total amount adsorbed after step 1 in case study 1 (Air+H_2O), and yellow diamond symbols represent the total amount adsorbed after step 2 in case study 1 (Air+H_2O followed by CO_2+H_2O). (b) A comparison of Case study 1 and Case study 2. Triangle markers are the final amount adsorbed in the first case study. Circles are total amount adsorbed in the second case study. The inlay in Fig. 5.3b is the pure water isotherm at 22°C.

It is worth noting that the gap of the total loading between the first and the second step becomes smaller when the relative humidity increases (Fig. 5.2). At 60% RH, the total loading barely changed when switching to CO_2+H_2O (Fig. 5.2). In addition, this total weight is comparable with the pure H_2O adsorption isotherm (Fig. 5.3a). This observation implies that water is preferentially adsorbed at high relative humidity (>60%). The adsorption of CO_2 at this RH is very small. This result is in agreement with the competitive CO_2+H_2O isotherm reported in the previous chapter. All data collected from case study 1 are shown in Fig. 5.3a.

5.4.2. Case study 2: CO_2+H_2O

Case study 2 only contained one step where CO_2+H_2O was used as the feed gas at various relative humidity values. Both CO_2 and H_2O were introduced at the same time. The final total loading was recorded after the equilibrium was reached and shown in Fig. 5.4.

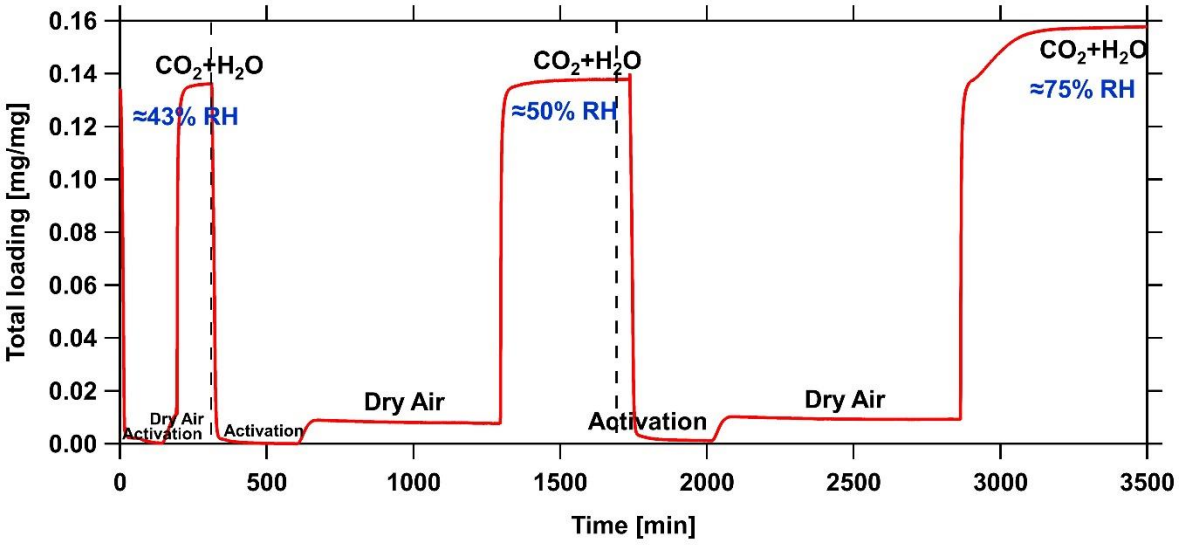

Figure 5.4: The transition of total amount adsorbed by time at RH values of 43%, 50% and 75% corresponding to case study 2.

In case study 2, each experiment starts with the activation at 150°C using dry air. The total loading drops to 0 mg/mg after the regeneration (Fig. 5.4). Afterwards, the temperature was reduced to the testing temperature, ≈22°C. This step was run for a while to let the system stabilize. A slight increase in the total loading, ≈0.01 mg/mg, was seen in all experiments after the temperature reached 22°C. This total loading corresponds to the adsorption of nitrogen and oxygen in the air since dry air was kept purging through the chamber during this step. Then, dry air was replaced by the CO_2/H_2O at various RH values depending on each experiment. A significant increase in the total loading was observed in the experiments (Fig. 5.2) due to the competitive adsorption of CO_2 and H_2O. It is worth noting that this loading only reflects the total loading of both CO_2 and H_2O. It is inadequate to quantify the amount adsorbed for each component using the total loading from the TGA alone.

At 75% RH, an interesting transition in the total loading was observed. A sharp increase followed by a wave was seen in this case. This can be explained due to the difference in the diffusion rate of CO_2 and H_2O. Since the feed is rich in CO_2, the adsorption of CO_2 happens faster, resulting in a sharp increase in the total loading. The adsorption of H_2O, in the meantime, occurs slower because of the small mole fraction of water in the gas phase, i.e. ≈2.8% at 22°C and 100% RH. This observation is not obvious at 43% and 50% RH where CO_2 still strongly competes with H_2O.

However, beyond 70% RH, water becomes dominant in the CO_2+H_2O competitive adsorption leading to a different transition in the total loading (Fig. 5.4).

Figure 5.3b shows the total loadings as a function of relative humidity from case study 1 and case study 2. Note that at the final state, the adsorbent was in equilibrium with CO_2+H_2O in both case studies. At RH<40%, Similar total loadings were observed for both scenarios. Interestingly, a noticeable difference in the total weight was seen when the relative humidity was greater than 40% RH. To explain this anomalous behaviour, possible scenarios are proposed and shown in Fig. 5.5.

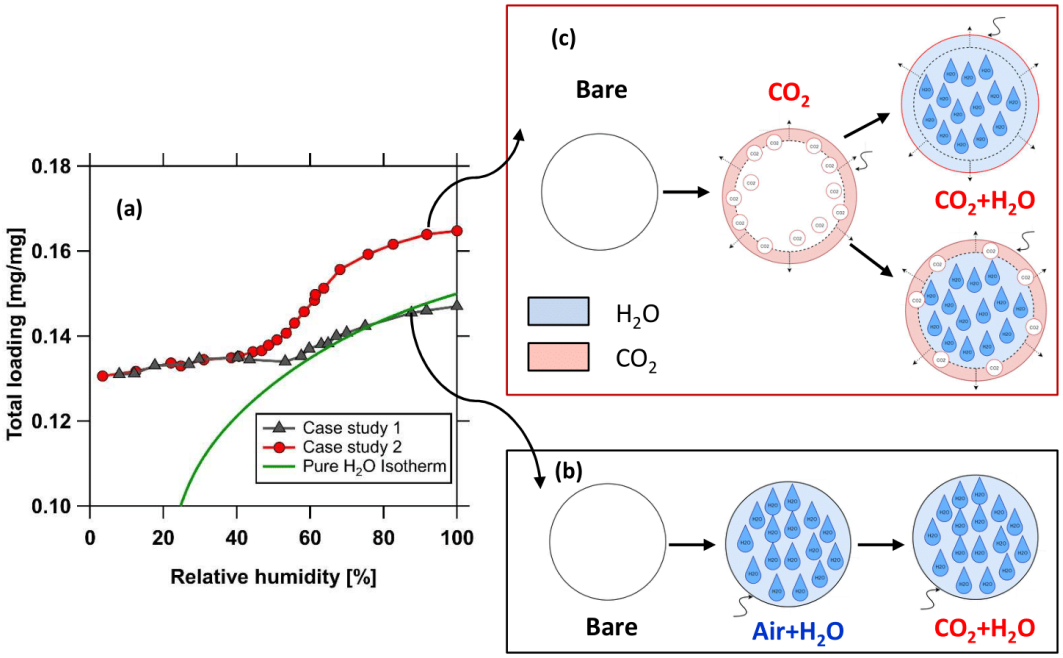

Figure 5.5: A possible explanation of the anomalous behaviour of CALF-20 in the presence of CO_2+H_2O. (a) The total loading as a function of relative humidity from case study 1 and case study 2. Triangle markers are the total loading from Air+H_2O followed by CO_2+H_2O (case study 1). Circles represent the total loading from CO_2+H_2O (case study 2). (b, c) Possible scenarios for the CO_2+H_2O competitive adsorption. The light red colour represents the adsorption of CO_2. The blue colour is water adsorption.

In the first case study, the adsorbent is saturated with water molecules before CO_2 is introduced (Fig 5.5b). In contrast, in the second case study, the adsorbent is filled with CO_2 first, then water is slowly adsorbed on the surface since the feed is rich in CO_2 (Fig. 5.5c). At the RH<40%, both

case studies show comparable total loadings (Fig. 5.5a). From the previous chapter, we learned that the adsorption of CO_2 on CALF-20 is stronger than the water adsorption at low to medium RH. Water does not adsorb strongly under these circumstances. Thus, CO_2 is a stronger component, and the total loadings do not change when the adsorbent is filled with CO_2 first or water first. As a result, both case studies show similar total loadings (Fig. 5.5a). The transition in the total loading from case study 1 also supports this explanation, where a steep change was observed after switching from Air+H_2O to CO_2+H_2O at RH<40% (Fig. 5.2).

When the relative humidity is greater than 40%, water becomes the stronger component. In the first case study, the total loadings overlap with the pure water adsorption when the relative humidity is greater than 70% RH (Fig. 5.3a). This can be explained based on the first scenario (Fig. 5.5b). After the activation, the adsorbent is empty without the presence of any guest molecules (bare). The water starts to be introduced into the pores when the humid feed enters the TGA chamber. At high relative humidity (>70% RH), the water loading almost reaches its saturation loading (Fig. 5.3a), and the capillary condensation occurs. The pores are filled with water, and there are no available sites for CO_2 to enter afterwards. As a result, the total loadings maintain the same after switching the feed gas to CO_2+H_2O, and it reflects the pure water loadings. This assumption is justified by comparing the total loadings with the pure water loadings at RH>70%, where they are overlapped (Fig. 5.3a).

A difference is seen in the total loading at high relative humidity (>40% RH) in the case study 2. It is worth noting that both case studies share the same final state. The adsorbent is in equilibrium with CO_2+H_2O at a certain relative humidity. From the thermodynamic perspective, they should have the same total loadings since they are in a similar equilibrium state. The experiments were confirmed by letting them run for a long time, up to 72 hours. The total loading did not have any further change. The result suggested that a new equilibrium state was established when CO_2 entered the pores first.

Figure 5.5c provides a hypothesis to explain this anomalous behaviour. Again, we start with the fresh adsorbent after the regeneration (bare). When CO_2 is introduced into the pores, the framework of CALF-20 expands. Without an expansion in the volume, the total loading should be the same. If we keep increasing the relative humidity, water becomes dominant in the CO_2/H_2O competition, and CO_2 is replaced by H_2O. There are two different possibilities: i) all CO_2 is

replaced by water; ii) Part of CO_2 remains on the surface (Fig. 5.5c). The competitive CO_2+H_2O reported in the previous chapter confirmed that only a very small amount of CO_2 is adsorbed at high relative humidity (RH>70%). The flexibility of the framework is a reasonable explanation, and this phenomenon was observed in several MOFs, i.e. MIL-53, HKUST-1, UiO-66 [122, 126, 170].

5.4.3. Case study 3: CO_2+H_2O followed by Air+H_2O

In case study 3, the adsorbent was in equilibrium with CO_2+H_2O first, and then it was replaced by Air+H_2O at the same RH. The purpose of this measurement is to explore whether the expansion of CALF-20 is reversible, and the structure does not change after exposure to CO_2. Six experiments were performed corresponding to six different relative humidity, at 25%, 46%, 55%, 66%, 70% and 81% RH (Fig. 5.6). The total loadings after each step were recorded.

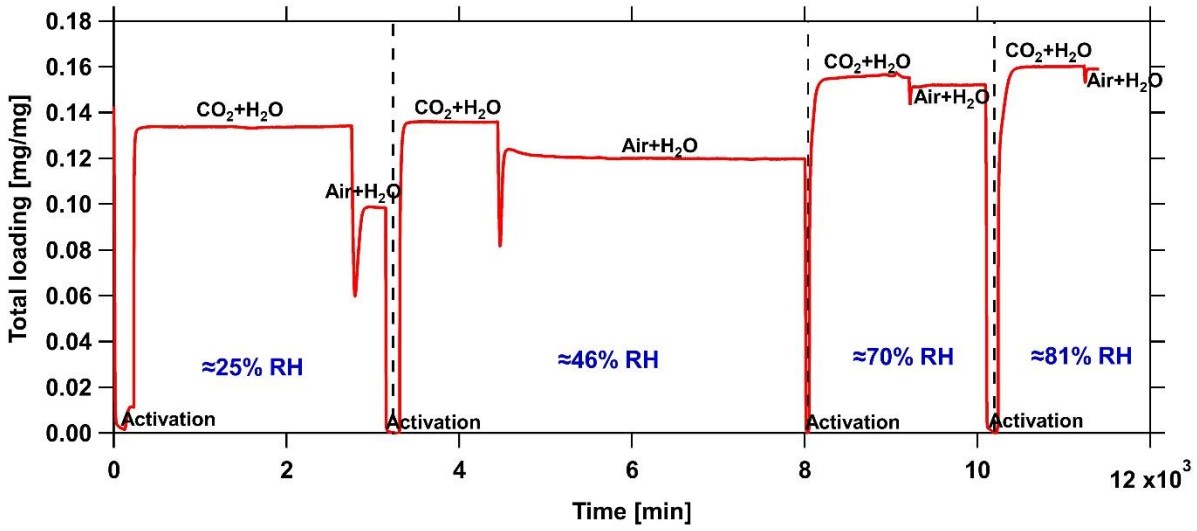

Figure 5.6: The transition of the total loading by time at 25%, 46%, 70% and 81% RH in case study 3 (CO_2+H_2O followed by Air+H_2O)

Every experiment in case study 3 includes an activation step, followed by the CO_2+H_2O adsorption and Air+H_2O adsorption (Fig. 5.6). The activation step was run using dry air until the total loading dropped to 0 mg/mg. A sharp increase is indicated in Fig. 5.6 after changing from dry air to CO_2+H_2O. The CO_2+H_2O feed was kept for at least 6 hours to confirm the equilibrium was established. Then, the feed gas was changed from CO_2+H_2O to Air+H_2O. Initially, there was a sharp decrease in the total loading, then it increased and constantly maintained at the final state.

The quick drop in the total loading is due to the desorption of CO_2 when changing to Air+H_2O. Then, the total loading increased because of the H_2O adsorption.

It is worth noting that the transition from step 1 to step 2 in case study 3 becomes less noticeable when increasing the relative humidity. At 70% and 81% RH, the difference in the total loadings between CO_2+H_2O and Air+H_2O was almost negligible (Fig. 5.6). This is because the adsorbed amount of CO_2 is very small at high relative humidity. Note that we still observe a small decrease in the total loading after changing to Air+H_2O. This observation confirms that a small amount of CO_2 is still adsorbed at high RH.

Figure 5.7 shows a comparison of the total loadings from case study 1, 2 and 3. The total loadings after the first step of case study 3 overlap with the total loadings from the second case study. This observation strengthens that the equilibrium is reached, which is similar to the one in case study 2 (CO_2+H_2O). When the feed gas is replaced by Air+H_2O, the total loadings decrease, and they are matched with the pure water adsorption isotherm. This means when CO_2 is removed, the framework maintains its initial shape. The total loadings reflect the pure water adsorption capacity since it is in equilibrium with Air+H_2O.

At the relative humidity higher than 70% RH, a different scenario was observed. The total loading after changing from CO_2+H_2O to Air+H_2O barely changed (Fig. 5.7). In fact, the total loading after the first step and the second step of case study 3 at 70% and 81% RH are nearly overlapped. From the previous explanation (Fig. 5.5c), the framework of CALF-20 is expanded under the presence of CO_2. At RH<70%, there is a strong competition between CO_2 and H_2O, and a relatively large amount of CO_2 is still adsorbed. When CO_2 is removed, the framework reverses to its initial shape, and the total loading at the end of case study 3 reflects the pure water adsorption (Fig. 5.7). However, at RH>70%, water is strongly adsorbed, and the capillary condensation occurs (Fig. 5.5c). Since the framework is already expanded, it is filled with mostly water. When CO_2 is removed, the water molecules still occupy the extra volume. Hence, a higher water loading compared to the pure H_2O isotherm was observed at 70% and 81%. This observation strengthens that the framework of CALF-20 is flexible.

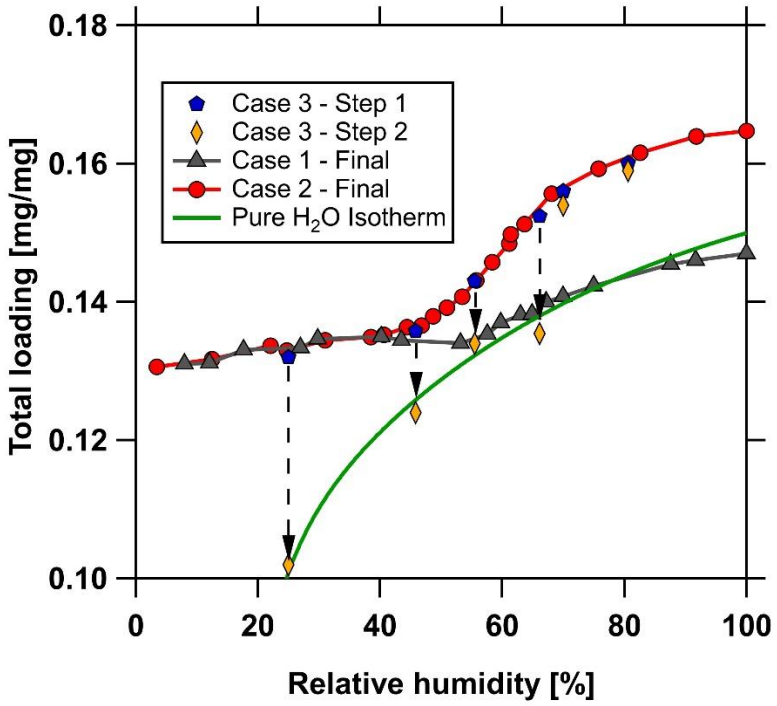

Figure 5.7: The total loading as a function of relative humidity from three case studies. Triangles represent the final total loading from case study 1 (Air+H_2O followed by CO_2+H_2O). Circles are the data collected from case study 2 (CO_2+H_2O). Pentagon markers indicate the total loading after the first step of case study 3 (CO_2+H_2O). The diamond markers are the final total loading of case study 3 (CO_2+H_2O followed by Air+H_2O).

The competitive dynamic column breakthrough (DCB) adsorption of CO_2+H_2O reported in the previous chapter also confirmed an increase in the total loading at high relative humidity values (RH>70%). A higher water loading was obtained from the competitive CO_2+H_2O at 87% RH, at 9.01 mmol/g (or 0.162 mg/mg). In contrast, the pure H_2O loading at 87% RH was 8.11 mmol/g (or 0.146 mg/mg). The result from the competitive CO_2+H_2O DCB is in a good agreement with what we observed in the TGA measurements from these case studies. The framework of CALF-20 is flexible under the presence of CO_2.

5.5. Conclusions

CALF-20 shows an anomalous behaviour under the CO_2+H_2O adsorption competition. Several case studies were carried out to explain this behaviour. In the first case study, the adsorbent was in equilibrium with Air+H_2O initially. A new equilibrium state was established when the feed gas

was switched to CO_2+H_2O. At low relative humidity (RH<40%), a steep change in the total loading was observed, indicating a strong competition of CO_2. In addition, the total loadings at a high relative humidity (>70% RH) were comparable with the pure water adsorption isotherm in this case. Since water is introduced to the adsorbent first, and the capillary condensation happens at high relative humidity, CO_2 has no access to the pore afterwards. This result is similar to the total loadings with the pure water isotherm at high RH, where CO_2 is barely adsorbed after the adsorbent exposes to water at high RH (>70%RH).

In the second case study, the adsorbent was contacted with CO_2+H_2O at various RH values. The total loadings were overlapped with the first case study when the RH was smaller than 40% RH. However, higher total loadings were seen when the relative humidity was higher than 40% RH. This unique observation indicates two different adsorption mechanisms on CALF-20. At low RH (<40%RH), CO_2 is favourable, which results in similar total loadings in both case studies. It does not matter if the adsorbent adsorbs water first or CO_2 first. The final equilibrium state is similar, where the adsorbent is in equilibrium with CO_2+H_2O at a certain RH. At high RH, water becomes dominant in the competition. If the adsorbent adsorbs water first, the CO_2 cannot enter the pores (case study 1). When CO_2 is introduced to the pore first, the framework is expanded, leading to higher total loadings at high RH (>40% RH).

Case study 3 further studied the differences in the total loading from case study 1 and case study 2. The adsorption was saturated with CO_2+H_2O at various RH, and then the feed gas was changed from CO_2+H_2O to Air+H_2O. The adsorbent is in equilibrium with Air+H_2O in the final state. A similar total loading with pure H_2O isotherm was observed at RH<70%. When CO_2 is removed, the framework reverses to its initial shape. The final state reflects the single H_2O adsorption, which is comparable with the pure H_2O isotherm. At RH>70%, water strongly adsorbs, and the capillary condensation occurs, which prevents the framework returns to the initial shape after removing CO_2. As a result, the total loading barely changed after switching from CO_2+H_2O to Air+H_2O. This higher H_2O loading indicates there is an expansion in the framework of CALF-20.

6 Post-Combustion CO_2 Capture By Vacuum Swing Adsorption Under Dry Conditions

6.1. Introduction

Carbon capture and storage (CCS) has been considered as a key technology to obtain a net zero-emission and negative emission by 2050 in numerous pathway scenarios [2]. The current state of the art for CO_2 capture, known as solvent-based technology, is limited in mass deployments because of its high cost of CO_2 capture [26]. Porous sorbent-based technology provides an alternative approach to capture CO_2 with lower costs due to a mild regeneration condition [26, 36]. However, most of the solid sorbents lose their CO_2 capacity under the presence of water vapour. The CO_2 capacity of Zeolite 13X, a commercial solid sorbent, reduces significantly even at 1% of relative humidity [87, 88]. Metal-organic frameworks (MOFs) have shown signs of progress in CO_2 capture thanks to their tunable and predicted frameworks [65, 69]. Among those materials, CALF-20 is a highly potential candidate due to its high water-resistant and strong CO_2 affinity.

An adsorption separation process depends on the adsorbent and the cycle configuration. Owing to the cyclic nature of the process, steady-state approaches are not available to design adsorption processes [109]. Detailed mathematical models with ordinary differential equations (ODE) and partial differential equations (PDE) are used to design and optimize adsorption processes [109, 171]. Since numerous process parameters contribute to an adsorption process, it is challenging to find optimal operating conditions for a specific objective function. Hundreds to thousands of operating conditions may have to be skimmed [171, 172].

A typical procedure to design an adsorption process comprises a sequence of steps involving in both experiments and simulations. The adsorption equilibrium measurement is the first step to decide whether the adsorbent shows reasonable potential for process deployment. Afterwards, dynamic column breakthrough experiments are performed to understand the column dynamics. A series of VSA/PSA experiments and parametric studies are conducted, and the experimental results will be compared with the modelling results. Several studies using this approach are reported in

the literature [173-176]. However, this approach results in a long time and requires excess resources. An alternative routine is the use of a rigorous optimization approach to guide experimental demonstrations. Depending on requirements, single-objective or multi-objective optimization can be performed to generate an optimal condition or a Pareto curve. These optimizations yield the operating conditions that correspond to the optimal solutions. Several points of the Pareto curve can then be randomly chosen to experimentally validate the prediction of the model experimentally. Perez and coworkers reported an experimental validation for a basic four-step VSA and four-step with light-product pressurization (LPP). The model predictions were translated to experiments to confirm the optimization results. This work shows the viability of using this approach to design an adsorption process [174].

In this work, CALF-20 is studied for post-combustion CO_2 capture under dry conditions. A rigorous optimization approach is used to predict process performance. Two different cycle configurations are employed: basic four-step VSA and four-step with light product pressurization (LPP). These two configurations are simple to implement, and many studies have been reported to confirm the viability of these cycles for CO_2 capture [50, 174]. The simulations are translated into experiments to validate the model predictions. The purity and recovery of each experiment were recorded and compared with the predictions from the model.

6.2. Materials and experimental methods

CALF-20 was prepared by Shimizu's group at the University of Calgary. A phase inversion method was used to structure the powder form of CALF-20. The structured CALF-20 has a cylindrical shape with an average length of 1-3 mm and a diameter of 1 mm (Fig. 6.1). To perform VSA experiments, premixed cylinders containing 15% CO_2 and 85% N_2 were purchased from Praxair Canada Inc. Pure CO_2 (99.998%), pure N_2 (99.998%) and pure Helium (99.998%) were also obtained from Praxair Canada Inc.

Single component CO_2 and N_2 isotherms were collected at various temperatures (22°C to 100°C) using the Micromeritics ASAP 2020 (Norcross, GA, USA). Prior to the static adsorption measurements, CALF-20 was regenerated at 150°C for 12 hours. The results were reported in previous studies.

The vacuum swing adsorption apparatus used in this study is indicated in Fig. 6.1. The heart of the system is two identical stainless-steel columns (length 26.5 cm, inner diameter 2.1 cm), each packed with 36.0 g structured CALF-20. Three mass flow controllers MFC-1, MFC-2 and MFC-3 (Alicat Scientific, Tucson, AZ, USA), were used to control the inlet flowrate. Three mass flow meters MFM-1, MFM-2 and MFM-3 (Alicat Scientific, Tucson, AZ, USA) were employed to monitor the outlet flowrate leaving the columns during the adsorption, blowdown and evacuation step, respectively. The pressure of the columns was measured by four pressure transducers PT-1 to PT-4 (Omega Engineering, USA) placed at each end of the columns. The blowdown and evacuation were performed by two diaphragm vacuum pumps, VP-1 and VP-2 (Pfeiffer Vacuum MVP 040-2, Germany). The temperature histories of the first column were measured using six thermocouples TC-1 to TC-6 (Omega Engineering, USA) placed at 1 cm, 4 cm, 7.8 cm, 11.5 cm, 15.5 cm and 19 cm from the inlet of the column. The CO_2 compositions during the adsorption, blowdown and evacuation step were measured using three CO_2 analyzers A_1, A_2 and A_3 (Quantek Instruments, Model 906, USA). This experimental VSA apparatus was controlled automatically using electrically activated solenoid valves (Peter Paul Electronics Co., USA). All the instruments were controlled and recorded by a LabVIEW data acquisition system. All mass flow controllers and mass flow meters were calibrated with different compositions and flowrates using a flow calibrator (Defender 510, Mesa Labs, USA). The CO_2 analyzers were also calibrated using different gases of known compositions.

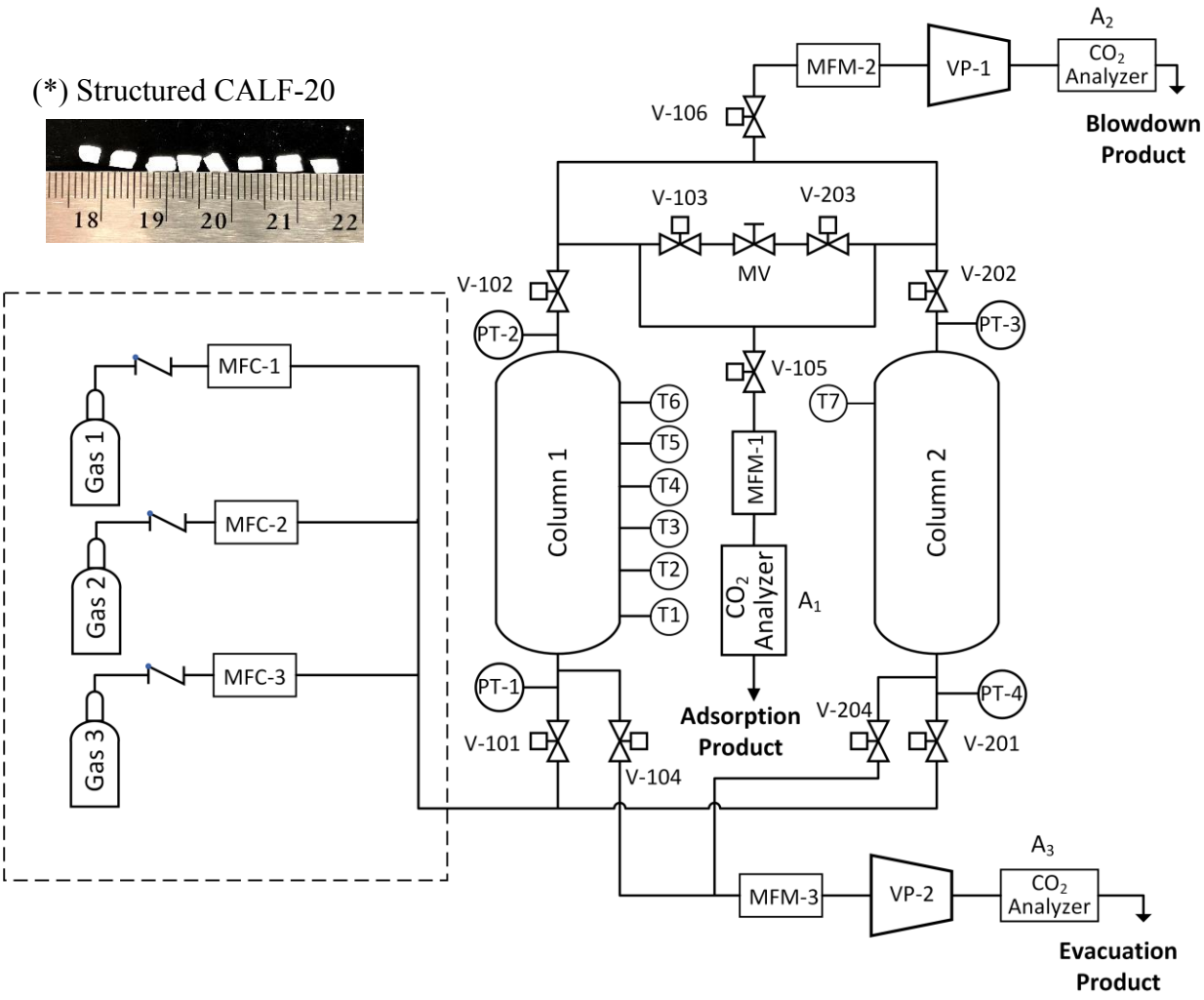

Figure 6.1: The schematic of the vacuum pressure swing apparatus. MFC – Mass flow controller; PT - Pressure transducer; MFM – Mass flow meter; T1 to T7 – Thermocouple at the position 1 to 7; VP – Vacuum pump; A_1 to A_3 – CO_2 analyzer 1 to 3. V-101 – Solenoid valves 101; MV – metering valve.

6.3. Modelling and simulations

6.3.1. Modelling adsorption processes

One dimensional axially dispersed plug flow model was used to simulate the column dynamics. The detailed model comprised of ordinary differential equations (ODE) and partial differential equations (PDE) have been provided in the previous studies [50, 109, 171, 174]. These are the main assumptions of this model: the gas phase is ideal, the column is one dimension without radial gradients for composition or temperature, the axial dispersion is considered, the pressure drop is

described by Darcy's law, thermal equilibrium reaches instantaneously, the column is uniform, and the mass transfer in the solid phase is defined by the linear driving force (LDF).

To reach a cyclic steady state (CSS) condition, the simulation of numerous cycles was required. A minimum of 50 cycles were run, and the CSS mass balance error was checked as follows:

$$Mass\ balance\ error\ [\%] = \frac{|mass_{in} - mass_{out}|}{mass_{in}} \times 100\% \tag{6.1}$$

Where $mass_{in}$ and $mass_{out}$ are the total amount of mass entering and leaving the system in one cycle, respectively. If the mass balance error is less than 1% for five consecutive cycles, the process is considered to have reached CSS. All simulation parameters are given in Table 6.1.

6.3.2. Vacuum swing adsorption configurations

Two vacuum swing adsorption (VSA) configurations are considered in this study. These schematics are shown in Fig. 6.2. The basic four-step VSA cycle (Fig. 6.2a) comprises of an adsorption step, a co-current blowdown step, a counter-current evacuation step, and a pressurization step. In the four-step VSA with light product pressurization (LPP), similar step constituents can be found. However, to pressurize the column, a part of the light product is used to increase the recovery of the process. Two columns are required to implement the four-step VSA with LPP. It is crucial to synchronize the adsorption step in the donor column and the LPP step in the receiver column by adding holding steps (Fig. 6.2b). The basic four-step represents a simple heavy product cycle, while the four-step with LPP represents the simplest and the most effective cycle for CO_2 capture [80, 171]. The primary purpose of this study is to validate the rigorous optimization approach using CALF-20. Hence, a simple cycle configuration was considered adequate.

6.3.3. Constituent steps

The VSA processes consist of four constituent steps that are explained below:

Adsorption (ADS): the feed gas containing 15% of CO_2 and 85% of N_2 enters the column at $z = 0$ at a given temperature T and high pressure P_H. In this step, the pressure of the column is kept constant at P_H. Most of the CO_2 in the feed is adsorbed while N_2 will be collected at the other end of the column $z = L$.

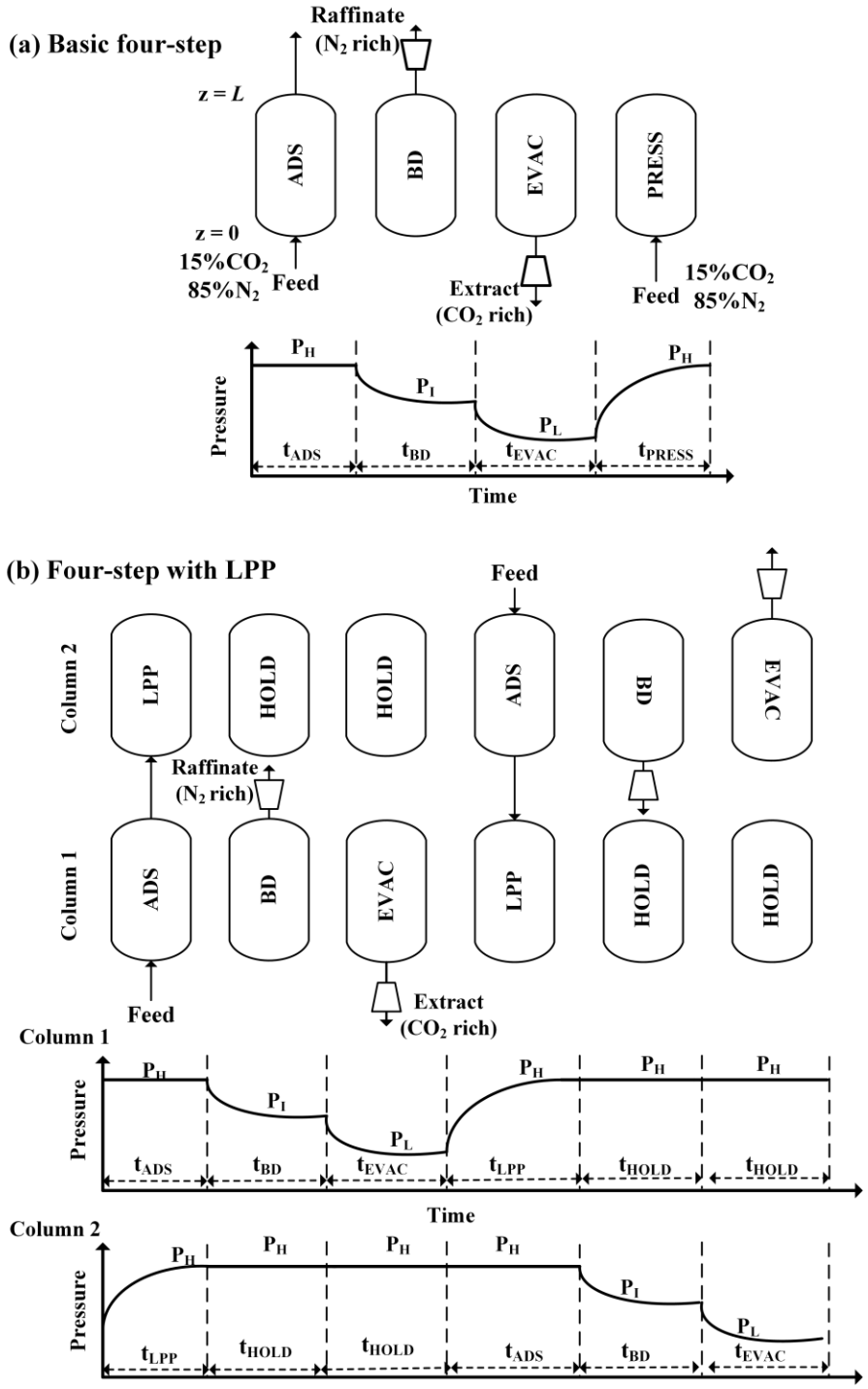

Figure 6.2: Vacuum swing adsorption (VSA) configurations. (a) Basic four-step VSA; (b) Four-step VSA with light-product pressurization (LPP); ADS - Adsorption; BD - Blowdown; EVAC - Evacuation; PRESS - Pressurization; P_H – High pressure; P_I – Intermediate pressure; P_L – Low pressure.

Blowdown (BD): The feed end is closed, and the column is evacuated from the $z = L$ end. The column pressure is reduced from the high pressure P_H to the intermediate pressure P_I. The purpose of this step is to remove the N_2 and concentrate the CO_2 in the column.

Evacuation (EVAC): The raffinate end ($z = L$) is closed, and the feed end is opened. A deep vacuum is applied to extract a high concentration of CO_2 from the column. The pressure keeps reducing from the intermediate pressure P_I to the low pressure P_L.

Pressurization (PRESS): The raffinate end ($z = L$) is closed, and the feed end is opened. The feed gas enters the bed to pressurize the column from low pressure P_L to high pressure P_H.

Light product pressurization (LPP): Part of the raffinate product from the adsorption step is used to pressurize the column from the low pressure P_L to the high pressure P_H. The feed end ($z = 0$) is closed in this step. The CO_2 front is sharpened and pushed back to the feed end of the column. Some of the CO_2 in the raffinate is also re-collected, resulting in higher CO_2 purity and recovery.

6.3.4. Multi-objective optimizations

To optimize the process, a genetic algorithm (GA) has been employed in the literature [78, 171]. In this method, the optimum solution is found by reproduction or genetic combination of initial population points. At first, an initial population is generated randomly, followed by the selection process. The crossover step is implemented by coupling individuals. A random modification is created by mutation to generate an offspring. In GA, the initial population of decision variables is used to generate the corresponding objective functions and evaluated using a detailed VSA model. Based on the objective functions the next "generation" of candidates is chosen following the principle of genetics. The population "evolves" with each generation thereby improving the objective function value. The objective function in the current case is to maximize purity and recovery. The objective functions are defined as:

$$\mathrm{CO_2\ Purity}\ (Pu_{CO_2}, \%) = \frac{n_{\mathrm{CO_2,EVAC}}}{n_{\mathrm{CO_2,EVAC}} + n_{\mathrm{N_2,EVAC}}}.100\% \tag{6.2}$$

$$\mathrm{CO_2\ Recovery}\ (Re_{CO_2}, \%) = \frac{n_{\mathrm{CO_2,EVAC}}}{n_{\mathrm{CO_2,ADS}}}.100\% \tag{6.3}$$

where n_{CO_2} and n_{N_2} are the number of moles of CO_2 and N_2 collected in a specific step within one cycle. Four decision variables were chosen to run the optimization for both cycle configurations: the adsorption time (t_{ads}), the intermediate pressure (P_I), the low pressure (P_L) and the feed velocity (v_{feed}). The blowdown, evacuation and pressurization steps were terminated using a pressure trigger when the column pressure reached the desired values. The upper and lower limits for each decision variable were decided depending on operational requirements: $t_{ads} = 20 - 300\ s$; $P_I = 0.04 - 0.45\ bar$; $P_L = 0.03 - 0.25\ bar$; $v_{feed} = 0.02 - 0.5\ m/s$.

Non-dominated sorting genetic algorithm toolbar built-in MATLAB was used to perform the optimization. The initial population equalled 50 times the number of decision variables (i.e. 200), and the GA ran for 50 generations. All optimizations were run on Compute Canada facilities. The objective functions were set to minimize J_1 and J_2, which were defined as:

$$J_1 = \frac{1}{Pu_{CO_2}} \tag{6.4}$$

$$J_2 = \frac{1}{Re_{CO_2}} \tag{6.5}$$

To optimize the VSA configurations, the optimizer is coupled with the detailed column model described in previous chapters. The operating conditions, e.g. adsorption time, intermediate pressure, low pressure and velocity, are chosen as decision variables for the optimization. A multi-dimensional search space is generated based on the boundary of each decision variable. The CO_2 purity and recovery are considered as the objective functions, and they can be calculated after the cyclic steady state (CSS) of the VSA cycle is reached. A Pareto curve is obtained after the optimizer meets the stopping criteria. A set of different operating conditions can be obtained at any point on the Pareto curve. This curve represents the optimal solutions between two conflict objective functions. Any point below this curve indicates the sub-optimal operating condition, and it is not feasible to obtain any point above this Pareto curve.

The energy and productivity were also calculated as references to evaluate process performances. The energy consumption is defined as the electrical energy equivalent required to capture a tonne of CO_2. The productivity is defined as the number of mole of CO_2 recovered in the evacuation step by one cubic meter of the adsorbent per second.

$$\text{Energy } (En, \frac{\text{kWh}_\text{e}}{\text{tonne CO}_2 \text{ captured}}) = \frac{E_{\text{ADS}} + E_{\text{BD}} + E_{\text{EVAC}} + E_{\text{PRESS}}}{m_{\text{CO}_2,\text{EVAC}}} \quad (6.6)$$

$$\text{Productivity } (Pr, \frac{\text{mol}_{\text{CO}_2}}{\text{m}^3\text{adsorbent s}}) = \frac{n_{\text{CO}_2,\text{EVAC}}}{V_{\text{adsorbent}} t_{\text{cycle}}} \quad (6.7)$$

where E_{ADS}, E_{BD}, E_{EVAC} and E_{PRESS} are the energy required for the adsorption, blowdown, evacuation and pressurization step, respectively; $m_{\text{CO}_2,\text{EVAC}}$ is the mass of CO_2 recovered in the evacuation step in one cycle. $V_{\text{adsorbent}}$ is the volume of the adsorbent in the column, and t_{cycle} is the total time of one cycle.

The energy consumption of each step depends on the initial and final pressure. In the adsorption step, only the frictional pressure drop in the column costs energy since the high pressure is equal to the pressure of the feed ($P_{\text{H}} = P_{\text{Feed}} = 1$ bar). In the blowdown step, the energy is required to evacuate the column from high pressure (P_{H}) to intermediate pressure (P_{I}). It is also required to evacuate the column from intermediate (P_{I}) to low pressure (P_{L}) in the evacuation step. In the pressurization step, the energy is required to pressurize the column from low pressure to high pressure. If the high pressure is equal to the feed pressure, energy is not required in case of LPP step. The energy consumption of each step is defined [51, 109]:

$$E_{\text{step}} = \frac{1}{\eta} \varepsilon \pi r_{\text{in}}^2 \frac{\gamma}{\gamma - 1} \int_{t=0}^{t=t_{\text{step}}} (v P_{out}) \left[\left(\frac{1}{P_{out}} \right)^{\frac{\gamma-1}{\gamma}} - 1 \right] dt \quad (6.8)$$

where ε is the bed voidage, r_{in} is the inner radius of the column, η is the vacuum pump efficiency ($\eta = 0.72$), γ is the adiabatic constant ($\gamma = 1.4$). Depending on the blowdown or evacuation step, P_{out} could be intermediate pressure or low pressure, respectively.

6.4. Results and discussion

6.4.1. Experimental cycle implementations

The schematic of the experimental vacuum swing adsorption apparatus is indicated in Fig.6.1. One column is sufficient to perform the four-step VSA cycle, while the four-step VSA with LPP requires two columns. In this case, only the first column is described; the second column will follow similar steps. The solenoid valves open when they are at the energized state. A description to implement each step is given below.

In the adsorption step, the mass flow controller MFC-1 is set at the desired flow rate to provide a constant feed. The valves V-101, V-102 and V-105 are energized to open the column since the adsorption occurs at the atmospheric pressure (P_H). The mass flow meter MFM-1 and the CO_2 analyzer A_1 record the composition and flow rate of the raffinate leaving the column. In the case of wet VSA cycles, a humid stream is generated using the humidifier before entering the bed.

In the co-current blowdown step, the pressure of the column decreases from atmospheric (P_H) to an intermediate pressure (P_I). Valve V-102 and V-106 are energized, and the column is evacuated using the vacuum pump VP-1. The MFM-2 and A_2 record the flowrate and the composition of the stream exiting the column. The blowdown step is terminated using a pressure trigger when the pressure of the column reaches the intermediate pressure P_I.

In the counter-current evacuation step, the pressure of the column continues to decrease from intermediate pressure (P_I) to low pressure (P_L) using the vacuum pump VP-2. Valve V-104 opens, and the MFM-3 and A_3 measure the exiting flow rate and the CO_2 composition. This data is used to calculate CO_2 purity and recovery in every cycle. Similar to the blowdown step, the completion of the evacuation step is controlled by a pressure trigger.

In the feed pressurization step, the product end is closed, and valve V-101 is energized to let the feed enter the column. When the pressure reaches the high pressure (P_H), this step is terminated using a pressure trigger, and the adsorption step occurs. Only the four-step VSA contains the feed pressurization. The light product pressurization replaces this step in the case of the four-step VSA with LPP.

In the light product pressurization (LPP) step, the raffinate leaving the first column in the adsorption step is used to pressurize the second column and vice versa. The MFC-1 is set at the desired feed flow rate, and valves V-101, V-102, V-103, V-203 and V-202 are energized. The pressure gradient allows the raffinate flow from column 1 to column 2. The metering valve MV on the LPP line supports to control of an excessive pressure drop. After a while, the pressure of column 2 reaches the high pressure (P_H), valves V-103, V-203 and V-202 close to disconnect the LPP line. Column 1 continues with the remaining of the adsorption step. It is necessary to synchronize the adsorption step and the LPP step in column 1 and column 2 using idle time. It means that the donor column undergoes the adsorption step while the receiver column is at the LPP step.

6.4.2. Description of pressure dynamics

Characterizing the vacuum pump performance (VP-1 and VP-2) is one of the key inputs in our model to capture the variation of column pressure with time. Depending on specific equipment and piping setup, different characterizations may be required. In the pressurization step, the pressure of the column increased linearly with time. Thus, a linear relationship was sufficient to describe the pressure history during this step. The following linear equation was used:

$$P_{Z=0} = \frac{(P_H - P_L)}{t_{step}} \times t + P_L \tag{6.9}$$

where P_H and P_L are the high pressure in the adsorption step and the low pressure in the evacuation step, respectively; $P_{Z=0}$ is the pressure at the column end; t_{step} is the total time of the pressurization step obtained from the experiment, and t is a specific time during the pressurization step.

The pressure histories of the blowdown and the evacuation step, as observed from the experiments, were a classical exponential decay form. A non-linear function containing one fitting parameter was used:

$$P_{Z=0} = P_I + (P_H - P_I) \times e^{-\lambda_{BD} \times t} \tag{6.10}$$

$$P_{Z=0} = P_L + (P_I - P_L) \times e^{-\lambda_{Evac} \times t} \tag{6.11}$$

where P_I is the intermediate pressure in the blowdown step, λ_{BD} and λ_{Evac} are the fitting parameters. A single VSA experiment was performed to fit λ_{BD} and λ_{Evac}. Thus, we could minimize the number of experiments. The values of λ_{BD} and λ_{Evac} are given in Table 6.1.

Table 6.1: Parameters for VSA simulations

Parameter	Symbol		Value	Source
Column length	L	m	0.267	measured
Inner column diameter	d_{in}	m	0.021	measured
Outer column diameter	d_{out}	m	0.025	measured
Bed voidage	ε	-	0.4	assumed
Particle void fraction	ϵ_p	-	0.35	assumed
Adsorbent mass	m_{ads}	g	36.0	measured
Tortuosity	τ	-	3.0	assumed

Universal gas constant	R	m^3 bar mol^{-1} K^{-1}	$8.314x10^{-5}$	standard
Adsorbent particle density	ρ_p	kg m^{-3}	570	measured
Column wall density	ρ_w	kg m^{-3}	7800	standard
Specific heat capacity	$C_{p,g}$	J kg^{-1} K^{-1} (N_2)	1040	NIST database
		(CO_2)	841	NIST database
		(H_2O)	4165	NIST database
Specific heat capacity of adsorbed phase	$C_{p,a}$	J kg^{-1} K^{-1}	$C_{p,g}$	assumed
Specific heat capacity of adsorbent	$C_{p,s}$	J kg^{-1} K^{-1}	1350	fitted
Specific heat capacity of column wall	$C_{p,w}$	J kg^{-1} K^{-1}	502	standard
Molecular diffusion	D_m	m s^{-2}	$1.496x10^{-5}$	standard
Effective gas thermal conductivity	K_z	W m^{-1} K^{-1}	0.4	fitted
Thermal conductivity of column wall	K_w	W m^{-1} K^{-1}	10	standard
Internal heat transfer coefficient	h_{in}	W m^{-2} K^{-1}	8	fitted
External heat transfer coefficient	h_{out}	W m^{-2} K^{-1}	10	fitted
Fluid viscosity	μ	kg m^{-1} s^{-1}	$1.812x10^{-5}$	standard
Blowdown exponential constant	λ_{BD}	s^{-1}	0.153	fitted
Evacuation exponential constant	λ_{Evac}	s^{-1}	0.075	fitted

The basic four-step VSA and four-step VSA with a light-product pressurization cycle were optimized using this VSA model coupled with the optimizer. Four decision variables were chosen, e.g. adsorption time, intermediate pressure, low pressure and feed velocity to optimize these cycle configurations. Dry condition is considered in this case, and the Pareto curve representing the optimal operating conditions can be obtained.

6.4.3. Optimization results

The multi-objective optimizations were performed for both basic-four step VSA and four-step VSA with the LPP cycle. The objective functions were to maximize the purity and recovery for each configuration within the operational range. The optimization results are shown in Fig. 6.3.

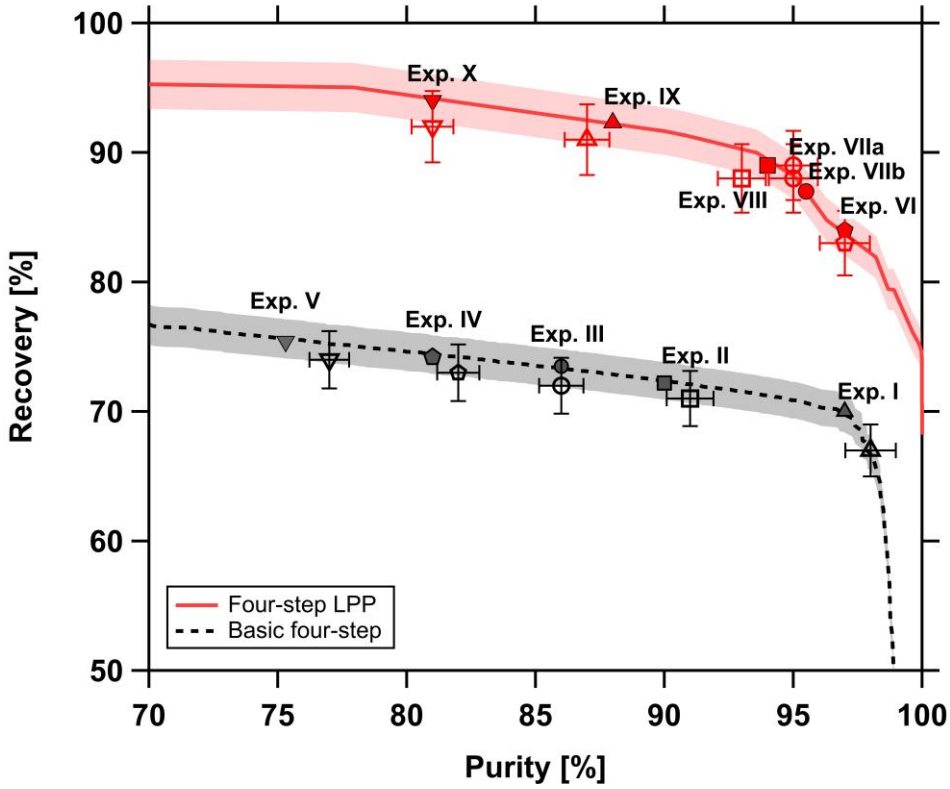

Figure 6.3: Pareto fronts of the basic four-step VSA and four-step VSA with LPP. The broken line corresponds to the basic four-step cycle, and the solid line corresponds to the four-step VSA with LPP cycle. The closed markers represent the purity and recovery from the optimized set of operating conditions that were experimentally demonstrated. The opened markers are the corresponding purity and recovery obtained from the experiments. The shaded area indicates the 2% uncertainty of the model.

Higher purity and recovery were indicated in the Pareto front of the four-step VSA with light product pressurization cycle. Note that the Pareto front shows the best set of purity and recovery that one could obtain from that specific configuration within the given operational range. The region above this Pareto curve is not feasible, while the region below indicates sub-optimal operating points. This result is in agreement with previous studies that the four-step VSA with LPP shows better performances than the basic four-step cycle [171, 174]. The CO_2 recovery is enhanced by moving the CO_2 front far away from the raffinate end of the column due to the light product pressurization step. Considering a CO_2 purity of 95%, the CO_2 recovery increases from 70% to 90% using the LPP step. The purpose of the optimization step is to obtain the Pareto front, which

guarantees the optimal conditions are found and operated. The uncertainty of the model is approximately 2% (shaded area), which is estimated in a previous study [174].

6.4.4. Basic four-step cycle

At first, the classic four-step cycle was considered due to its simplicity. Five experiments corresponding to five different sets of operating conditions on the Pareto curve were performed to validate the optimization results. Each point was a combination of specific purity and recovery values that translated into an experiment using exact operating conditions from the model. Prior to each experiment, the column was saturated with pure nitrogen. The purity (*Pu*) and recovery (*Re*) from the simulations and experiments were given in Table 6.2.

Table 6.2: List of basic four-step experiments under the dry condition

Exp.	t_{ads}	P_I	P_L	v_{feed}	**Model**				**Experimental**		
	[s]	[bar]	[bar]	[m/s]	*Pu* [%]	*Re* [%]	*En**	*Pr***	Pu [%]	Re [%]	Pr
I.	176	0.119	0.031	0.093	97	70	115	0.63	98	67	0.65
II.	174	0.148	0.031	0.065	90	72	120	0.54	91	71	0.52
III.	174	0.189	0.031	0.058	86	73	115	0.51	86	70	0.48
IV.	174	0.233	0.031	0.055	81	74	112	0.50	82	72	0.46
V.	174	0.263	0.031	0.046	76	75	112	0.44	78	72	0.40

(*) En – Energy [kWh_e/tonne CO_2]

(**) Pr – Productivity [mol $CO_2/m^3/s$]

Fig. 6.4 shows the obtained purity-recovery from the experiments along with the predicted values from the model. The specific operating conditions for each experiment are provided in Table 6.2. A slight difference in the purity was observed between the experiments and the simulations. In the case of the recovery, a non-negligible difference between the model and the experiments was recorded with an error of ± 3%. This is because the blowdown step and the evacuation step were controlled by a pressure trigger in the experiments. The experiments showed a slight difference in the length of the evacuation step between cycles, ≈5-10 seconds. The recovery shown in Fig. 6.3 was the average value of ten different cycles from the cyclic steady state (CSS), and the error bar presented the uncertainty from the experiments.

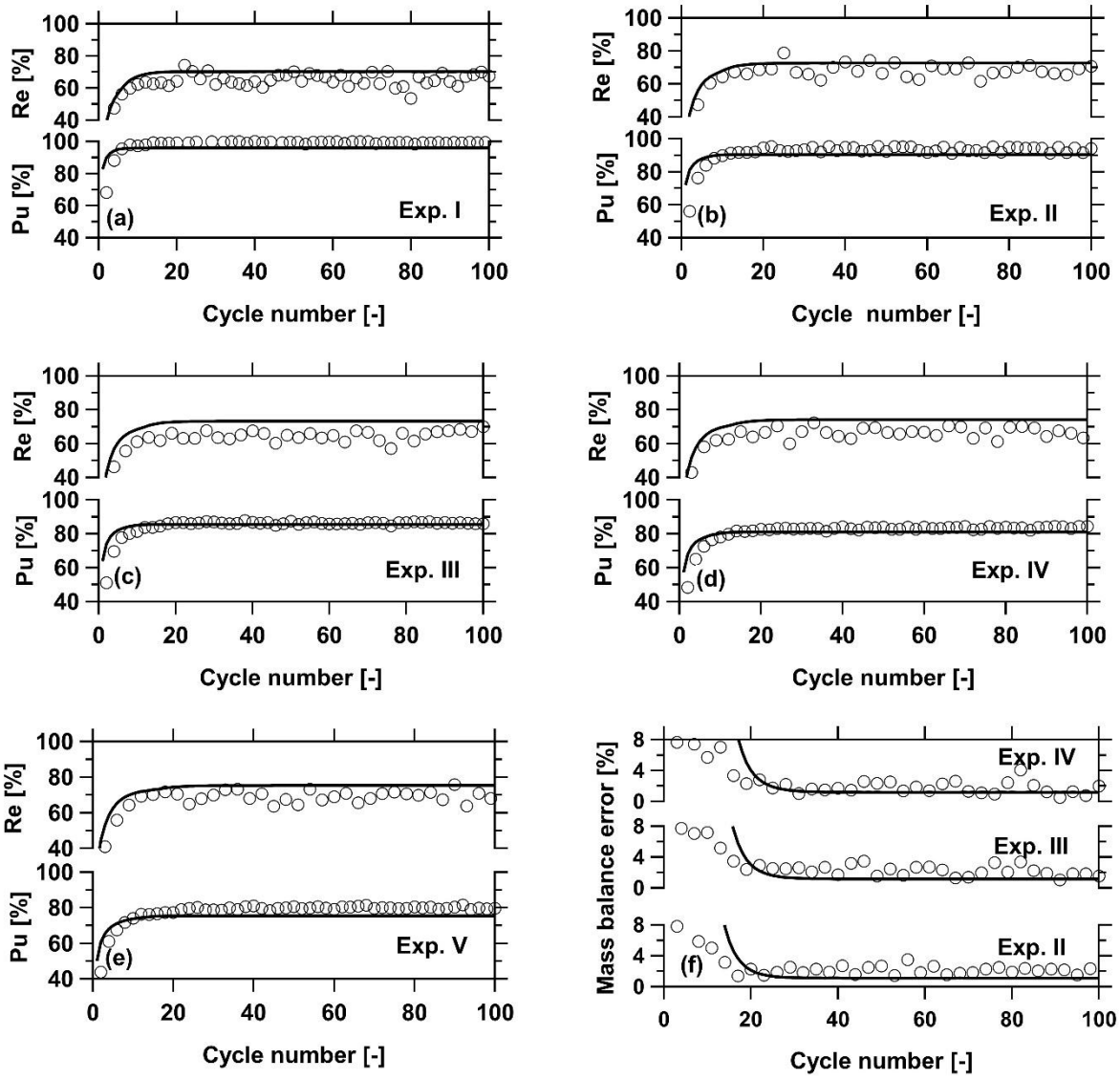

Figure 6.4: The evolution of purity-recovery over 100 cycles for the basic four-step experiments under dry condition. Markers represent the experimental data, and solid lines are the simulated data. (a-e) are the purity-recovery data from experiment I (Exp. I) to experiment V (Exp. V), respectively. (f) is the total mass balance error over 100 cycles from experiments II-IV.

To demonstate the model predictions, several points on the Pareto curve were randomly chosen, covering a wide range of purity (Fig. 6.3), i.e., 75% to 97%. The recovery did not change much within the range of the Pareto curve, i.e., 70% to 80%. The feed velocity was reduced from Exp. I to Exp. V, i.e., 0.093 m/s to 0.046 m/s. Fig. 6.4 shows a reduction in purity from Exp. I to Exp. II. This observation suggests that lower feed velocity results in a lower purity when other parameters

are held (nearly) constant. This is reasonable since the CO_2 front does not penetrate further to the other end of the column. A relatively high amount of N_2 still remains in the column, resulting in a lower purity. Higher feed velocity, on the other hand, can fill the bed faster, and the CO_2 front moves farther to the raffinate end, which leaves less space for N_2 to contaminate the column.

Figure 6.4 (a-e) show the evolution of purity and recovery as a function of cycle number for the five experiments. Note that the simulation not only predicts the steady-state values well, but also the transients with excellent accuracy. The results also demonstrate the excellent stability of the material and process for a prolonged duration of cycling. Finally, Fig. 6.4f shows the experimentally measured and simulated mass balance errors. Both of them show a nice convergence after ≈25 cycles. Overall, a good agreement between the experiments and the simulations was observed, which indicated the validation of the model.

Fig. 6.5 shows a comparison of the experimental and the simulated transitions from experiment II. The transient evolution of other experiments can be found in the Appendix. The temperature histories indicated in Fig. 6.5a shows an interesting propagation. The temperature measured at the feed inlet (T2) increased with time and reached a maximum value, then it decayed smoothly and kept fluctuating around a small range once CCS was reached. This temperature peak is associated with the heat of adsorption, and can be used a proxy to follow the propagation of the CO_2 front. The temperature measurements at T4 and T6 also confirmed the movement of the CO_2 front. A variation of ≈ 15°C was recorded at the temperature peak, while only a fluctuation of 8°C in the temperature was seen at CSS (Fig. 6.5b). The simulation captured both the temperature propagation and the temperature histories well.

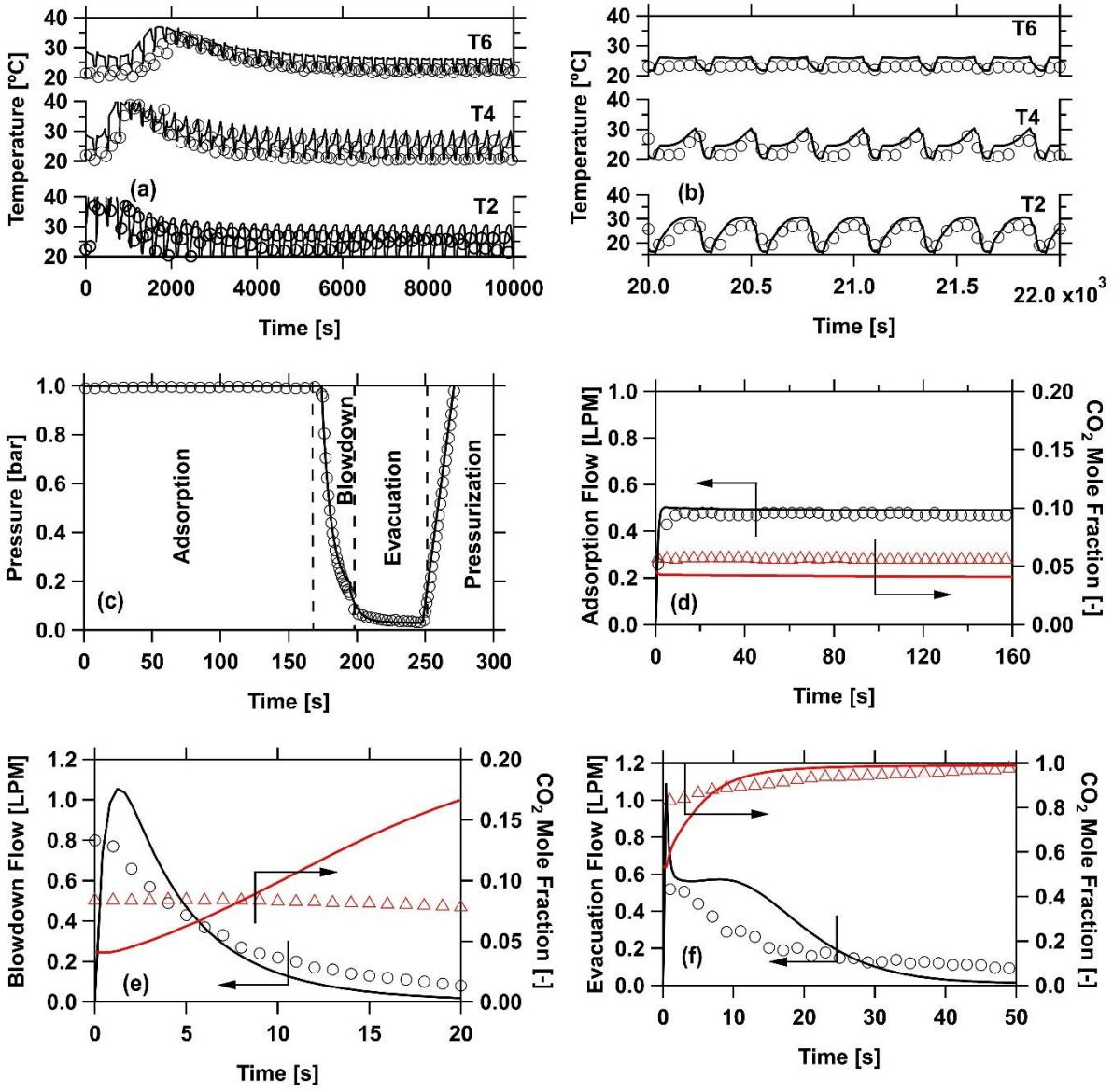

Figure 6.5: The comparison of experimental and simulated transitions for the basic four-step cycle from experiment II (Exp. II). The solid lines represent the simulation data, and the markers are the experimental data. (a, b) The temperature histories at three different locations; (c) The pressure histories of one cycle at CCS; (d, e, f) The CO_2 composition and the outlet flow rate of the adsorption step, blowdown step and evacuation step, respectively.

Fig. 6.5c represents the pressure history of one cycle at CSS from the experiment and the simulation. Both the experimental and simulated histories show a good agreement. The pressure histories during the blowdown and evacuated step were described based on one fitting parameter

model. It is crucial to capture the pressure transition in these steps, which results in the purity and the recovery of the cycle. The pressure drops sharply at the beginning of these steps. Furthermore, a higher flow rate is also observed at the beginning of blowdown and evacuation step. Thus, a small discrepancy in the pressure curve could lead to a significant discrepancy in the purity and recovery from the model predictions and the experiments.

Figure 6.5 (d,e,f) represents the CO_2 composition and the outlet flow rate during the adsorption, blowdown and evacuation step. The adsorption step shows a good agreement between the simulation and experiment for both CO_2 composition and the outlet flowrate. A small amount of CO_2 is seen at the outlet during the adsorption step, which indicates CO_2 has travelled through the column. This CO_2 trace also indicates a lower value in the recovery due to the loss of CO_2 at the raffinate end. A ≈6% of CO_2 mole fraction was recorded. A small gap is seen in the blowdown step, and the evacuation step since the transitions between these steps happened quickly. In the blowdown step, the outlet flowrate was comparable between the experiment and the simulation. The CO_2 mole fraction from the experiment, however, is lower than the simulation, at 8% vs 16%, respectively. The pressure and the flowrate quickly dropped within a couple of seconds, and the CO_2 analyzer needs ≈5 seconds to stabilize the signal. Fig. 6.5c also shows a relatively small flow rate after 5 seconds, which makes it harder to detect the composition precisely. This is the reason why there is a difference in the CO_2 mole fraction, which is associated with the corresponding time of the CO_2 analyzer. Even though the difference seems noticeable, the flow rate at this time is relatively small, i.e., nearly zero, which only results in a small difference in the recovery eventually. Similar to the blowdown step, the evacuation step also shows a slight difference during the first few seconds due to a quick transition in the pressure and the flowrate. Overall, the model well predicted the transient evolution in each step, and the purity-recovery evolution from the experiment and the simulation.

6.4.5. Four-step with light product pressurization under the dry condition

To enhance the purity and recovery, the four-step cycle with light product pressurization (LPP) was examined. This is the simplest and the most effective cycle for CO_2 capture reported in the literature [80, 109]. Similarly, five different points on the Pareto curve were chosen, and the operating conditions corresponding to these points were translated into the experiments to validate the optimization results. Two columns were required to perform the four-step VSA with the LPP

cycle. Both columns were saturated with pure nitrogen before each experiment. The specific cycle parameters are given in Table 6.3.

Table 6.3: List of four-step with light product pressurization experiments under the dry condition

Exp.	T_{ads}	P_I	P_L	v_{feed}	Model				Experimental		
	[s]	[bar]	[bar]	[m/s]	*Pu* [%]	*Re* [%]	*En**	*Pr***	*Pu* [%]	*Re* [%]	*Pr*
VI.	193	0.063	0.031	0.041	97	84	140	0.28	97	83	0.30
VII.a	157	0.046	0.031	0.024	96	87	183	0.14	95	89	0.14
VII.b	157	0.046	0.031	0.024	96	88	183	0.14	95	88	0.13
VIII	162	0.060	0.034	0.023	94	89	168	0.16	93	88	0.17
IX	156	0.066	0.031	0.021	88	92	176	0.14	87	91	0.13
X.	156	0.080	0.031	0.022	81	94	192	0.13	81	92	0.15

(*) En – Energy [kWh_e/tonne CO_2]

(**) Pr – Productivity [mol $CO_2/m^3/s$]

The purity-recovery obtained from the experiments are shown in Fig.6.6 in comparison with the model predictions. It is evident that the recovery is enhanced for a given purity corresponding to the basic four-step cycle. For instance, Exp. I and Exp. VI had similar purity, but the recovery increased by 14% for the LPP cycle, at 84% recovery in contrast with 70% for the basic four-step. Similarly, Exp. III and Exp. IX indicated an improvement in CO_2 recovery for a comparable purity. The results undoubtedly confirmed the enhancement of CO_2 recovery in the LPP cycle. Besides, the CO_2 purity values obtained from the experiments are very similar to the model predictions. There is a slight difference in the recovery between the experiments and the simulations. The purity-recovery shown in Fig. 6.3 was calculated from ten different cycles at CSS. The error bar indicated the uncertainty in the experiments. Exp. VII was repeated (VII.a and VII.b) to confirm the repeatability of the experimental configuration. Fig 6.6(f) showed the mass balance error of the four-step LPP cycle. It took longer to reach the cyclic steady state than the basic four-step, and the mass balance error at CSS was less than 5%.

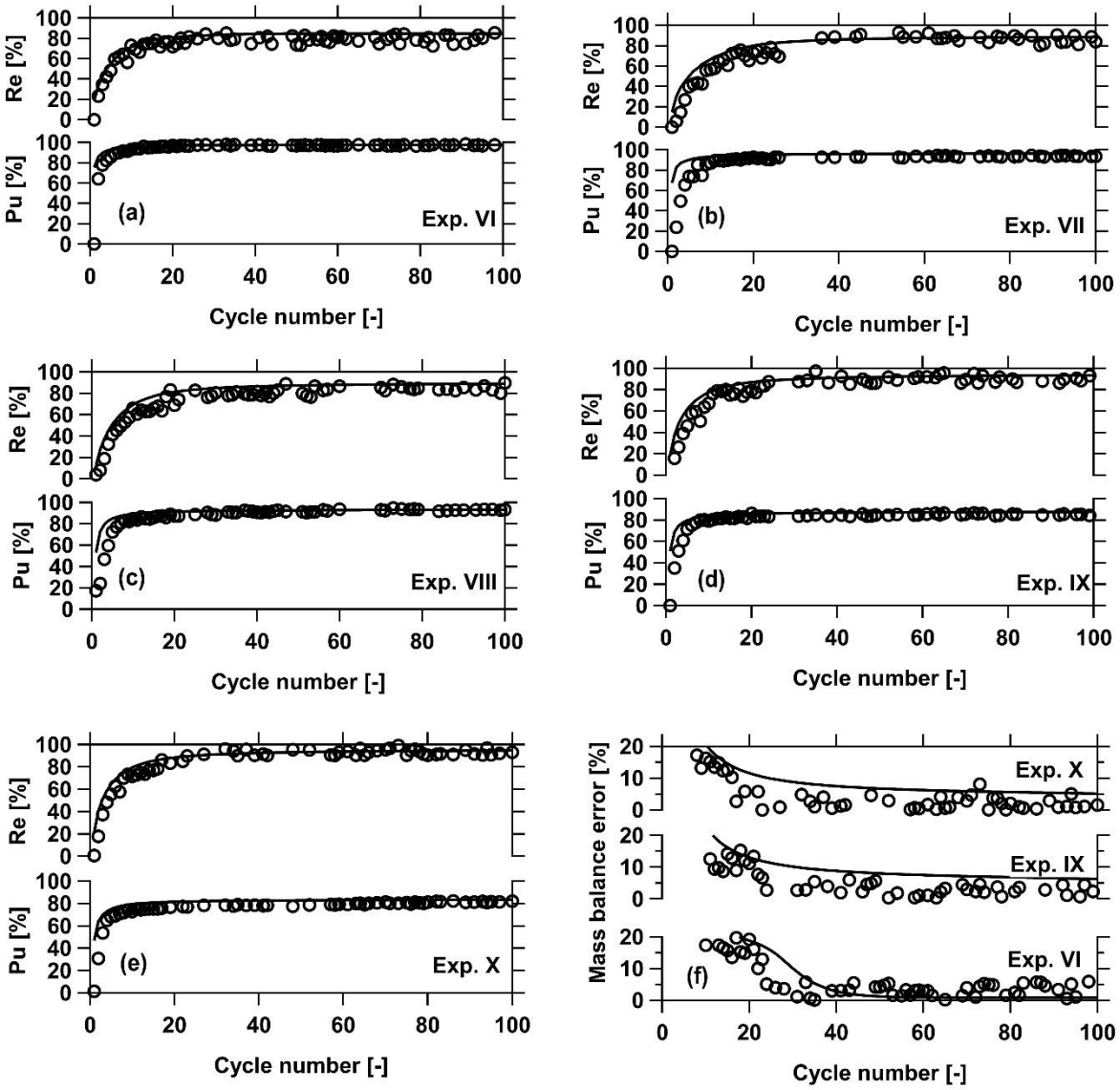

Figure 6.6: The evolution of purity-recovery over 100 cycles for the four-step with light product pressurization (LPP) under dry condition. Markers represent the experimental data, and solid lines are the simulated data. Fig. 6.6 (a-e) are the purity-recovery data from experiment VI (Exp. VI) to experiment X (Exp. X), respectively. Fig. 6.6 (f) is the total mass balance error over 100 cycles from experiments VI, IX, and X.

Figure 6.6 shows that the purity and recovery barely change after 20 cycles in all experiments (Exp. VI to Exp. X). The total mass balance error is convergent, and its values are less than 5% after ≈40 cycles. This result suggests that the CSS is reached. The purity was predicted very well in all experiments. The model is able to predict both the transition and the value of purity and

recovery over cycles. The experiments' total mass balance error shows a large oscillation during the first 20 cycles, but it is convergent and fluctuating in a small range at the CSS, e.g. less than 5%. Briefly, the model provides a good prediction for all experiments.

Figure 6.7 shows the transient histories of the four-step VSA with the LPP cycle from Exp. VII.a. The temperature histories at three different locations were captured well by the model (Fig 6.7a-b). A similar trend in the temperature history was observed in the four-step VSA with LPP. The temperature increased to a maximum value, then it dropped slowly and reached the cyclic steady state. The temperature peak represented the CO_2 front also moved along the column, but the magnitude of the temperature peak was smaller while travelling across the column. At cyclic steady state, the temperature fluctuated from 5°C to 8°C (Fig. 6.7b). Fig. 6.7b shows the temperature history for ten cycles during the CSS. An excellent prediction in the temperature at different locations of the column was obtained.

The model also described pressure history well, as shown in Fig. 6.7c. Note that there was a slight dip in the experimental pressure history during the LPP step. This is because of the pressure difference between the donor column (P_H) and the receiver column (P_L). In fact, a pronounced drop in the pressure was observed during the first LPP campaign, where the metering valve was not in place [174]. The pressure gap was a significant driving force, which made the pressure in the donor column suddenly drop. To reduce this effect, a metering valve was installed in the LPP line, which could facilitate the flow coming from the donor column to the receiver column. The pressure histories of the blowdown and evacuation steps were captured well using the same fitting parameters for the vacuum pump. As we indicated in the basic four-step cycle, it is important to precisely describe the pressure curves during the blowdown step and the evacuation step. Hence, the purity and recovery can be predicted well. In the LPP step, the model shows a sharp increase in pressure linearly. The experimental pressure history also shows a jump in pressure history but slightly non-linear. Afterwards, the pressure curve slope slightly decreased since the receiver column's pressure was close to the donor column.

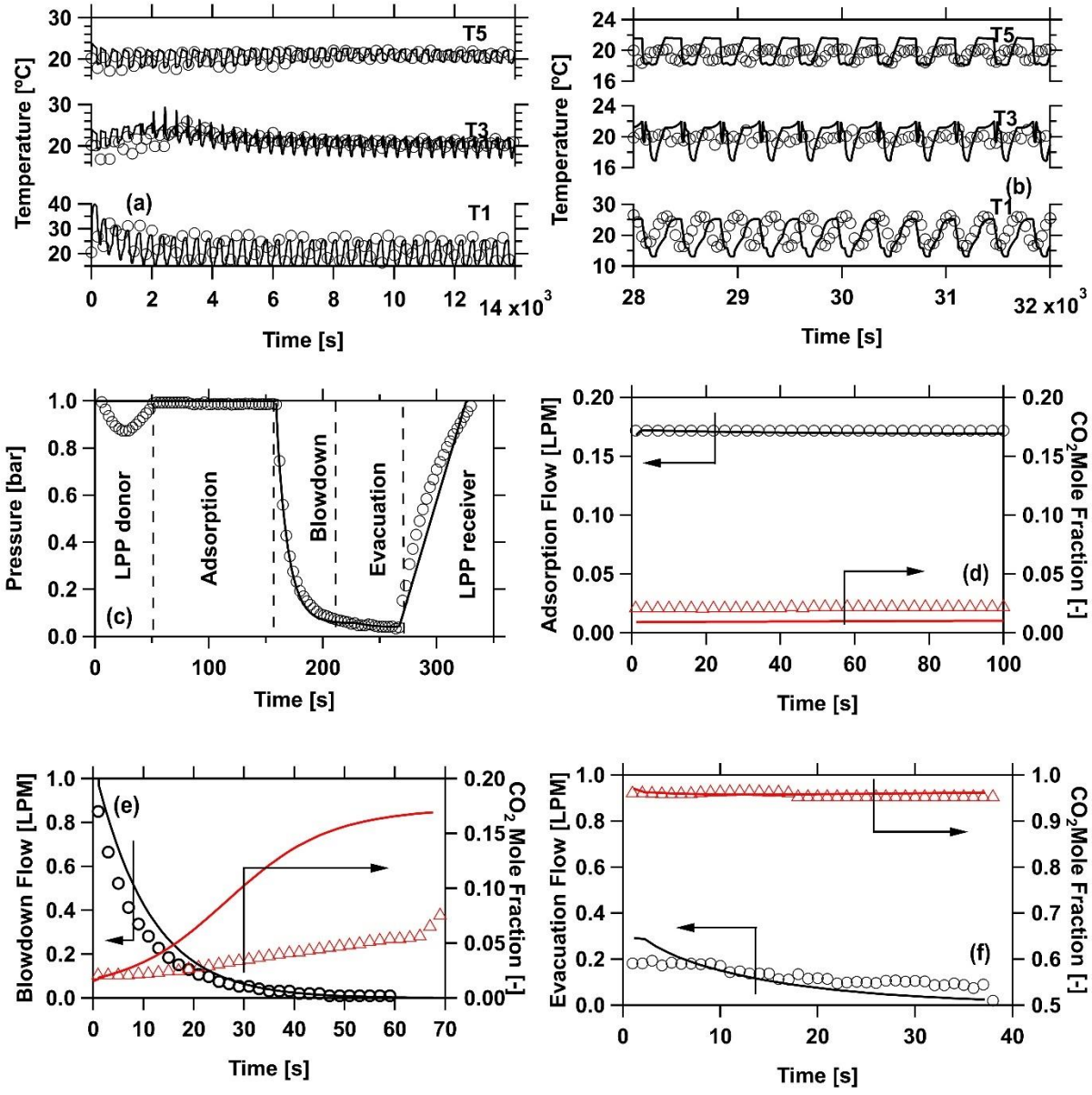

Figure 6.7: The comparison of experimental and simulated transients for the four-step VSA with the LPP cycle from experiment VII (Exp. VII.a). The solid lines represent the simulation data, and the markers are the experimental data. (a,b) The temperature histories at three positions in the column; (c) The pressure histories of one cycle at CSS; (d, e, f) The CO_2 composition and the outlet flow rate of the adsorption step, blowdown step and evacuation step, respectively.

Figure 6.7(d-f) show the transition of the outlet flow rate and the CO_2 mole fraction in the adsorption blowdown and evacuation step. In the adsorption step, the model predicted the outlet flowrate very well. Only a slight difference was seen in the CO_2 mole fraction between the experiment and the model, i.e. ≈1%. In the four-step LPP, the CO_2 mole fraction at the outlet during the adsorption step indicates a smaller value than the basic four-step at ≈2% vs 6%, respectively. This observation explains a higher recovery can be obtained in the four-step LPP. The light product pressurization helps to push the CO_2 front further down to the inlet end; thus, less CO_2 is lost during the adsorption, resulting in improved recovery.

The blowdown step also shows a good agreement between the simulation and the experiment. The outlet flow rate was captured well during this step. However, the CO_2 mole fraction between the simulation and the experiment still shows a discrepancy. Like the basic four-step, the transition of this step was quick, and the pressure dropped quickly within ten seconds. The flow rate was also reduced rapidly, and its value was relatively low afterwards. Hence, it is difficult for the CO_2 analyzer to respond promptly, leading to a smaller CO_2 mole fraction value. However, the overall prediction is still reasonable since the flow rate is very low, i.e. close to zero, which does not have a significant contribution to the error. Briefly, the transient profiles between the experiments and the simulation are comparable.

The obtained results confirmed the superiority of the LPP cycle. A higher recovery was obtained at a comparable purity in comparison with the basic four-step cycle. The model predicted the transients well in both basic four-step and four-step LPP cycle. 95% of purity and 90% of recovery can be obtained from the LPP cycle.

6.5. Conclusions

Two adsorption configurations were studied to evaluate the performance of CALF-20 under dry conditions. The basic four-step VSA represents a classic adsorption cycle, and the four-step with light-product pressurization (LPP) cycle represents the simplest and the most effective cycle for post-combustion CO_2 capture. A multi-objective optimization was performed to obtain the Pareto curves, which indicate the highest purity-recovery could be achieved under certain conditions. The basic four-step could obtain a 95% purity and 70% recovery using CALF-20. The four-step LPP proved that a higher recovery could be achieved with a comparable purity, at 95% purity and 90% recovery. This result agreed with previous studies reported earlier.

To validate the model predictions, both basic four-step VSA and four-step with LPP cycle were implemented experimentally. Five distinct points on the Pareto curves in each configuration were chosen with a set of different operating conditions. One column was required to perform the basic four-step cycle, while the four-step LPP cycle needed two identical columns. The purity-recovery over a hundred cycles and the transient histories were compared with the model predictions. Both cycles showed a good agreement with the predictions. Only a slight difference in purity and recovery was observed at approximately ± 2%. This is because the blowdown and evacuation step were terminated by a pressure trigger. Thus, the duration of these steps between cycles was slightly different. The temperature histories at different positions, the pressure histories, the CO_2 mole fraction and the outlet flowrates in every step were also compared with the simulation. The temperature and pressure histories indicated an excellent agreement with the prediction. The CO_2 mole fraction and the outlet flowrate during the adsorption, blowdown and evacuation were also in good agreement. The results confirmed the validation of the model predictions.

The experimental results obtained from ten different cycle experiments strongly support the validation of the rigorous optimization approach. The model successfully predicts process performances based on the column parameters described by the dynamic column breakthrough experiments. It is worth noting that the description of the pressure history in the blowdown step and evacuation step is of importance. A slight discrepancy between the experiments and simulations might result in significant differences. The Pareto curve obtained from the optimization provides a better guide to optimize the process. Fewer experiments are required to optimize the adsorption process. Thus, the entire optimization process is shorter. The transient history of the pressure, flow rate and CO_2 concentration were well described by the model. The purity and recovery evolution over cycles were also well captured. The results of this study confirmed the efficiency of the rigorous optimization approach.

7 Experimental Demonstration Of Humid Post-Combustion CO_2 Capture By Vacuum Swing Adsorption

7.1. Introduction

Studying CO_2 capture under humid conditions is challenging due to many uncertainties associated with a humid environment [87, 129]. To the best of our knowledge, there are no experimental studies on the moist CO_2 adsorption process using metal-organic frameworks (MOFs). Several numerical studies on MOFs for CO_2 capture have been reported. Zhao and coworkers studied a four-step temperature swing adsorption (TSA) for dry CO_2 capture using Mg-MOF-74 and compared its performance with zeolite 13X [74]. Compared to zeolite 13X, Mg-MOF-74 showed higher productivity and less energy consumption using this configuration, at 0.1583 mole/m^3/s and 594 kWh/tonne, respectively [74]. In another study, Rajagopalan *et al*. evaluated the performance of Mg-MOF-74 and zeolite 13X for dry CO_2 capture using a four-step pressure swing adsorption (PSA) with light-product pressurization (LPP) [50]. The optimization results showed that zeolite 13X could obtain a lower energy consumption, at 114 kWh/tonne, while Mg-MOF-74 required 220 kWh/tonne to have similar productivity [50]. Performing an experimental adsorption process using MOFs, either wet or dry conditions, is still in need while the number of new MOFs keeps increasing robustly [172].

The flue gas from a power plant, specifically after SO_x and NO_x removal, is invariably saturated with H_2O. While water is not a big concern in liquid absorption, it is a major concern when used with solid sorbents. Very few studies in the literature have considered this situation. It is very challenging to perform a wet adsorption cycle experimentally due to numerous uncertainties. Controlling and recording the relative humidity in the feed, raffinate stream, and product stream is also difficult in a cyclic experiment. Water condensation that can potentially happen within the column is another concern. Very few studies on running a wet adsorption cycle were reported. Li *et al*. reported a three-step vacuum swing adsorption to separate CO_2 from the feed containing 95% RH using zeolite 13X [133]. The water loaded zone in the column was identified by a “cold spot”

as a result of the cooling and heating effect by CO_2/H_2O desorption/adsorption [177]. This water loaded zone tended to move further in the column by time. There were no relative humidity histories reported, and the recovery and productivity dropped by ≈20% in the presence of water within the length of the experiment [133].

It takes time to perform a wet cycle experiment, and monitoring a long experiment requires significant attention in every detail. The wet cycle itself usually reach the cyclic steady state after hundreds of cycles. Furthermore, each cycle also takes a longer time to finish than the dry cycles due to a long evacuation step. Each wet cycle experiment is completed after running for a couple of days to a week. However, it is crucial to understand the competition between CO_2 and H_2O in the cyclic experiment. By studying the transient histories of the temperature, CO_2 and H_2O across the column, we would have better insights into the column dynamic and adsorption kinetic in an adsorption process

In this work, two different case studies were examined to evaluate CALF-20 performance under humid conditions. The dry reference cases were chosen from the LPP Pareto curve reported in the previous chapter. In the first case study, we considered a high feed flow rate (v_{feed} = 0.081 m/s) with 97% purity and 72% recovery. In the second case study, we chose a lower feed flow rate (v_{feed} = 0.024 m/s) with higher recovery, at 94% purity and 86% recovery. The operating conditions of these Pareto points were evaluated under the dry condition first to verify the model prediction. Using the same operating conditions, humid cycles can be performed at various relative humidity (RH) values. A humidifier was used to create a humid feed, and the relative humidity was monitored by an RH meter. Before entering the column, the premixed gas (15% CO_2 and 85% N_2) travelled through the humidifier to create a certain relative humidity stream. It took 4-5 hours to reach a stable humid feed before starting the experiments. A wide range of RH was examined for each Pareto point: 13%, 25%, 45% and 70% RH. All the transient histories and the purity, recovery evolutions were recorded and compared with the dry cycles. The productivity evolution over cycles were also reported.

7.2. Materials and methods

7.2.1. Materials

Structured CALF-20 was synthesized and characterized by our colleagues at the University of Calgary. Polysulfone was used as a binder to structure the powder CALF-20. The obtained

adsorbent has a cylindrical shape with a diameter of 1 mm and a length of 1-3 mm. Premixed gas 15% CO_2 (balance N_2) was obtained from Praxair Canada Inc. Pure CO_2 (99.998%), pure N_2 (99.998%) were also purchased from Praxair Canada.

Single-component equilibrium isotherms of CO_2 and N_2 were measured at various temperature by volumetric and gravimetric methods. Pure H_2O isotherms at various temperatures were collected using the thermogravimetric analyzer (TGA). The adsorption and desorption H_2O isotherms at 22°C were also measured by the Micromeritics ASAP 2020 (Norcross, GA, USA) equipped with water vapor generation available at the University of Calgary (Shimizu's group). The adsorbent was activated at 150°C for 12 hours prior to each measurement. All isotherms data are reported in previous chapters.

7.2.2. Humid vacuum swing adsorption apparatus

A similar vacuum swing adsorption (VSA) apparatus from chapter 6 was used in this study. To perform the humid cycle, a bubble humidifier was retrofitted in the current VSA setup. The schematic of this humid VSA is shown in Fig. 7.1.

The four-step vacuum swing adsorption with light-product pressurization (LPP) configuration is chosen to study the humid CO_2 capture. Two identical stainless-steel columns (L = 26.5 cm, d_{in} = 2.1 cm) are required to perform the LPP cycle, each column was packed with 36.0 g of structured CALF-20. The humid feed was created by controlling the ratio of the wet and the dry flows using two mass flow controllers MFC-1 and MFC-2 (Alicat Scientific, Tucson, AZ, USA). The pressure at each end of the column was measured by a pressure transducer, e.g. PT-1 to PT-4 (Omega Engineering, USA). The column temperature was measured at different locations, i.e. T1 to T6 (Omega Engineering, USA) placed at 1 cm, 4 cm, 7.8 cm, 11.5 cm, 15.5 cm and 19 cm from the the column inlet. The columns were evacuated using two diaphragm vacuum pump, VP-1 and VP-2 (Pfeiffer Vacuum MVP 040-2, Germany). The CO_2 composition at the outlet of each step was measured by three CO_2 analyzers A_1 to A_3 (Quantek Instruments, Model 906, USA). The relative humidity at the inlet and at the outlet of each step were recorded using four relative humidity meters RH1 to RH4 (SensorPush, Brooklyn, NY, USA). The experimental device was controlled automatically using electrically activated solenoid valves (Peter Paul Electronics Co., USA). A LabVIEW data acquisition system was used to control all equipment and to record all data during the experiment. Prior to each experiment, all mass flow controllers and mass flow meters were

calibrated at different CO_2/N_2 compositions and flow rates using a flow calibrator (Defender 510, Mesa Labs, USA). The CO_2 analyzers were calibrated using different gases whose compositions were known. The relative humidity meters were calibrated using saturated magnesium chloride and sodium chloride solutions.

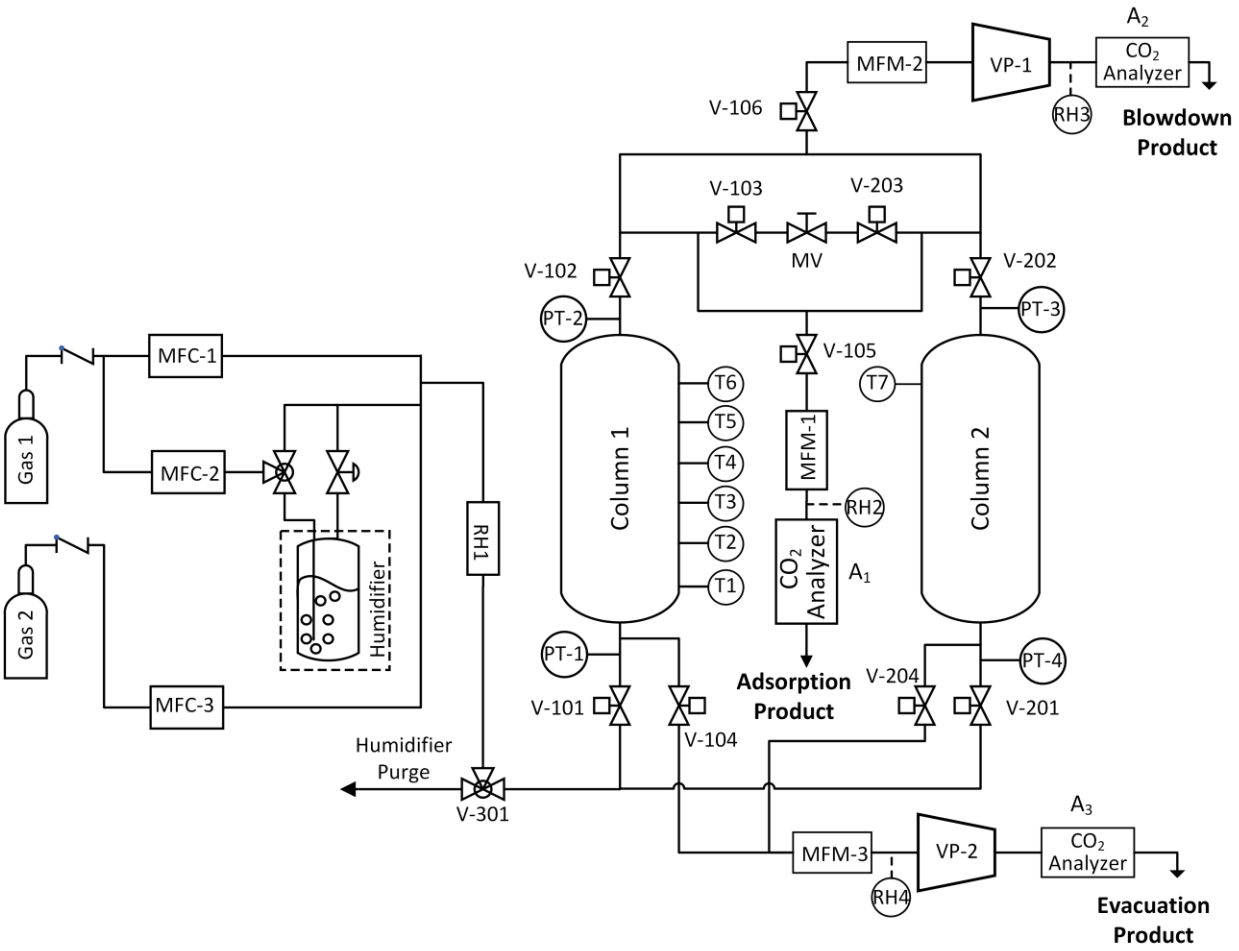

Figure 7.1: Humid vacuum swing adsorption apparatus. MFC - Mass flow controller; MFM - Mass flow meter; RH – Relative humidity meter; PT – Pressure transducer; T1 to T7 - Thermocouple 1 to 7; A_1 to A_3 – CO_2 analyzer 1 to 3; V-101 to V-301: Solenoid valves; MV – metering valve; VP – vacuum pump.

7.2.3. Four-step vacuum swing adsorption with light-product pressurization configuration

The four-step VSA with LPP consists of an adsorption step, a blowdown step, an evacuation step and a light-product pressurization step. To perform the LPP step, a part of the raffinate in the adsorption step from the first column is used to pressurize the second column and vice versa. Thus,

the donor column is under the adsorption step, while the receiver column is in the LPP step. The specific configuration of this cycle is indicated in Fig. 7.2.

Adsorption (ADS): The feed gas (15/85 CO_2/N_2) is introduced to the column at z = 0. The pressure is maintained at high pressure P_H during this step. Most of the N_2 is collected at the raffinate end (z = L), while CO_2 is trapped in the column.

Blowdown (BD): The feed gas is terminated, and the column is evacuated from the raffinate end (z = L). The pressure decreases from high pressure to intermediate pressure P_I. The step supports to further remove N_2 from the bed and concentrate the CO_2.

Evacuation: The feed end (z = 0) is opened and the raffinate end (z = L) is closed. The pressure of the column is further evacuated to low pressure (P_L). The product rich in CO_2 is collected from the column in this step.

Light-product pressurization (LPP): The receiver column is pressurize using part of the raffinate product from the donor column, which is going through the adsorption step. The pressure of the receiver column increases from low pressure (P_L) to high pressure (P_H). The purpose of this step is to pressurize the column and sharpen the CO_2 front in the column, hence higher recovery can be obtained.

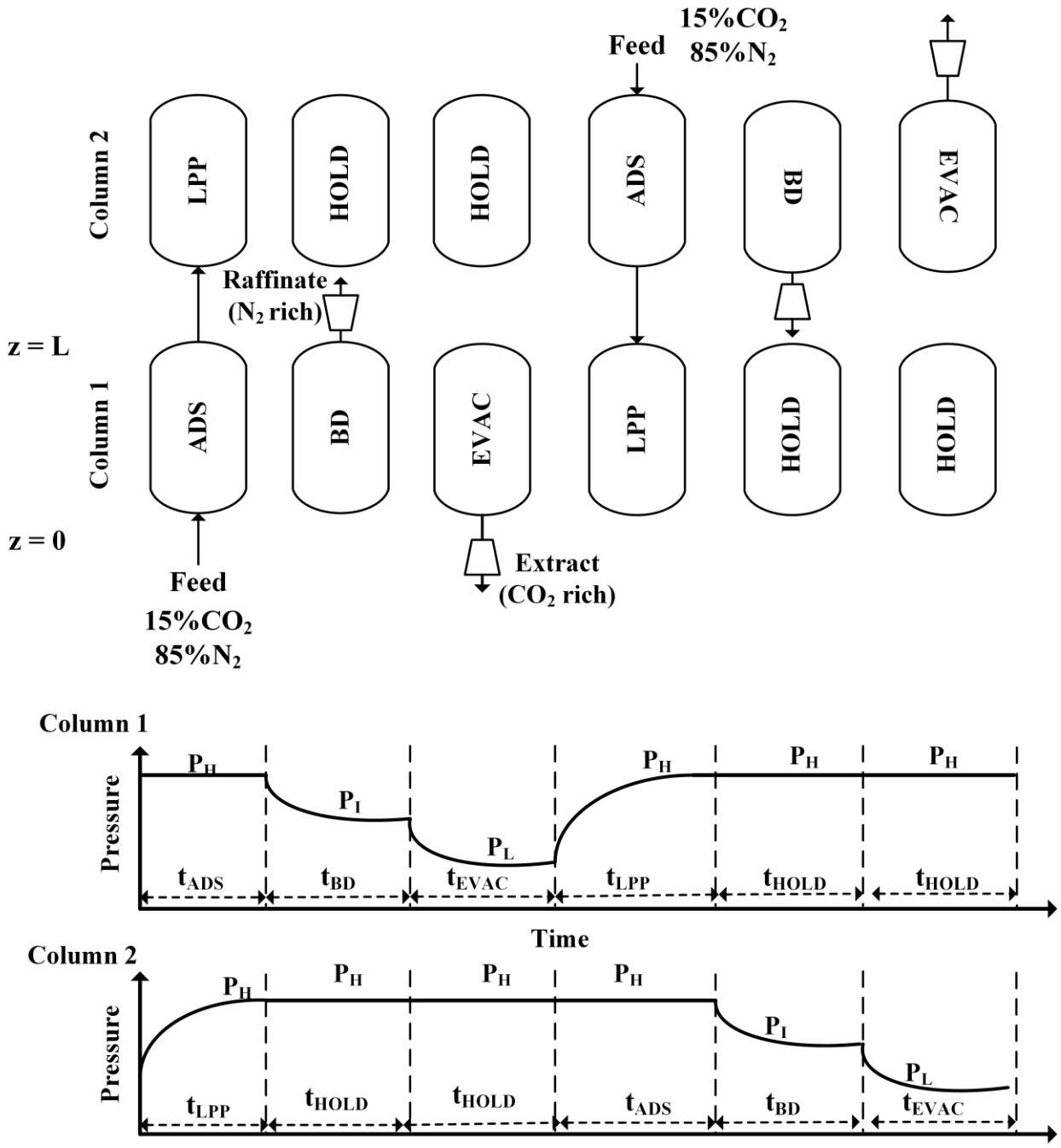

Figure 7.2: Four-step vacuum swing adsorption with light-product pressurization configuration. ADS – Adsorption; BD – Blowdown; EVAC – Evacuation; LPP – Light product pressurization; P_H – High pressure; P_I – Intermediate pressure; P_L – Low Pressure.

7.2.4. Cyclic steady state calculations

Numerous cycles are performed prior to reach the cyclic steady state. In this configuration, a minimum of 100 cycles is required, and the mass balance errors can be checked using the following expression (Eqn. 7.1):

$$\text{Mass balance error [\%]} = \frac{|mass_{in} - mass_{out}|}{mass_{in}} \times 100\% \tag{7.1}$$

Where $mass_{in}$ and $mass_{out}$ are the total amount of mass entering and leaving the system in one cycle at cyclic steady state. The CSS is considered to be reached when the mass balance error is less than 3% for ten consecutive cycles. The CO_2 purity, recovery and productivity of each cycle can also be estimated, defined as:

$$\text{CO}_2 \text{ Purity } (Pu_{CO_2}, \%) = \frac{n_{CO_2,EVAC}}{n_{CO_2,EVAC} + n_{N_2,EVAC}} . 100\% \tag{7.2}$$

$$\text{CO}_2 \text{ Recovery } (Re_{CO_2}, \%) = \frac{n_{CO_2,EVAC}}{n_{CO_2,ADS}} . 100\% \tag{7.3}$$

$$\text{CO}_2 \text{ Productivity } (Pr_{CO_2}, mol_{CO_2} m^{-3} s^{-1}) = \frac{n_{CO_2,EVAC}}{V_{Adsorbent} t_{cycle}} \tag{7.4}$$

where n_{CO_2} and n_{N_2} are the number of moles of CO_2 and N_2, $V_{Adsorbent}$ is the total volume of the adsorbent packed in the column, and t_{cycle} is the total duration of one cycle.

7.3. Results and discussions

Capturing carbon dioxide from a flue gas under a humid environment is challenging because of a low concentration of CO_2 (12% - 15% CO_2) and strong competition of water vapour. CALF-20 has shown a high affinity of CO_2, and the water capacity is strongly affected by the adsorption of CO_2 depending on the relative humidity (RH). By exploiting process conditions where the adsorption of CO_2 is favourable, an effective adsorption process of CO_2 in the humid environment could be designed. In this study, four-step with light product pressurization (LPP) were examined under wet conditions and compared with dry conditions. The transient histories of the wet and the dry cycles were compared to evaluate the performance of CALF-20 under the moist conditions. Two relative humidity ranges were studies: low to intermediate RH and intermediate to high RH. The specific operating conditions are given in Table 7.1.

Table 7.1: List of four-step VSA with LPP cycle experiments under humid condition

RH	Exp.	t_{ads}	P_I	P_L	v_{feed}	Experimental		
[%]		[s]	[bar]	[bar]	[m/s]	*Pu* [%]	*Re* [%]	*Pr* mol $CO_2/m^3/s$
Case study 1								
Dry	A0	180	0.119	0.032	0.081	97	72	0.57 ± 0.02
13	A1	180	0.119	0.032	0.081	97	70	0.56 ± 0.03
25	A2	180	0.119	0.032	0.081	97	68	0.56 ± 0.03
45	A3	180	0.119	0.032	0.081	97	71	0.56 ± 0.03
70	A4	180	0.119	0.032	0.081	96	67	0.55 ± 0.03
Case study 2								
Dry	B0	157	0.046	0.031	0.024	94	86	0.14 ± 0.01
14	B1	157	0.046	0.031	0.024	94	72	0.13 ± 0.02
25	B2	157	0.046	0.031	0.024	93	70	0.13 ± 0.02
45	B3	157	0.046	0.031	0.024	94	74	0.13 ± 0.02
70	B4	157	0.046	0.031	0.024	92	70	0.13 ± 0.02

7.3.1. VSA experiments from low to intermediate relative humidity (0% to 45% RH)

In the competitive CO_2/H_2O adsorption study, CALF-20 showed favourable adsorption of CO_2 over H_2O when the relative humidity was below 40% RH. To verify this observation, we performed the VSA with LPP cycle at 13%, 25% and 45% relative humidity. The column temperature history at different positions, the pressure histories, the CO_2 mole fraction transients, the inlet and outlet flowrate in each step and the purity and recovery were recorded and compared with the dry cases.

The temperature histories at three different locations in the column are indicated in Fig. 7.3. Both case studies showed a similar temperature evolution between the dry case and wet cases. There was no obvious difference in these transitions, no matter what the relative humidity was. The temperature transitions at different positions were overlapping in these cases. The length of each wet cycle was also comparable with the dry cases.

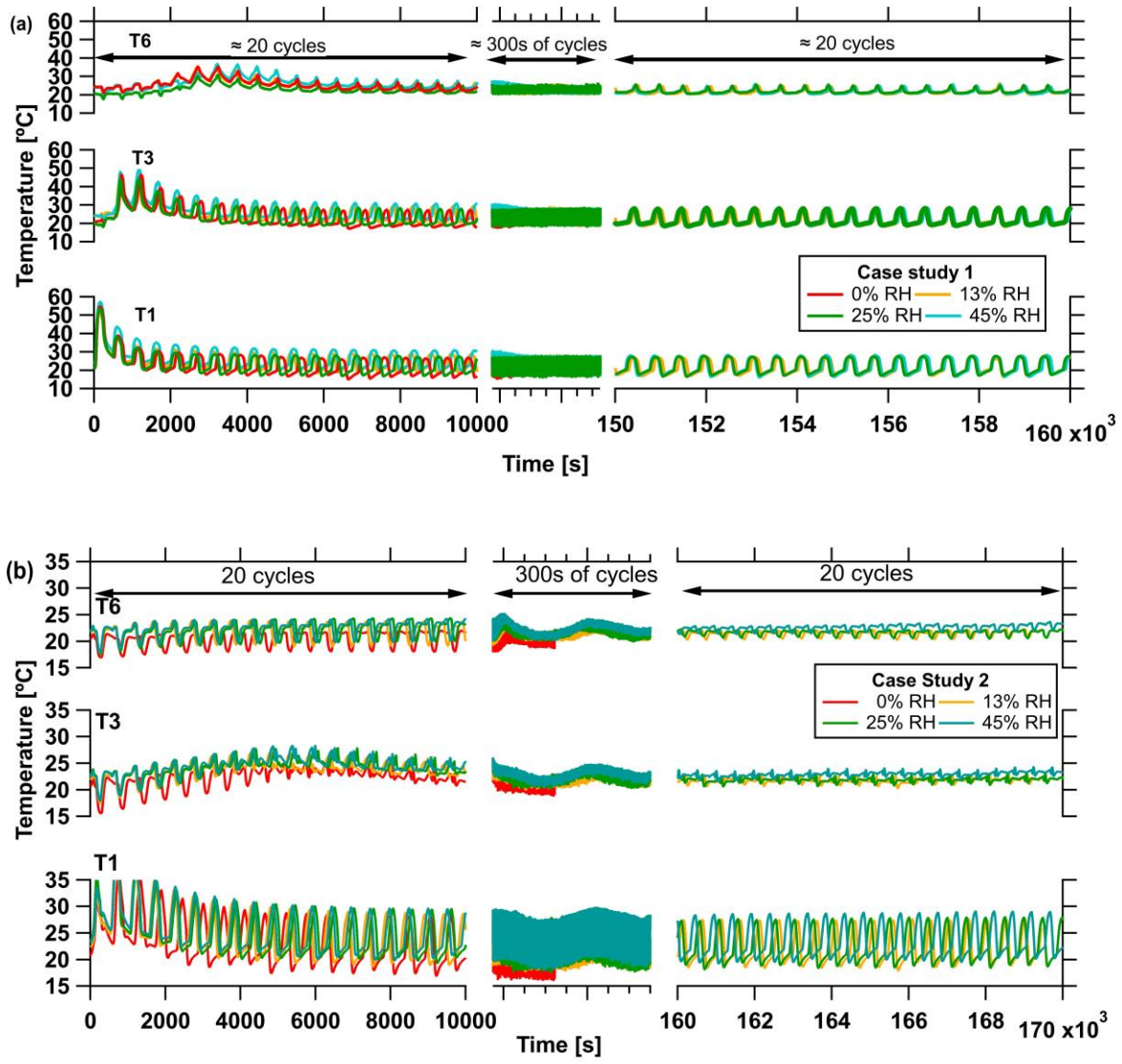

Figure 7.3: Temperature histories at three different positions in the column from low to intermediate relative humidity (0% to 45% RH). T1, T3 and T6 were placed at 1 cm, 8 cm and 19 cm from the feed inlet. (a) Case study 1; (b) Case study 2

In the first case study, the temperature peak was observed in the first 20 cycles, and it propagated close to the raffinate end of the column (Fig. 7.3a). Depending on the location of the thermocouple, the magnitude of the temperature peak varied from 20°C to 40°C. A higher temperature peak was observed close to the feed end of the column. When the temperature peak propagated further to the raffinate end of the column, its magnitude decreased because of the convective heat transfer. Afterwards, the temperature slowly decreased and fluctuated in a small range at the cyclic steady state (5°C to 10°C). The temperature transitions indicated that the cyclic steady state was reached

after the 20s of cycles, and they maintained the same over hundreds of cycles. There was no difference between the wet and the dry cycles at low to intermediate relative humidity.

In the second case study, a similar transition was recorded (Fig. 7.3b). However, the temperature peak was smaller (10°C to 20°C), and we did not observe this temperature peak at the thermal couple six (T6). The lower flow rate produced less heat, and the heat transfer through the walls led to the cooling down of the temperature peak. Thus, the magnitude of the temperature peak in the second case study was lower compared to the first case. Then, it slowly decayed and remained in a small range at the cyclic steady state. Similarly, the cyclic steady state was established after the 20s of cycles, and the wet and the dry cycle transients were observed to overlap. The results implied that water has little effect on the CO_2 adsorption at the low to intermediate relative humidity. The temperature transitions in both case studies showed a similar tendency and the cyclic steady state was reached after around 20 cycles. The results agree with the competitive CO_2/H_2O DCB studies, where CO_2 is strongly adsorbed at RH<45%. Note that we did not observe any "cold-spot" in the column in all experiments. In the case of zeolite 13X, the propagation of water in the column was characterized by a "cold-spot" where there was a minimum in the temperature curve [119, 177]. This was because the large amount of CO_2 was desorbed due to the water adsorption leading to a decrease in the temperature.

Figure 7.4 shows the evolution of the CO_2 mole fraction in the adsorption, blowdown and evacuation step for both dry cycle and wet cycles. Once again, there was no distinct difference recorded between the dry and wet cycles at low to intermediate relative humidity. Both case study one and case study two shared similar qualitative trends. In the adsorption step, the CO_2 mole fraction slowly increased from 0% to 5%. After around 20 cycles, the CO_2 mole fraction oscillated between 3% to 5% and no further trend was observed. The CO_2 mole fraction evolution in the blowdown and evacuation step also showed similar trends. They gradually increased from 0% and reached the cyclic steady state after the 20s of cycles. The CO_2 mole fraction in the blowdown step was 8% to 10% at the CSS, while it was over 90% during the evacuation step, which was comparable with the dry case value. To confirm that no further change occurred, the CO_2 mole fraction transients at the 300s of cycles were also analyzed, and they were identical with previous cycles, which implied the CSS was established. This observation strengthened the expectation that

the CO_2 was favourably adsorbed, and water did not have a significant effect at low to intermediate relative humidity.

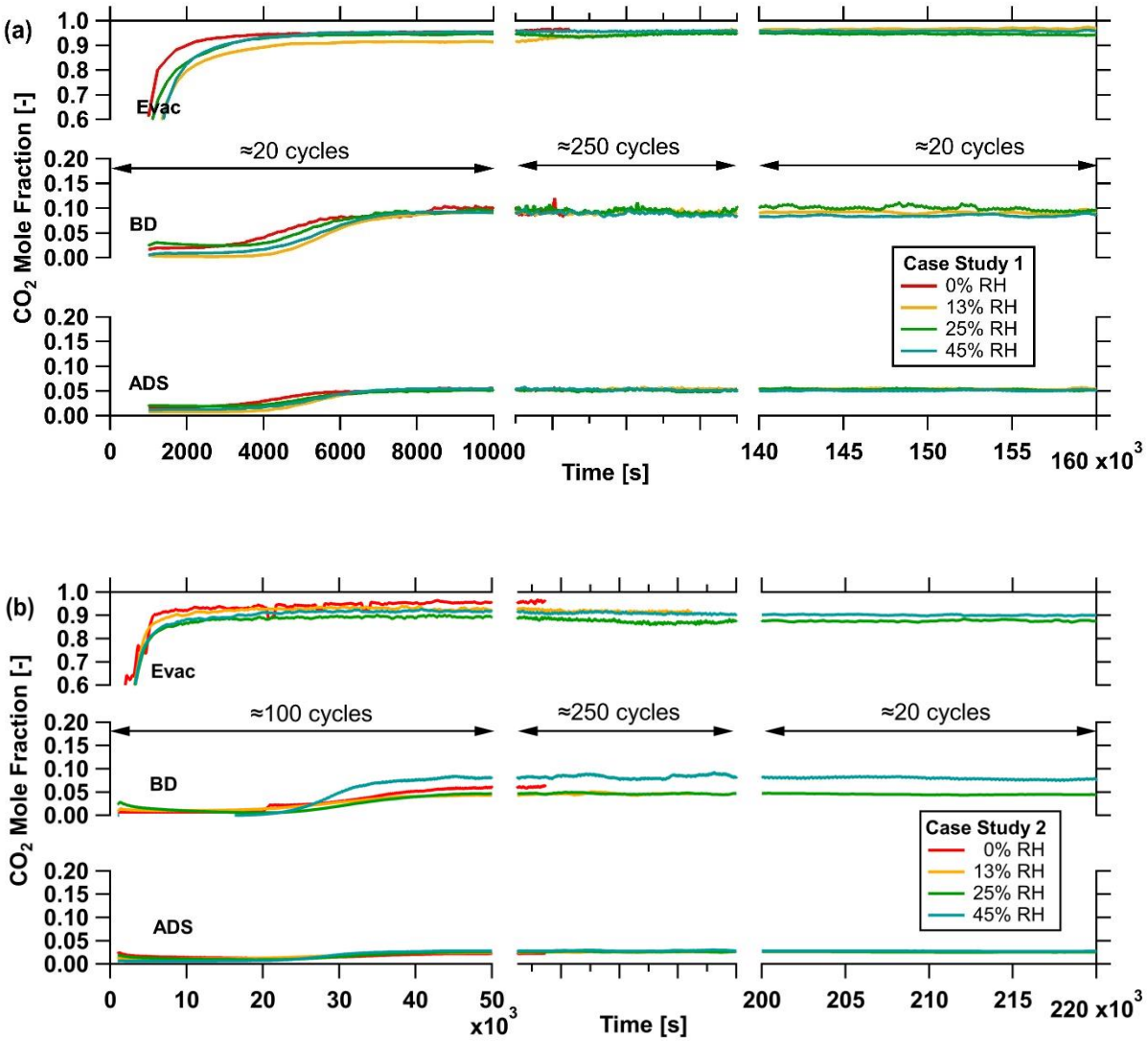

Figure 7.4: CO_2 mole fraction evolution during the adsorption, blowdown and evacuation step from low to intermediate relative humidity (0% to 45% RH). (a) Case study 1, the middle period was from 10,000 s to 140,000s; (b) Case study 2, the middle period was from 50,000 s to 200,000 s. ADS – Adsorption step; BD – Blowdown step; Evac – Evacuation step

The relative humidity histories at the feed inlet and at the outlet of the adsorption, blowdown and evacuation are indicated in Fig. 7.5. Note that the RH meter in the evacuation step was placed upstream of the vacuum pump to prevent water from condensing in the housing. Both case study

1 and case study 2 shared similar RH evolutions over the course of the experiment. A stable RH value at the feed inlet was indicated in each experiment. This observation confirmed that the humid feed created by the humidifier was constant at the desired value over the whole experiment.

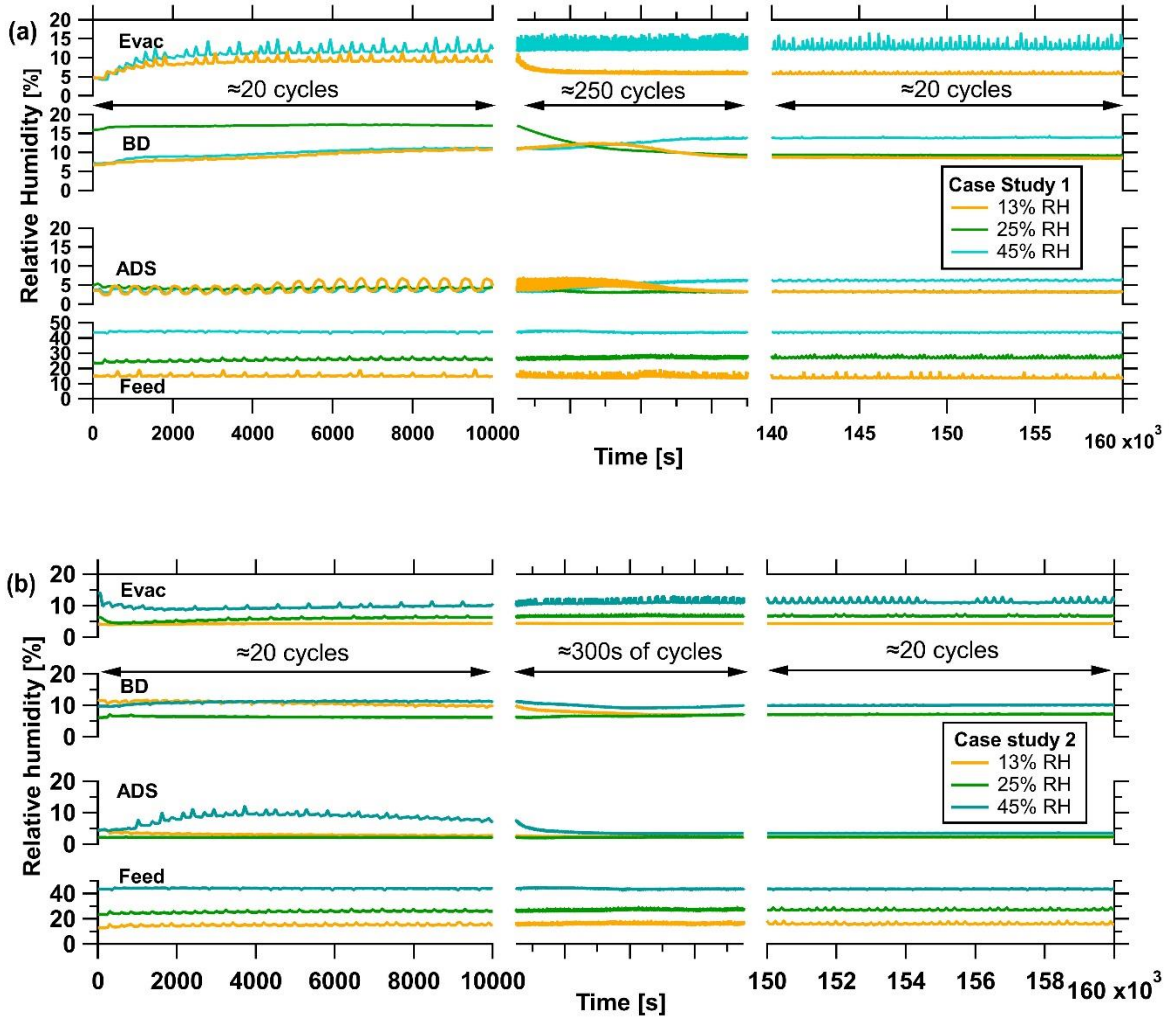

Figure 7.5: Relative humidity transient histories at the outlet of the feed, the adsorption, blowdown and evacuation step from low to intermediate relative humidity (0% to 45% RH). (a) Case study 1; (b) Case study 2.

In the adsorption step, the relative humidity at the raffinate outlet was at 4% - 8% during the first 20 cycles in each experiment (Fig. 7.5). This RH value was also comparable with previous cycles at the 300s of cycles in all wet experiments. This observation implied that a small amount of water broke through the column during the adsorption step. The RH in the blowdown step also showed

a similar trend, but a higher value of RH was recorded at 8% - 15% RH. More water was removed from the bed during the blowdown step due to a low affinity of water on the solid surface under the low pressure. In the evacuation step, the RH gradually increased and fluctuated between 8% - 15% RH. Although the RH value was similar to the blowdown, the RH meter was placed upstream of the vacuum pump. The RH was significantly higher if the RH meter was placed downstream of the vacuum pump. In fact, a little amount of water condensed after leaving the vacuum pump during the evacuation step at 45% RH, whose gas was fully saturated with water vapour. No condensation was observed in the case of 13% and 25% RH. Placing the RH meter upstream of the vacuum pump also allowed to calculate the mass balance of water around the column. The total water mass balance error was at 5% to 10% for each cycle over the length of each experiment.

The water condensation during the evacuation step indicated that a large amount of water was removed from the column. This result confirmed that water could be desorbed easily from CALF-20 at low pressure and low to intermediate relative humidity. In contrast, it is problematic to remove water from zeolite 13X. High temperature and long activated time are required to regenerate the column [87]. In the cyclic experiment, a part of the column is "poisoned" by the adsorption of water using zeolite 13X [133, 177]. The column needs to be guarded by filling with a layer of activated alumina, or the flue gas requires a pre-treatment to remove the water prior to entering the column [88, 133]. Briefly, CO_2 is favourably adsorbed on CALF-20 at low to intermediate relative humidity. The result is consistent with the competitive CO_2/H_2O adsorption isotherm reported in chapter 4. Water does not seem to have a significant impact on the CO_2 adsorption under this condition, and it is also easy to remove water from the column.

The purity and recovery evolution for each experiment of both case studies were indicated in Fig. 7.6. There was no obvious difference observed in the purity over hundreds of cycles between the dry and the wet experiments. In fact, the purity of the wet cycles was overlapping with the dry case, which implied that there was no loss in the purity at low to the intermediate relative humidity in both case studies. After around 20 cycles, the purity reached close to its value at the cyclic steady state. Afterwards, it maintained constantly over the course of the experiment. In the first case study, the purity was approximate 97%, and in the second case study, it was 94%. These values are comparable with the purity of the dry case (Table 7.1).

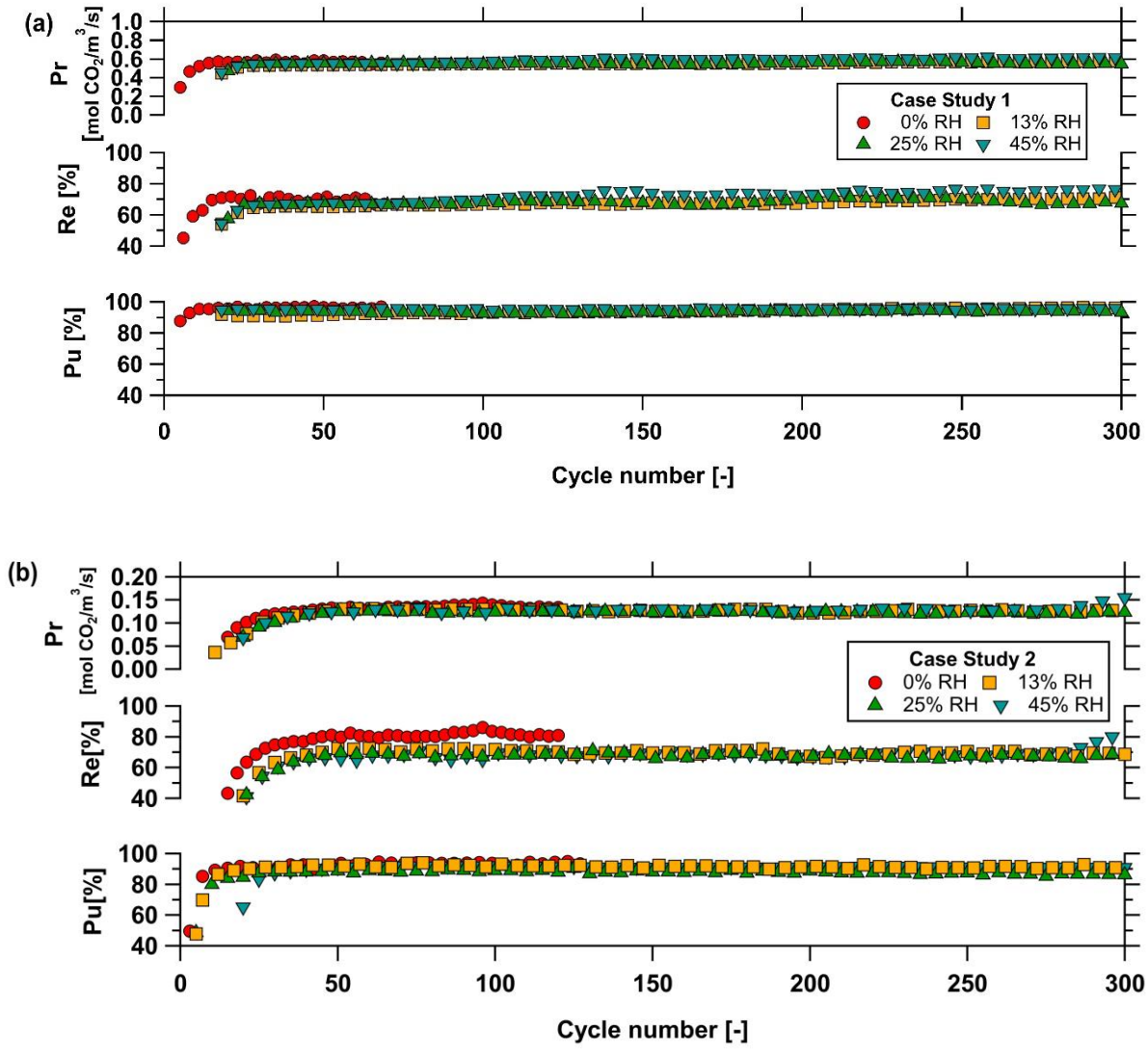

Figure 7.6: Purity (Pu), recovery (Re) and productivity (Pr) evolution after hundreds of cycles at low to intermediate relative humidity (0% to 45% RH). (a) Case study 1; (b) Case study 2.

Similarly, the recovery evolution also showed an overlap at different relative humidity values (Fig. 7.6). However, its value was lower than the dry case in both case studies (Table 7.1). The recovery fluctuated in the range of ± 5% since the length of the evacuation step was slightly different between cycles. The recovery reported here was the average value of 20 consecutive cycles, approximately 70% and 75% for the first and the second case study, respectively. The standard deviation for all experiments was around 5%. The oscillation in the recovery evolution was also seen in a VSA cycle study reported by Perez *et al*. [174].

The productivity was defined as the total number of moles of CO_2 recovered in the evacuation step per volume of the adsorbent per second. The average cycle time of case study 1 and 2 was 310 s and 290 s, respectively. The productivity was also comparable with the dry cycle in both case study 1 and case study 2, at 0.57 mol $CO_2/m^3/s$ and 0.14 mol $CO_2/m^3/s$, respectively. A higher feed flowrate showed better productivity. Overall, there was no change in the purity and productivity between the wet and the dry cycles at low to intermediate relative humidity. The recovery of wet cycles was lower than the dry case. The water does not have a significant impact on the CO_2 separation under these conditions. The results suggest that CALF-20 is a potential candidate for CO_2 capture at low to intermediate relative humidity without losing purity and productivity.

7.3.2. VSA experiments at high relative humidity (70% RH)

As discussed earlier, at RH>40%, the competitive CO_2 capacity is severely decreased. Under high RH conditions, the performance of CALF-20 can be severely impacted. Nevertheless, we were interested in performing experiments at high RH to understand the dynamics of the process and the performance of the material.

To further evaluate the effect of water on CALF-20, higher relative humidity cycles were implemented for both case study 1 and case study 2. The competitive CO_2/H_2O adsorption isotherm shows an inflection point at approximately 65% RH. Above the inflection point, the CO_2 loading quickly decreases, and the H_2O adsorption becomes stronger. When the relative humidity is greater than 70%, the competitive water loading reaches the saturation capacity, and the competitive CO_2 loading is closed to 0 mmol/g. To verify this behaviour, the four-step VSA with LPP was performed at 70% RH. All transient histories, purity, recovery and productivity of each experiment were compared with the dry case and the wet case at 45% as references and shown in Fig. 7.7.

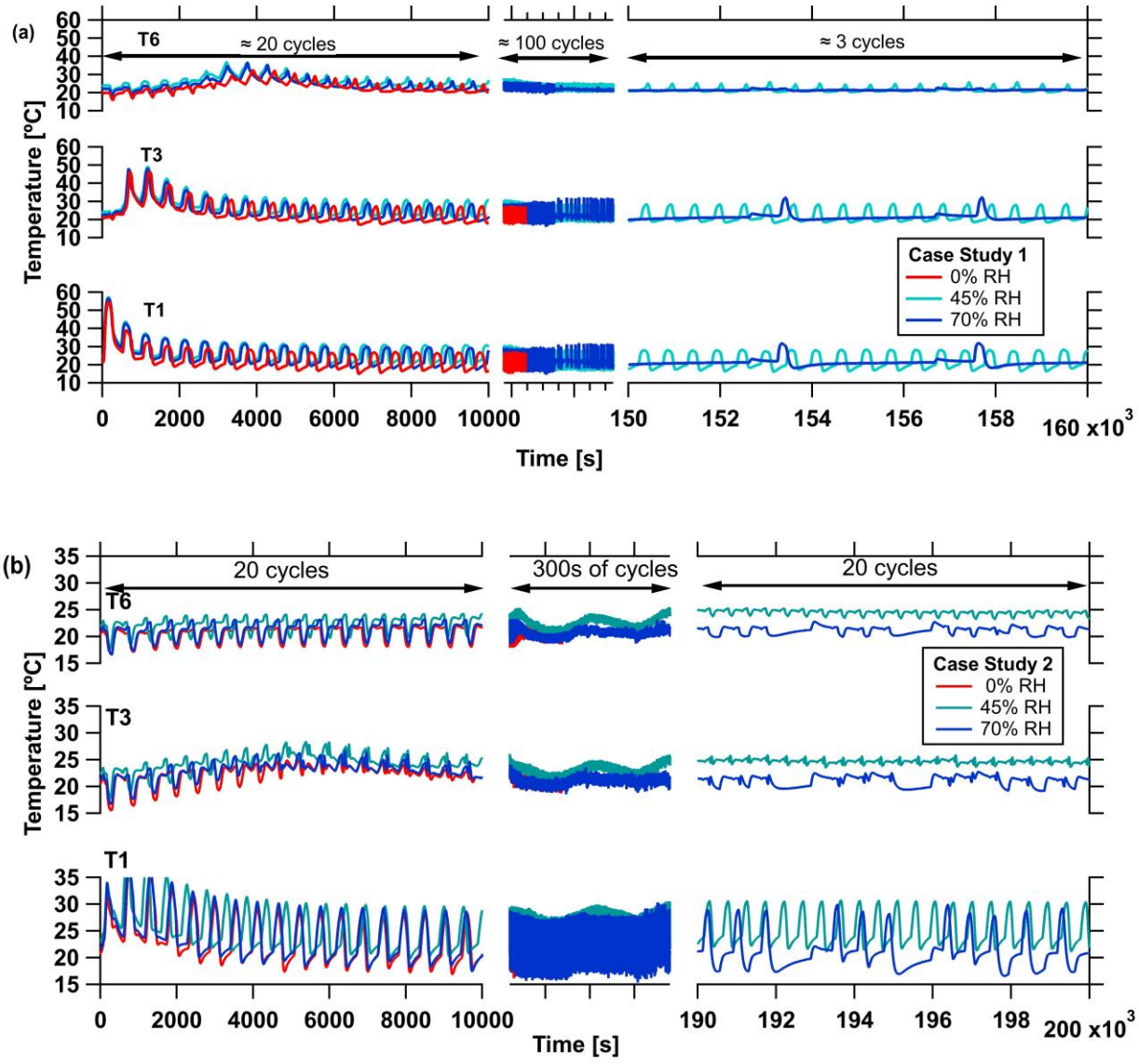

Figure 7.7: Temperature histories at three positions in the column from intermediate to high relative humidity (45% RH to 70% RH). T1, T3 and T6 were placed at 1 cm, 8 cm and 19 cm from the feed inlet. (a) Case study 1; (b) Case study 2.

Figure 7.7 shows the temperature history of the wet cases and dry cases. In the first 20 cycles, we could see a similar transition in the temperature at different positions of the column. The temperature reached a peak, and it propagated across the column, which we also saw in the low to intermediate RH cases. The magnitude of the temperature was also comparable, which indicated a similar CO_2 heat of adsorption in those cases. Afterwards, it decayed and fluctuated within a small range of temperatures, at 5°C - 10°C. However, in the first case study, a different history was seen

at 70% RH beyond the 100s of cycles. The distance between two temperature peaks was farther apart, which indicated that the duration of the cycle was longer due to a longer evacuation step, up to 3600 seconds. The magnitude of the temperature was still comparable. The possible water condensation caused a longer evacuation step. In fact, a large amount of liquid water was seen downstream of the vacuum pump, which made it harder to reach the low pressure. The column pressure was at around 0.038 bar for thousands of seconds while the low pressure was set at 0.031 bar. The evacuation step was terminated after 3600 seconds. The duration of this step also varied between cycles, which confirmed the effect of water condensation on the vacuum pump performance. In the second case study, a similar cycle length was observed for the first 300 cycles. Afterwards, the evacuation step of several cycles was also longer than the previous ones. The column was still able to reach the low pressure after thousands of seconds. Note that this happened occasionally, it did not apply for every cycle. This observation confirmed that water condensation made the evacuation step harder to operate and control.

The CO_2 mole fraction at the outlet of the adsorption, blowdown and evacuation showed a similar trend with the dry case in both case studies (Fig. 7.8). In the adsorption step, the CO_2 mole fraction increased from 0% to 5% after around 20 cycles. It maintained at that value during the whole experiment for both wet and dry cycles. The blowdown step also showed a gradual increase in the CO_2 mole fraction, and it maintained at 8% - 10%. However, a slight decrease in the CO_2 mole fraction was seen in the evacuation step for both case studies. During the first 50 cycles, the CO_2 mole fraction of the first and the second case study was at 95% and 91%, respectively. No obvious change was recorded in the second case study, where a lower feed velocity was used.

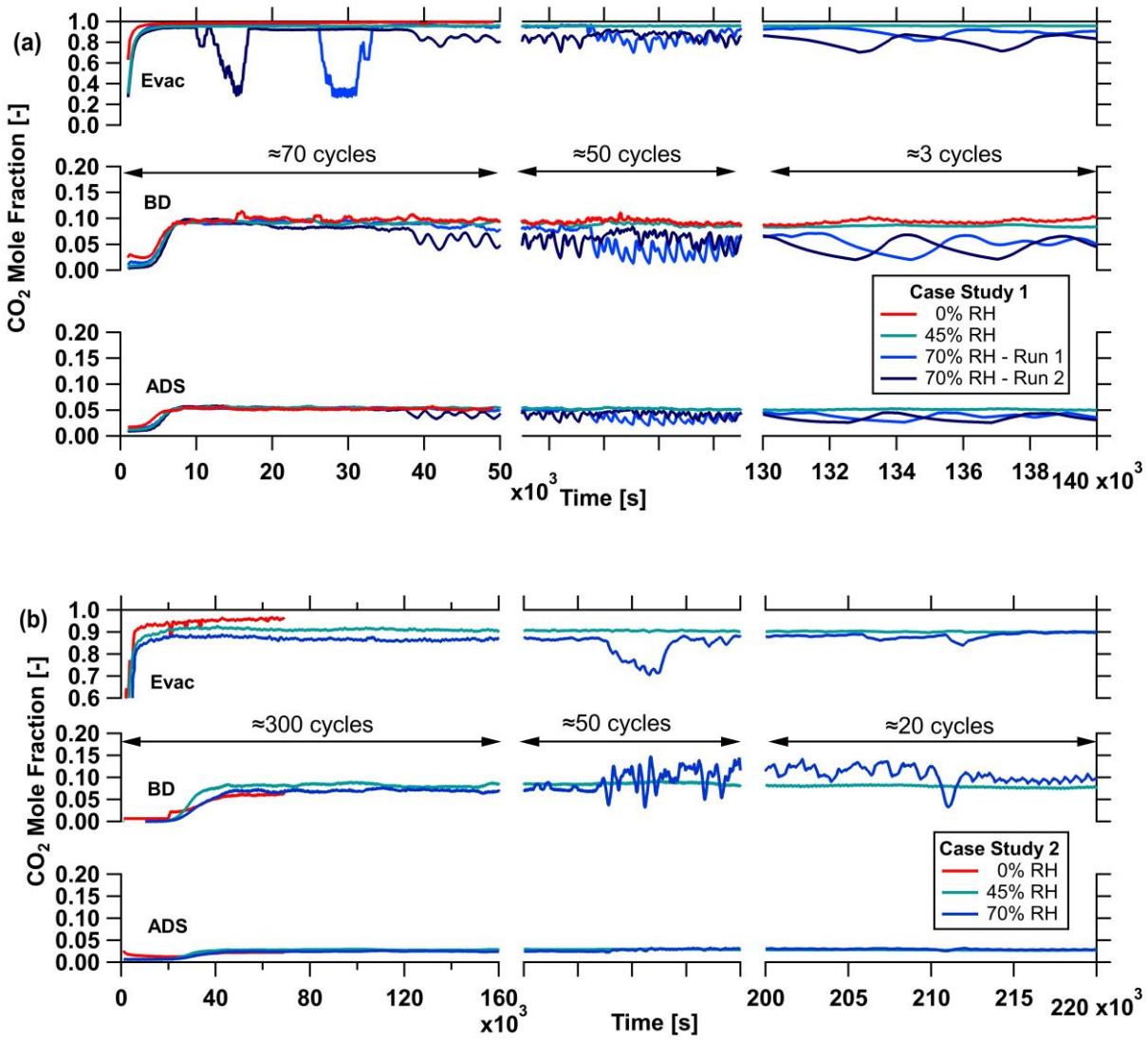

Figure 7.8: CO_2 mole fraction evolution during the adsorption, blowdown and evacuation step from intermediate to high relative humidity (45% to 70% RH). (a) Case study 1; (b) Case study 2.

In the first case study, an interesting observation in the CO_2 mole fraction was seen at 70% RH. After 30-40 cycles, a significant drop in the CO_2 mole fraction at the evacuation step was observed. Then, it increased and maintained at a similar CO_2 mole fraction. After 70 cycles, the CO_2 mole fraction was oscillated in a broader range, from 65% to 90%. This experiment was repeated, and a similar profile was also recorded (Fig. 7.8a). It appeared that the CO_2 analyzer signal was affected by the water condensation. When the liquid water existed, the signal of the CO_2 analyzer was unstable, and it tended to decrease. The analyzer needed to be dried completely and calibrated

again before starting a new experiment. Because of this effect, the purity and recovery at 70% RH were calculated based on the first 100 cycles only.

The second case study also showed the uncertainty of the CO_2 mole fraction after 300 cycles. It took longer to make the CO_2 analyzer unstable in this case since the feed velocity was lower. The accumulated amount of liquid water was less than the first case study. However, when there was more water condensation, we also observed this effect in the CO_2 mole fraction. The purity and recovery were also calculated based on the first 100 cycles. The wet cycle at 70% RH showed that water condensed intensively in the evacuation step, leading to many uncertainties in the measurements. Some noises may show up in the experimental transitions. It is not conclusive whether water affects the CO_2 separation since the purity and productivity were comparable. However, water condensation does make the evacuation step become more difficult.

The relative humidity histories show better insight into the water dynamics during the cyclic experiments (Fig. 7.9). In both case studies, the feed RH was constant during the whole experiment, which means the humid stream was stable. The RH histories from the adsorption, blowdown and evacuation step indicated a similar transition with the low to intermediate RH experiments. It gradually increased from 0% and reached a certain RH. In the adsorption step, the RH fluctuated in a small range, from 4% to 6%. At 70% RH, higher RH was seen in the blowdown step and evacuation step, at 15% RH and 20% RH, respectively. In the first case study, a non-neglectable transition was also observed in the RH histories after 100 cycles, especially the blowdown and evacuation step. The RH quickly increased from 15% to 20% in the blowdown step, while it changed from 20% to 25% in the evacuation step. The second case study also indicated a similar behaviour, but we only could observe after 300 cycles. Note that the RH meter in the evacuation step was put under a vacuum. The gas was fully saturated with water vapour after leaving the vacuum pump. This observation indicated that water was removed at both ends of the column. In other words, the water vapour travelled across the column. Because of the water condensation, it is challenging to close the water mass balance at 70% RH. During the first 100 cycles, the water mass balance error was approximately 5% to 10%. However, it is uncertain to estimate the water mole fraction above 100 cycles.

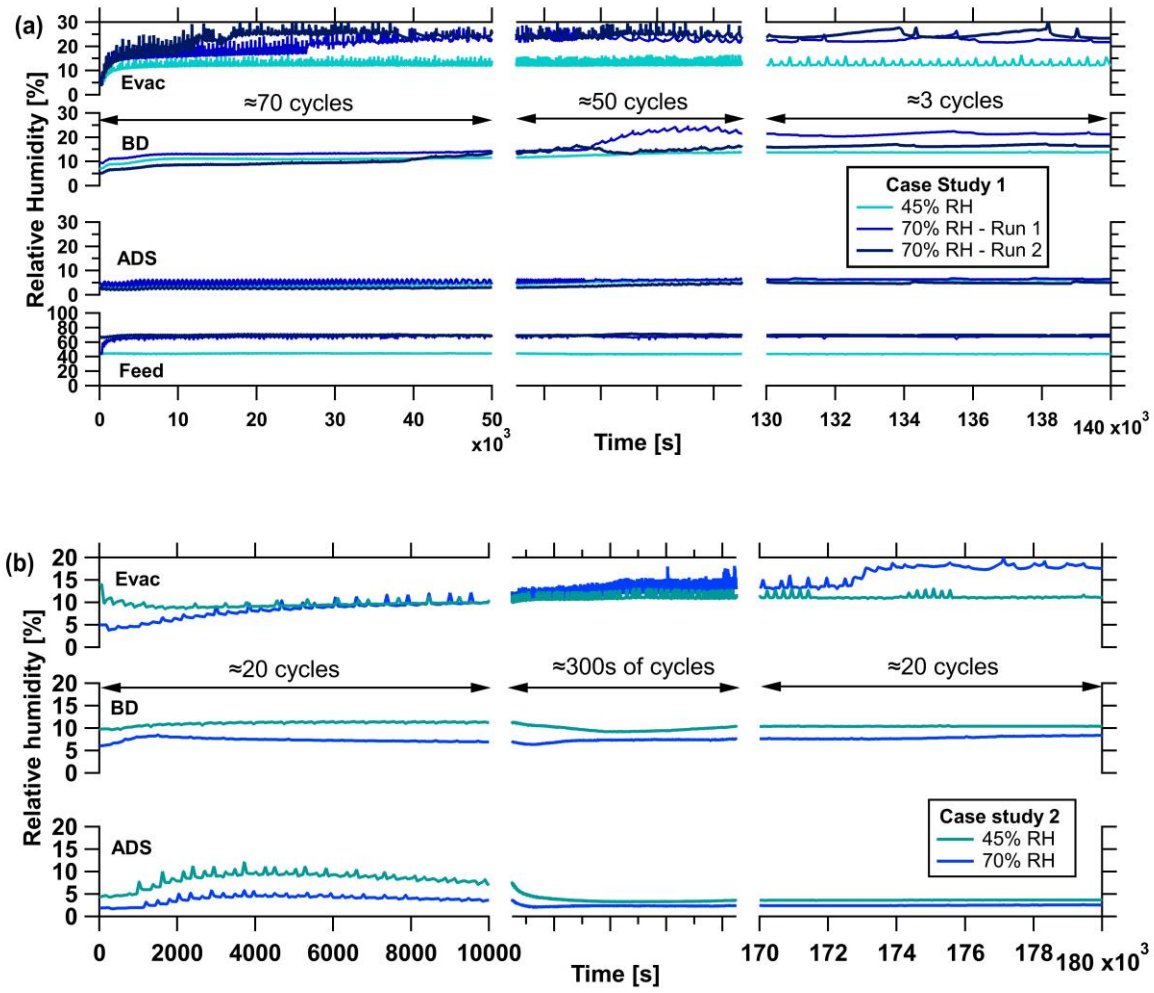

Figure 7.9: Relative humidity transient histories at the outlet of the adsorption, blowdown and evacuation step from intermediate to high relative humidity (45% to 70% RH). (a) Case study 1; (b) Case study 2.

Figure 7.10 shows the purity, recovery and productivity evolution over cycles for both wet and dry experiments. Both case studies indicated a similar transient history. In all cases, the purity nearly reached its value at the cyclic steady state after 20 cycles. Afterwards, it maintained at a certain value. A slight decrease in purity was observed at 70% RH between the wet and dry cycle in both case studies, approximately 2% difference. This result agrees with the CO_2 mole fraction histories discussed earlier. The recovery was lower than the dry case and it oscillated in a broader range at 70% RH experiments. Thus, the recovery was reported as an average value of 20 consecutive cycles with a standard deviation of 10%. The water condensation during the evacuation step might

contribute to the fluctuating of the recovery, which also can be seen in the CO_2 mole fraction transient histories. Because of this phenomenon, it is very challenging to perform a high RH cycle experimentally. All transient histories reflected a high oscillation beyond 100 cycles.

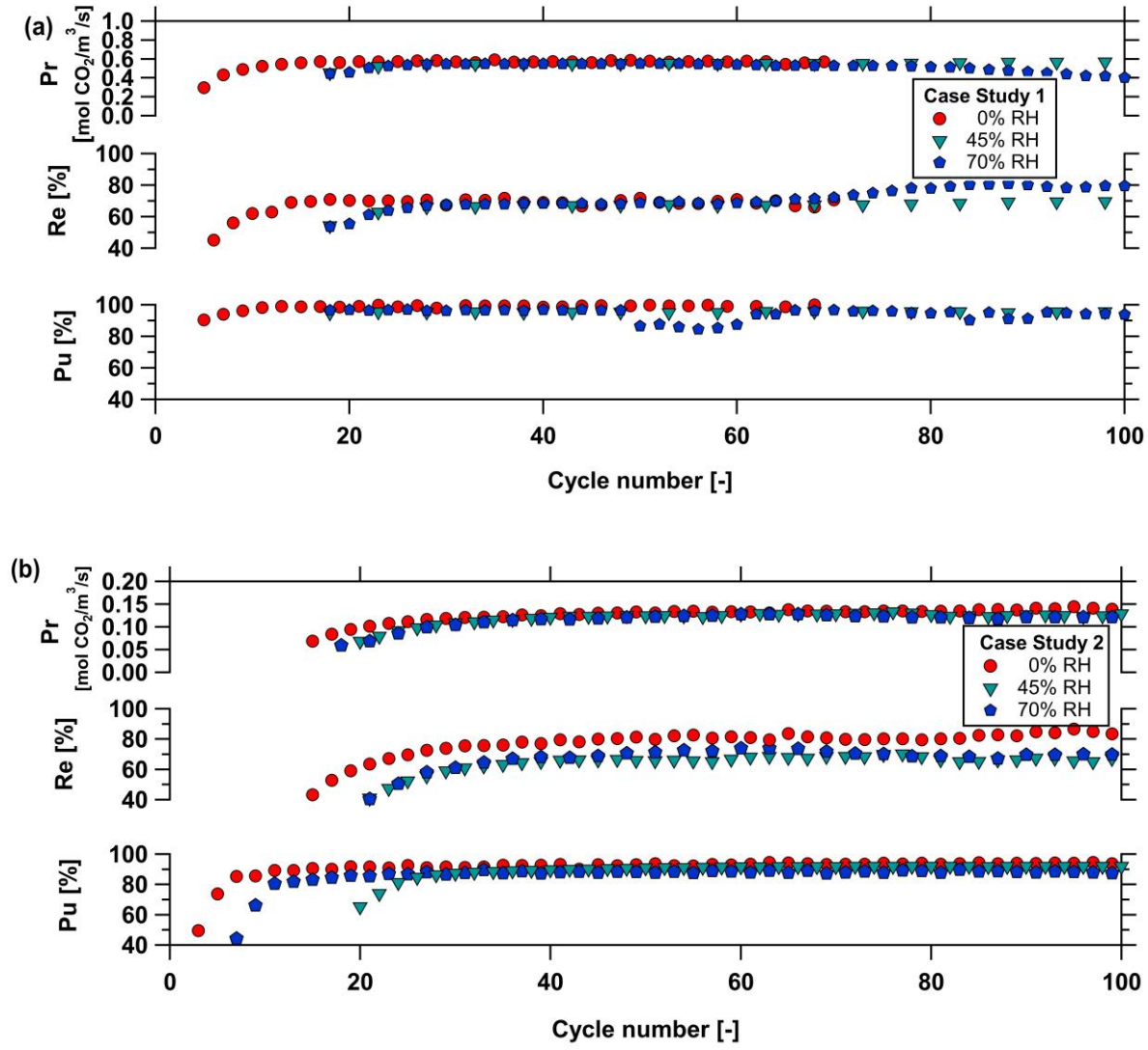

Figure 7.10: Purity, recovery and productivity evolution after hundreds of cycles from intermediate to high relative humidity (45% to 70% RH). (a) Case study 1; (b) Case study 2.

The productivity evolution at 70% RH also reinforced this observation. During the first 100 cycles in the first case study, the productivity was comparable with the dry case, at approximately 0.57 mol $CO_2/m^3/s$. From the 100th cycle, it became unstable because of the oscillation in the CO_2 mole fraction. In the second case study, the feed velocity was three times smaller than the first case study. In this case, the productivity was smaller, and it was similar to the dry experiment, at 0.14

mol $CO_2/m^3/s$. The results indicated that the recovery decreased, the purity and productivity were still comparable with the dry case. CALF-20 showed that a high purity and relatively high recovery are still achievable even at high relative humidity conditions.

7.3.3. Cyclic stability of CALF-20

The cyclic stability of sorbents is a critical performance parameter for the evaluation of a new adsorbent. This characteristic will contribute to the lifetime of an adsorbent. High cyclic stability allows the adsorbent reused thousands of cycles. Thus, the operating cost can be reduced by cutting down the cost of replacement and the cost of maintenance during the operating phase. To test the cyclic stability of CALF-20, after 12 months, the sample was taken out of the bottom of the column after running for more than 10,000s of cycles under both wet and dry conditions. Note that the adsorbent at the bottom of the column was extensively exposed to the water adsorption since it was closed to the feed end. Thus, this sample could provide a good estimation of the stability of the sample. The CO_2 and N_2 isotherms were measured at 30°C and 60°C, and the obtained data was compared with the fresh sample (Fig. 7.11).

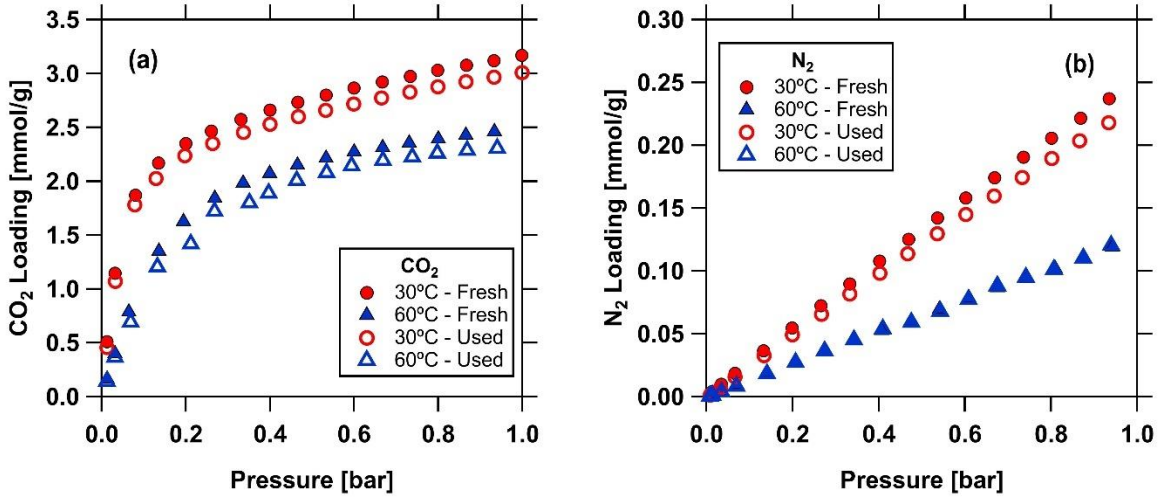

Figure 7.11: The single-component isotherms of CO_2 and N_2 at 30°C and 60°C from the fresh sample and used sample (after 10,000s cycles). (a) The pure CO_2 isotherm; (b) The pure N_2 isotherm. Closed markers correspond to the fresh CALF-20 sample, and hollow markers are the sample after running for more than 10,000 cycles.

Figure 7.11 shows the CO_2 and N_2 isotherms of CALF-20 at 30°C, from 0 bar to 1.0 bar. The results show that the CO_2 and N_2 isotherms of the sample after running for 10,000s of cycles

slightly decrease. A difference of ≈5% in the loadings was observed in both CO_2 and N_2 isotherms. After running for more than 10,000 cycles, the adsorbents went through many adsorption and desorption processes with different gases, i.e. H_2O, CO_2, and N_2. They were also exposed to vacuum pressure during the blowdown and evacuation step. The ageing of the adsorbent is inevitable. However, the slight decrease in the loadings is still reasonable, considering the number of cycles that the sample was tested.

Figure 7.12 shows the appearance of CALF-20 sample after using for 10,000s of cycles. There was no obvious difference observed from the samples with unaided eyes. The sample still maintains its cylindrical shape without any fragments. The used sample still indicates a milky white colour, without any sign of ageing. Briefly, no significant damage was observed in the used sample after running for more than 10,000s of cycles. This result suggests that CALF-20 has high cyclic stability. The mechanical strength of this structure is also reasonable without any damage observed from the sample.

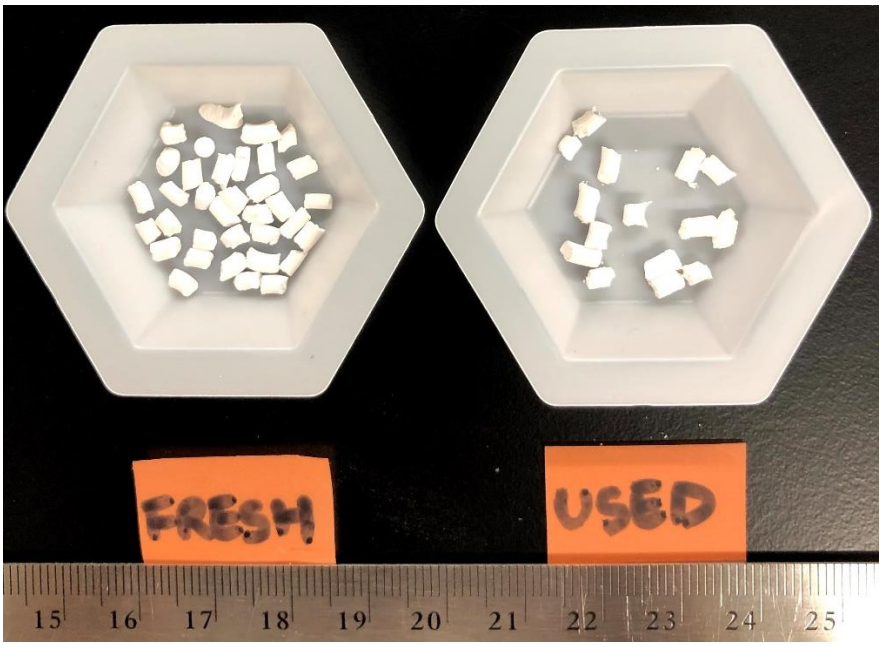

Figure 7.12: The appearance of the fresh CALF-20 and the used sample

7.4. Conclusions

To evaluate the impact of water on the CO_2 separation under the humid condition, the four-step with LPP cycle was chosen for further investigations. Two case studies were performed, which represented a high feed velocity (0.081 m/s), and a low feed velocity (0.024 m/s). In each case study, two different ranges of relative humidity were chosen: a low to intermediate RH (13%, 25% and 45%), and an intermediate to high relative humidity (45% and 70%). Even though it is complicated and time-consuming to perform a wet cycle experiment, it is crucial to understand the behaviour of CO_2 and H_2O cyclically. Since there is an inflection point at around 65% RH in the competitive CO_2/H_2O isotherm, different behaviours are expected. Below the inflection point (<45% RH), the CO_2 is favourably adsorbed on CALF-20. Beyond 70% RH, water is strongly adsorbed, which affects the adsorption of CO_2. Two different ranges of RH allow us to have a better insight to understand this interesting transition in the competitive CO_2/H_2O isotherm.

At low to intermediate relative humidity, the results from both case studies showed similar behaviour with the dry cycle. The temperature histories were overlapping, and the CO_2 mole fraction in each step indicated a similar transition over hundreds of cycles. The relative humidity histories indicated that water broke through the column during the adsorption. Water was also removed from the column during the blowdown and evacuation step. This observation suggested that water can be removed from CALF-20 easily under a vacuum. There was no change in purity and a slight decrease in recovery. The first case study showed a 97% purity and 71% recovery, while the second case study indicated a 94% purity and 86% recovery. The productivity was also comparable with the dry cycle, at 0.57 mol $CO_2/m^3/s$ and 0.14 mol $CO_2/m^3/s$ for the first and the second case studies. The higher feed velocity shows higher productivity. Briefly, the performance of CALF-20 does not change at the relative humidity smaller than 45%. Water does not affect the CO_2 adsorption, and it can be removed from the column easily.

At high relative humidity (70% RH), a different transition was observed in both case study 1 and case study 2. During the first 100 cycles, the temperature histories, the CO_2 mole fraction evolutions, the relative humidity transitions and the purity-recovery evolutions were comparable with the dry case. Afterwards, the CO_2 mole fraction was unstable because of the effect of water condensation. A slight decrease in purity was observed after 100 cycles, at ≈ 5%. The recovery was reduced and oscillated in a broad range, at ± 10%. The recovery was reported as the average

of 20 consecutive cycles with a standard deviation of 10%. A large amount of water condensed during the evacuation step is the reason for these uncertainties. Also, the evacuation step in the first case study could not reach the low pressure. The vacuum pump took thousands of seconds to evacuate the column because of the water condensation. This step was terminated after 3600 seconds since the pressure was at 0.038 bar for thousands of seconds. It could not reach the low pressure at 0.031 bar. The productivity was comparable in the first 100 cycles, at 0.60 mol $CO_2/m^3/s$. Overall, high purity and recovery are still achievable at high relative humidity. However, the water condensation phenomenon makes the evacuation step more difficult.

The results suggest that CALF-20 could be a potential candidate for humid post-combustion CO_2 capture. H_2O does not seem to have any effect on CO_2 adsorption at low to intermediate relative humidity (0% - 45% RH). All process performances, e.g. purity, recovery, productivity, show comparable values with the dry case. This could be a good opportunity to exploit the use of CALF-20 where the relative humidity is relatively low. Beyond 70%, it is difficult to precisely perform the humid cycle due to the water condensation. The vacuum pump took more than 3000 seconds to evacuate the column. In case study 1, it could not reach the low pressure at 70% RH due to a significant amount of liquid water. However, the purity, recovery and productivity of the first 100 cycles still showed good performance compared to the dry case. There was no obvious damage observed on the sample after using for 10,000s of cycles. The appearance of the sample showed no sign of ageing. A slight decrease in the CO_2 and N_2 loadings, ≈5%, was observed.

8 Conclusions And Future Work

8.1. Conclusions

The thesis presented different characterizations to study the ability of CALF-20 for humid post-combustion CO_2 capture. The lab-scale vacuum swing adsorption processes were also demonstrated in this work. Many challenges in characterizing CALF-20 for humid post-combustion CO_2 capture have been addressed in this thesis. It is challenging to quantify the amount adsorbed of each component in a binary system where one component is strongly adsorbed. Studying dynamic column breakthrough (DCB) of water is also difficult since it is required several days to a week to complete an experiment. Maintaining a stable humid feed is of importance to perform a proper water DCB. Water condensation occurring at the dew point is also another challenge. The water isotherm on CALF-20 exhibits a type V isotherm with an inflection point. It also shows a hysteresis loop in a narrow range of relative humidity. Therefore, it is very challenging to model the water isotherm precisely. CALF-20 shows an interesting competition between CO_2 and H_2O. Depening on the relative humidity, either CO_2 or H_2O is preferably adsorbed on CALF-20. Most solid porous materials for CO_2 capture ignore the effect of CO_2 on the water adsorption due to their high affinity to water. The unique behaviour of CALF-20 in the CO_2+H_2O competitive adsorption is critical, and it is required to be studied carefully. Note that it is a major obstacle to quantify the amount adsorbed for each component in a binary mixture, i.e., CO_2 and H_2O, especially under the presence of water. Performing a humid vacuum swing adsorption process is also very difficult since it is longer to reach the cyclic steady state than the dry cycles, i.e., a couple of hundreds of cycles. A humid cycle experiment usually takes five to seven days to perform.

The key achievements of this thesis are discussed below:

The competitive loadings of CO_2 and N_2 on CALF-20 were quantified using a dynamic column breakthrough (DCB) technique coupled with a mass spectrometer. The obtained data have a significant contribution to simulating the CO_2/N_2 competitive adsorption. Dual-site Langmuir

isotherm model with equal energy site was used to describe the competitive CO_2 and N_2 isotherm. The results suggested that using the single equilibrium data is not sufficient to predict the competitive form precisely. While the heavy component did not seem to have any difference, the lighter component showed different competitive loadings depending on the combinations of each site in the dual-site Langmuir model. This observation indicates a need to perform the binary DCB to build a complete competitive isotherm.

The water isotherms on CALF-20 at various temperatures were measured using volumetric and thermogravimetric analyzer. The water isotherm exhibited a type V isotherm with an inflection point. Furthermore, it also showed a hysteresis loop within a narrow range of relative humidity (8% - 22%). The Quadratic-Langmuir isotherm model described the water isotherm at various temperatures successfully. Both H_2O adsorption and desorption DCB were performed at 8%, 22% and 45% to examine the shape of the isotherm. This work showed that using the bubbler humidifier can produce a very stable humid stream over a long period of time. The water DCB curves showed unique transitions in both adsorption and desorption experiments. These transitions characterized the shape of the isotherm. This study also showed the importance of quantifying the hysteresis loop precisely. A slight discrepancy in the H_2O loadings could lead to a totally different breakthrough curve. Dealing with the isotherm with inflection point, a more complex isotherm model is usually required. This study suggests using the discrete equilibrium data model to describe any complex isotherms. Similar simulated breakthrough curves were obtained using this approach compared to the continuous functional form of the isotherm. Thus, the complexity in describing the isotherm can be reduced.

The competitive adsorption of CO_2+H_2O was successfully studied. Since the water isotherm of CALF-20 showed unique behaviour, it is important to understand its competition with CO_2. To quantify the competitive loading of H_2O and CO_2, a new approach was suggested. The total loading of CO_2 and H_2O were collected using the thermogravimetric analyzer. In the meantime, the competitive H_2O loadings could be obtained by performing competitive CO_2/H_2O DCB at various RH values. The competitive CO_2 loadings can be estimated from the difference of these two measurements. It is worth noting that the CO_2/H_2O DCB took a long time to perform, e.g. two to three days, but it is necessary to wait and obtain a complete breakthrough curve for both H_2O and CO_2. False data may be seen due to a lack of breakthrough profiles.

The competitive CO_2/H_2O showed that the adsorption of water was strongly affected by the CO_2 adsorption. The loading of CO_2 barely changed, and only a small amount of H_2O was adsorbed at low RH (<45%). This observation is unique since most of the adsorbents show an unchanged water isotherm under the presence of CO_2. To describe this unique competitive isotherm, the modified Langmuir model was used to describe the competitive CO_2 since it depended on both water loading and temperature. The competitive H_2O loading could be described by the Quadratic Langmuir model. Excellent breakthrough curves were predicted using these isotherm models.

The competitive CO_2+H_2O adsorption also showed an anomalous behaviour under the presence of CO_2. The framework of CALF-20 seems to be extended when the CO_2 molecules enter the pores. The total loading of CO_2 and H_2O at high RH (>40%) showed a discrepancy depending on water, or CO_2 enters the pore first. When the adsorbent "sees" water first, at high RH, the capillary condensation likely occurs, which hinders the CO_2 adsorption. Thus, the total loadings at high RH are similar to the pure H_2O loading (>70% RH). If CO_2 enters the pore first, the framework is extended, resulting in a higher total loading of CO_2 and H_2O. This effect is reversible when CO_2 is removed. The observation in this study confirmed the flexibility in the framework of MOFs.

The ability to use CALF-20 for CO_2 capture under dry and wet conditions was also demonstrated using vacuum swing adsorption. The rigorous optimization approach showed an effective way to optimize the adsorption processes. Fewer experiments were required to develop and validate the optimization. The basic four-step cycle and four-step with light-product pressurization cycle were chosen to evaluate the performance of CALF-20 due to their simplicity and effectiveness. Several points on the Pareto curves were selected randomly to validate the model prediction experimentally. The results confirmed that all process performances, e.g. purity, recovery, were well predicted.

This study also showed the CO_2 capture under humid conditions using vacuum swing adsorption experimentally. To the best of our knowledge, there was no study on humid CO_2 capture using MOFs in the literature. This work provided a procedure to study the CO_2 separation under moist conditions. A humidifier was used to generate stable gas streams during the entire experiment. Each humid experiment required an extremely long time to reach the cyclic steady state, e.g. hundreds of cycles, and it took almost a week to perform an experiment. Under 45% RH, the results showed that there was no difference between the wet and dry cycle using CALF-20. This is in

agreement with the competitive CO_2+H_2O DCB results. Beyond 70% RH, water condensation usually occurred, which made it challenging to perform the experiments. However, the results from the first 100 cycles also showed similar performances compared to the dry cycle. This study also observed that the use of the vacuum pump is hindered because of the water condensation. The evacuation step could not be performed properly due to this phenomenon.

8.2. Future work

Based on the obtained results from the study conducted in this thesis, the following recommendations are proposed for future work.

It is certain to confirm that the separation of CO_2 is barely affected by water at low to intermediate relative humidity (<45%). However, it is difficult to conclude what happens at high RH. The cycle results above 70% RH are still limited due to the water condensation. The experiment only could run for ≈100 cycles due to this effect. Hence, it is not conclusive to decide how water affects the adsorption of CO_2 and the process performance under this condition. A better approach to eliminate the liquid water during the evacuation step might be of interest to reduce its effect to the instruments, i.e. vacuum pump, CO_2 analyzer.

Further optimizations are required to guide the experiments and to design a better process. It is also possible to consider a more complex configuration in order to improve the process performances further, i.e. six-step with pressure equalization, six-step with light reflux and heavy reflux. The vacuum pump showed an ineffective performance when the water condensation occurs. A different process where the use of a vacuum pump is not necessary may be beneficial, i.e. pressure swing adsorption.

The water isotherm shows a strong dependence on both relative humidity and temperature. We could exploit this unique behaviour to design a CO_2 capture process where the adsorption of H_2O does not play an important role, e.g. <45% RH. The flue gas can be mildly treated to remove part of the water before entering the separation unit. Since water does not show high capacity at high temperature, a temperature swing adsorption might be of interest.

The structured CALF-20 used in this study showed excellent mechanical stability and thermal stability. There was no obvious difference or sign of ageing on the appearance of CALF-20 after using for more than 10,000 cycles. However, the density of this structure is relatively low, ≈570

kg/m^3, which is not favourable for use on a large scale. Better structure with a higher mass transfer rate could be of importance for future structures. Several options could be considered, such as monoliths, honeycomb or layered sheets.

CALF-20 showed anomalous behaviour in the competitive CO_2 and H_2O adsorption. The TGA experiments provided evidence that higher total loading of CO_2+H_2O was observed at RH>40% if CO_2 entered the pores first. The results from TGA measurements and DCB experiments suggested that the framework of CALF-20 is extended under the presence of CO_2. However, it is not conclusive to understand the flexibility in the structure of CALF-20 based on TGA and DCB data only. Further investigation is critical to understand this anomalous behaviour. Powder X-ray diffraction (PXRD) technique may provide a better understanding of the structural level of CALF-20. The structure of CALF-20 can be examined under various environments, e.g., CO_2, N_2, vacuum, humid environment, gas mixtures. Furthermore, the temperature may also affect the flexibility of the framework. Hence, performing PXRD measurements at various temperatures may also be required.

Bibliography

1. The National Aeronautics and Space Administration (NASA), *Observed Global Temperature* 2020.
2. The Intergovernmental Panel on Climate Change (IPCC), *Global Warming of 1.5°C.* 2020.
3. L. Olsson, D. Chadee, O. Hoegh-Guldberg, M. Oppenheimer, J. Porter, H.-O. Pörtner, D. Satterthwaite, K. Smith, M.I. Travasso, and P. Tschakert, *Cross-chapter box on heat stress and heat waves*, in *Climate Change 2014: Impacts, Adaptation, and Vulnerability. Part A: Global and Sectoral Aspects. Contribution of Working Group II to the Fifth Assessment Report of the Intergovernmental Panel on Climate Change*. 2014, Cambridge University Press. p. 109-111.
4. C. Donnelly, W. Greuell, J. Andersson, D. Gerten, G. Pisacane, P. Roudier, and F. Ludwig, *Impacts of climate change on European hydrology at 1.5, 2 and 3 degrees mean global warming above preindustrial level.* Climatic Change, 2017. **143** (1-2): p. 13-26.
5. S. Thober, R. Kumar, N. Wanders, A. Marx, M. Pan, O. Rakovec, L.E. Samaniego, J. Sheffield, E.F. Wood, and M. Zink, *Multi-model ensemble projections of European river floods and high flows at 1.5, 2, and 3 degree global warming.* AGUFM, 2017. **2017**: p. GC53A-0870.
6. H.S. Baker, R.J. Millar, D.J. Karoly, U. Beyerle, B.P. Guillod, D. Mitchell, H. Shiogama, S. Sparrow, T. Woollings, and M.R. Allen, *Higher CO_2 concentrations increase extreme event risk in a 1.5° C world.* Nat. Clim. Chang., 2018. **8** (7): p. 604.
7. O. Hoegh-Guldberg, P.J. Mumby, A.J. Hooten, R.S. Steneck, P. Greenfield, E. Gomez, C.D. Harvell, P.F. Sale, A.J. Edwards, and K. Caldeira, *Coral reefs under rapid climate change and ocean acidification.* Science, 2007. **318** (5857): p. 1737-1742.
8. N. Bindoff, J. Willebrand, V. Artale, A. Cazenave, J. Gregory, S. Gulev, K. Hanawa, C. Le Quéré, S. Levitus, and Y. Nojiri, *Observations: oceanic climate and sea level. In:/Climate change 2007: The physical Science Basis. Contribution of Working Group I to the Fourth Assessment report of the Intergouvernmental Panel on Climate Change.* 2007.

9. X. Chen, X. Zhang, J.A. Church, C.S. Watson, M.A. King, D. Monselesan, B. Legresy, and C. Harig, *The increasing rate of global mean sea-level rise during 1993–2014.* Nat. Clim. Chang., 2017. **7** (7): p. 492-495.

10. M. Oppenheimer, M. Campos, R. Warren, J. Birkmann, G. Luber, B. O'Neill, K. Takahashi, M. Brklacich, S. Semenov, and R. Licker, *Emergent risks and key vulnerabilities*, in *Climate Change 2014 Impacts, Adaptation and Vulnerability: Part A: Global and Sectoral Aspects*. 2015, Cambridge University Press. p. 1039-1100.

11. N.E. Rafferty, *Effects of global change on insect pollinators: multiple drivers lead to novel communities.* Current Opinion in Insect Science, 2017. **23**: p. 22-27.

12. The Intergovernmental Panel on Climate Change (IPCC), *Managing the Risks of Extreme Events and Disasters to Advance Climate Change Adaptation.* 2012.

13. The Intergovernmental Panel on Climate Change (IPCC), *Climate Change 2014: Impacts, Adaptation, and Vulnerability.* 2014: p. Part A: Global and Sectoral Aspects. Contribution of Working Group II to the Fifth Assessment Report of the Intergovernmental Panel on Climate Change.

14. R.M. Hoesly, S.J. Smith, L. Feng, Z. Klimont, G. Janssens-Maenhout, T. Pitkanen, J.J. Seibert, L. Vu, R.J. Andres, and R.M. Bolt, *Historical (1750-2014) anthropogenic emissions of reactive gases and aerosols from the Community Emission Data System (CEDS).* Geosci. Model Dev., 2018. **11**: p. 369-408.

15. J.G. Canadell and M.R. Raupach, *Managing forests for climate change mitigation.* Science, 2008. **320** (5882): p. 1456-1457.

16. K. Paustian, J. Lehmann, S. Ogle, D. Reay, G.P. Robertson, and P. Smith, *Climate-smart soils.* Nature, 2016. **532** (7597): p. 49-57.

17. S. Frank, P. Havlík, J.-F. Soussana, A. Levesque, H. Valin, E. Wollenberg, U. Kleinwechter, O. Fricko, M. Gusti, and M. Herrero, *Reducing greenhouse gas emissions in agriculture without compromising food security?* Environ. Res., 2017. **12** (10): p. 105004.

18. B. Wang, Y. Li, N. Wu, and C.Q. Lan, *CO_2 bio-mitigation using microalgae.* Appl. Microbiol. Biotechnol., 2008. **79** (5): p. 707-718.

19. M. Anjos, B.D. Fernandes, A.A. Vicente, J.A. Teixeira, and G. Dragone, *Optimization of CO_2 bio-mitigation by Chlorella vulgaris.* Bioresour. Technol., 2013. **139**: p. 149-154.

20. M.K. Lam and K.T. Lee, *Effect of carbon source towards the growth of Chlorella vulgaris for CO_2 bio-mitigation and biodiesel production.* Int. J. Greenh. Gas Con., 2013. **14**: p. 169-176.

21. M. Ha-Duong and D.W. Keith, *Climate strategy with CO_2 capture from the air.* Submitted to Climatic Change, 2002.

22. R. Socolow, M. Desmond, R. Aines, J. Blackstock, O. Bolland, T. Kaarsberg, N. Lewis, M. Mazzotti, A. Pfeffer, and K. Sawyer, *Direct air capture of CO_2 with chemicals: a technology assessment for the APS Panel on Public Affairs*. APS, 2011.

23. C. Gough and P. Upham, *Biomass energy with carbon capture and storage (BECCS or Bio-CCS).* Greenh. Gases, 2011. **1**(4): p. 324-334.

24. The International Energy Agency, *Storing CO_2 underground.* 2007.

25. International Energy Agency, *Market report series: Gas 2019.* 2019.

26. CCS Knowledge, *Global status of CCS Report.* 2019.

27. International Energy Agency, *World Energy Outlook.* 2018.

28. L. Irlam, *Global costs of carbon capture and storage.* Global CCS Institute, Melbourne, Australia, 2017.

29. Global CCS Institute, *CO_2RE Database: Climate Change Report.* 2019.

30. F. Birol, *The future of hydrogen. Seizing today's opportunities. IEA.* 2019.

31. Alberta Department of Energy, *Quest Carbon Capture and Storage Project: Annual Summary Report.* 2018.

32. Dakota Gasification Company, *Great Plains Synfuels Plant: At a glance.* https://www.dakotagas.com/about-us/at-a-glance, 2020.

33. SaskPower, *Boundary Dam Carbon Capture Project.* http://www.saskpower.com/our-power-future/carbon-capture-and-storage/boundary-dam-carbon-capture-project/, 2016.

34. NRG Energy, *Petra Nova Carbon Capture System (CCS) placed in reserve shutdown.* https://www.nrg.com/about/newsroom/2020/petra-nova-status-update.html, Retrieved on October 11, 2020.

35. Food and Agriculture Organization of The United Nations, *Biannual report on global food markets. November 2017*. 2018, Rome.

36. The US Department of Energy, *Compendium of Carbon Capture Technology.* 2018.

37. Climeworks, *Interview by the Global CCS Institute* 2019.

38. D. Singh., E. Croiset., P.L. Douglas., and M.A. Douglas., *Techno-economic study of CO_2 capture from an existing coal-fired power plant: MEA scrubbing vs. O_2/CO_2 recycle combustion.* Energ. Convers. Manage., 2003. **44**: p. 3073.

39. P. Muchan., C. Saiwan., J. Narku-Tetteh., R. Idem., T. Supap., and P. Tontiwachwuthikul., *Screening tests of aqueous alkanolamine solutions based on primary, secondary, and tertiary structure for blended aqueous amine solution selection in post combustion CO_2 capture.* Chem. Eng. Sci., 2017. **170**: p. 574.

40. Shell Canada, *Quest Carbon Capture and Storage.* http://www.shell.ca/en_ca/about-us/projects-and-sites/quest-carbon-capture-and-storage-project.html, 2016.

41. X. Hea., A. Lindbråthena., T.-J. Kimb., and M.-B. Hägg., *Pilot testing on fixed-site-carrier membranes for CO_2 capture from flue gas.* Int. J. Greenh. Gas Con., 2017. **64**: p. 323.

42. W.J. Thomas. and B. Crittenden., *The development of adsorption technology.* Adsorption Technology and Design, 1998.

43. D.M. Ruthven., *Principles of adsorption and adsorption process.* John Wiley & Sons, 1984.

44. D.M. Ruthven, S. Farooq, and K. Knaebel, *Pressure swing adsorption. 1994.* New York: UCH, 352p.

45. C.F. Martín, M.G. Plaza, J.J. Pis, F. Rubiera, C. Pevida, and T.A. Centeno, *On the limits of CO_2 capture capacity of carbons.* Sep. Purif. Technol., 2010. **74**: p. 225.

46. M.G. Plaza, S. García, F. Rubiera, J.J. Pis, and C. Pevida, *Post-combustion CO_2 capture with a commercial activated carbon: Comparison of different regeneration strategies.* Chem. Eng. J., 2010. **163**: p. 41.

47. Z. Liu., C.A. Grande., P. Li., J. Yu., and A.E. Rodrigues., *Multi-bed Vacuum Pressure Swing Adsorption for carbon dioxide capture from flue gas.* Sep. Purif. Technol., 2011. **81**: p. 307.

48. S.J. Chen., M. Zhu., Y. Fu., Y.X. Huang., Z.C. Tao., and W.L. Li., *Using 13X, LiX, and LiPdAgX zeolites for CO_2 capture from post-combustion flue gas.* Appl. Energy, 2017. **191**: p. 87.

49. D.M. Ruthven, *Principles of adsorption and adsorption processes*. 1984: John Wiley & Sons.

50. A.K. Rajagopalan, A.M. Avila, and A. Rajendran, *Do adsorbent screening metrics predict process performance? A process optimisation based study for post-combustion capture of CO_2.* Int. J. Greenh. Gas Con., 2016. **46**: p. 76-85.

51. K.N. Pai, J.D. Baboolal, D.A. Sharp, and A. Rajendran, *Evaluation of diamine-appended metal-organic frameworks for post-combustion CO_2 capture by vacuum swing adsorption.* Sep. Purif. Technol., 2019. **211**: p. 540-550.

52. M. Hefti, D. Marx, L. Joss, and M. Mazzotti, *Adsorption equilibrium of binary mixtures of carbon dioxide and nitrogen on zeolites ZSM-5 and 13X.* Microporous Mesoporous Mater., 2015. **215**: p. 215-228.

53. J. Bailar, *Coordination Polymers, Vol. 1*. 1964, Prep. Inorg. React., Jr.

54. S. Kitagawa, R. Kitaura, and S.i. Noro, *Functional porous coordination polymers.* Angewandte Chemie International Edition, 2004. **43** (18): p. 2334-2375.

55. O.M. Yaghi. and Q. Li., *Reticular Chemistry and Metal - Organic Frameworks for Clean Energy.* MRS BULLETIN, 2009. **34**: p. 682.

56. H. Furukawa, N. Ko, Y.B. Go, N. Aratani, S.B. Choi, E.W. Choi, A. Özgür Yazaydin, R.Q. Snurr, M. O'Keeffe, J. Kim, and O.M. Yaghi, *Ultrahigh Porosity in Metal-Organic Frameworks.* Science, 2010. **329**: p. 424-428.

57. M.P. Suh, H.J. Park, T.K. Prasad, and D.-W. Lim, *Hydrogen storage in metal-organic frameworks.* Chem. Rev., 2012. **112**: p. 782-835.

58. J.R. Li., J. Kuppler., and H.C. Zhou., *Selective gas adsorption and separation in metal–organic frameworks.* Chem. Soc. Rev., 2009. **38**: p. 1477-1540.

59. A. Phan., A.U. Czaja., F.G. ., C.B. Knobler., and O.M. Yaghi., *Metal-organic frameworks of Valadium as catalysts for conversion of methane to acetic acid.* Inorg. Chem., 2011. **50**: p. 7388-7390.

60. J.Y. Lee, O.K. Farha, J. Roberts, and K.A. Scheidt, *Metal - organic framework materials as catalysts.* Chem. Soc. Rev., 2009. **38**: p. 1450-1459.

61. D.J. Tranchemontagne, J.L. Mendoza-Cortes, M. O'Keeffe, and O.M. Yaghi, *Secondary buiding units, nets and bonding in chemistry of metal-organic frameworks.* Chem. Soc. Rev., 2009. **38**: p. 1257-1283.

62. O.M. Yaghi, H. Li, M. Eddaoudi, and M. O'Keeffe, *Design and synthesis of an exceptionally stable and highly porous metal-organic frameworks.* Nature, 1999. **42**: p. 276-279.

63. R. Sabouni., H. Kazemian., and S. Rohani., *Carbon dioxide capturing technologies: a review focusing on metal organic framework materials (MOFs).* Environ Sci Pollut Res., 2014. **21**: p. 5427.

64. H. Huang., W. Zhang., F. Yang., B. Wang., Q. Yang., Y. Xie., C. Zhong., and J.-R. Li., *Enhancing CO_2 adsorption and separation ability of Zr(IV)-based metal–organic frameworks through ligand functionalization under the guidance of the quantitative structure–property relationship model.* Chem. Eng. J., 2016. **289**: p. 247.

65. A. Torrisi., R.G. Bell., and C. Mellot-Draznieks., *Functionalized MOFs for Enhanced CO_2 Capture.* Cryst. Growth Des., 2010. **10**: p. 2839.

66. Z. Hu., M. Khurana., Y.H. Seah., M. Zhang., Z. Guo., and D. Zhao., *Ionized Zr-MOFs for highly efficient post-combustion CO_2 capture.* Chem. Eng. Sci., 2015. **124**: p. 61.

67. R. Babarao. and J.W. Jiang., *Cation Characterization and CO_2 Capture in Li^+-Exchanged Metal-Organic Frameworks: From First-Principles Modeling to Molecular Simulation.* Ind. Eng. Chem. Res., 2011. **50**: p. 62.

68. J. Hu., Y. Liu., J. Liu., C. Gu., and D. Wu., *High CO_2 adsorption capacities in UiO type MOFs comprising heterocyclic ligand.* Microporous Mesoporous Mater., 2017.

69. Q. Yang., S. Vaesen., F. Ragon., A.D. Wiersum., D. Wu., A. Lago., T. Devic., C. Martineau., F. Taulelle., P.L. Llewellyn., H. Jobic., C. Zhong., C. Serre., G.D. Weireld., and G. Maurin., *A Water Stable Metal–Organic Framework with Optimal Features for CO_2 Capture.* Angew. Chem., 2013. **125**: p. 10506.

70. J. Liu., Y. Wang., A.I. Benin., P. Jakubczak., R.R. Willis., and M.D. LeVan., *CO_2/H_2O Adsorption Equilibrium and Rates on Metal-Organic Frameworks: HKUST-1 and Ni/DOBDC.* Langmuir, 2010. **26**: p. 14301.

71. N. Chanut., S. Bourrelly., B. Kuchta., C. Serre., J.-S. Chang., P.A. Wright., and P.L. Llewellyn., *Screening the Effect of Water Vapour on Gas Adsorption Performance: Application to CO_2 Capture from Flue Gas in Metal–Organic Frameworks.* Chem. Sus. Chem., 2017. **10**: p. 1543.

72. N.A. Qasem and R. Ben-Mansour, *Energy and productivity efficient vacuum pressure swing adsorption process to separate CO_2 from CO_2/N_2 mixture using Mg-MOF-74: A CFD simulation.* Appl. Energy, 2018. **209**: p. 190-202.

73. R. Ben-Mansour and N.A. Qasem, *An efficient temperature swing adsorption (TSA) process for separating CO_2 from CO_2/N_2 mixture using Mg-MOF-74.* Energ. Convers. Manage., 2018. **156**: p. 10-24.

74. R. Zhao, L. Liu, L. Zhao, S. Deng, S. Li, and Y. Zhang, *A comprehensive performance evaluation of temperature swing adsorption for post-combustion carbon dioxide capture.* Renew. Sust. Energ. Rev., 2019. **114**: p. 109285.

75. K.T. Leperi, Y.G. Chung, F. You, and R.Q. Snurr, *Development of a general evaluation metric for rapid screening of adsorbent materials for postcombustion CO_2 capture.* Sus. Chem. Eng., 2019. **7** (13): p. 11529-11539.

76. D. Bahamon, A. Díaz-Márquez, P. Gamallo, and L.F. Vega, *Energetic evaluation of swing adsorption processes for CO_2 capture in selected MOFs and zeolites: Effect of impurities.* Chem. Eng. J., 2018. **342**: p. 458-473.

77. I. Majchrzak-Kucęba, D. Wawrzyńczak, and A. Ściubidło, *Application of metal-organic frameworks in VPSA technology for CO_2 capture.* Fuel, 2019. **255**: p. 115773.

78. Y. Lian, S. Deng, S. Li, Z. Guo, L. Zhao, and X. Yuan, *Numerical analysis on CO_2 capture process of temperature swing adsorption (TSA): Optimization of reactor geometry.* Int. J. Greenh. Gas Con., 2019. **85**: p. 187-198.

79. G.N. Nikolaidis, E.S. Kikkinides, and M.C. Georgiadis, *Modelling, Simulation and Optimisation of an Integrated Two-Stage P/VSA Process for Post-Combustion CO_2 Capture Using Combinations of Adsorbents*, in *Computer Aided Chemical Engineering*. 2017, Elsevier. p. 2647-2652.

80. A.K. Rajagopalan., A. M.Avila., and A. Rajendran., *Do adsorbent screening metrics predict process performance? A process optimisation based study for post-combustion capture of CO_2.* Int. J. Greenh. Gas Con., 2016. **46**: p. 76.

81. N. Casas, J. Schell, R. Blom, and M. Mazzotti, *MOF and UiO-67/MCM-41 adsorbents for pre-combustion CO_2 capture by PSA: Breakthrough experiments and process design.* Sep. Purif. Technol., 2013. **112**: p. 34-48.

82. A. Sinha, L.A. Darunte, C.W. Jones, M.J. Realff, and Y. Kawajiri, *Systems design and economic analysis of direct air capture of CO_2 through temperature vacuum swing adsorption using MIL-101 (Cr)-PEI-800 and mmen-Mg2 (dobpdc) MOF adsorbents.* Ind. Eng. Chem. Res., 2017. **56**(3): p. 750-764.

83. K.T. Leperi, R.Q. Snurr, and F. You, *Optimization of two-stage pressure/vacuum swing adsorption with variable dehydration level for postcombustion carbon capture.* Ind. Eng. Chem. Res., 2016. **55**(12): p. 3338-3350.

84. M. Khurana and S. Farooq, *Simulation and optimization of a 6-step dual-reflux VSA cycle for post-combustion CO_2 capture.* Chem. Eng. Sci., 2016. **152**: p. 507-515.

85. S.U. Rege and R.T. Yang, *A simple parameter for selecting an adsorbent for gas separation by pressure swing adsorption.* Sep. Sci. Technol., 2001. **36** (15): p. 3355-3365.

86. M. Hefti, L. Joss, Z. Bjelobrk, and M. Mazzotti, *On the potential of phase-change adsorbents for CO_2 capture by temperature swing adsorption.* Faraday discussions, 2016. **192**: p. 153-179.

87. N.S. Wilkins, J.A. Sawada, and A. Rajendran, *Measurement of competitive CO_2 and H_2O adsorption on zeolite 13X for post-combustion CO_2 capture.* Adsorption, 2020.

88. M. Hefti and M. Mazzotti, *Postcombustion CO_2 capture from wet flue gas by temperature swing adsorption.* Ind. Eng. Chem. Res., 2018. **57** (45): p. 15542-15555.

89. A. Samanta, A. Zhao, G.K. Shimizu, P. Sarkar, and R. Gupta, *Post-combustion CO_2 capture using solid sorbents: a review.* Ind. Eng. Chem. Res., 2012. **51** (4): p. 1438-1463.

90. C. Gouedard, D. Picq, F. Launay, and P.-L. Carrette, *Amine degradation in CO_2 capture.* Int. J. Greenh. Gas Con., 2012. **10**: p. 244-270.

91. S.E. Zanco, L. Joss, M. Hefti, M. Gazzani, and M. Mazzotti, *Addressing the criticalities for the deployment of adsorption-based CO_2 capture processes.* Energy Procedia, 2017. **114**: p. 2497-2505.

92. N.S. Wilkins and A. Rajendran, *Measurement of competitive CO_2 and N_2 adsorption on Zeolite 13X for post-combustion CO_2 capture.* Adsorption, 2019. **25** (2): p. 115-133.

93. A.M. Fracaroli, H. Furukawa, M. Suzuki, M. Dodd, S. Okajima, F. Gándara, J.A. Reimer, and O.M. Yaghi, *Metal–organic frameworks with precisely designed interior for carbon dioxide capture in the presence of water.* J. Am. Chem. Soc., 2014. **136** (25): p. 8863-8866.

94. D.M. D'Alessandro, B. Smit, and J.R. Long, *Carbon dioxide capture: prospects for new materials.* Angewandte Chemie International Edition, 2010. **49** (35): p. 6058-6082.

95. Z.R. Herm, J.A. Swisher, B. Smit, R. Krishna, and J.R. Long, *Metal− organic frameworks as adsorbents for hydrogen purification and precombustion carbon dioxide capture.* J. Am. Chem. Soc., 2011. **133** (15): p. 5664-5667.

96. L. Borchardt, Q.-L. Zhu, M.E. Casco, R. Berger, X. Zhuang, S. Kaskel, X. Feng, and Q. Xu, *Toward a molecular design of porous carbon materials.* Mater. Today, 2017. **20** (10): p. 592-610.

97. X. Lian, L. Xu, M. Chen, C.-e. Wu, W. Li, B. Huang, and Y. Cui, *Carbon dioxide captured by metal organic frameworks and its subsequent resource utilization strategy: a review and prospect.* Journal of nanoscience and nanotechnology, 2019. **19** (6): p. 3059-3078.

98. R.-B. Lin, S. Xiang, H. Xing, W. Zhou, and B. Chen, *Exploration of porous metal–organic frameworks for gas separation and purification.* Coord. Chem. Rev., 2019. **378**: p. 87-103.

99. R. Sabouni, H. Kazemian, and S. Rohani, *Carbon dioxide capturing technologies: a review focusing on metal organic framework materials (MOFs).* Environmental Science and Pollution Research, 2014. **21** (8): p. 5427-5449.

100. V. Subramanian Balashankar, A.K. Rajagopalan, R. de Pauw, A.M. Avila, and A. Rajendran, *Analysis of a batch adsorber analogue for rapid screening of adsorbents for postcombustion CO_2 capture.* Industrial & Engineering Chemistry Research, 2019. **58** (8): p. 3314-3328.

101. S. Sircar, *Basic research needs for design of adsorptive gas separation processes.* Industrial & engineering chemistry research, 2006. **45** (16): p. 5435-5448.

102. P. Xiao, J. Zhang, P. Webley, G. Li, R. Singh, and R. Todd, *Capture of CO_2 from flue gas streams with zeolite 13X by vacuum-pressure swing adsorption.* Adsorption, 2008. **14** (4-5): p. 575-582.

103. S. Krishnamurthy, V.R. Rao, S. Guntuka, P. Sharratt, R. Haghpanah, A. Rajendran, M. Amanullah, I.A. Karimi, and S. Farooq, *CO_2 capture from dry flue gas by vacuum swing adsorption: a pilot plant study.* AIChE Journal, 2014. **60** (5): p. 1830-1842.

104. J.A. Ritter, S.J. Bhadra, and A.D. Ebner, *On the use of the dual-process Langmuir model for correlating unary equilibria and predicting mixed-gas adsorption equilibria.* Langmuir, 2011. **27** (8): p. 4700-4712.

105. N.S. Wilkins, A. Rajendran, and S. Farooq, *Dynamic column breakthrough experiments for measurement of adsorption equilibrium and kinetics.* Adsorption, 2020: p. 1-26.

106. T. Hocker, A. Rajendran, and M. Mazzotti, *Measuring and modeling supercritical adsorption in porous solids. Carbon dioxide on 13X zeolite and on silica gel.* Langmuir, 2003. **19** (4): p. 1254-1267.

107. S. Gumma and O. Talu, *Net adsorption: a thermodynamic framework for supercritical gas adsorption and storage in porous solids.* Langmuir, 2010. **26** (22): p. 17013-17023.

108. D. Broom, *Characterizing Adsorbents for Gas Separations.* Chem. Eng. Prog., 2018. **114** (3): p. 30-37.

109. R. Haghpanah, A. Majumder, R. Nilam, A. Rajendran, S. Farooq, I.A. Karimi, and M. Amanullah, *Multiobjective optimization of a four-step adsorption process for postcombustion CO_2 capture via finite volume simulation.* Ind. Eng. Chem. Res., 2013. **52** (11): p. 4249-4265.

110. S. Guntuka, S. Banerjee, S. Farooq, and M. Srinivasan, *A-and B-site substituted lanthanum cobaltite perovskite as high temperature oxygen sorbent. 1. Thermogravimetric analysis of equilibrium and kinetics.* Ind. Eng. Chem. Res., 2008. **47** (1): p. 154-162.

111. S. Builes, S.I. Sandler, and R. Xiong, *Isosteric heats of gas and liquid adsorption.* Langmuir, 2013. **29** (33): p. 10416-10422.

112. M. Mazzotti and A. Rajendran, *Equilibrium theory–based analysis of nonlinear waves in separation processes.* Annu. Rev. Chem. Biomol., 2013. **4**: p. 119-141.

113. S.A. Hosseinzadeh Hejazi, A. Rajendran, J.A. Sawada, and S.M. Kuznicki, *Dynamic column breakthrough and process studies of high-purity oxygen production using silver-exchanged titanosilicates.* Ind. Eng. Chem. Res., 2016. **55** (20): p. 5993-6005.

114. B. Medi and M. Amanullah, *Application of a finite-volume method in the simulation of chromatographic systems: effects of flux limiters.* Ind. Eng. Chem. Res., 2011. **50** (3): p. 1739-1748.

115. E. Lemmon, M. Huber, and M. McLinden, *NIST Standard Reference Database 23, Reference Fluid Thermodynamic and Transport Properties (REFPROP), version 9.0, National Institute of Standards and Technology.* 2010. **22**: p. 2010.

116. P.C. Wankat and P.C. Wankat, *Separation Process Engineering:" Formerly Published as Equilibrium Staged Separations.".* 2007: Prentice Hall.

117. G. Avijegon, G. Xiao, G. Li, and E.F. May, *Binary and ternary adsorption equilibria for $CO_2/CH_4/N_2$ mixtures on Zeolite 13X beads from 273 to 333 K and pressures to 900 kPa.* Adsorption, 2018. **24** (4): p. 381-392.

118. A.H. Farmahini, S. Krishnamurthy, D. Friedrich, S. Brandani, and L. Sarkisov, *From crystal to adsorption column: challenges in multiscale computational screening of materials for adsorption separation processes.* Ind. Eng. Chem. Res., 2018. **57** (45): p. 15491-15511.

119. G. Li, P. Xiao, P.A. Webley, J. Zhang, and R. Singh, *Competition of CO_2/H_2O in adsorption based CO_2 capture.* Energy Procedia, 2009. **1** (1): p. 1123-1130.

120. C. Altintas, G. Avci, H. Daglar, A. Nemati Vesali Azar, S. Velioglu, I. Erucar, and S. Keskin, *Database for CO_2 separation performances of MOFs based on computational materials screening.* ACS applied materials & interfaces, 2018. **10** (20): p. 17257-17268.

121. J. Yu, L.-H. Xie, J.-R. Li, Y. Ma, J.M. Seminario, and P.B. Balbuena, *CO_2 capture and separations using MOFs: computational and experimental studies.* Chem. Rev., 2017. **117** (14): p. 9674-9754.

122. N. Chanut, S. Bourrelly, B. Kuchta, C. Serre, J.S. Chang, P.A. Wright, and P.L. Llewellyn, *Screening the effect of water vapour on gas adsorption performance: application to CO_2 capture from flue gas in metal–organic frameworks.* ChemSusChem, 2017. **10** (7): p. 1543-1553.

123. N.C. Burtch, H. Jasuja, and K.S. Walton, *Water stability and adsorption in metal–organic frameworks.* Chem. Rev., 2014. **114** (20): p. 10575-10612.

124. J. Canivet, A. Fateeva, Y. Guo, B. Coasne, and D. Farrusseng, *Water adsorption in MOFs: fundamentals and applications.* Chem. Soc. Rev., 2014. **43** (16): p. 5594-5617.

125. K. Sumida, D.L. Rogow, J.A. Mason, T.M. McDonald, E.D. Bloch, Z.R. Herm, T.-H. Bae, and J.R. Long, *Carbon dioxide capture in metal–organic frameworks.* Chem. Rev., 2012. **112** (2): p. 724-781.

126. J. Liu, Y. Wang, A.I. Benin, P. Jakubczak, R.R. Willis, and M.D. LeVan, *CO_2/H_2O adsorption equilibrium and rates on metal− organic frameworks: HKUST-1 and Ni/DOBDC.* Langmuir, 2010. **26** (17): p. 14301-14307.

127. E. Soubeyrand-Lenoir, C. Vagner, J.W. Yoon, P. Bazin, F. Ragon, Y.K. Hwang, C. Serre, J.-S. Chang, and P.L. Llewellyn, *How water fosters a remarkable 5-fold increase in low-pressure CO_2 uptake within mesoporous MIL-100 (Fe)*. J. Am. Chem. Soc., 2012. **134** (24): p. 10174-10181.

128. N.A. Qasem and R. Ben-Mansour, *Adsorption breakthrough and cycling stability of carbon dioxide separation from $CO_2/N_2/H_2O$ mixture under ambient conditions using 13X and Mg-MOF-74.* Appl. Energy, 2018. **230**: p. 1093-1107.

129. M. Hefti, L. Joss, D. Marx, and M. Mazzotti, *An experimental and modeling study of the adsorption equilibrium and dynamics of water vapor on activated carbon.* Ind. Eng. Chem. Res., 2015. **54** (48): p. 12165-12176.

130. L.F. Velasco, R. Guillet-Nicolas, G. Dobos, M. Thommes, and P. Lodewyckx, *Towards a better understanding of water adsorption hysteresis in activated carbons by scanning isotherms.* Carbon, 2016. **96**: p. 753-758.

131. M. Thommes, B. Smarsly, M. Groenewolt, P.I. Ravikovitch, and A.V. Neimark, *Adsorption hysteresis of nitrogen and argon in pore networks and characterization of novel micro-and mesoporous silicas.* Langmuir, 2006. **22** (2): p. 756-764.

132. W. Zhang, Y. Shan, and A. Seidel-Morgenstern, *Breakthrough curves and elution profiles of single solutes in case of adsorption isotherms with two inflection points.* J. Chromatogr. A, 2006. **1107** (1-2): p. 216-225.

133. G. Li, P. Xiao, P. Webley, J. Zhang, R. Singh, and M. Marshall, *Capture of CO_2 from high humidity flue gas by vacuum swing adsorption with zeolite 13X.* Adsorption, 2008. **14** (2-3): p. 415-422.

134. R. Arvind, S. Farooq, and D. Ruthven, *Analysis of a piston PSA process for air separation.* Chem. Eng. Sci., 2002. **57** (3): p. 419-433.

135. K. Sing, D. Everett, R. Haul, L. Moscou, R. Pierotti, J. Rouquerol, and T. Siemieniewska, . 1985, Pure Appl Chem.

136. M. Thommes, K. Kaneko, A.V. Neimark, J.P. Olivier, F. Rodriguez-Reinoso, J. Rouquerol, and K.S. Sing, *Physisorption of gases, with special reference to the evaluation of surface*

area and pore size distribution (IUPAC Technical Report). Pure Appl. Chem., 2015. **87** (9-10): p. 1051-1069.

137. H. Dureckova, *Robust Machine Learning QSPR Models for Recognizing High Performing MOFs for Pre-Combustion Carbon Capture and Using Molecular Simulation to Study Adsorption of Water and Gases in Novel MOFs*. 2018, Université d'Ottawa/University of Ottawa.

138. M. Thommes, *Physical adsorption characterization of nanoporous materials.* Chem. Ing. Tech., 2010. **82** (7): p. 1059-1073.

139. G.M. Martinez and D. Basmadjian, *Towards a general gas adsorption isotherm.* Chem. Eng. Sci., 1996. **51** (7): p. 1043-1054.

140. M. Ilić, D. Flockerzi, and A. Seidel-Morgenstern, *A thermodynamically consistent explicit competitive adsorption isotherm model based on second-order single component behaviour.* J. Chromatogr. A, 2010. **1217** (14): p. 2132-2137.

141. T. Hill, *An Introduction to Statistical Thermodynamics, Adison-Wesley.* Reading, MA, 1960.

142. G.A. Baker, G.A. Baker Jr, G. Baker, P. Graves-Morris, and S.S. Baker, *Pade Approximants: Encyclopedia of Mathematics and It's Applications, Vol. 59 George A. Baker, Jr., Peter Graves-Morris*. Vol. 59. 1996: Cambridge University Press.

143. R. Haghpanah, A. Rajendran, S. Farooq, I.A. Karimi, and M. Amanullah, *Discrete equilibrium data from dynamic column breakthrough experiments.* Ind. Eng. Chem. Res., 2012. **51** (45): p. 14834-14844.

144. A. Rajendran, R.T. Maruyama, H.O.R. Landa, and A. Seidel-Morgenstern, *Modelling binary non-linear chromatography using discrete equilibrium data.* Adsorption, 2020: p. 1-15.

145. The Intergovernmental Panel on Climate Change (IPCC), *Carbon Dioxide Capture and Storage.* 2005.

146. J. Davison. *CCS Costs and Economics*. in *IEAGHGOPEC Workshop on CCS CDM*. 2013.

147. S. Choi, J.H. Drese, and C.W. Jones, *Adsorbent materials for carbon dioxide capture from large anthropogenic point sources.* ChemSusChem, 2009. **2** (9): p. 796-854.

148. A. Sayari and Y. Belmabkhout, *Stabilization of amine-containing CO_2 adsorbents: dramatic effect of water vapor.* J. Am. Chem. Soc., 2010. **132** (18): p. 6312-6314.

149. R. Ben-Mansour, N.A. Qasem, and M.A. Antar, *Carbon dioxide adsorption separation from dry and humid CO_2/N_2 mixture.* Comput. Chem. Eng., 2018. **117**: p. 221-235.

150. A.C. Kizzie, A.G. Wong-Foy, and A.J. Matzger, *Effect of humidity on the performance of microporous coordination polymers as adsorbents for CO_2 capture.* Langmuir, 2011. **27** (10): p. 6368-6373.

151. G.D. Pirngruber, L. Hamon, S. Bourrelly, P.L. Llewellyn, E. Lenoir, V. Guillerm, C. Serre, and T. Devic, *A method for screening the potential of MOFs as CO_2 adsorbents in pressure swing adsorption processes.* ChemSusChem, 2012. **5** (4): p. 762-776.

152. A. Lorek and J. Majewski, *Humidity Measurement in Carbon Dioxide with Capacitive Humidity Sensors at Low Temperature and Pressure.* Sensors, 2018. **18** (8): p. 2615.

153. A.L. Myers and J.M. Prausnitz, *Thermodynamics of mixed-gas adsorption.* AIChE journal, 1965. **11** (1): p. 121-127.

154. M. Ding, R.W. Flaig, H.-L. Jiang, and O.M. Yaghi, *Carbon capture and conversion using metal–organic frameworks and MOF-based materials.* Chem. Soc. Rev., 2019. **48** (10): p. 2783-2828.

155. G. Lal, M. Derakhshandeh, F. Akhtar, D.M. Spasyuk, J.-B. Lin, M. Trifkovic, and G.K. Shimizu, *Mechanical properties of a metal–organic framework formed by covalent cross-linking of metal–organic polyhedra.* J. Am. Chem. Soc., 2018. **141** (2): p. 1045-1053.

156. R. Vaidhyanathan, S.S. Iremonger, K.W. Dawson, and G.K. Shimizu, *An amine-functionalized metal organic framework for preferential CO_2 adsorption at low pressures.* Chem. Commun., 2009 (35): p. 5230-5232.

157. X. Kong, E. Scott, W. Ding, J.A. Mason, J.R. Long, and J.A. Reimer, *CO_2 dynamics in a metal–organic framework with open metal sites.* J. Am. Chem. Soc., 2012. **134** (35): p. 14341-14344.

158. Y.G. Chung, J. Camp, M. Haranczyk, B.J. Sikora, W. Bury, V. Krungleviciute, T. Yildirim, O.K. Farha, D.S. Sholl, and R.Q. Snurr, *Computation-ready, experimental metal–organic frameworks: A tool to enable high-throughput screening of nanoporous crystals.* Chem. Mater., 2014. **26** (21): p. 6185-6192.

159. Y.G. Chung, E. Haldoupis, B.J. Bucior, M. Haranczyk, S. Lee, H. Zhang, K.D. Vogiatzis, M. Milisavljevic, S. Ling, and J.S. Camp, *Advances, Updates, and Analytics for the Computation-Ready, Experimental Metal–Organic Framework Database: CoRE MOF 2019.* Journal of Chemical & Engineering Data, 2019. **64** (12): p. 5985-5998.

160. F. Kolbe, S. Krause, V. Bon, I. Senkovska, S. Kaskel, and E. Brunner, *High-pressure in situ 129Xe NMR spectroscopy: insights into switching mechanisms of flexible metal–organic frameworks isoreticular to DUT-49.* Chem. Mater., 2019. **31** (16): p. 6193-6201.

161. V. Bon, I. Senkovska, M.S. Weiss, and S. Kaskel, *Tailoring of network dimensionality and porosity adjustment in Zr-and Hf-based MOFs.* CrystEngComm, 2013. **15** (45): p. 9572-9577.

162. S.B. Choi, H. Furukawa, H.J. Nam, D.Y. Jung, Y.H. Jhon, A. Walton, D. Book, M. O'Keeffe, O.M. Yaghi, and J. Kim, *Reversible interpenetration in a metal–organic framework triggered by ligand removal and addition.* Angew. Chem., 2012. **124** (35): p. 8921-8925.

163. O.M. Yaghi, M. Eddaoudi, H. Li, J. Kim, and N. Rosi, *Isoreticular metal-organic frameworks, process for forming the same, and systematic design of pore size and functionality therein, with application for gas storage*. 2005, Google Patents.

164. S.M. Cohen, *Postsynthetic methods for the functionalization of metal–organic frameworks.* Chem. Rev., 2012. **112** (2): p. 970-1000.

165. S.J. Garibay and S.M. Cohen, *Isoreticular synthesis and modification of frameworks with the UiO-66 topology.* Chem. Commun., 2010. **46** (41): p. 7700-7702.

166. C. Serre, F. Millange, C. Thouvenot, M. Nogues, G. Marsolier, D. Louër, and G. Férey, *Very Large Breathing Effect in the First Nanoporous Chromium (III)-Based Solids: MIL-53 or CrIII (OH)⊙{O₂C− C₆H₄− CO₂}⊙{HO₂C− C₆H₄− CO₂H} x⊙ H₂O y.* J. Am. Chem. Soc., 2002. **124** (45): p. 13519-13526.

167. T. Loiseau, C. Serre, C. Huguenard, G. Fink, F. Taulelle, M. Henry, T. Bataille, and G. Férey, *A rationale for the large breathing of the porous aluminum terephthalate (MIL-53) upon hydration.* Chemistry–A European Journal, 2004. **10** (6): p. 1373-1382.

168. F. Salles, A. Ghoufi, G. Maurin, R.G. Bell, C. Mellot-Draznieks, and G. Férey, *Molecular Dynamics Simulations of Breathing MOFs: Structural Transformations of MIL-53 (Cr) upon Thermal Activation and CO_2 Adsorption.* Angewandte Chemie International Edition, 2008. **47** (44): p. 8487-8491.

169. N. Nijem, H. Wu, P. Canepa, A. Marti, K.J. Balkus Jr, T. Thonhauser, J. Li, and Y.J. Chabal, *Tuning the gate opening pressure of metal–organic frameworks (MOFs) for the selective separation of hydrocarbons.* J. Am. Chem. Soc., 2012. **134** (37): p. 15201-15204.

170. G.D. Pirngruber, L. Hamon, S. Bourrelly, P.L. Llewellyn, E. Lenoir, V. Guillerm, C. Serre, and T. Devic, *A method for screening the potential of MOFs as CO_2 adsorbents in pressure swing adsorption processes.* Chem. Sus. Chem., 2012. **5** (4): p. 762-776.

171. R. Haghpanah, R. Nilam, A. Rajendran, S. Farooq, and I.A. Karimi, *Cycle synthesis and optimization of a VSA process for postcombustion CO_2 capture.* AIChE Journal, 2013. **59** (12): p. 4735-4748.

172. V. Subramanian Balashankar and A. Rajendran, *Process Optimization-Based Screening of Zeolites for Post-Combustion CO_2 Capture by Vacuum Swing Adsorption.* Sus. Chem. Eng., 2019. **7** (21): p. 17747-17755.

173. S.A. Hosseinzadeh Hejazi, L. Estupiñan Perez, A. Rajendran, and S. Kuznicki, *Cycle development and process optimization of high-purity oxygen production using silver-exchanged titanosilicates.* Ind. Eng. Chem. Res., 2017. **56** (19): p. 5679-5691.

174. L.E. Perez, P. Sarkar, and A. Rajendran, *Experimental validation of multi-objective optimization techniques for design of vacuum swing adsorption processes.* Sep. Purif. Technol., 2019. **224**: p. 553-563.

175. N. Casas, J. Schell, L. Joss, and M. Mazzotti, *A parametric study of a PSA process for pre-combustion CO_2 capture.* Sep. Purif. Technol., 2013. **104**: p. 183-192.

176. D. Marx, L. Joss, M. Hefti, M. Gazzani, and M. Mazzotti, *CO_2 Capture from a Binary CO_2/N_2 and a Ternary $CO_2/N_2/H_2$ Mixture by PSA: Experiments and Predictions*. Industrial & Engineering Chemistry Research, 2015. **54** (22): p. 6035-6045.

177. G. Li, P. Xiao, J. Zhang, P.A. Webley, and D. Xu, *The role of water on postcombustion CO_2 capture by vacuum swing adsorption: Bed layering and purge to feed ratio.* AIChE Journal, 2014. **60** (2): p. 673-689.

Appendix

Table A2.1: List of CO_2 and N_2 adsorption breakthrough experiments on CALF-20

Test gas	Q_{in} **[ccm]**	**T [°C]**	**P [bar]**	y_{CO_2} **[-]**	y_{N_2} **[-]**	$q^*_{CO_2}$ **[mmol/g]**	$q^*_{N_2}$ **[mmol/g]**
N_2+He	100	23.2	0.97	-	0.15	-	0.032
N_2+He	50	22.3	0.97	-	0.50	-	0.131
N_2+He	25	22.0	0.97	-	1.00	-	0.248
CO_2+He	50	22.4	0.97	0.50	-	2.510	-
CO_2+He	50	22.3	0.97	0.70	-	2.744	-
CO_2+He	50	22.4	0.97	1.00	-	2.945	-
CO_2+N_2	100	23.4	0.97	0.05	0.95	1.514	-
CO_2+N_2	100	20.3	0.97	0.15	0.85	2.101	-
CO_2+N_2	100	21.8	0.98	0.30	0.70	2.392	-
CO_2+N_2	100	23.2	0.98	0.40	0.60	2.520	-
CO_2+N_2	100	22.4	0.97	0.50	0.50	2.672	-
CO_2+N_2	100	22.5	0.97	0.70	0.30	2.810	-
CO_2+N_2	100	22.3	0.97	0.80	0.20	2.910	-

Table A2.2: List of CO_2 and N_2 desorption breakthrough experiments on CALF-20. Helium was used as the purge gas for all experiments

Test gas	Q_{in} **[ccm]**	**T [°C]**	**P [bar]**	y_{CO_2} **[-]**	y_{N_2} **[-]**	$q^*_{N_2}$ **[mmol/g]**
CO_2+N_2	25	22.4	0.97	0.05	0.95	0.177
CO_2+N_2	25	21.1	0.97	0.15	0.85	0.145
CO_2+N_2	100	22.1	0.98	0.30	0.70	0.110
CO_2+N_2	25	23.4	0.98	0.40	0.60	0.079
CO_2+N_2	25	23.3	0.97	0.50	0.50	0.061
CO_2+N_2	25	22.2	0.97	0.70	0.30	0.039
CO_2+N_2	25	23.2	0.97	0.80	0.20	0.028

Table A4.1: The relative humidity calibration data in the air and pure CO_2 environment at 22°C and 0.97 bar with a total flowrate of 200 ccm

Dry flow [ccm]	**Wet flow [ccm]**	**RH in Air [%]**	**RH in CO_2 [%]**
178	22	12.1	12.5
140	60	29.8	25.4
110	90	43.5	35.9
65	135	64.9	52.5
40	160	81.3	66.7
10	190	91.7	75.7

Table A4.2: The modified Langmuir isotherm parameters of CO_2 on CALF-20

Parameter		**CO_2**
q_{sb}	mmol/g	2.387
b_0	m^3/mol	5.519 x 10^{-7}
ΔU_b	kJ/mol	-35.06
q_{sd}	mmol/g	3.271
d_0	m^3/mol	5.187 x 10^{-8}
ΔU_d	kJ/mol	-28.95
λ_1	g/mmol	0.027
λ_2	g/mmol	0.703

Table A4.3: The Quadratic-Langmuir adsorption isotherm parameters for H_2O on CALF-20

Parameter		Pure H_2O	Competitive H_2O
q_{sb}	mmol/g	1.629	1.795
$b_{0,1}$	m^3/mol	-2.685 x 10^{-17}	-5.936 x 10^{-15}
$b_{0,2}$	$(m^3/mol)^2$	1.158 x 10^{-16}	1.013 x 10^{-15}
$b_{0,3}$	$(m^3/mol)^3$	5.374 x 10^{-17}	6.197 x 10^{-15}
ΔU_1	kJ/mol	-97.99	-81.67
q_{sd}	mmol/g	5.781	8.056
d_0	m^3/mol	8.773 x 10^{-12}	5.448 x 10^{-11}
ΔU_2	kJ/mol	-64.72	-54.41

Table A4.4: List of CO_2/H_2O competitive adsorption DCB experiments

Test gas	Q_{in} [ccm]	T [°C]	P [bar]	RH [%]	$q^*_{H_2O}$ [mmol/g]	$q^*_{CO_2}$ [mmol/g]
CO_2/H_2O	200	22.2	0.97	13	0.137	2.95
CO_2/H_2O	200	22.5	0.97	18	0.22	2.93
CO_2/H_2O	200	24.2	0.97	23	0.45	2.90
CO_2/H_2O	200	22.7	0.97	32	1.07	2.51
CO_2/H_2O	206	23.1	0.97	47	2.08	2.00
CO_2/H_2O	200	23.1	0.97	72	7.85	0.26
CO_2/H_2O	201	22.5	0.97	87	9.01	0.03

Table A4.5: Dynamic column breakthrough simulation parameters

Parameter	**Symbol**		**Value**	**Source**
Column length	L	m	0.0786	measured
Inner column diameter	d_{in}	m	0.0282	measured
Outer column diameter	d_{out}	m	0.0318	measured
Bed voidage	ε	-	0.4	measured
Particle void fraction	ϵ_p	-	0.35	assumed
Adsorbent mass	m_{ads}	g	16.7	measured
Tortuosity	τ	-	3.0	assumed
Universal gas constant	R	m^3 bar mol^{-1} K^{-1}	$8.314x10^{-5}$	standard
Adsorbent particle density	ρ_p	kg m^{-3}	570	measured
Column wall density	ρ_w	kg m^{-3}	7800	standard
Specific heat capacity	$C_{p,g}$	J kg^{-1} K^{-1} (He)	5200	NIST database
		(CO_2)	841	NIST database
		(H_2O)	4165	NIST database
Specific heat capacity of adsorbed phase	$C_{p,a}$	J kg^{-1} K^{-1}	$C_{p,g}$	assumed
Specific heat capacity of adsorbent	$C_{p,s}$	J kg^{-1} K^{-1}	1371	fitted
Specific heat capacity of column wall	$C_{p,w}$	J kg^{-1} K^{-1}	502	standard
Molecular diffusion	D_m	m s^{-2}	$1.496x10^{-5}$	standard
Effective gas thermal conductivity	K_z	W m^{-1} K^{-1}	0.4	fitted
Thermal conductivity of column wall	K_w	W m^{-1} K^{-1}	16	standard
Internal heat transfer coefficient	h_{in}	W m^{-2} K^{-1}	6.963	fitted
External heat transfer coefficient	h_{out}	W m^{-2} K^{-1}	14	fitted
Fluid viscosity	μ	kg m^{-1} s^{-1}	$1.812x10^{-5}$	standard
H_2O dispersion coefficient	D	m^2 s^{-1}	$9.364x10^{-5}$	fitted
H_2O mass transfer coefficient	k	s^{-1}	0.005	fitted

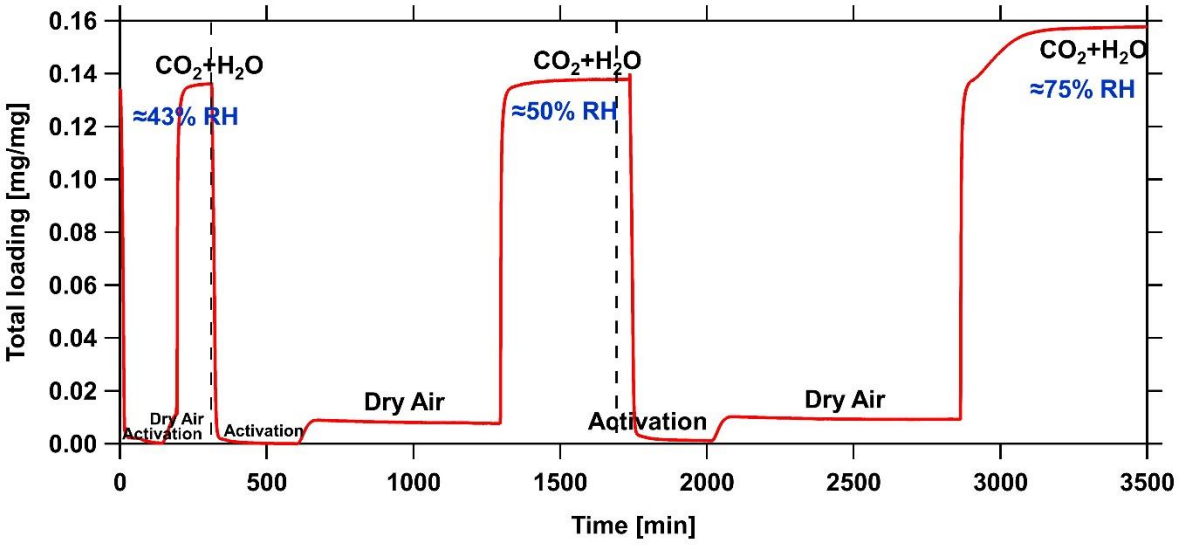

Figure A4.1: The total loading of CO_2 and H_2O (Adsorption) measured by the thermogravimetric analyzer (TGA). The adsorbent was activated at 150°C prior to each experiment. Pure CO_2 was used as the carrier gas to create a humid stream at a certain relative humidity (RH). The difference between the initial and final weight yields the total loading of CO_2 + H_2O.

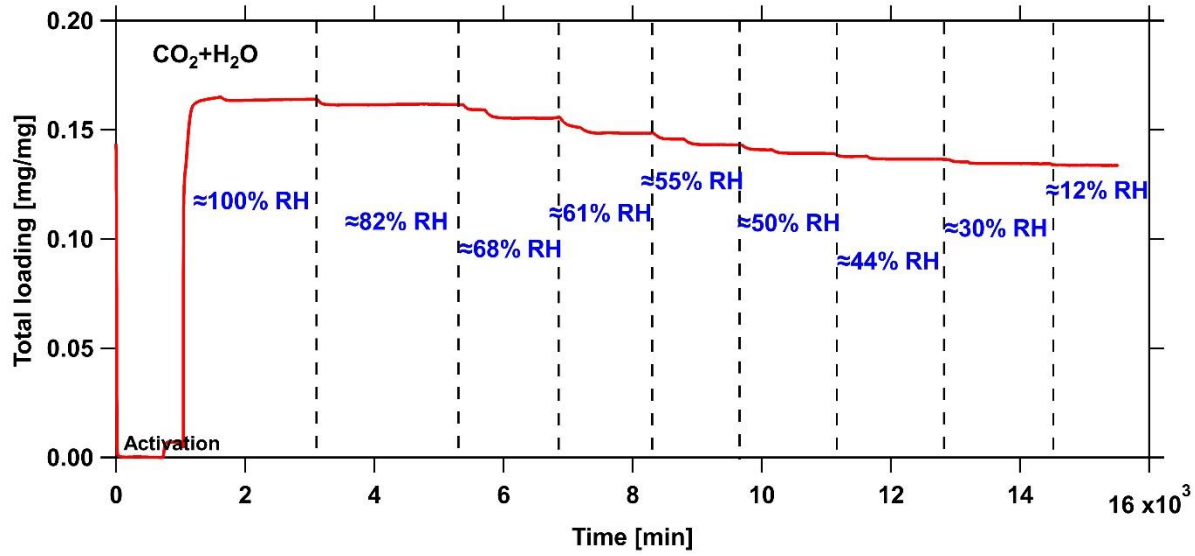

Figure A4.2: The total loading of CO_2 and H_2O (Desorption) measured by the thermogravimetric analyzer (TGA). The adsorbent was saturated with CO_2+H_2O at 100% RH initially. Then, the relative humidity was kept reducing to measure the desorption of CO_2+H_2O.

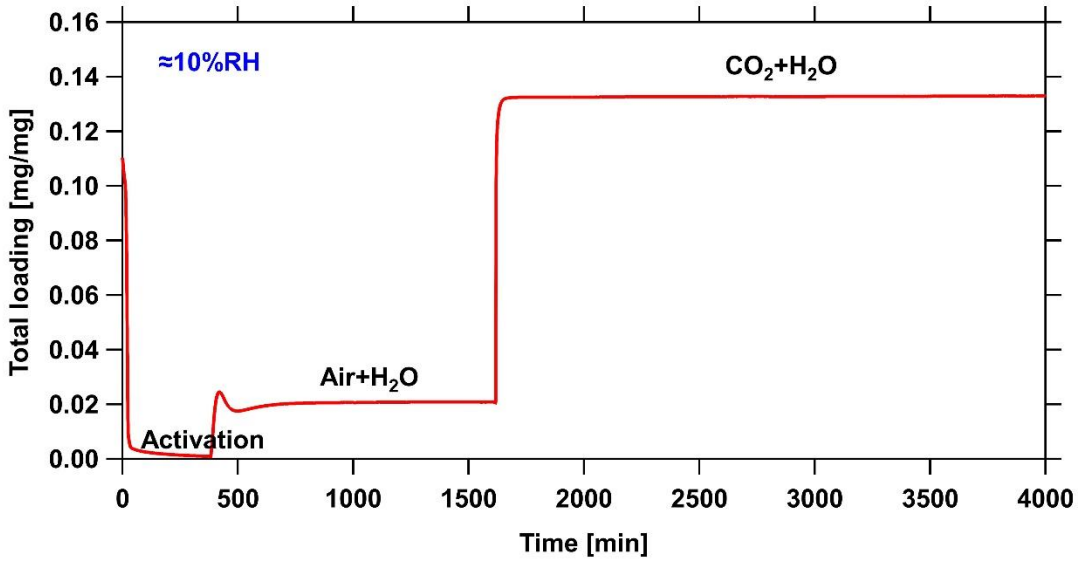

Figure A5.1: The total loading of Air+H_2O followed by CO_2+H_2O at ≈10% RH. The final step was running for two days to confirm that the final equilibrium was established

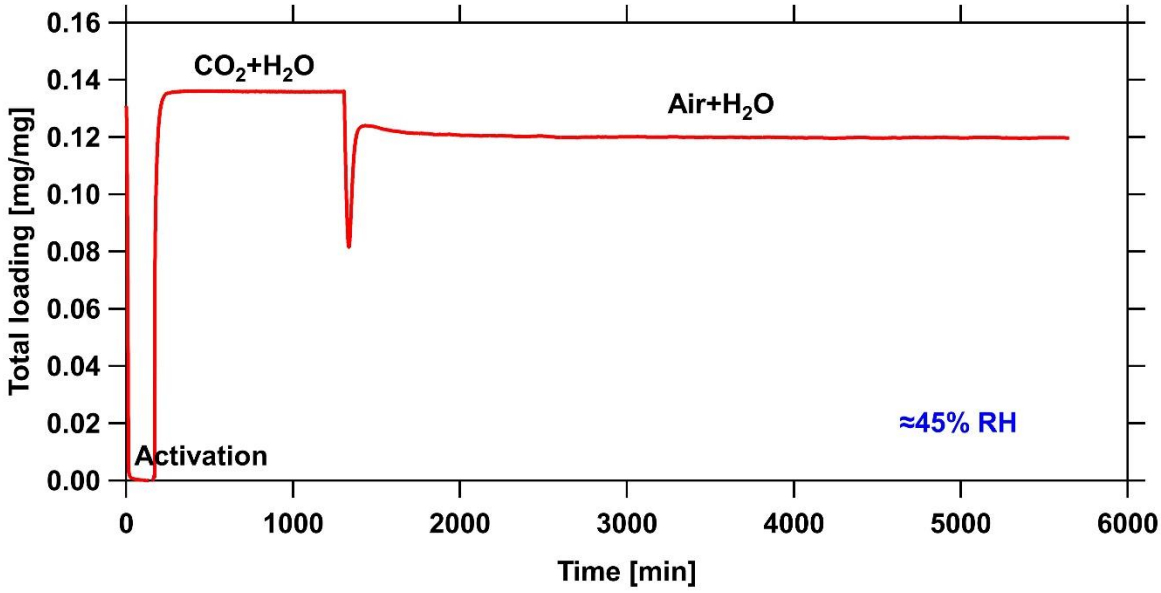

Figure A5.2: The total loading of CO_2+H_2O followed by Air+H_2O at ≈45% RH. The final step was running for almost three days to confirm that the final equilibrium was established

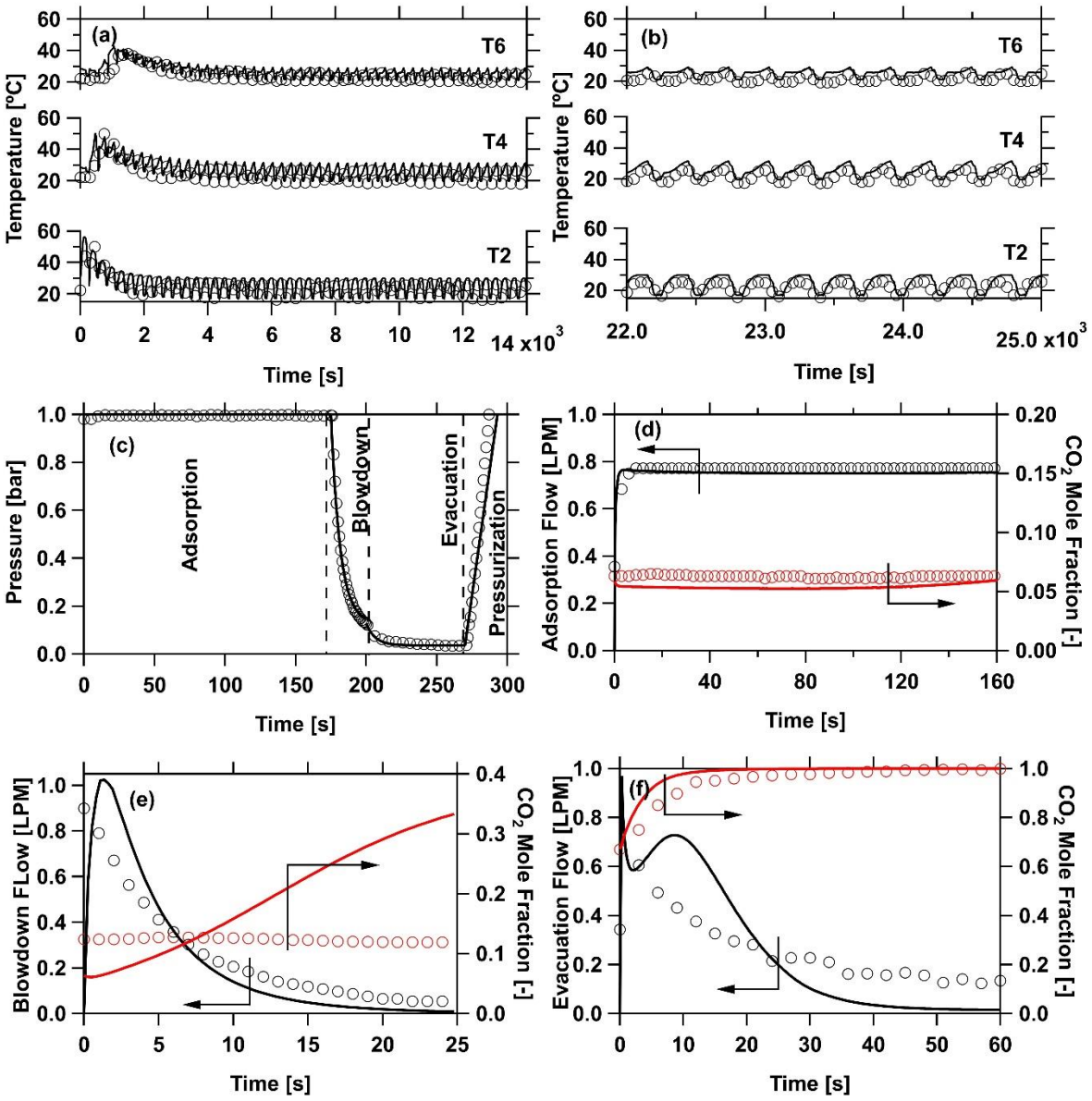

Figure A6.1: The comparison of experimental and simulated transitions for the basic four-step cycle from experiment I (Exp. I). The solid lines represent the simulation data, and the markers are the experimental data. (a, b) The temperature histories at three different locations; (c) The pressure histories of one cycle at CCS; (d, e, f) The CO_2 composition and the outlet flow rate of the adsorption step, blowdown step and evacuation step, respectively.

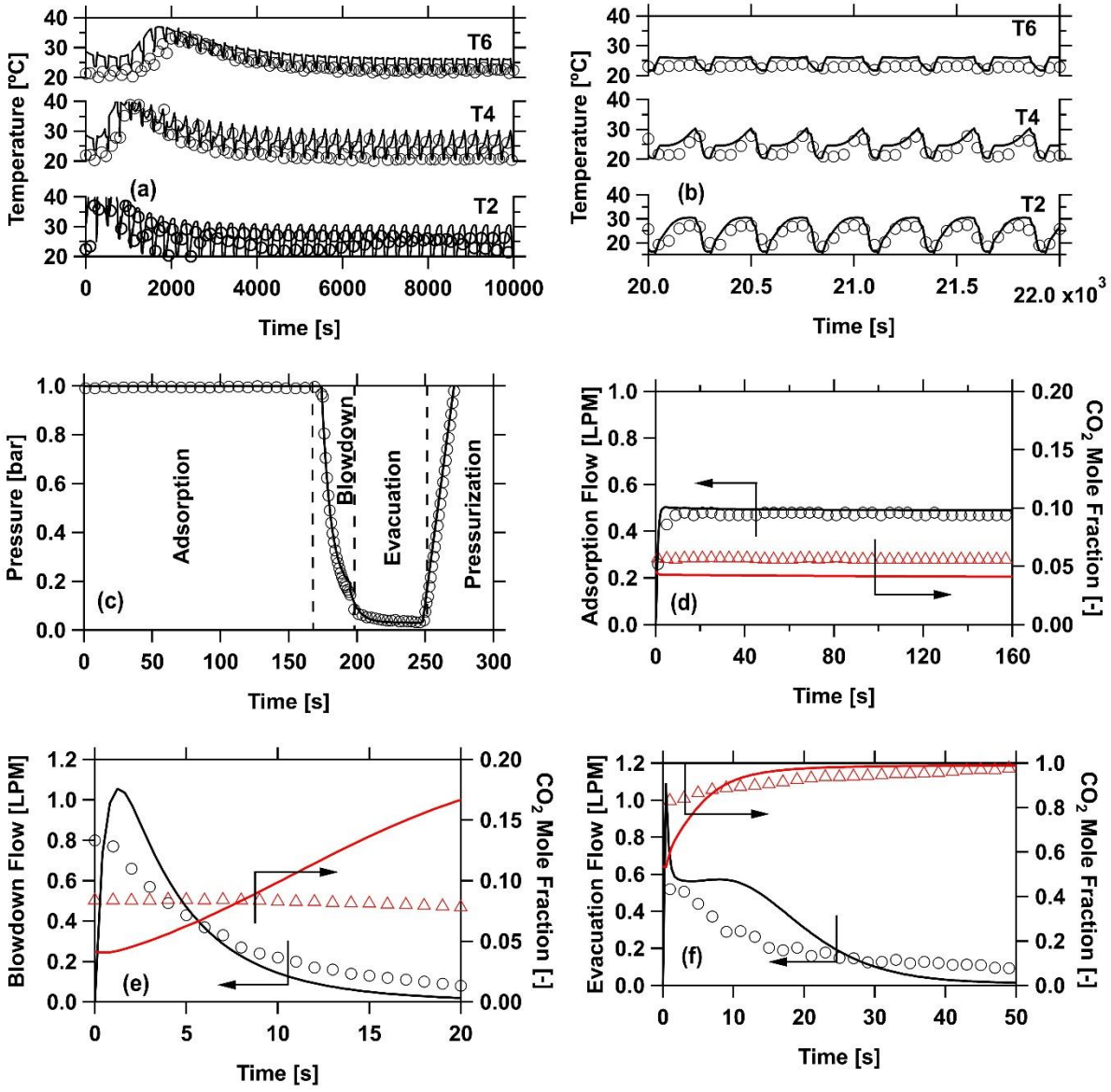

Figure A6.2: The comparison of experimental and simulated transitions for the basic four-step cycle from experiment II (Exp. II). The solid lines represent the simulation data, and the markers are the experimental data. (a, b) The temperature histories at three different locations; (c) The pressure histories of one cycle at CCS; (d, e, f) The CO_2 composition and the outlet flow rate of the adsorption step, blowdown step and evacuation step, respectively.

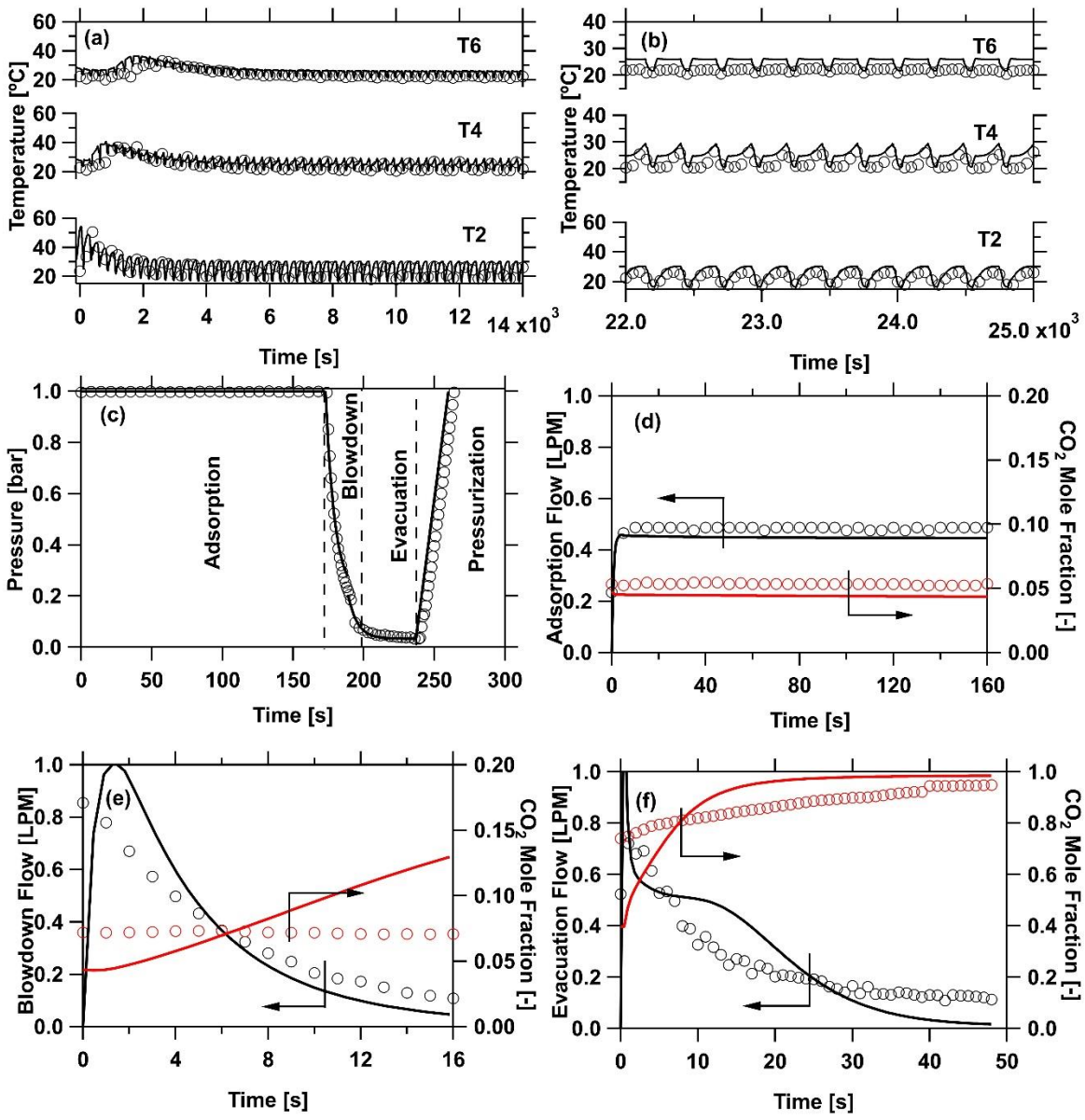

Figure A6.3: The comparison of experimental and simulated transitions for the basic four-step cycle from experiment III (Exp. III). The solid lines represent the simulation data, and the markers are the experimental data. (a, b) The temperature histories at three different locations; (c) The pressure histories of one cycle at CCS; (d, e, f) The CO_2 composition and the outlet flow rate of the adsorption step, blowdown step and evacuation step, respectively.

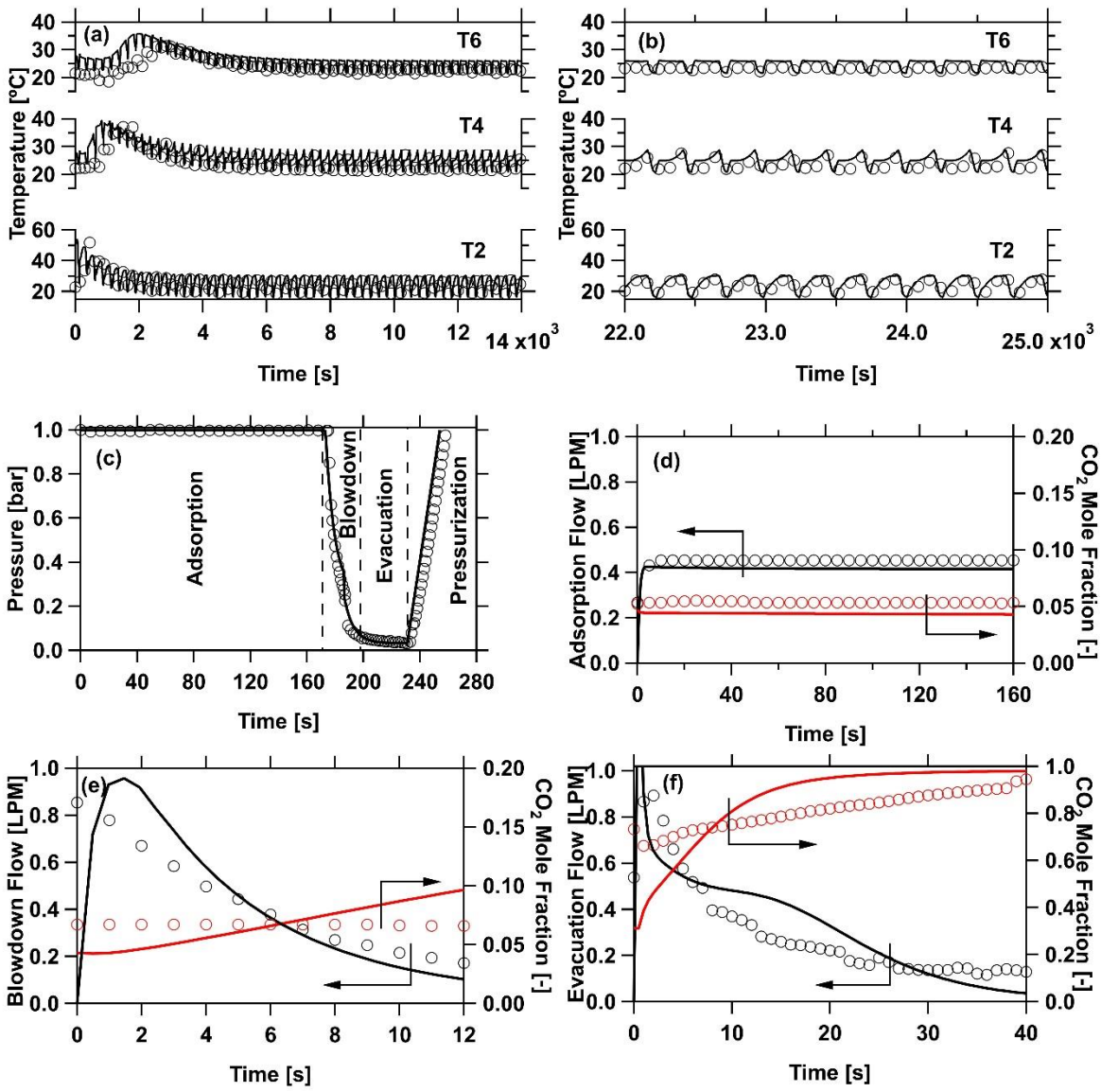

Figure A6.4: The comparison of experimental and simulated transitions for the basic four-step cycle from experiment IV (Exp. IV). The solid lines represent the simulation data, and the markers are the experimental data. (a, b) The temperature histories at three different locations; (c) The pressure histories of one cycle at CCS; (d, e, f) The CO_2 composition and the outlet flow rate of the adsorption step, blowdown step and evacuation step, respectively.

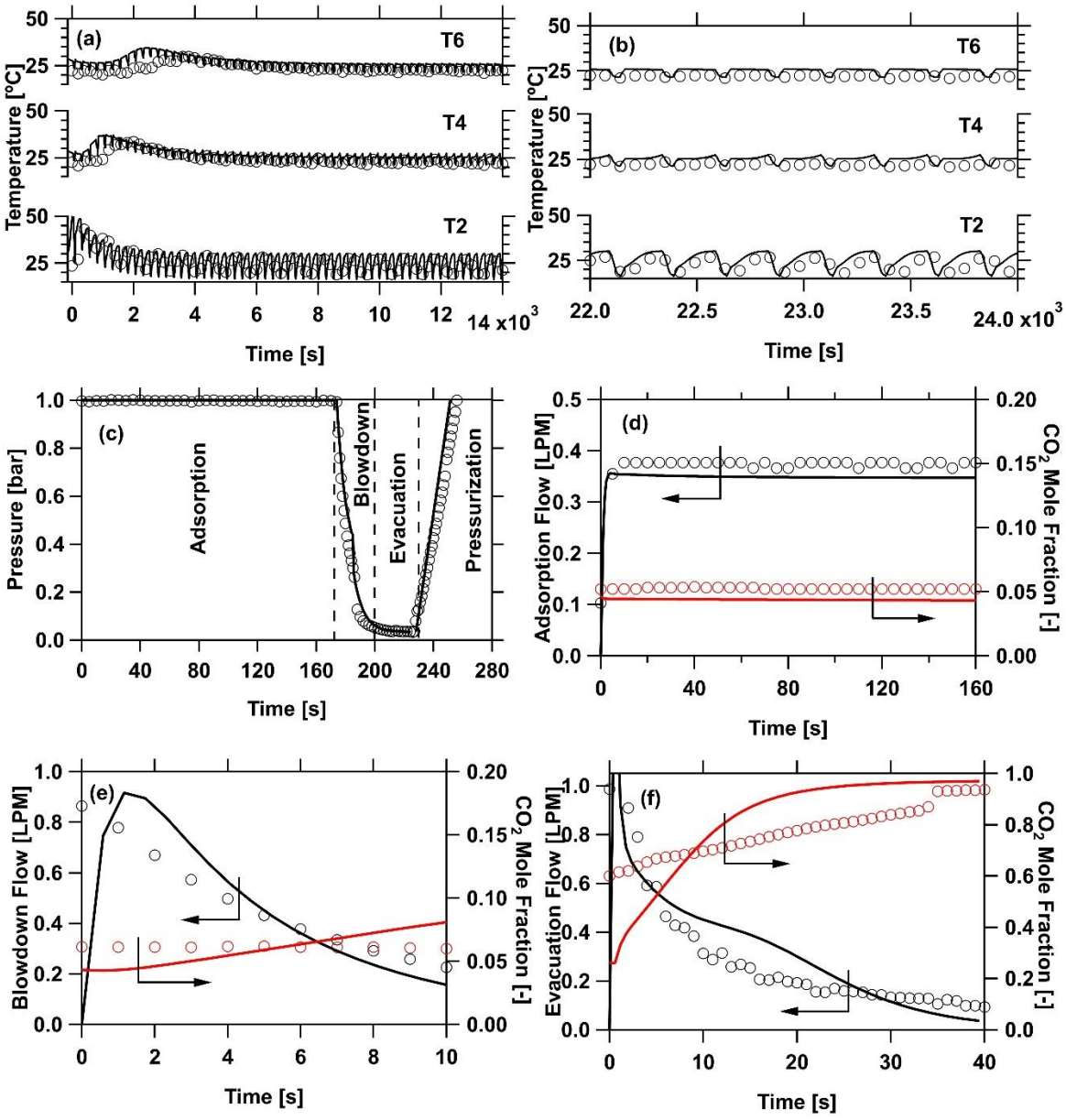

Figure A6.5: The comparison of experimental and simulated transitions for the basic four-step cycle from experiment V (Exp. V). The solid lines represent the simulation data, and the markers are the experimental data. (a, b) The temperature histories at three different locations; (c) The pressure histories of one cycle at CCS; (d, e, f) The CO_2 composition and the outlet flow rate of the adsorption step, blowdown step and evacuation step, respectively.

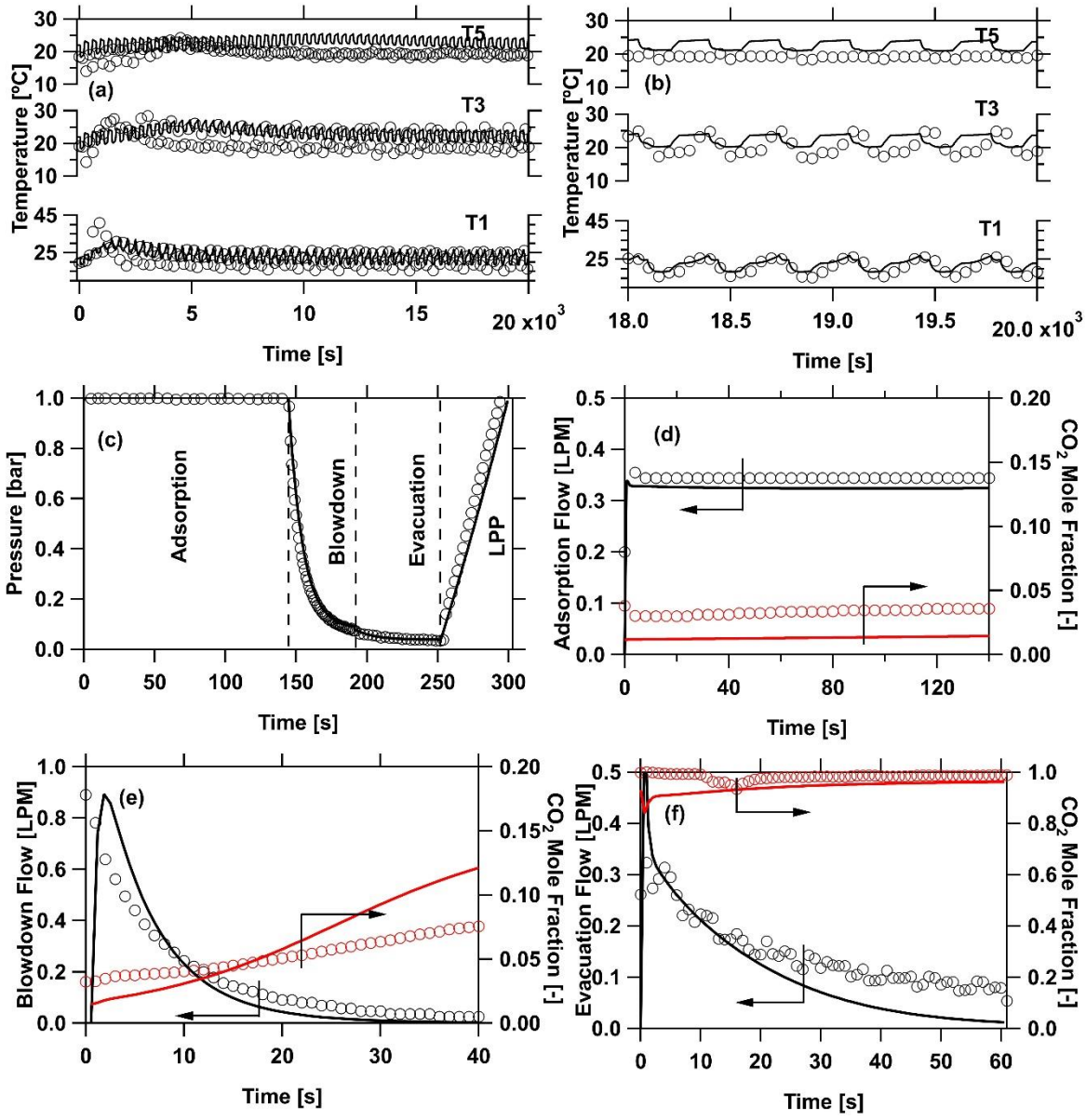

Figure A6.6: The comparison of experimental and simulated transients for the four-step VSA with LPP cycle from experiment VI (Exp. VI). The solid lines represent the simulation data, and the markers are the experimental data. (a,b) The temperature histories at three positions in the column; (c) The pressure histories of one cycle at CCS; (d, e, f) The CO_2 composition and the outlet flow rate of the adsorption step, blowdown step and evacuation step, respectively.

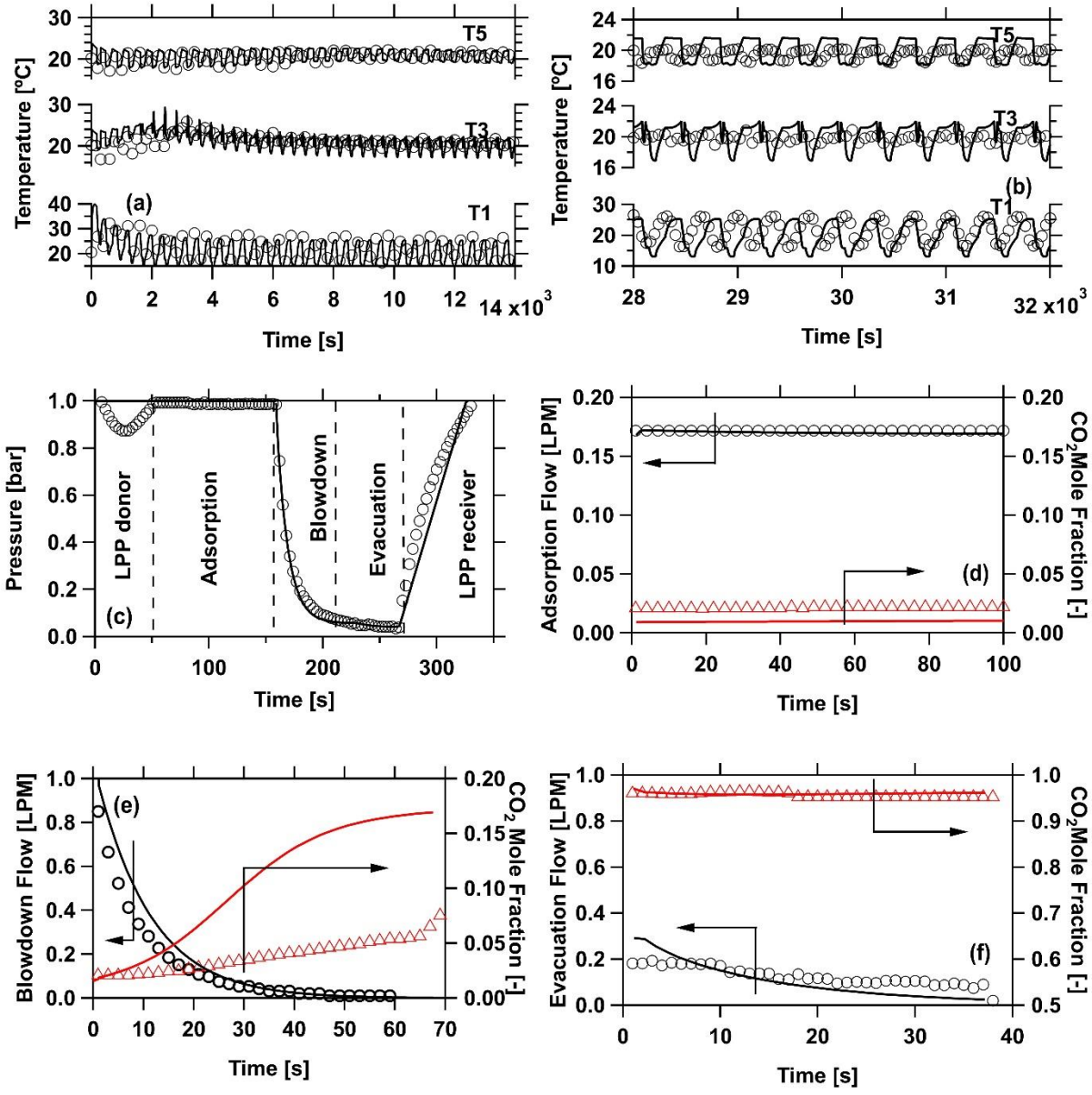

Figure A6.7: The comparison of experimental and simulated transients for the four-step VSA with LPP cycle from experiment VII (Exp. VII.a). The solid lines represent the simulation data, and the markers are the experimental data. (a,b) The temperature histories at three positions in the column; (c) The pressure histories of one cycle at CCS; (d, e, f) The CO_2 composition and the outlet flow rate of the adsorption step, blowdown step and evacuation step, respectively.

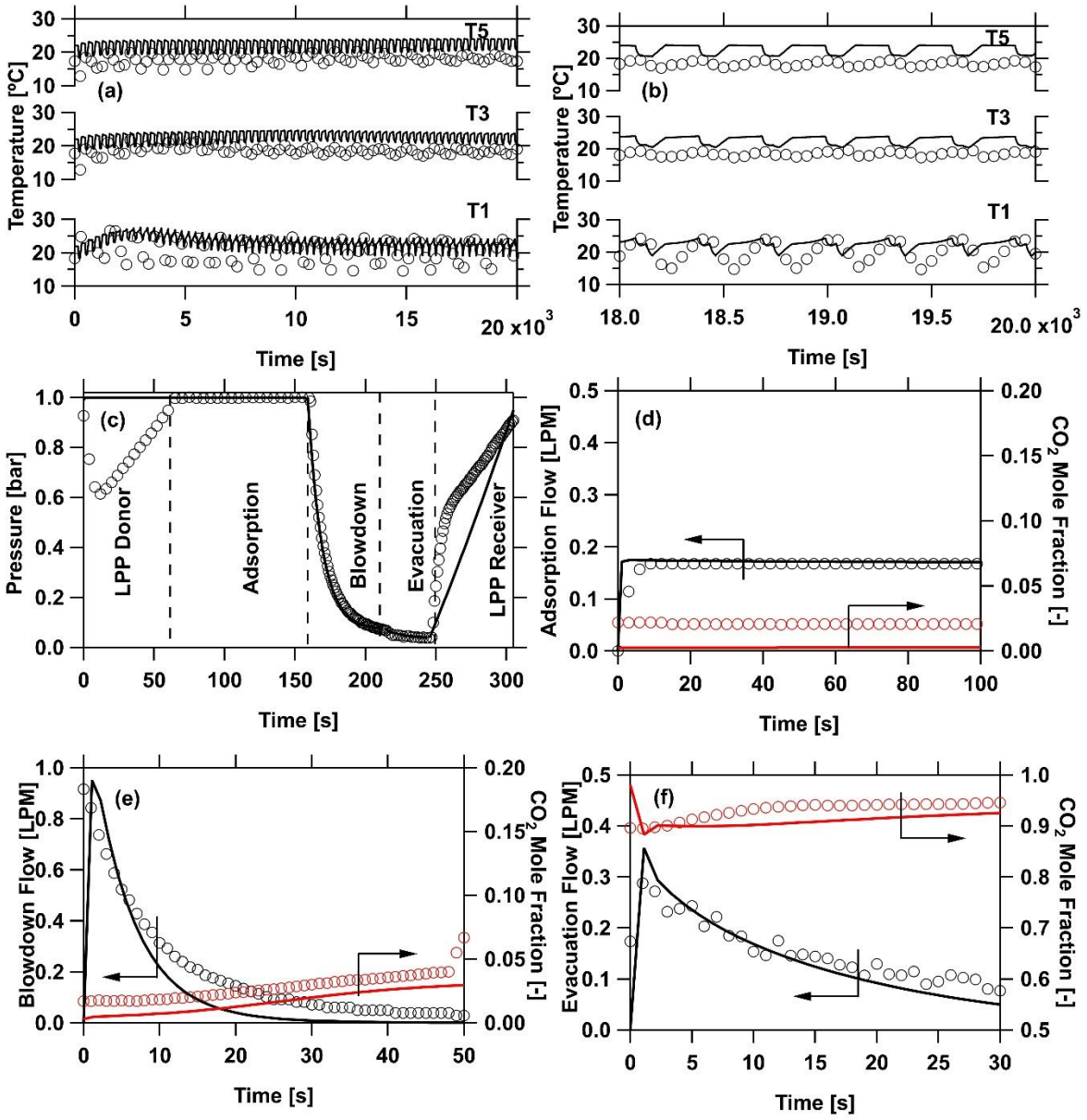

Figure A6.8: The comparison of experimental and simulated transients for the four-step VSA with LPP cycle from experiment VIII (Exp. VIII). The solid lines represent the simulation data, and the markers are the experimental data. (a,b) The temperature histories at three positions in the column; (c) The pressure histories of one cycle at CCS; (d, e, f) The CO_2 composition and the outlet flow rate of the adsorption step, blowdown step and evacuation step, respectively.

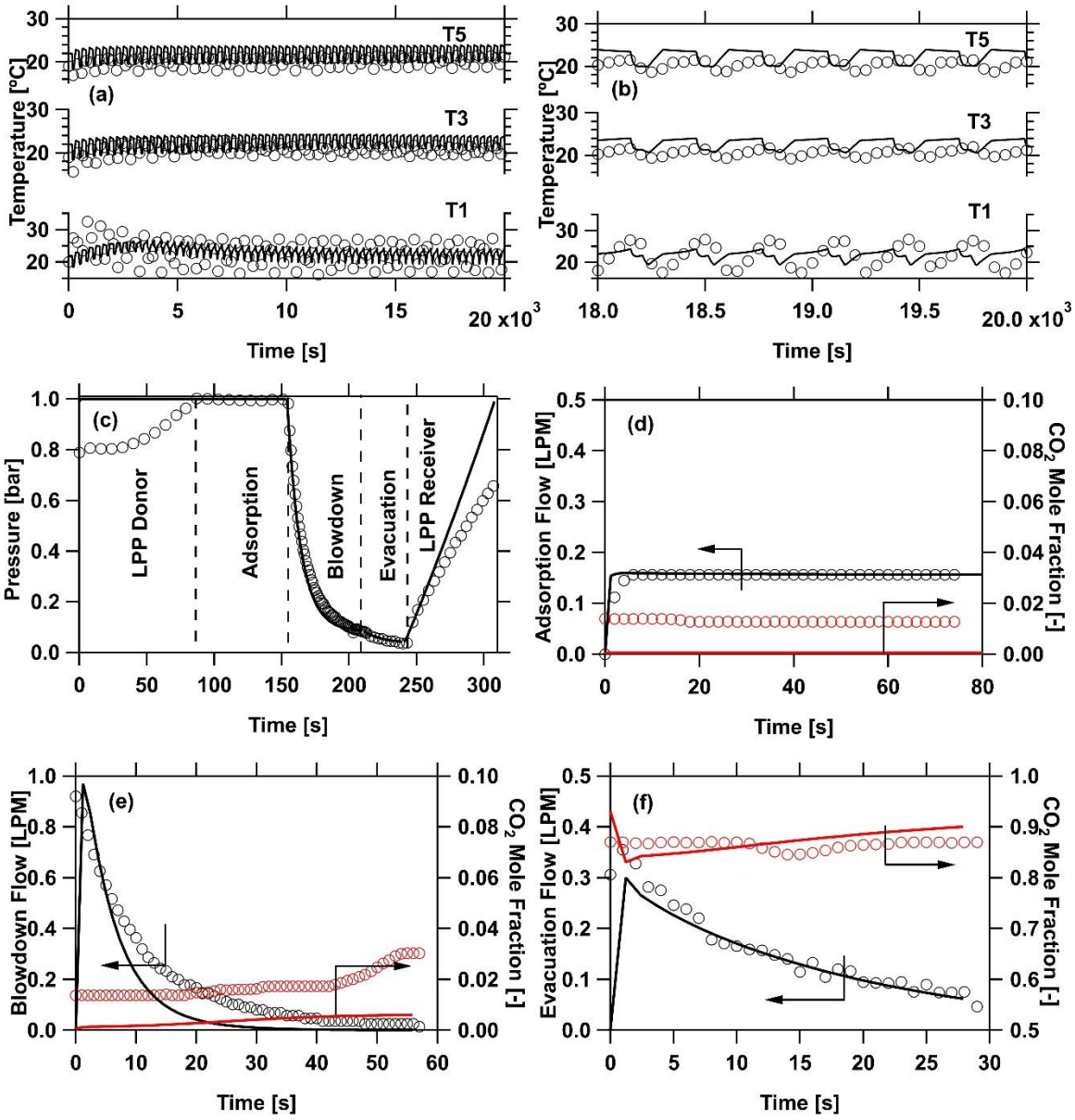

Figure A6.9: The comparison of experimental and simulated transients for the four-step VSA with LPP cycle from experiment IX (Exp. IX). The solid lines represent the simulation data, and the markers are the experimental data. (a,b) The temperature histories at three positions in the column; (c) The pressure histories of one cycle at CCS; (d, e, f) The CO_2 composition and the outlet flow rate of the adsorption step, blowdown step and evacuation step, respectively.

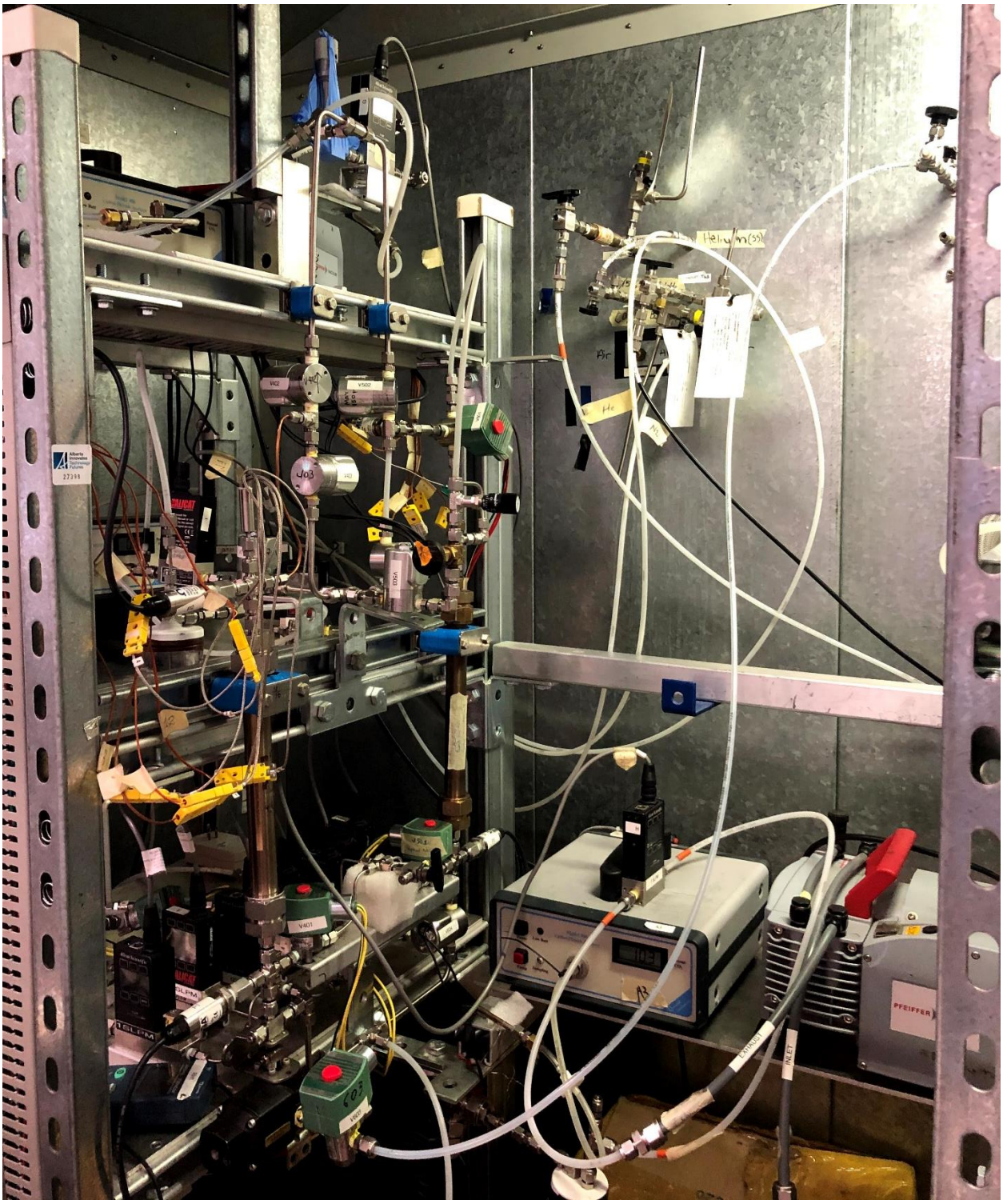

Figure A6.10: The vacuum swing adsorption rig used in this study